1625-210

Galileo

Solid-State Imaging Subsystem Calibration Report: Part 2

K. Klaasen

March 22, 1993

JPL
Jet Propulsion Laboratory
California Institute of Technology
Pasadena, California 91109

JPL D-5880

Distribution

Galileo Imaging Science Team
SSI Associated IDSs
Imaging Science Group

D. Alexander	168-514
C. Avis	168-514
M. Baxter	168-514
R. Carlson	183-601
A. Collins	300-315
R. Davis	264-211
W. Fawcett	264-441
S. Howell	PSI, Tucson
T. Johnson	183-501
K. Klaasen (20)	168-222
S. LaVoie	168-514
R. Mitchell	264-419
C. Stevens	168-227
G. Stuffelbeam	264-419
L. Wainio	168-514
R. West	169-237
K. Wilson	161-135
G. Yagi	168-427
J. Yoshimizu	168-514
Vellum (2)	lll-B25
GLL Project Library (2)	264-419

ACKNOWLEDGEMENTS

Thanks are due to the following individuals for their efforts in acquiring the SSI calibration data analyzed for this report: H. Breneman, B. Paczkowski, J. Farrar, D. Thiessen, J. Bousman/ M. Clary, P. Kobzeff, B. Woo, and J. Johnston.

I am also indebted to the following JPL Multi-mission Image Processing Laboratory (MIPL) personnel for their roles in data processing and analysis: C. Avis, D. Alexander, M. Baxter, M. Pestana, L. Wainio, and L. Wynn.

Sections of this document were written and many of the figures were prepared by H. Breneman, C. Hansen, A. Harch, and C. Hefferman, whose contributions are also much appreciated.

TABLE OF CONTENTS

GALILEO SOLID-STATE IMAGING SUBSYSTEM CALIBRATION REPORT - PART 2

Section I - Introduction

This report documents the results of laboratory calibrations and tests performed between 1986 and 1989 on the Solid-State Imager (SS1) camera for the Galileo mission. It serves as a supplement to Part 1 of this report (Reference 1) , which documents calibration results prior to 1986 and contains much essential background information not repeated here.

SSI calibrations addressed here consist of subsystem-level thermal/vacuum chamber calibrations conducted in June 1988 and January 1989 at camera temperatures of -10°, +8°, and +18°C as well as some room temperature tests of camera gain settings, geometric distortion, and focus performed in May/June 1988 to verify acceptable performance after certain hardware changes had been made. Calibration results reported will refer to data taken during the final pre-launch calibration in 1989 at the expected flight temperature of +8°C unless otherwise indicated. SSI performance characteristics not discussed in this volume should be assumed to remain unchanged from those described in Reference 1. The SSI hardware changes affecting instrument performance characteristics made after 1986 are: 1) modifications to the voltage clocking of the CCD transfer gate to eliminate a geometric distortion problem, and 2) widening of the signal chain post-amp filter bandwidth and readjustment of the "4:1" gain setting to eliminate CCD saturation at less than the full-scale 255 DN level in gain state 2.

Section II - Calibration Equipment

Some modifications to the calibration equipment were made since the 1985 calibration, and some of the equipment was recalibrated prior to the 1988 and 1989 calibrations. The Gamma Scientific spectroradiometer was recalibrated in May, 1988, as a spectral radiance standard, and the Photo Research LS-65 luminance standard was also recalibrated at that time. A secondary absolute luminance standard, a Photo Research BSR-1OO, with a nominal output of 100 ftL was obtained and used as an additional brightness cross-check during the 1989 calibration.

A. Light Cannons

1. Spectral curves

The tungsten and xenon light cannons were recalibrated" Compared to the 1985 calibration, the calibrated spectrum of the tungsten cannon showed a substantial increase in radiance at wavelengths beyond 800 nm relative to that in the visible. At 1000 nm, the radiance relative to that in the visible increased 26% from 1985 to 1988 and another 18% from 1988 to 1989. This increase is in contrast to a total decrease of 31% in the

calibrated 1000-nm output relative to that in the visible between 1982 and 1985. The calibrated tungsten cannon output in the violet at 400 nm has also been highly variable over the years showing a decrease relative to the green output of 15% from 1985 to 1988 followed by an increase of 43% from 1988 to 1989 (compared to a 25% decrease between 1982 and 1985). No satisfactory explanation for this spectral variability has been developed. It is recognized that the measurement accuracy of the Gamma spectroradiometer is poorer at the wavelength extremes since its silicon detector is less sensitive there. However, the measurement errors were not expected to be as large as the amount of variation seen in the calibrated spectrum from year to year.

When the response of the SSI to the tungsten cannon is examined over the years from 1983 to 1989 for each of the SSI filters with respect to that for the green filter, and taking into account the effects of adding light flood to the SSI and changing to a thermal vacuum chamber window with different spectral transmission (see Section II.D. below) , the variation in response is only about 9% (one sigma) in the violet, 6% in the >9680 A filter, and less than 3% in the other filters. The significantly larger variations in the calibrated relative spectral output from the tungsten light cannon leads to suspicion that the light cannon spectral calibration contains errors (either the light cannon spectral output at the time of its calibration was not representative of its actual output during the SSI calibration or the spectral calibration of the Gamma spectroradiometer contained

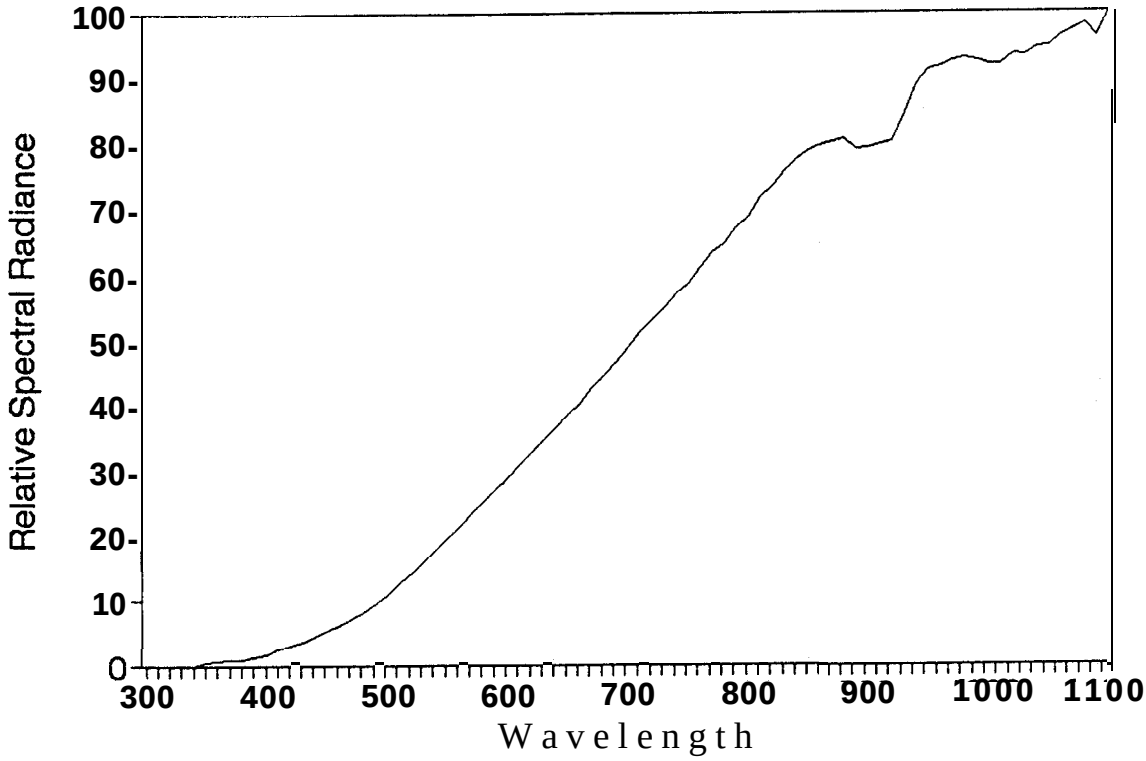

Figure 2-1. Relative spectral radiance for tungsten light cannon

time variable errors) since the probability that the SSI spectral response was varying in exactly the opposite sense as the light cannon spectral output was varying so as to produce small variations in SSI response over the years is very unlikely. Therefore, in reducing the 1989 SSI calibration data, a mean tungsten light cannon relative spectrum of all spectra measured between 1982 and 1989 was assumed. Figure 2-1 shows, and Table 2-1 lists, the relative spectral radiance curve for the tungsten cannon scaled to a brightness level of about 65 ftL at the center of the diffuser.

Table 2-1. Tungsten Light Cannon Relative Spectral Radiance

λ (nm)	value	λ (rim)	value	λ (rim)	value	λ (rim)	value
350	0.53	540	17.75	730	54.79	920	79.97
360	0.67	550	19.87	740	57.22	930	84.43
370	0.82	560	21.55	750	58.49	940	88.88
380	0.82	570	23.57	760	60.87	950	91.11
390	1.30	580	25.25	770	63.27	960	91.57
400	1.63	590	27.26	780	64.52	970	92.43
410	2.52	600	28.85	790	66.76	980	92.75
420	2.98	610	30.75	800	68.65	990	92.48
430	3.68	620	32.86	810	71.54	1000	91.86
440	4.42	630	34.54	820	73.12	1010	91.79
450	5.33	640	36.42	830	75.52	1020	93.44
460	6.22	650	38.46	840	77.28	1030	93.18
470	7.11	660	40.07	850	78.60	1040	94.43
480	8.26	670	42.35	860	79.46	1050	94.52
490	9.61	680	44.30	870	79.99	1060	96.11
500	10.98	690	46.39	880	80.38	1070	96.97
510	12.71	700	48.73	890	78.84	1080	97.86
520	14.29	710	51.24	900	79.10	1090	95.94
530	16.12	720	53.14	910	79.53	1100	100.00

Figure 2-2 shows, and Table 2-2 lists, the relative spectral radiance curve for the xenon cannon set to a brightness level of about 300 ftL at the center of the diffuser. One of the xenon bulbs had to be replaced just prior to beginning the 1989 SSI calibration. These data reflect the configuration of the cannon after the bulb replacement.

2. Field flatness

Figures 2-3 and 2-4 show the remeasured tungsten and xenon light cannon brightness falloff as a function of distance from the center of the diffuser.

3. Brightness calibration

The relative brightness versus iris Veeder root counter setting for the light cannons showed no apparent change from previous calibrations. The absolute brightness scale was determined periodically during the SSI calibration period using the Gamma Model 2000 telephotometer to compare the outputs from the light

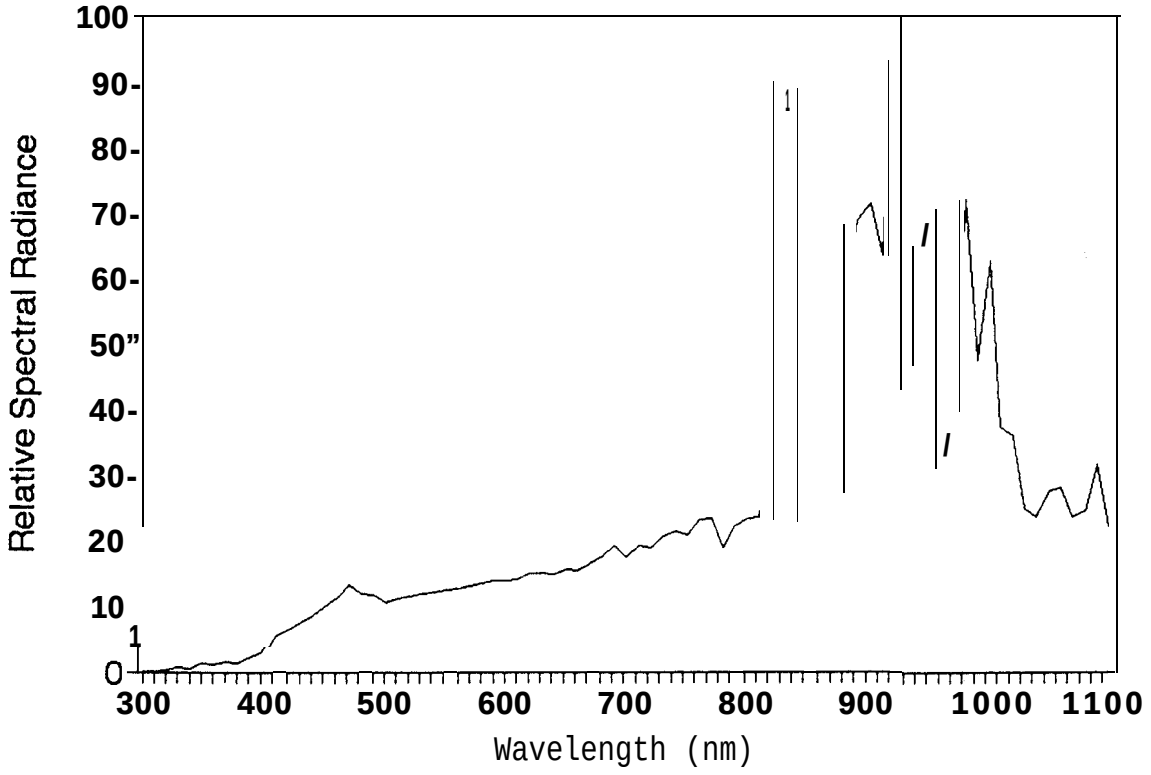

Figure 2-2. Relative spectral radiance for xenon light cannon

Table 2-2. Xenon Light Cannon Relative Spectral Radiance

λ (nm)	value	λ (nm)	value	λ (nm)	value	λ (nm)	value
300	0.11	510	11.18	710	19.21	910	63.46
310	0.18	520	11.47	720	18.76	920	100.00
320	0.27	530	11.86	730	20.64	930	43.06
330	0.66	540	12.08	740	21.31	940	64.58
340	0.48	550	12.57	750	20.81	950	70.64
350	1.29	560	12.77	760	23.04	960	31.17
360	1.16	570	13.16	770	23.34	970	43.05
370	1.42	580	13.51	780	18.83	980	71.88
380	1.36	590	13.89	790	22.13	990	47.34
390	2.15	600	13.79	800	23.32	1000	62.43
400	2.95	610	14.14	810	23.57	1010	37.28
410	5.67	620	15.00	820	38.78	1020	35.97
420	6.44	630	15.07	830	92.55	1030	24.97
430	7.55	640	14.84	840	52.43	1040	23.49
440	8.59	650	15.68	850	23.10	1050	27.64
450	9.98	660	15.55	860	21.53	1060	28.13
460	11.33	670	16.51	870	27.84	1070	23.58
470	13.38	680	17.53	880	57.81	1080	24.49
480	11.99	690	19.25	890	69.07	1090	31.63
490	11.79	700	17.34	900	71.62	1100	22.22
500	10.60						

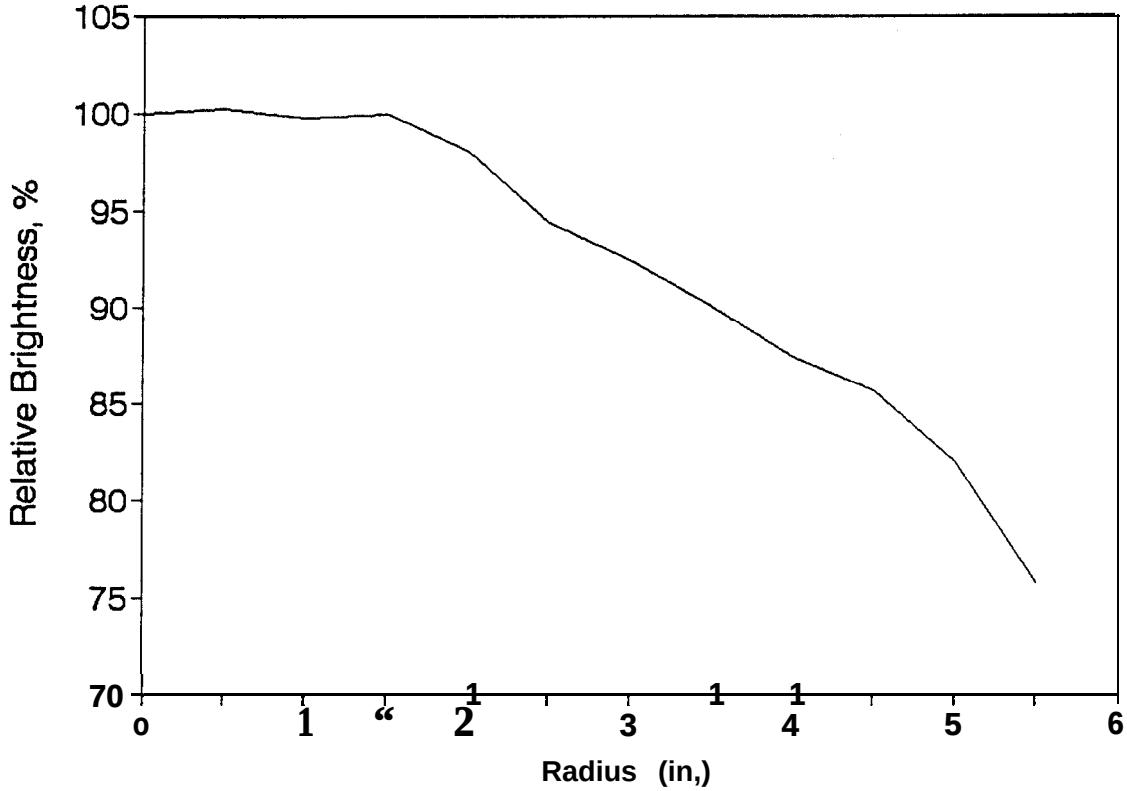

Figure 2-3. Tungsten light cannon field flatness

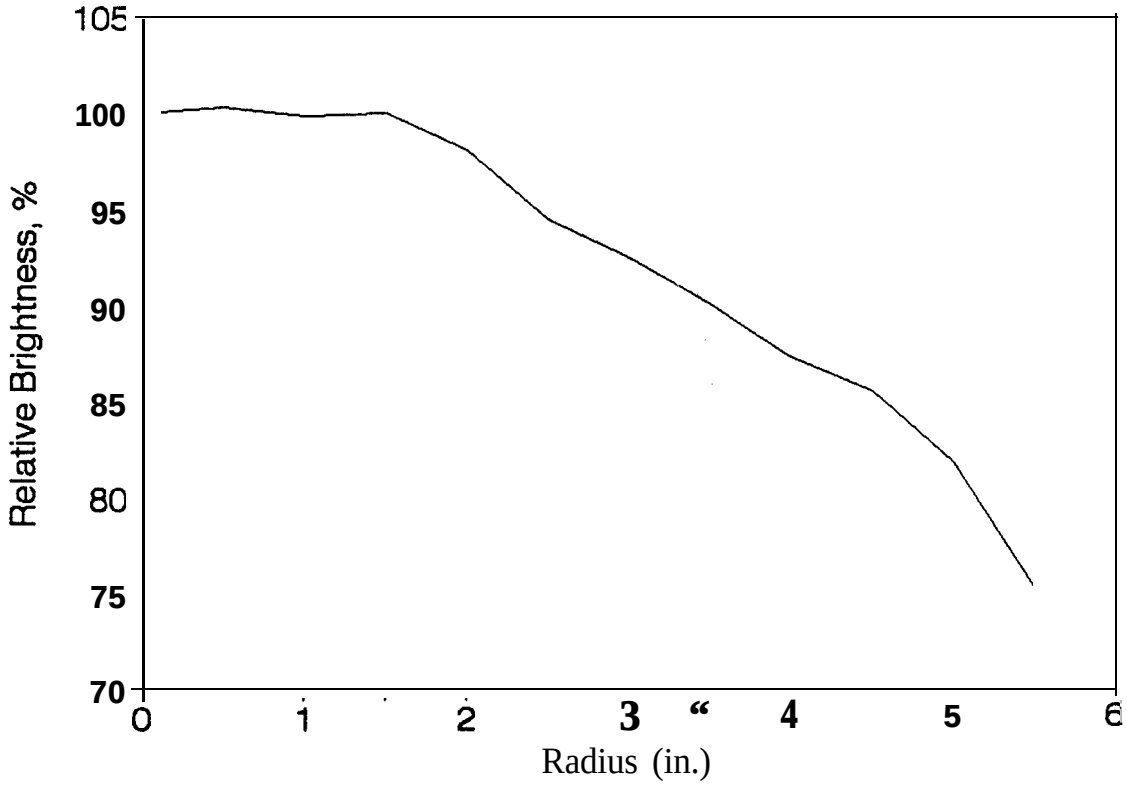

Figure 2-4. Xenon light cannon field flatness

cannon and the LS-65 and BSR-100 luminance standards. The LS-65 and BSR-100 brightness levels were measured to be stable and consistent relative to each other to within better than ±2%. The tungsten cannon Veeder root setting that yielded the same telephotometer reading as the LS-65 standard was determined for LS-65 settings of 67, 12.5 and 1.0 ftL before and after the SSI radiometric calibrations at each of the three camera temperatures. The Veeder root settings varied only slightly and randomly for different measurements corresponding to equivalent brightness variations of 2.4% at 67 ftL, 3.0% at 12.5 ftL, and 6.3% at 1.0 ftL (1 sigma). The xenon cannon Veeder root setting that yielded the same telephotometer reading as the LS-65 set to 300 ftL was also determined regularly throughout the SSI calibration period. Again, the Veeder root settings varied only slightly yielding corresponding equivalent brightness variations of 2.2%. Based on these measurements, the SSI data were reduced assuming that the tungsten light cannon remained stable and repeatable over the course of the calibration period, and that the light cannon brightness varied only as the Veeder root setting was changed.

B. Collimators

All of the thermal vacuum chamber SSI imaging calibrations as well as some imaging tests at room temperature were performed with the GLL MVM collimator. Figure 2-5 shows, and Table 2-3 lists, the relative spectral radiance output by the collimator

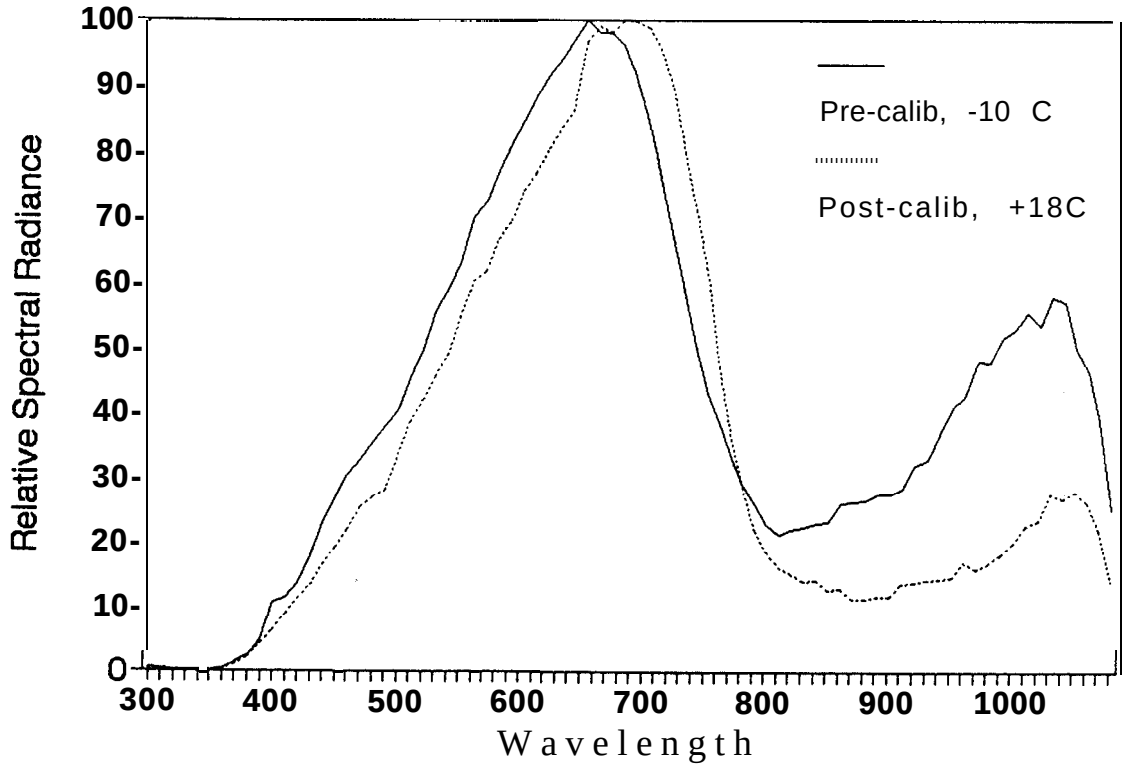

Figure 2-5. Relative spectral radiance for MVM collimator

Table 2-3. MVM Collimator Relative Spectral Radiance, Pre-calibration, -lO°C

λ (rim)	value	λ (nm)	value	λ (rim)	value	λ (rim)	value
350	0.1	540	49.7	730	76.8	920	27.5
360	0.1	550	55.4	740	67.5	930	28.2
370	0.2	560	58.9	750	59.8	940	32.0
380	0.3	570	63.0	760	50.5	950	32.8
390	1.4	580	70.0	770	42.9	960	36.6
400	2.3	590	72.3	780	38.7	970	40.8
410	4.8	600	76.8	790	33.2	980	42.3
420	10.6	610	81.5	800	28.8	990	47.9
430	11.4	620	84.5	810	25.9	1000	47.6
440	13.5	630	88.4	820	22.6	1010	51.5
450	17.7	640	91.3	830	21.2	1020	52.7
460	23.0	650	94.0	840	21.9	1030	55.2
470	27.1	660	96.7	850	22.4	1040	53.3
480	30.4	670	100.0	860	22.9	1050	57.5
490	32.9	680	97.8	870	23.2	1060	56.7
500	35.5	690	98.0	880	26.1	1070	49.6
510	38.0	700	96.0	890	26.3	1080	46.4
520	40.5	710	91.2	900	26.6	1090	38.8
530	45.2	720	84.5	910	27.4	1100	25.2

lamp/optics combination as measured prior to the start of the 1989 SSI calibration. The 1989 calibration with the SSI at -lO°C was done with the collimator in the configuration that was calibrated. However, at the start of the +8°C SSI imaging calibrations, the collimator bulb burned out and was replaced. The bulb burned out again and had to be replaced at the start of the +18°C calibrations. Therefore, the collimator spectral radiance was never measured with the bulb used for the +8°C SSI calibration. Figure 2-5 also shows, and Table 2-4 lists, the MVM collimator relative spectral radiance as measured after completion of the 1989 SSI calibrations with the bulb used for the +18°C calibration. Some differences in spectral output are seen for different lamp bulbs. For the +8°C calibration, the best we could do is reconstruct a typical spectral radiance curve for the MVM collimator. By assuming that the SSI relative spectral response remained the same over all three temperatures, the SSI response to the MVM collimator using different spectral filters was used to constrain the shape of the reconstructed spectral radiance curve of the collimator at 8°C. This curve is shown in Figure 2-6, and the values are listed in Table 2-5.

Both the SSI and the MVM collimator were focused against the Fairchild collimator after it had been focused using an autocollimation technique. During thermal vacuum calibrations, the MVM collimator focus was rechecked at each temperature by using the SSI to image a focus target in the collimator with the collimator focus set at varying distances. The collimator focus position that resulted in maximum contrast in the SSI images shifted by up to 0.004 inch for the thermal vacuum chamber images relative to

Table 2-4. MVM Collimator Relative Spectral Radiance, Post-calibration, +18°C

λ (nm)	value	λ (nm)	value	λ (nm)	value	λ (nm)	value
350	0.1	540	42.1	730	95.6	920	11.5
360	0.1	550	45.5	740	89.4	930	13.4
370	0.2	560	49.0	750	79.9	940	13.8
380	0.3	570	54.6	760	71.0	950	14.1
390	1.0	580	60.1	770	60.5	960	14.2
400	2.1	590	61.6	780	47.0	970	14.4
410	4.1	600	66.4	790	35.8	980	16.8
420	6.1	610	69.4	800	28.5	990	15.7
430	8.8	620	73.9	810	21.7	1000	16.7
440	11.2	630	76.7	820	18.3	1010	18.0
450	13.2	640	80.4	830	16.0	1020	19.8
460	16.4	650	83.5	840	15.0	1030	22.6
470	19.1	660	86.0	850	13.8	1040	23.3
480	21.9	670	96.6	860	14.0	1050	27.5
490	25.4	680	99.0	870	12.6	1060	26.7
500	27.0	690	97.9	880	12.7	1070	27.8
510	28.0	700	100.0	890	11.1	1080	26.0
520	33.5	710	99.8	900	11.2	1090	21.7
530	38.8	720	98.7	910	11.5	1100	13.9

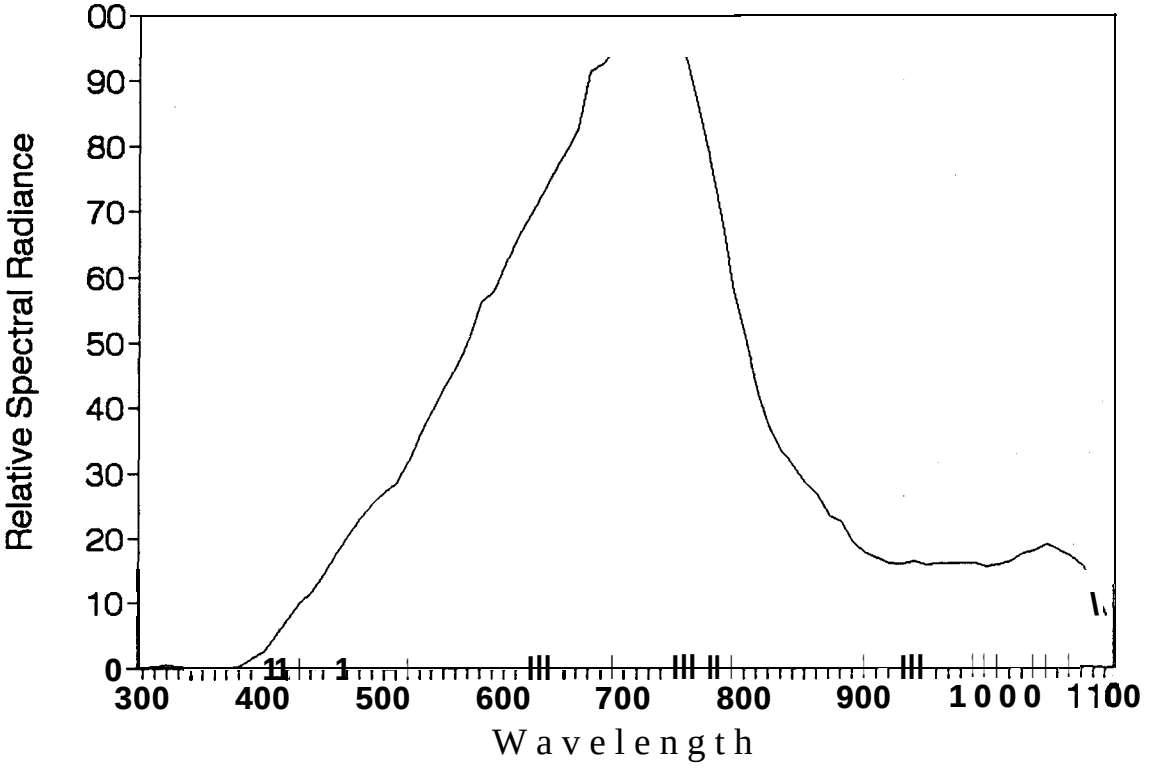

Figure 2-6. Relative spectral radiance for MVM collimator at 8°C

Table 2-5. MVM Collimator Relative Spectral Radiance, Estimated Reconstruction, +8°C

λ (nm)	value	λ (nm)	value	λ (nm)	value	λ (nm)	value
350	0.1	540	39.9	730	100.0	920	16.1
360	0.1	550	43.6	740	98.2	930	16.1
370	0.2	560	46.6	750	92.8	940	16.5
380	0.3	570	50.8	760	85.8	950	15.8
390	1.5	580	56.2	770	77.2	960	15.9
400	2.6	590	58.0	780	68.1	970	15.9
410	5.1	600	62.2	790	57.7	980	15.9
420	7.6	610	66.1	800	49.9	990	15.9
430	10.1	620	69.3	810	42.3	1000	15.5
440	11.8	630	72.6	820	36.9	1010	15.8
450	14.2	640	75.9	830	33.1	1020	16.5
460	17.8	650	79.5	840	31.2	1030	17.6
470	20.5	660	83.0	850	28.6	1040	18.0
480	23.1	670	91.4	860	26.9	1050	19.0
490	25.5	680	92.7	870	23.5	1060	18.0
500	27.3	690	94.9	880	22.6	1070	17.0
510	28.6	700	98.5	890	19.3	1080	15.4
520	32.2	710	99.5	900	17.7	1090	12.8
530	36.5	720	100.0	910	16.9	1100	8.0

the best collimator focus position determined at room temperature against the Fairchild collimator. The best focus position also changed slightly for different camera temperatures in the thermal vacuum chamber. These shifts are attributed to the optical effects of the thermal vacuum chamber window. Therefore, imaging tests in the thermal vacuum chamber were conducted with the MVM collimator refocused at each temperature to yield maximum SSI image contrast, and the SSI was assumed to remain in focus over the range of camera temperatures tested.

c. Targets

In addition to the targets used in the pre-1986 calibrations, two new types of test targets were incorporated into the SSI imaging tests for the latest calibrations. A knife-edge target was constructed and used to test for scattered light within the SSI field of view and/or charge spreading within the CCD as a function of wavelength. This MVM collimator target consisted of a blackened razor blade covering half of the SSI field of view with the other half left clear.

To provide an improved measure of the SSI spectral response characteristics, a set of images were taken through each SSI filter of the MVM collimator with the collimator output being filtered in turn by one of a set of spectral filters placed in the collimator target holder. The target filters' spectral bands combined to span the SSI spectral response range. The target holder was moved out of the collimator focal plane for these

tests in order to blur out the effects of pinholes in the target filters. Figure 2-7 shows the spectral transmission of each of the target filters used.

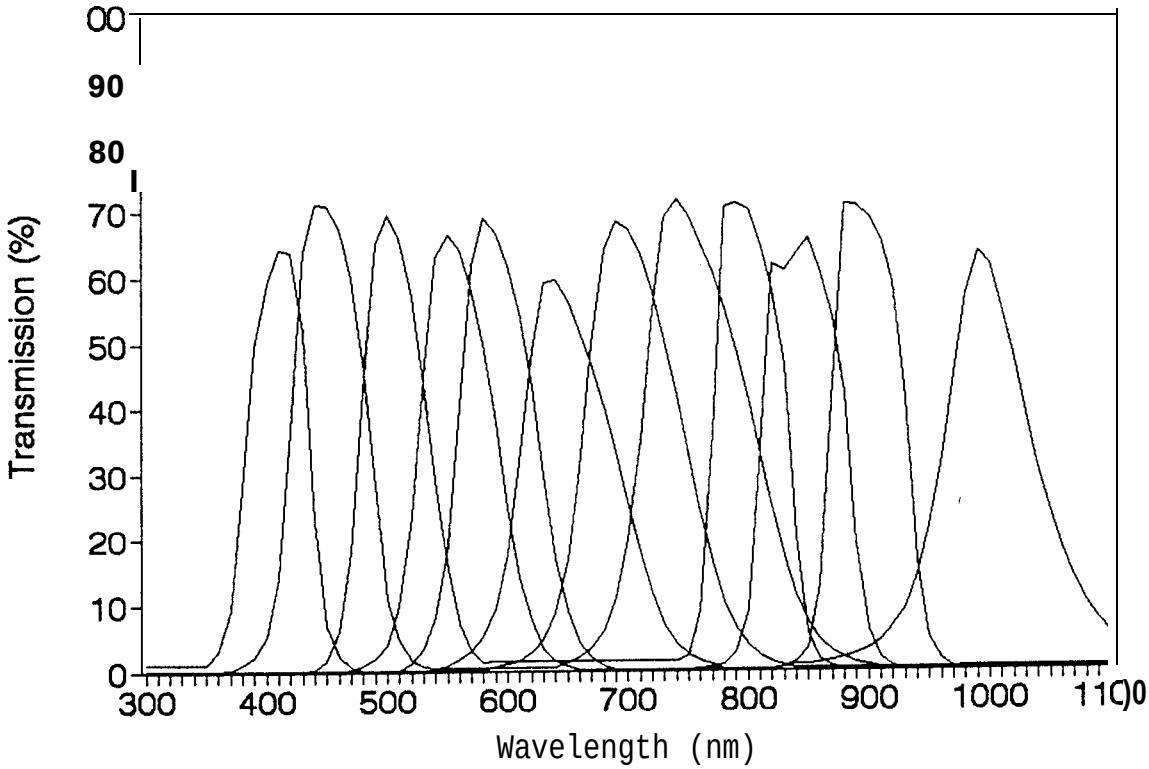

Figure 2-7. Spectral transmission of collimator target spectral filters

D. Calibration Environment

The window in the thermal vaccum chamber used for SSI calibration was broken between the 1985 and 1988 calibrations. Therefore,the calibrations reported in this volume were conducted with a new window having different optical coatings in place. The absolute spectral transmission of the new chamber window is documented in Figure 2-8 and Table 2-6.

Section III - Radiometric Calibrations

A. Reciprocity and Hysteresis

Data from SSI reciprocity tests acquired at all three calibration temperatures were analyzed to determine the SSI shutter offset. Figures 3-1 through 3-3 plot the computed shutter offset, to , versus image line number for each camera temperature tested. The scatter in the values of t_{os} at a given line number is an indication of the accuracy of the t_{os} determination, which

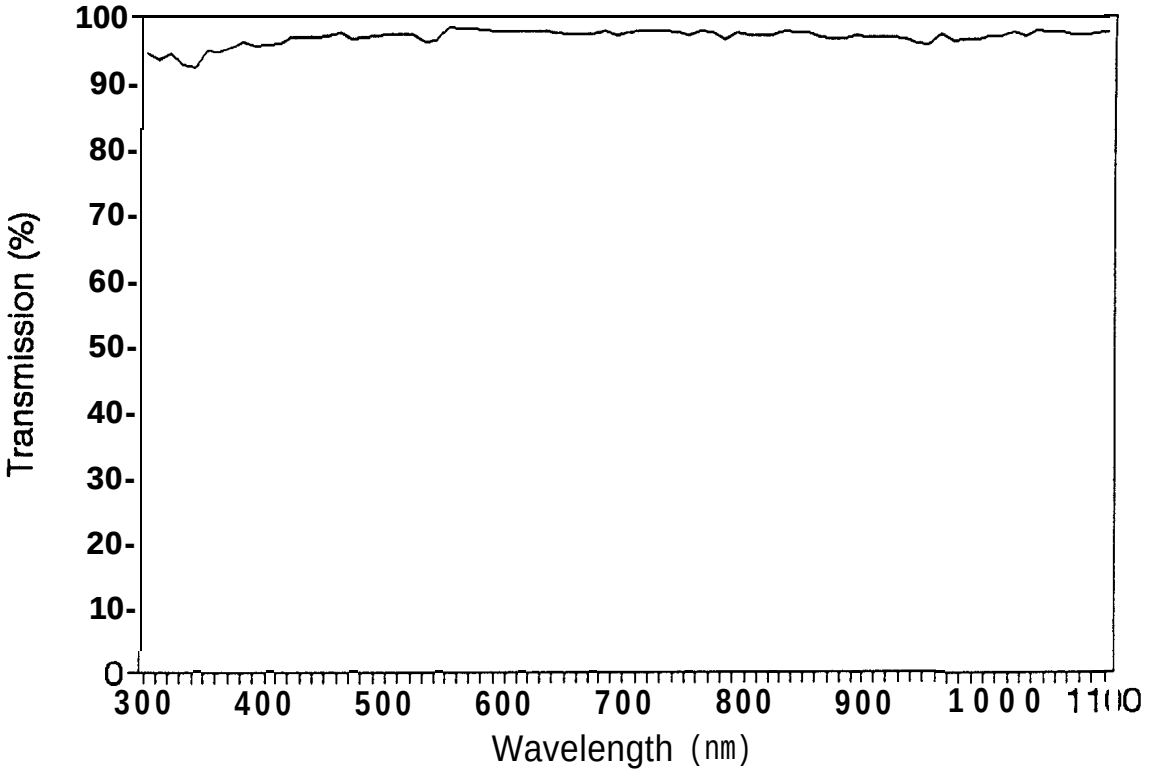

Figure 2-8. Spectral transmission of thermal vacuum chamber window

Table 2-6. Thermal Vacuum Chamber Window Spectral Transmission

λ (nm)	%	λ (nm)	%	λ (nm)	%	λ (nm)	%
350	94.8	540	96.3	730	97.6	920	96.8
360	94.5	550	98.1	740	97.3	930	96.6
370	95.3	560	98.0	750	97.0	940	96.0
380	96.2	570	97.9	760	97.6	950	95.8
390	95.6	580	97.7	770	97.3	960	97.1
400	95.8	590	97.6	780	96.4	970	96.1
410	96.0	600	97.6	790	97.3	980	96.4
420	96.7	610	97.5	800	96.9	990	96.4
430	96.7	620	97.5	810	96.9	1000	96.7
440	96.7	630	97.5	820	97.0	1010	96.7
450	96.9	640	97.4	830	97.5	1020	97.4
460	97.3	650	97.1	840	97.4	1030	96.8
470	96.6	660	97.2	850	97.4	1040	97.5
480	96.8	670	97.1	860	96.8	1050	97.3
490	96.9	680	97.6	870	96.5	1060	97.3
500	97.2	690	96.9	880	96.5	1070	97.0
510	97.1	700	97.3	890	97.0	1080	97.0
520	97.2	710	97.6	900	96.7	1090	97.1
530	96.1	720	97.5	910	96.8	1100	97.5

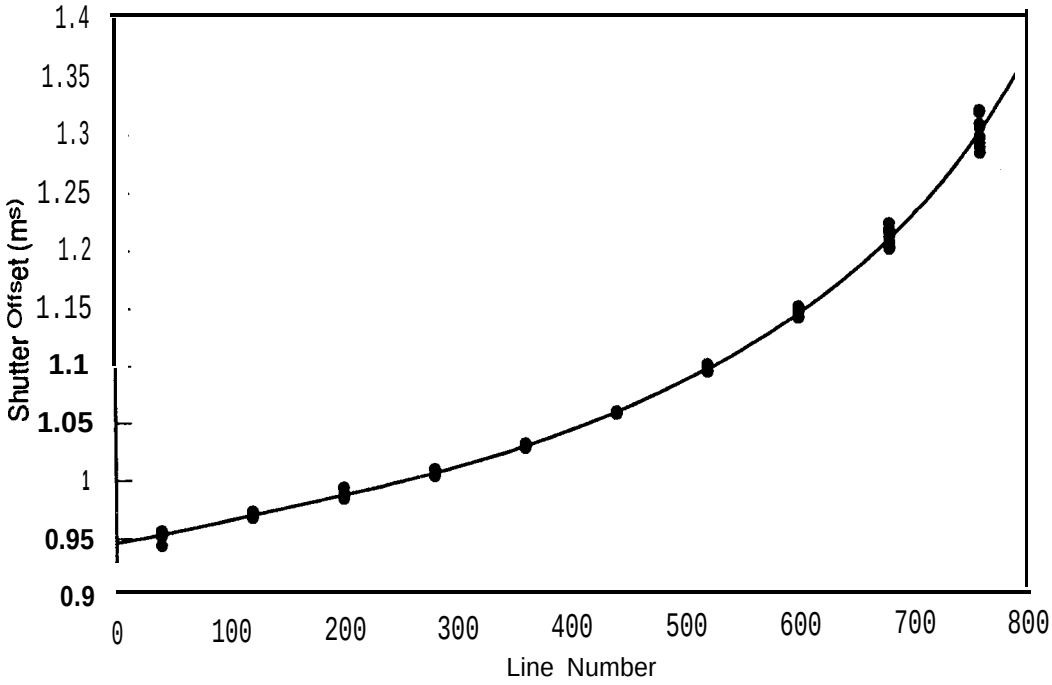

Figure 3-1. Shutter offset t_{os} vs. image line number at instrument temperature of -10° C

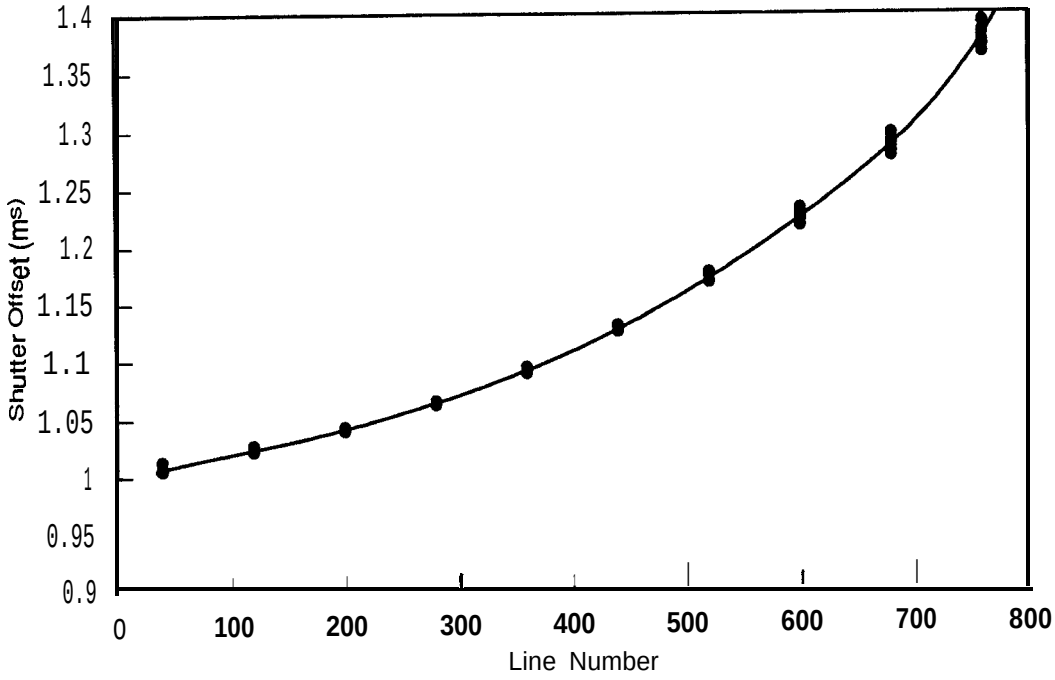

Figure 3-2. Shutter offset t_{os} vs. image line number at instrument temperature of +8°C

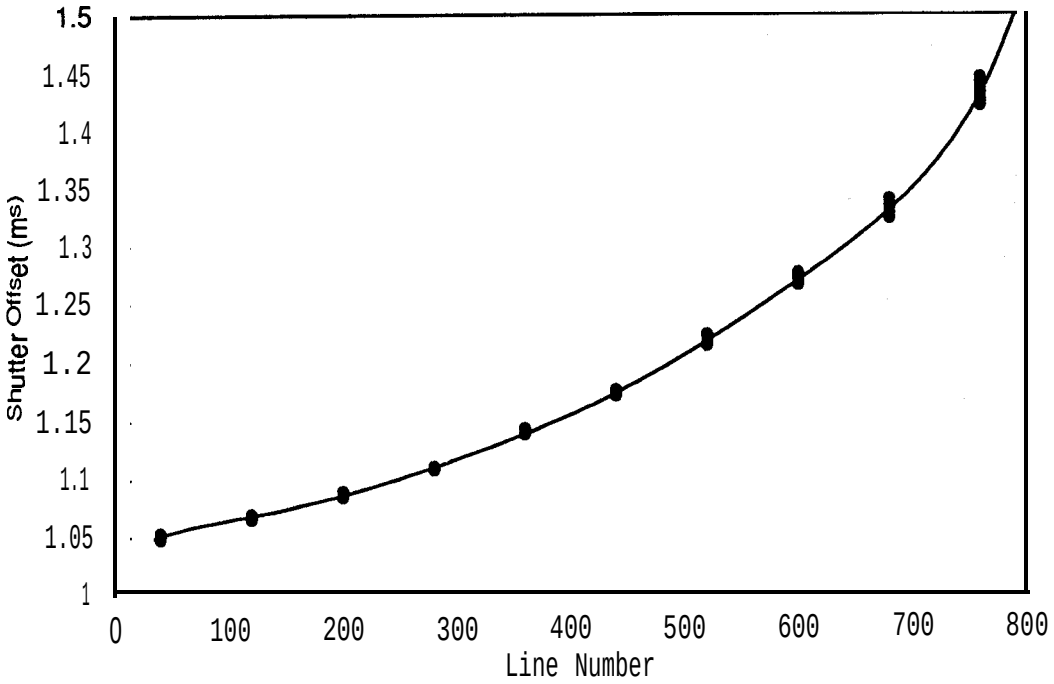

Figure 3-3. Shutter offset t_{os} vs. image line number at instrument temperature of +18°

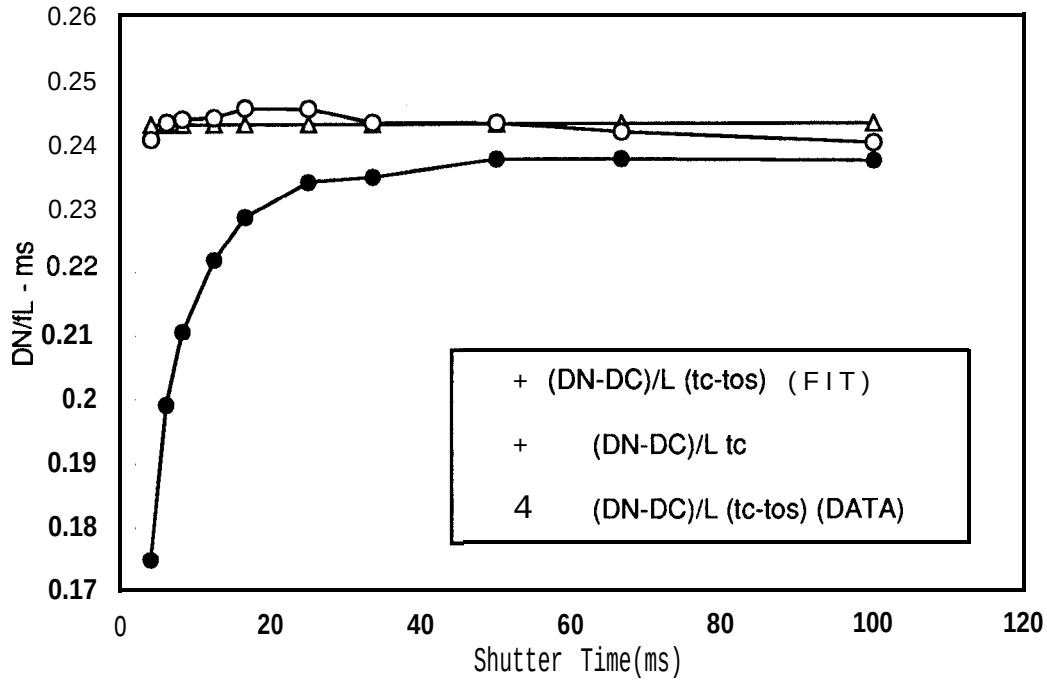

Figure 3-4. The quantities (DN-DC)/Lt and (DN-DC)/L(t_c-t_{os}) vs. shutter time (see text for definition of symbols)

is estimated to be better than + 0.01 msec. Figure 3-4 plots the quantity $(DN-DC)/L(t_c-t_{os})$, which for a fully reciprocal system should be a constant for any values of L and t_{os} and the uncorrected quantity $(DN-DC)/Lt_c$ versus t_c for the 8°C case where

DC = DN of a zero-exposure frame
L = light source brightness (ftL)
t_c = commanded exposure time (msec)
t_{0s} = shutter offset (msec) .

Note that the shutter offset correction results in almost perfect reciprocity (to within ±1%, which is as good as the relative light cannon brightness is known).

No measurable hysteresis was observed in the SSI response.

B. Flat-field Light Transfer

1. Method

The method of light transfer calibration used was the same as that used in the 1985 calibration (see Reference 1) with the following changes. The number of different light cannon settings used to acquire all the different light transfer sets was reduced to 3 to minimize the number of variables involved in solving for the best-fit SSI radiometric response model. Dark frames were inserted between successive high-signal-level frames taken in the summation mode to eliminate any charge spillover from one frame to another in the low-full-well columns. Light transfer sets were added in the summation mode in all gain states with the CCD clock voltages set to the inverted level to better assess any vertical striations in the summation mode. Finally, a series of two-point (zero exposure and near-full-scale signal) light transfer sets were added in order to 1) serve as a check on the absolute repeatability of the light cannon settings and the SS1 response and 2) acquire summation-mode data in the higher gain states for each filter position for use in calibration file construction (10-point transfer data were acquired for high-gain summation modes only through the green filter) .

Figures 3-5 through 3-8 show examples of contrast-enhanced flat-field images acquired as part of the light transfer data sets. The location and number of the dust-speck “donuts” remains unchanged from 1985 except for the removal of two specks from the inside surface of the quartz radiation plug (which was cleaned during the course of the SSI hardware rework).The most significant difference from the 1985 results is the elimination of the summation-mode vertical striations in the first 100 columns (see Figure 3-8). The change in the CCD transfer gate clocking apparently also corrected whatever was causing these striations, which had been thought to occur at the transfer gate.

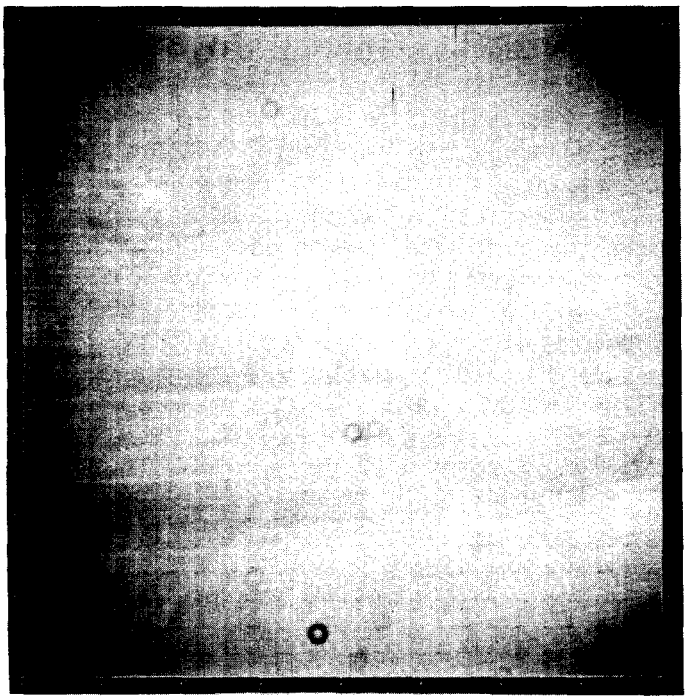

Figure 3-5. Contrast-enhanced flat-field image acquired using the violet filter, 8 2/3-see frame rate and gain state 2.

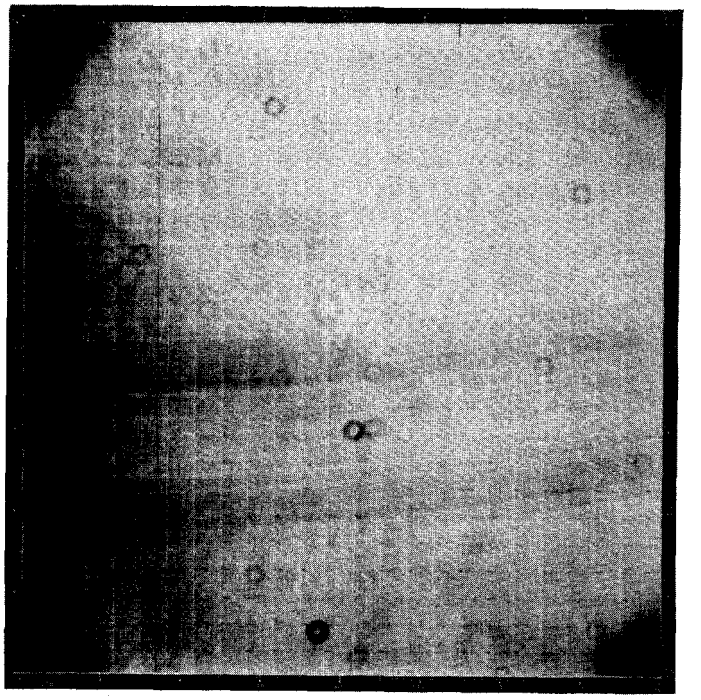

Figure 3-6. Contrast-enhanced flat-field image acquired using the 7560 A filter, 8 2/3-see frame rate and and gain state 3.

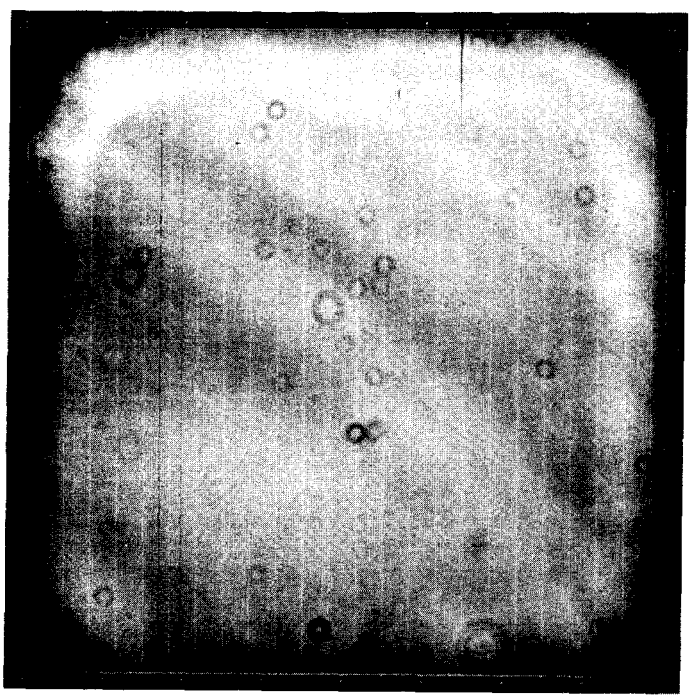

Figure 3-7. Contrast-enhanced flat-field image acquired using the >9680 A filter, 8 2/3-see frame rate and gain state 3.

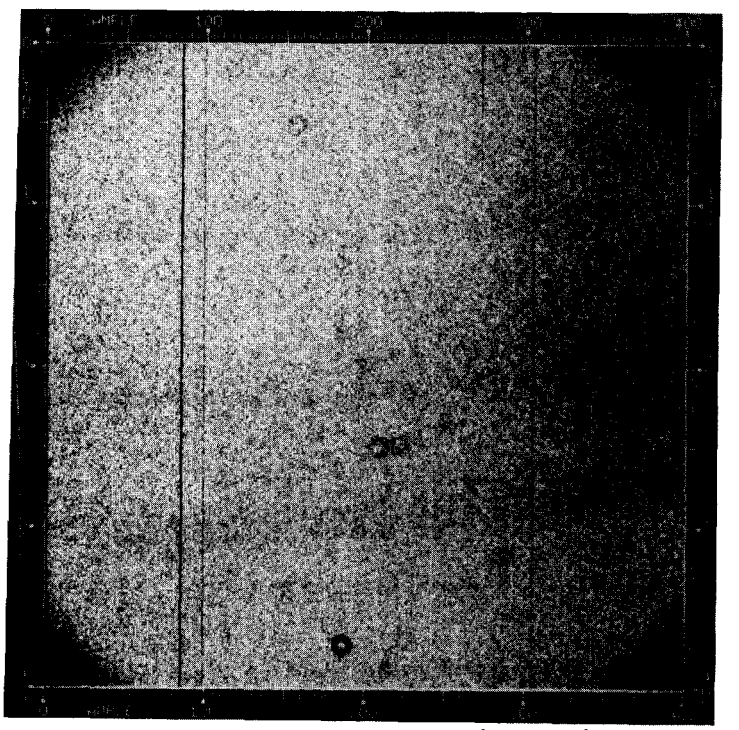

Figure 3-8. Contrast-enhanced flat-field image acquired using the green filter, summation mode, 2 l/3-see frame rate, gain state 1

2. Gain factors

The high-gain state conversion factor from signal electrons to DN (called the system gain constant) as determined by the photon transfer curve technique is 35.9 e^-/DN for the +8°C 1989 calibration. The uncertainty in the calculation of this value is quite large, ±10%. Table 3-1 shows the history of the determinations of this factor for the SSI high-gain state. The 1983 determination is thought to be more uncertain than the others since the SSI uneven bit weighting was significantly worse for that calibration, the increased noise of which can cause the photon transfer technique to yield an incorrect answer (a lower value of e^-\DN than actually exists). The SSI gain was reduced about 5% between 1983 and 1984, which should have caused a corresponding increase in the system gain constant (i.e., more electrons are required to produce a given DN level). The SSI gain was increased by about 10% between 1985 and 1988. Thus the +8°C system gain constant was expected to be about 38.7 e^-/DN in 1988 and 1989 (0.9 x 43.0, the average value from 1984 and 1985). While the values actually measured in 1988 and 1989 differed substantially, they average to the expected 38.7 e^-/DN and both are within the quoted 10% error from this mean. Therefore, we assume that the correct SSI system gain constant at +8°C for the 1988/89 calibrations was 38.7 e^-/DN. Using this assumption, Table 3-1 also lists the expected system gain constants at the other calibration temperatures based on the SSI sensitivity ratios at these temperatures as determined from a best-fit to all the radiometric calibration data. The trend of increasing system gain constant with increasing camera temperature is confirmed although the slope determined using the photon transfer technique is somewhat steeper than that from the overall radiometric calibration fit. The best-fit to the entire radiometric calibration data set actually yields a system gain constant at +8°C of 38.1 e^-/DN.

Table 3-1. System Gain Constant (e^-/DN) History

	SSI Temperature		
Year	-l0°c	+8°C	+18°C
1983	36.7	33.8	33.0
1984		42.0	
		43.2	
1985		43.8	
1988	36.5	41.5	44.2
1989	35.0	35.9	42.7
'89 best-fit temp dependence	36.9	38.7*	40.5

*assumed value

The gain state ratios were measured in several different ways. The most straightforward measurement involves simply ratioing the mean DN-DN_0 for the same pixel area of two frames for which only the gain state has been changed. From 2 to 9 pairs of frames were available for the various gain ratios at

each temperature. No differences in gain ratio with temperature were apparent within the measurement accuracy (typically better than 2% standard deviation, 5% worst case). The 2x2 pixel summation mode train factor was determined using only violet and green filter data to avoid any residual bulk image effects. Combining the data for all temperatures yielded the gain ratios listed in Column A of Table 3-2-.

Table 3-2. Gain State Ratio Factors

gain state	A	B	C
1	46.646±.301	47.187±.294	47.142±.957
	9.720±.048	9.794±.055	9.809±.160
	4.799±.020	4.818±.013	4.806±.058
4	1.0	1.0	1.0
2 x 2 sum	0.2027±.0016	0.2021±.0016	0.1988±.0011

gain state	D	E	F
1	47.223±.361	47.233±.127	47.135±.l03
2	9.779±.064	9.775±.o19	9.771±.016
3	4.829±.019	4.832±.009	4.824±.007
4	1.0	1.0	1.0
2 x 2 sum	0.1984±.0008	0.1999±.0007	0.1997±.0004

The additional summation mode gain factor, due to slightly different sample timing in this mode, is about 1.25, reduced from the value of about 1.32 in 1985 because of the change in the signal chain post-amp filter bandwidth.

A second approach to determining the gain ratios involved performing least-squares linear fits to the mean DN level versus exposure time for a 50X50 pixel area for light transfer sets acquired at the same camera temperature, light cannon setting, and filter position but using different gain states and then ratioing the resulting slopes of the light transfer functions. Summation-mode cases in filters other than violet were excluded because they include distortions due to the effects of residual bulk image. Combining the resulting ratios for all temperatures yields the values listed in Column B of Table 3-2.

A third approach involved ratioing the slopes of best-fit linear light transfer function slopes determined from fits of mean DN versus exposure (ftL-msec) for 256 20x20 pixel areas for light transfer data sets acquired at the same temperature and filter position but using different gain states. This was done only for +8°C data. The major error source in this approach is the accuracy of the light cannon brightness calibration since different light cannon settings are often used for the different gain states. The resulting ratios are given in Column C of Table 3-2. They are consistent with the values determined by the other methods although the uncertainties are greater.

A fourth approach involved ratioing the mean values of the best-fit linear light transfer function slopes determined on a pixel-by-pixel basis (see subsection III.B.6. below) for data sets with the same filter and a temperature of +8°C. Again, the

use of different light cannon settings for the different gain states tends to increase the scatter in the computed ratios, which are listed in Column D of Table 3-2.

Finally, a least-squares adjustment to all camera and light cannon radiometric parameters to best match the entire radiometric calibration data set resulted in the gain ratios of Column E in Table 3-2.

The weighted means of the gain ratio values determined in these various ways are listed in Column F of Table 3-2 and represent the best determination of the SSI gain switch ratios. The uncertainties in the ratios are only about 0.2%.

3. Filter factors

The SSI filter factors for the tungsten light cannon as viewed through the thermal vacuum chamber window were determined in several different ways. The most straightforward measurement involves simply ratioing the mean $DN-DN_0$ for the same pixel area of two frames for which only the filter and gain state have been varied (allowing the gain to vary is necessary in order to be able to relate each filter back to the clear filter using chains of response ratios) . The resulting filter factors have uncertainties of about ±2%. Contrary to the results of 1985, no detectable variation in the filter factors with camera temperature was observed. Column A of Table 3-3 lists the filter factors determined using the above method.

Table 3-3. Thermal Vacuum Calibration Filter Factors

Filter	Position	A	B	C	D
Clear	0	1.0	1.0	1.0	1.0
Green	1	12.22	12.39	12.39	12.34 ±.05
Red	2	5.414	5.381	5.370	5.387±.032
Violet	3	339.5	342.0	341.8	338.6 ±3.9
7560 A	4	21.82	21.46	21.63	21.52 ±.13
>9680 A	5	59.99	58.84	59.57	58.87 ±.93
7270 A	6	43.49	43.00	43.16	43.02 ±.25
8890 A	7	73.69	72.27	72.99	72.15 ±.86

A second approach to determining calibration-source filter factors was to ratio the best-fit DN/exposure slopes for 256 20x20 pixel areas for light transfer data sets acquired through different filters. This was done for data acquired in gain state 2 (-380 e^-/DN). The resulting filter factors are given in Column B of Table 3-3. The estimated uncertainties are ±2%. These values agree with those in Column A to within 2%.

A third approach involved ratioing the means of the best-fit light transfer function slopes determined on a pixel-by-pixel basis for data sets acquired at an SSI temperature of +8°C at the same light cannon setting using the previously derived gain state ratios to adjust for any gain differences. The results are listed

Table 3-4. Filter factors and effective wavelengths for SSI filters (based on best-fit spectral response model).

source spectrum		filter clear	green	red	violet	7560A	9680A	7270A	8890A
gray	FF	1.000	7.209	5.793	23.80	34.14	139.5	62.52	157.8
	eff wvl	634.9	559.2	664.4	409.4	756.8	991.3	731.2	887.5
solar	FF	1.000	6.092	5.868	24.50	42.73	281.3	73.91	254.9
	eff wvl	612.1	558.9	663.4	410.8	756.7	989.6	731.1	887.4
Jupiter NTrZ	FF	1.000	5.488	5.628	28.72	42.56	686.0	97.68	1820.
	eff wvl	603.6	558.8	663.4	411.8	756.6	988.7	731.6	885.5
Jupiter EQ	FF	1.000	5.394	5.234	38.37	40.74	628.4	92.75	1400.
	eff wvl	612.0	559.2	663.4	412.7	756.5	989.0	731.5	885.8
Jupiter S PH	FF	1.000	5.556	5.475	32.82	40.90	369.1	78.07	449.4
	eff wvl	610.0	558.9	663.4	412.1	756.6	989.6	731.3	887.3
Io reddest	FF	1.000	6.111	4.937	85.80	35.20	241.3	61.61	217.8
	eff wvl	638.3	559.9	663.7	417.8	756.7	989.5	731.1	887.4
Io average	FF	1.000	6.295	5.179	47.51	36.93	253.2	64.62	228.5
	eff wvl	629.8	559.5	663.7	414.2	756.7	989.5	731.1	887.4
Io whitest	FF	1.000	6.649	5.569	25.09	39.71	272.3	69.49	245.7
	eff wv1	617.0	559.1	663.7	411.6	756.7	989.5	731.1	887.4
Europa leading	FF	1.000	5.928	5.494	37.74	40.30	276.1	69.70	246.6
	eff wv1	621.5	558.9	663.6	412.6	756.7	989.2	731.1	887.4
Europa trailing	FF	1.000	5.651	5.235	63.29	38.40	263.1	66.41	234.9
	eff wvl	630.0	559.0	663.6	414.7	756.7	989.2	731.1	887.4
Ganymede	FF	1.000	6.097	5.417	35.75	40.10	276.5	67.91	244.8
	eff wvl	622.3	559.3	663.6	412.1	756.7	989.2	731.1	887.4
Callisto	FF	1.000	6.003	5.541	36.11	38.74	259.5	69.79	230.7
	eff wv1	622.8	559.0	663.5	412.4	756.7	989.3	731.1	887.4
Moon	FF	1.000	6.534	5.416	36.32	35.25	197.2	62.84	190.8
	eff wv1	633.4	559.5	664.0	412.2	756.8	990.5	731.1	887.5
Venus	FF	1.000	5.833	5.611	38.60	40.87	269.0	70.68	243.7
	eff wvl	620.1	558.9	663.4	413.5	756.7	989.6	731.1	887.4

in Column C of Table 3-3. The standard deviations in the computed filter factor values were typically about 0.4%.

Finally, a least squares adjustment to all SSI and light cannon radiometric parameters to best match the entire calibration data set resulted in the filter factors given in Column D of Table 3-3 along with their uncertainties.

Table 3-4 lists the SSI filter factors and effective wavelengths computed from the best-fit SSI spectral response model for various other source spectra of interest.

4. Linearity

Fits of linear response functions to the average SSI DN level over a 50X50 pixel area versus exposure time were performed for each light transfer data set acquired. The best-fit shutter offset correction was made. For full-resolution mode data, the typical rms error in the fits was about 0.12 DN, with a typical maximum error of about 0.21 DN. The largest rms error was 0.23 DN, and the largest error was 0.49 DN. For the summation mode, the typical rms error in the fits was about 0.21 DN, with a typical maximum error of 0.46 DN. The largest summation-mode rms error was 0.65 DN, and the largest error was 1.10 DN. These errors are similar to those found for the 1985 calibration data. Figures 3-9 through 3-20 show examples of typical residuals (in both DN and percent) of mean response versus relative exposure for various gain states, filters, and summation mode. These residuals are from linear fits to the average response over 256 20x20 pixel areas distributed over the CCD array and are generally somewhat larger than those from the fits to the single 50x50 pixel area discussed above. The residuals are randomly distributed with exposure level and are typically less than 1% except for the offset level (zero exposure) .

5. Sensitivity

SSI absolute sensitivity was determined using the light transfer data to compute the response in DN/exposure time for the light cannon, which represents a known, calibrated source. Using the light cannon and thermal vacuum chamber window calibration data presented in Sections II.A. and II.D. above, the absolute brightness level in the annulus seen by the SSI through the chamber window can be determined in units of ftL. Thus, we can specify the SSI response in units of DN/ftL-msec to the known calibration source spectral radiance. The results for the clear filter in gain state 2 averaged over 256 20x20 pixel areas are as follows:

Temperature (°C)	-l0	+8	+18
Sensitivity (DN/ftL-msec)	0.1407	0.1349	0.1291

The average sensitivity values for other filters or gain states can be derived using the filter factors and gain state ratios

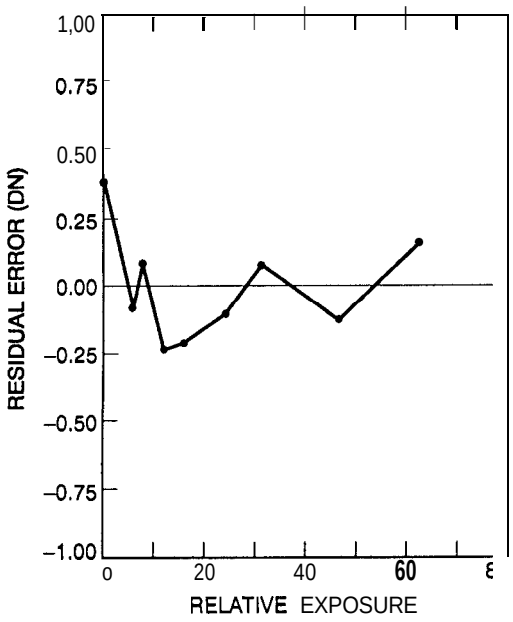

Figure 3-9. Residuals in DN from linear fits to the mean response vs relative exposure for the clear filter, gain state 4.

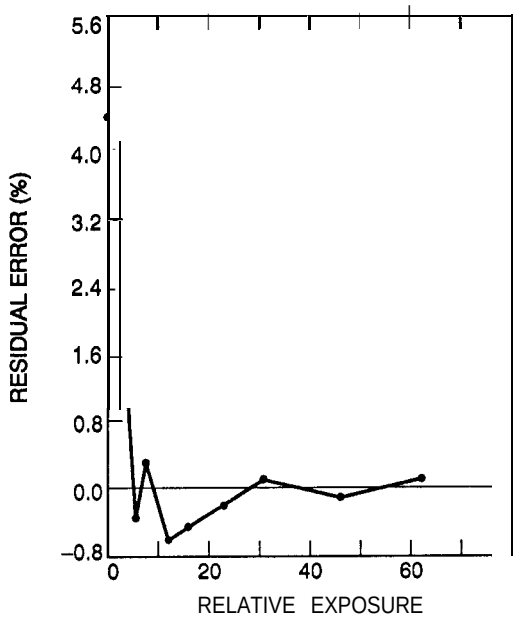

Figure 3-10. Residuals in % from linear fits to the mean response vs relative exposure for the clear filter, gain state 4.

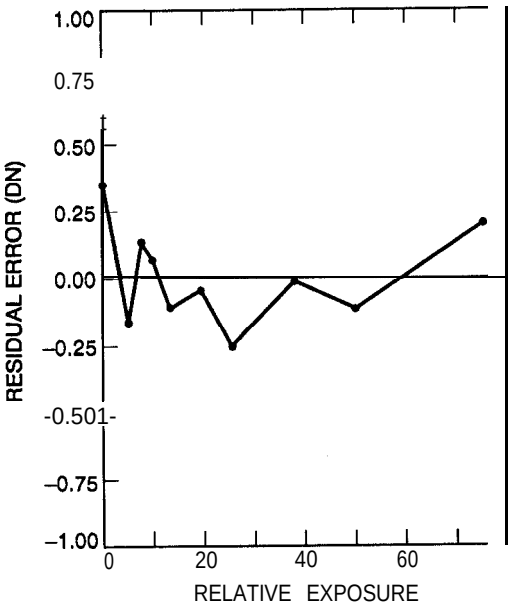

Figure 3-11. Residuals in DN from linear fits to the mean response vs relative exposure for the clear filter, gain state 3.

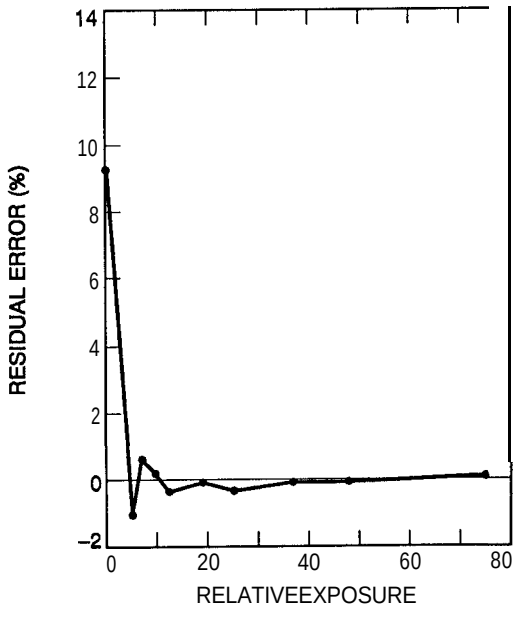

Figure 3-12. Residuals in % from linear fits to the mean response vs relative exposure for the clear filter, gain state 3.

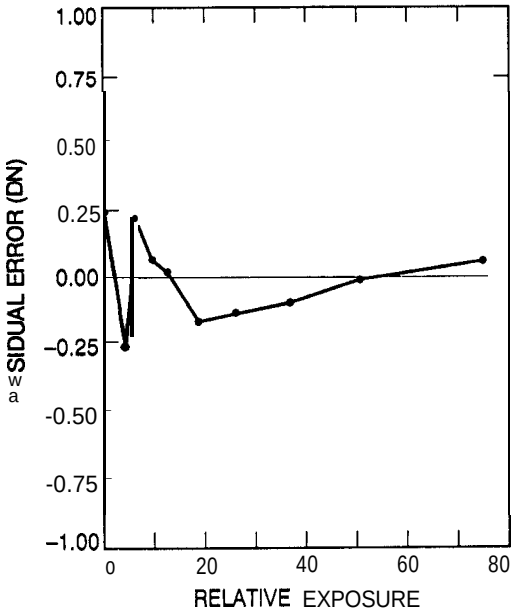

Figure 3-13. Residuals in DN from linear fits to the mean response vs relative exposure for the clear filter, gain state 2.

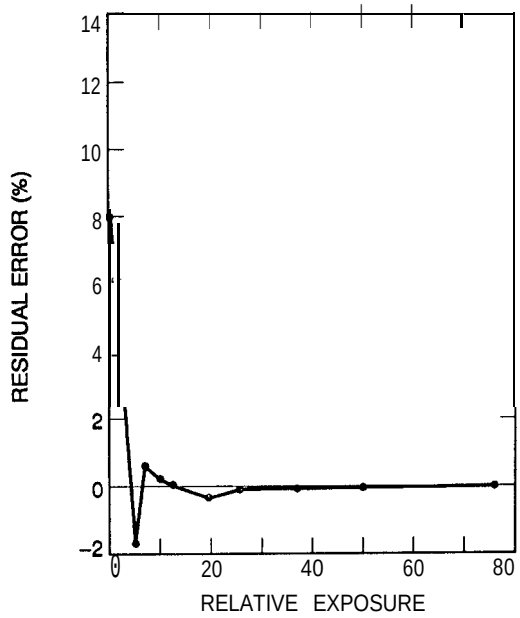

Figure 3-14. Residuals in % from linear fits to the mean response vs relative exposure for the clear filter, gain state 2.

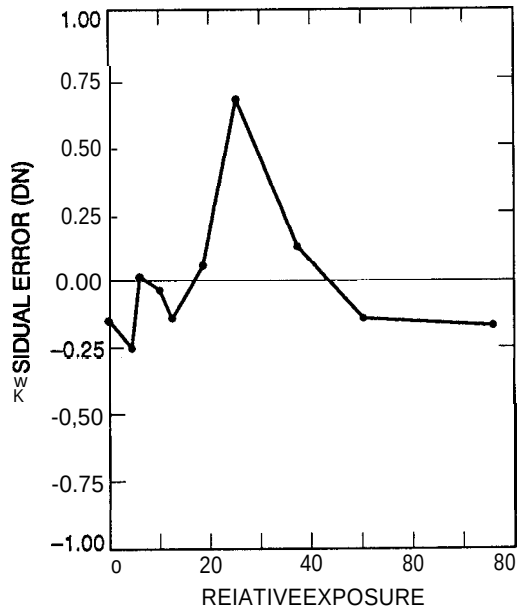

Figure 3-15. Residuals in DN from linear fits to the mean response vs relative exposure for the clear filter, gain state 1, summation mode.

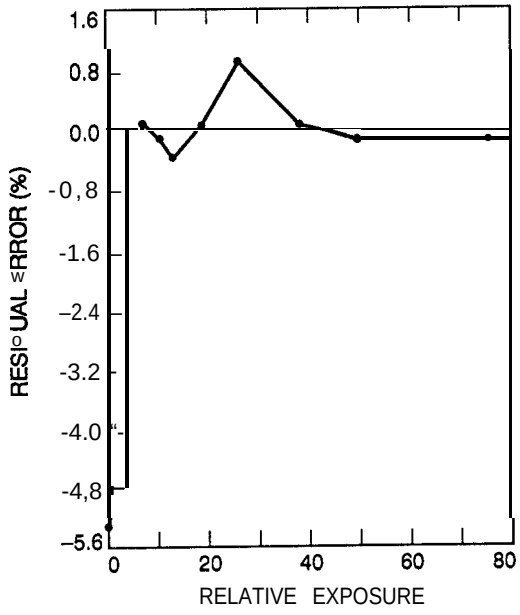

Figure 3-16. Residuals in % from linear fits to the mean response vs relative exposure for the clear filter, gain state 1, summation mode.

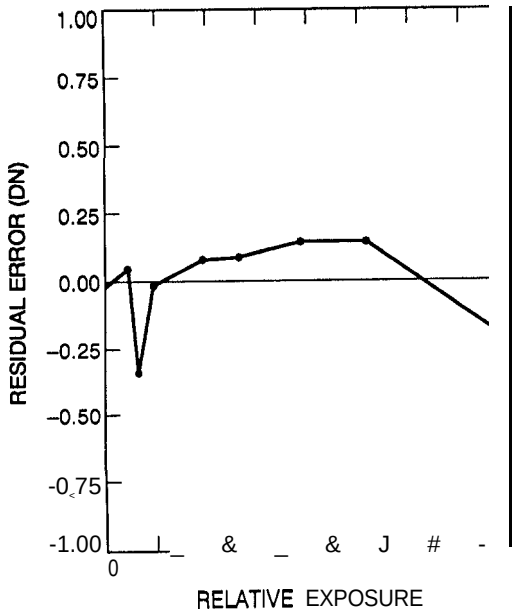

Figure 3-17. Residuals in DN from linear fits to the mean response vs relative exposure for the violet filter, gain state 2.

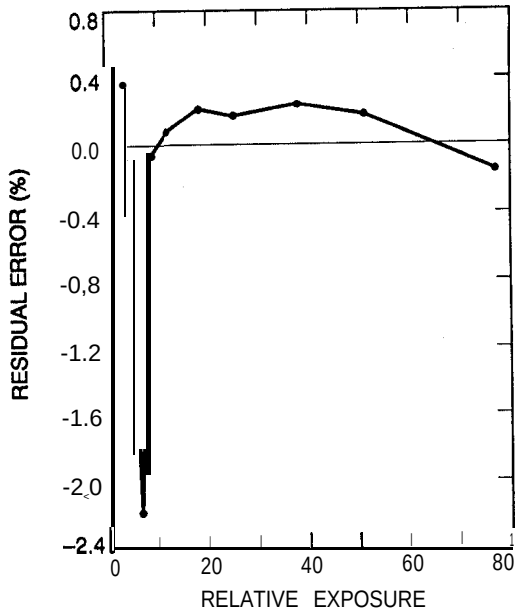

Figure 3-18. Residuals in % from linear fits to the mean response vs relative exposure for the violet filter, gain state 2.

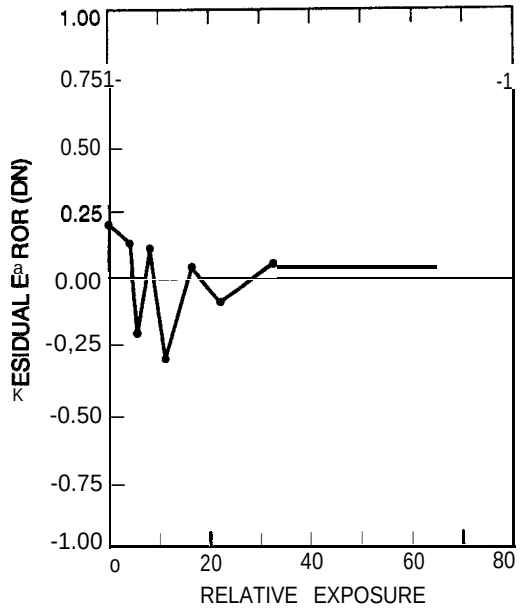

Figure 3-19. Residuals in DN from linear fits to the mean response vs relative exposure for the >9680 A filter, gain state 2.

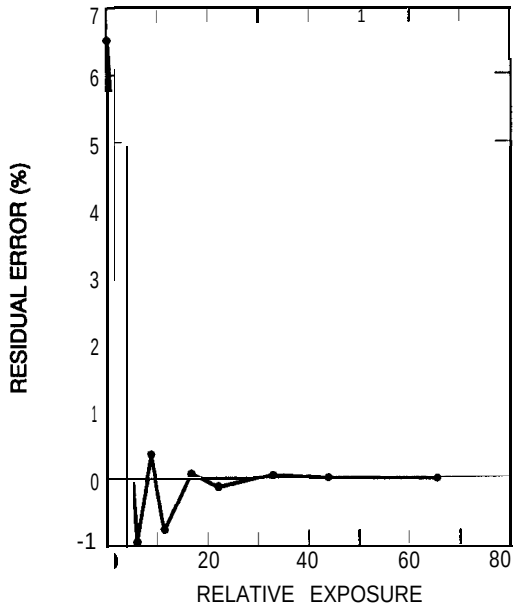

Figure 3-20. Residuals in % from linear fits to the mean response vs relative exposure for the >9680 A filter, gain state 2.

given in previous sections. Figure 3-21 plots the sensitivity versus camera temperature. The sensitivity values in each filter have been normalized to that of clear at +8°C; the clear filter points are connected by a line.

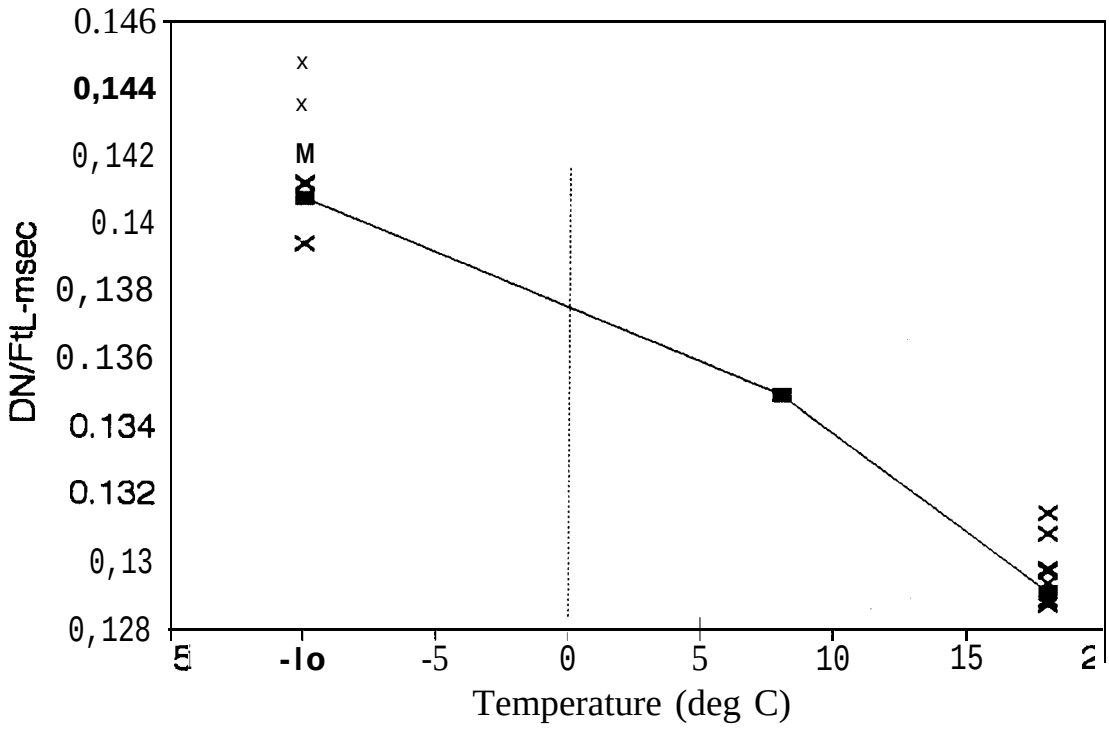

Figure 3-21. SSI sensitivity vs. temperature

Attempts to determine how stable the SSI absolute sensitivity has been with time present some difficulties since at first glance the sensitivity seems to have varied from year to year, contrary to our expectations for an instrument with a solid-state detector. One complicating factor is the changes in the spectrum of the calibration source that have occurred. Section II.A.1 discusses possible variations in the tungsten,light cannon output spectrum. In addition, the spectral transmission of the thermal vacuum chamber window changed when the window was replaced prior to the 1988 calibration. These difficulties can be largely overcome if we only compare the green filter sensitivities (since the calibration source brightness is given in units of ftL, which measures the brightness over a spectral bandpass similar to that of the SSI green filter). A comparison over time of the SSI sensitivity in other filter positions relative to green was discussed earlier in Section II.A.1.

Table 3-5 gives the calculated SSI absolute sensitivity at +8°C in the green filter in gain state 2 as a function of time in units of DN/ftL-sec of calibration source exposure.

Table 3-5. Calculated SSI Green Absolute Sensitivity (8°C)

Year	DN\ftL-sec
1983	11.05
1984	10.61
1985	11.40
1988	10.21
1989	10.99

When the expected changes in sensitivity due to SSI gain changes are accounted for (5% decrease between 1983 and 1984; 10% increase between 1985 and 1988), variations of up to 15% are observed in the calibrated SSI response to the tungsten cannon seen through the thermal vacuum chamber window over the 5 calibrations conducted.

It is not possible to confidently determine if these variations are due to real changes in the SSI response or to errors in the absolute calibration of the light cannon (i.e., errors in the luminance value of the standard reference lamp against which the light cannon was calibrated). Prior to 1989, when use of two separate luminance reference standards was begun, the only other reference that might allow discrimination between SSI changes and reference lamp calibration errors was the tungsten cannon itself. Interestingly, a rather strong correlation is observed between the changes in the SSI calibrated green response and changes in the implied light cannon output at a given iris setting as determined from comparisons to the calibrated luminance standard output. Figure 3-22 plots for each of the 5 calibrations the ratio of the calibrated SSI green response to the expected response for a stable SSI versus the relative brightness of the light cannon at a Veeder root setting of 230 as implied by the light cannon calibration. The year of the calibration and the SSI temperature are indicated for each data point, and a line is plotted showing the ratio that would have resulted if the light cannon had actually been perfectly stable with a constant output for the fixed Veeder root setting rather than changing as was implied by its calibrations against the reference luminance standard. This plot strongly implies that it is the reference luminance standard that has varied and gone out of calibration over the years. Interestingly, the reference standard was calibrated by the vendor shortly before the 1983 and the 1988 calibrations, and for calibrations performed closest to these times, the relative light cannon output implied lies within about 6% of its mean value of 1.0. The implied light cannon output changes also show a systematic drift downward with time beginning with each reference standard recalibration. If the SSI were changing sensitivity over the years, as would be implied if the light cannon calibrations had always been accurate, there would be no expected correlation between the quantities plotted in Figure 3-22. Finally, if the reference standard calibrations had always been accurate, random changes in the light cannon output are implied. Although changes in the light cannon bulb and/or iris mechanism are certainly possible (and in fact might be more to be expected than calibration drifts in the luminance standard) , the bulbs were not replaced between the 1983 and 1989

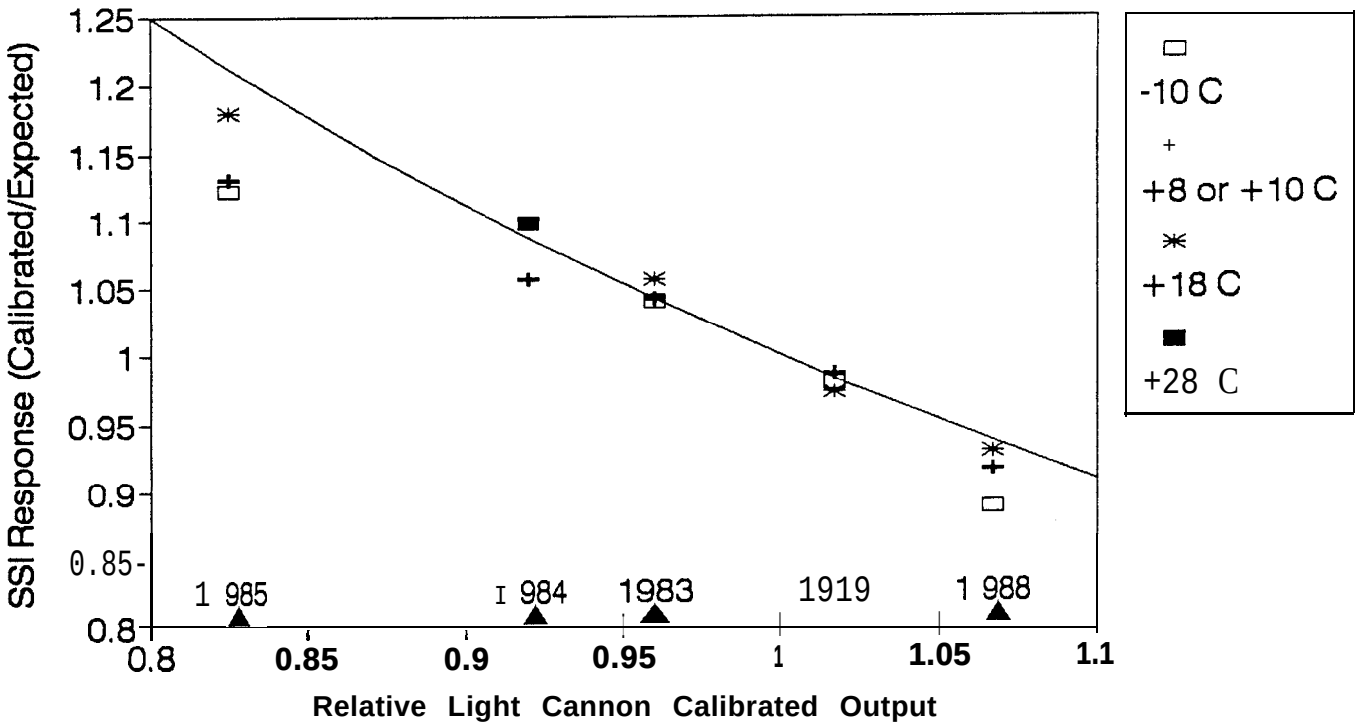

Figure 3-22. Calibrated SSI sensitivity trends vs. calibrated light cannon variations

calibrations, and any changes in a given bulb might be expected to be monotonic with time rather than variable as is implied by the light cannon calibrations. Iris mechanism changes are unpredictable and could explain the changes in the light cannon calibration. But the strong correlation with changes in the calibrated SSI sensitivity (changes which were not expected) points to poor stability in the calibration reference standard. If this were true, then the SSI calibration results give no indication of any drifts in SSI absolute green sensitivity with time at greater than about the 4% level.

The average sensitivity across the entire CCD array derived from pixel-by-pixel fits to the 1989 light transfer data sets at +8°C are given in Table 3-6 for each filter.

Table 3-6. Average SSI Sensitivity from GALGEN (gain state 2)

Filter	Sensitivity (DN/ftL-msec)
Clear	1.348×10^{-1}
Green	1.085×10^{-2}
Red	2.502×10^{-2}
Violet	3.924×10^{-4}
7560 A	6.224×10^{-3}
>9680 A	2.266×10^{-3}
7270 A	3.126×10^{-3}
8890 A	1.849×10^{-3}

Best-fit adjustments of all SSI and calibration source parameters to match the entire +8°C radiometric calibration data set result in sensitivities as qiven in Table 3-7. The uncertainties listed are a measure of the precision of the sensitivity measurements (i.e., the internal consistency of the entire +8°C calibration data set). The absolute calibration accuracy is not as good since the systematic error in knowledge of the luminance reference standard used is about ±4%.

Table 3-7. Average SSI Sensitivity from Best Fit to Entire Radiometric Calibration Data Set (gain state 2)

Filter	Sensitivity lDN\ftL-msec)	Percent Uncertainty
Clear	(1.341±ooo47)xlo-l	0.35
Green	$(1.086\pm.0056)\times10^{-2}$	0.52
Red	$(2.492\pm.011)\times10^{-2}$	0.43
Violet	$(3.960\pm.019)\times10^{-4}$	0.47
7560 A	$(6.188\pm.023)\times10^{-3}$	0.37
>9680 A	$(2.251\pm.012)\times10^{-3}$	0.51
7270 A	$(3.107\pm.014)\times10^{-3}$	0.46
8890 A	$(1.844\pm.0082)\times10^{-3}$	0.45

The conversion factors from units of calibration source ftL to units of surface reflectivity or to units of source radiance are given in Table 3-8 for each filter in gain state 2 at an SSI temperature of +8°C. These conversion factors were calculated using spectral curves for the various SSI components that had been adjusted slightly from their component-level measured values such that the resulting SSI spectral response model best fit the entire radiometric calibration data set (see Section III.C below). All pre-launch radiometric calibration data were taken with the SSI protective optics cover off. However, early flight data may be taken with the cover still in place. Table 3-9 presents the radiometric conversion factors when the cover is on.

Table 3-8. SSI Sensitivity in Radiometric Units (gain state 2)

Filter	DN/msec/reflectivity unit*	DN/msec/watt/cm^2/sr/nm
Clear	32.16	1.749×10^7
Green	5.092	2.337×10^6
Red	5.375	2.948×10^6
Violet	1.263	7.068×10^5
7560 A	0.7373	5.013×10^5
>9680 A	0.1124	1.233×10^5
7270 A	0.4311	2.769×10^5
8890 A	0.1233	1.082×10^5

*for solar illumination at a range of 5.2 A.U.

Table 3-9. SSI Sensitivity in Radiometric Units with Optics Cover On (gain state 2)

Filter	DN/msec/reflectivity unit*	DN/msec/watt/cm^2/sr/nm
Clear	12.46	6.839 X 10^6
Green	2.063	9.467 X 10^5
Red	2.336	1.286 x 10^6
Violet	0.2002	1.094 x 10^5
7560 A	0.3259	2.216 X 10^5
>9680 A	0.03466	3.782 x 10^4
7270 A	0.1913	1.229 x 1 0^5
8890 A	0.04817	4.229 X 10^4

*for solar illumination at a range of 5.2 A.U.

The light transfer data set for the violet filter in the summation mode in gain state 1 was acquired using the xenon light cannon since the tunqsten cannon could not be set to a high enough brightness level f-or available exposure times to be used. Therefore, the conversion factors to radiometric units had to be recalculated for this case. The factors derived (with the optics cover off) are:

(a) 9.557 x 10-* $\frac{\text{reflectivity units}}{\text{calibration source ftL}}$

(b) 1.708 x 10^{-9} $\frac{\text{watts/cm}^2\text{/sr/nm}}{\text{calibration source ftL}}$

6. Pixel-by-Pixel Radiometric Calibration

For each light transfer data set acquired at the expected nominal SSI flight temperature (+8°C), linear fits to the response functions of each pixel were determined using the Multimission Image Processing Laboratory (MIPL) program GALGEN. The GALGEN output files were next examined by the program BLEMGEN to determine those pixels that are considered to be blemishes that are impossible to calibrate. The maximum allowable DN error or rms error in the linear fit for a pixel before it is classified as a blemish are listed below:

	MAXERR	MAXRMS
10K gain	3 DN	1 DN
40K gain	2	1
100K gain	2	1
400K gain	1	1

The only exception to these values is for the 10K gain summation-mode case with the CCD clock voltages set to the inverted settings. In this case, the MAXERR threshold was 5 DN, and the MAXRMS threshold was 3 DN.

Table 3-10 gives the mean values of the GALGEN-produced slopes and offsets excluding any pixels defined as blemishes. The standard deviations listed represent the variation across the entire array of non-blemished pixels, not the uncertainty in the computed slope or offset for any given pixel, which is much smaller.

Figures 3-23 through 3-38 present photographs of the slope terms across the array for several combinations of filter, gain and use of the summation mode. The images have been contrast-enhanced; the range of slopes between black and white are listed

Table 3-10. Mean Values and Standard Deviations of GALGEN-produced Slopes and Offsets.

Filter	Gain	Slope (ftL-msec/DN)	Std deviation		Offset (D N)	St dev
Clear	1 (sum)	7.357	0.274	(3.7 %)	2.924	0.131
	2	7.417	0.150	(2.0 %)	2.761	0.143
	3	3.674	0.068	(1.9 %)	3.352	0.225
	4	0.763	0.015	(2.0 %)	8.620	0.698
Green	1 (sum)	89.03	3.63	(4.1 %)	2.607	0.131
	2	92.18	1.84	(2.0 %)	2.771	0.132
	2 (sum)	18.36	0.91	(5.0 %)	3.806	0.352
	3	45.67	0.83	(1.8 %)	3.393	0.218
	3 (sum)	9.009	0.484	(5.4 %)	5.876	0.725
	4	9.390	0.210	(2.2 %)	8.619	0.707
	4 (sum)	1.863	0.105	(5.6 %)	18.631	3.253
Red	1 (sum)	39.03	0.56	(1.4 %)	2.669	0.153
	2	39.97	0.87	(2.2 %)	2.770	0.145
	3	19.77	0.37	(1.9 %)	3.328	0.235
	4	4.073	0.095	(2.3 %)	8.632	0.719
Violet	1 (sum)	933.9	47.5	(5.1 %)	4.996#	0.336
	2	2548.	68.2	(2.7 %)	3.016	0.225
	3	1257.	33.6	(2.7 %)	3.591	0.346
	4	259.2	7.79	(3.0 %)	8.614	0.721
7560 A	1 (sum)	160.2	6.49	(4.1 %)	2.881	0.160
	2	160.7	3.58	(2.2 %)	2.714	0.150
	3	79.58	1.52	(1.9 %)	3.314	0.224
	4	16.46	0.37	(2.3 %)	8.605	0.716
>9680 A	1 (sum)	449.4	16.3	(3.6 %)	2.832	0.142
	2	441.3	9.77	(2.2 %)	2.804	0.147
	3	218.4	4.60	(2.1 %)	3.389	0.228
	4	45.60	1.09	(2.4 %)	8.679	0.737
7270 A	1 (sum)	320.4	12.9	(4.0 %)	2.658	0.130
	2	319.9	7.52	(2.4 %)	2.710	0.147
	3	158.5	3.43	(2.2 %)	3.350	0.238
	4	32.97	0.79	(2.4 %)	8.615	0.728
8890 A	1 (sum)	548.1	20.7	(3.8 %)	2.755	0.134
	2	541.0	13.7	(2.5 %)	2.696	0.147
	3	268.2	6.42	(2.4 %)	3.391	0.246
	4	55.72	1.35	(2.4 %)	8.636	0.683

(*) xenon light cannon (#) CCD clocks inverted

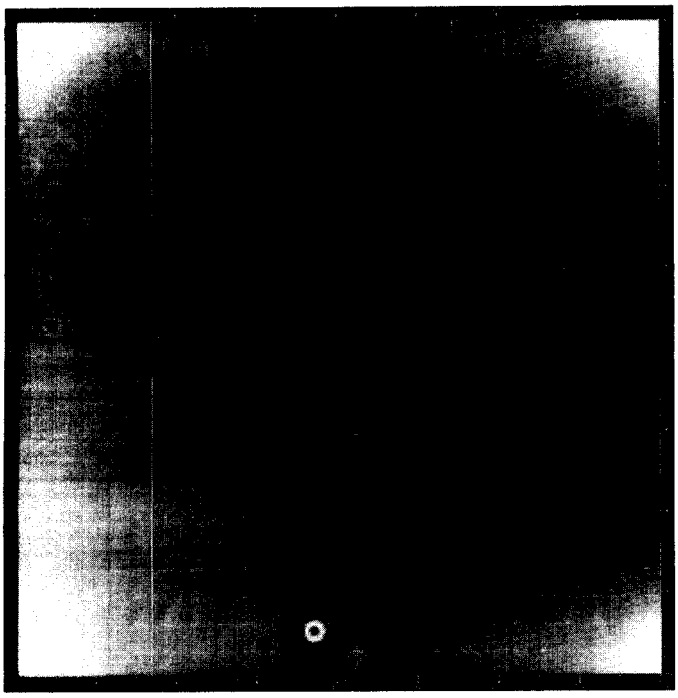

Figure 3-23. Slope term image for violet filter, gain state 4. Slope range = 249.3 - 280.4

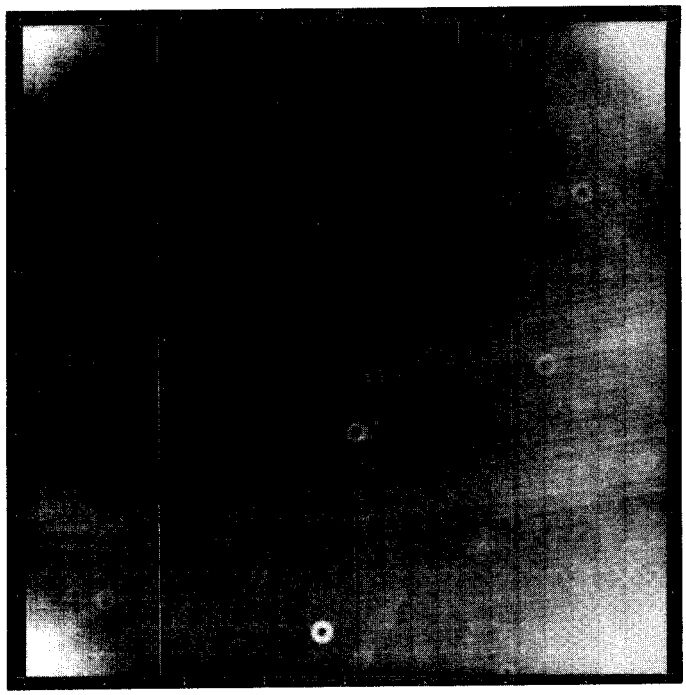

Figure 3-24. Slope term image for 7270 A filter, gain state 4. Slope range = 32.08 - 34.52

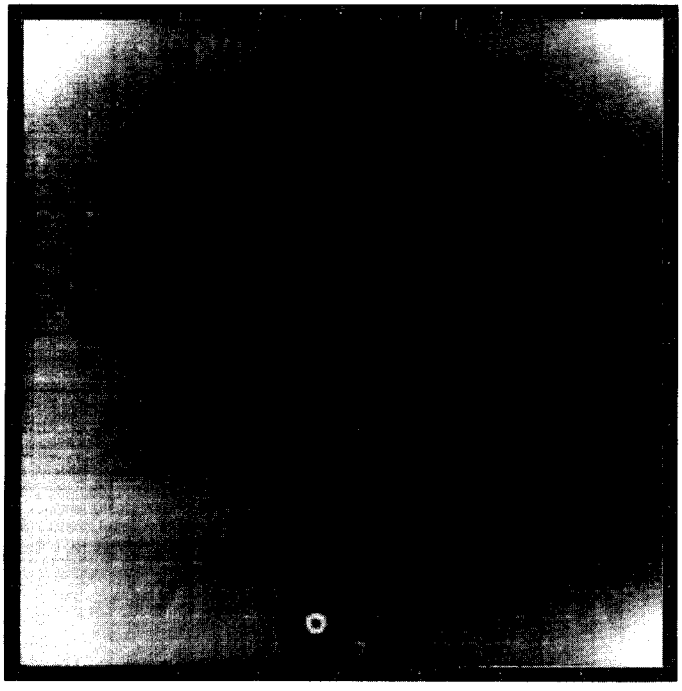

Figure 3-25. Slope term image for violet filter, gain state 3. Slope range = 1209 - 1358

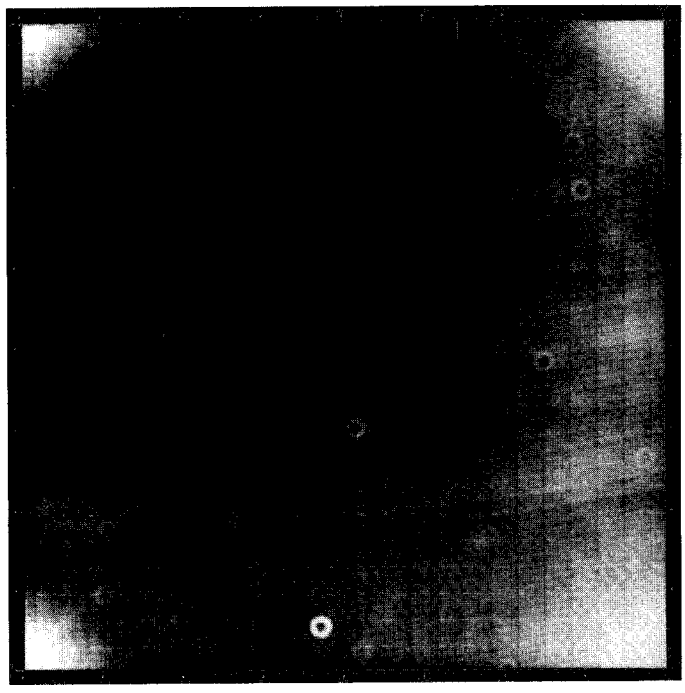

Figure 3-26. Slope term image for 7270 A filter, gain state 3. Slope range = 154.5 - 166.0

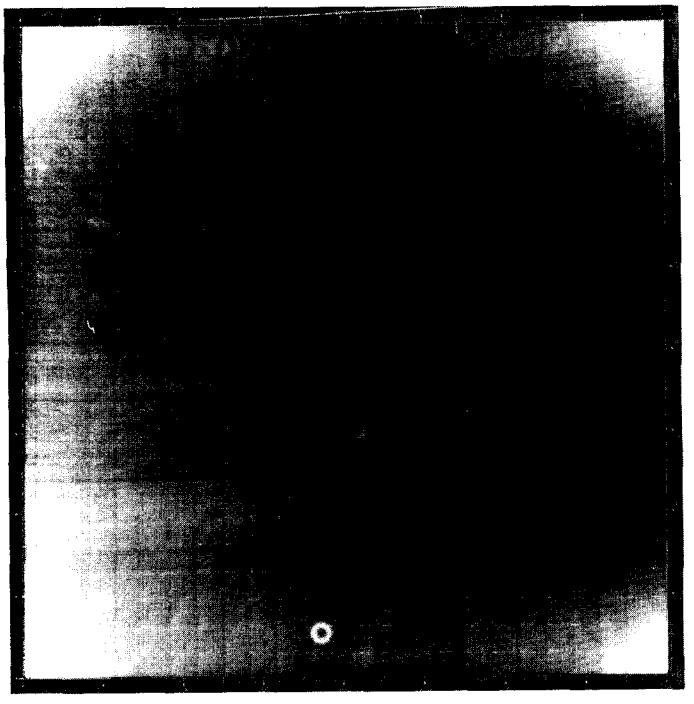

Figure 3-27. Slope term image for violet filter, gain state 2. Slope range = 2454 - 2755

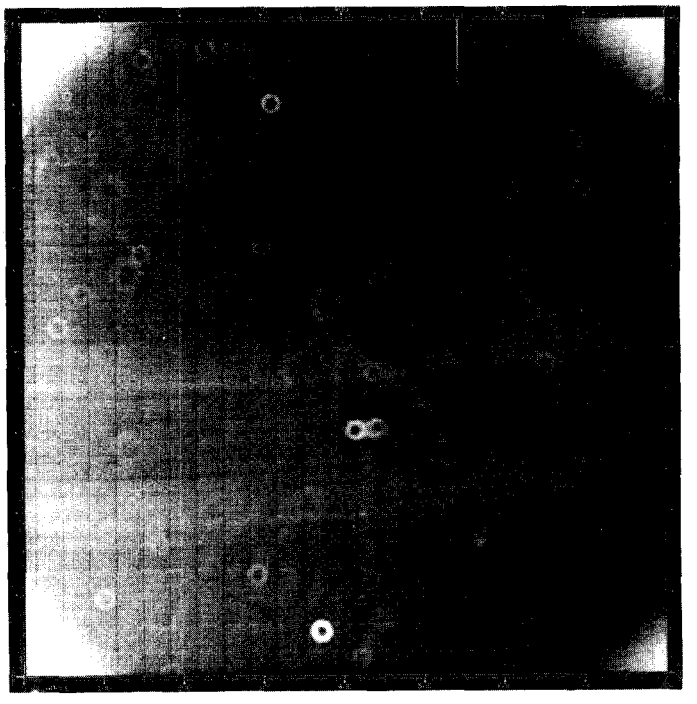

Figure 3-28. Slope term image for green filter, gain state 2. Slope range = 90.40 - 95.69

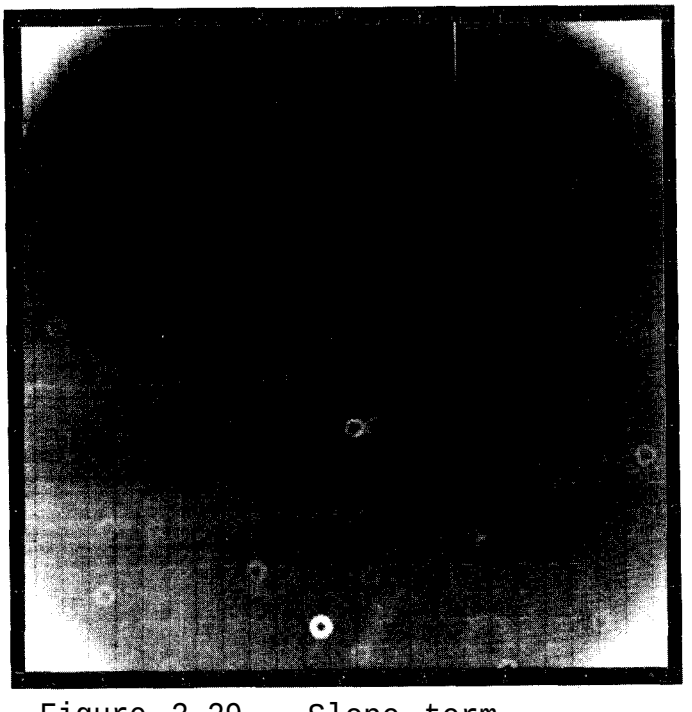

Figure 3-29. Slope term image for red filter, gain state 2. Slope range = 39.17 - 41.85

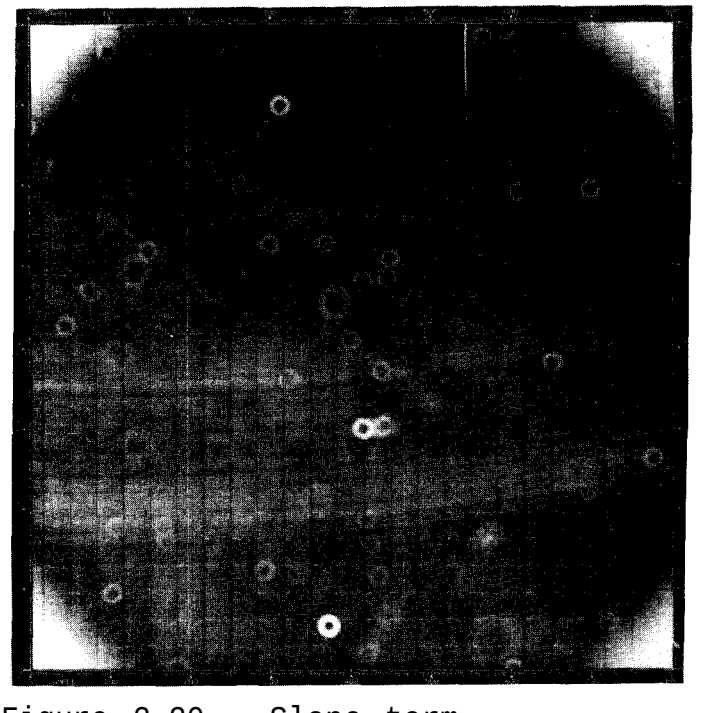

Figure 3-30. Slope term image for clear filter, gain state 2. Slope range = 7.304 - 7.659

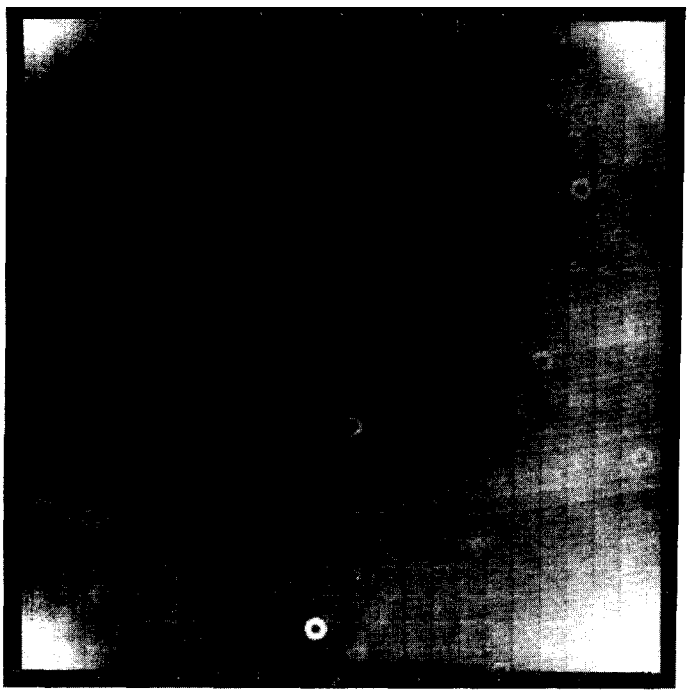

Figure 3-31. Slope term image for 7270 A filter, gain state 2. Slope range = 312.1 - 335.3

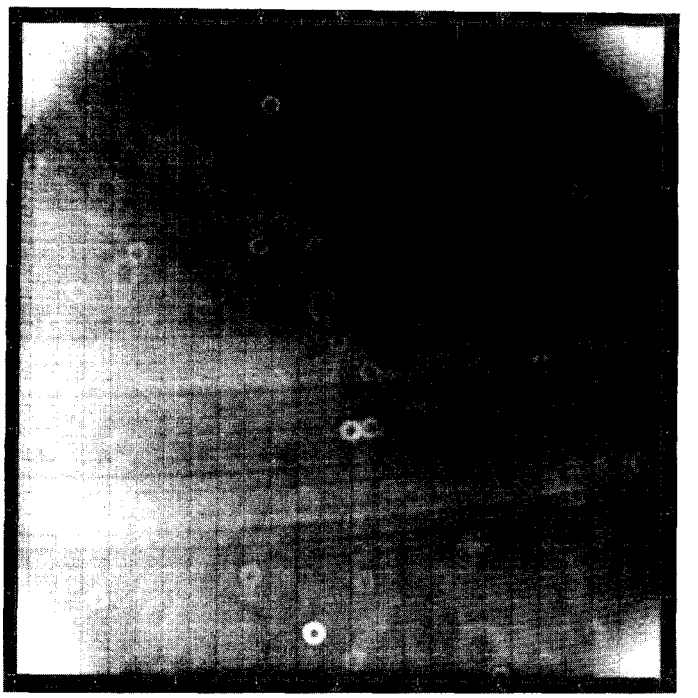

Figure 3-32. Slope term image for 7560 A filter, gain state 2. Slope range = 156.7 - 167.1

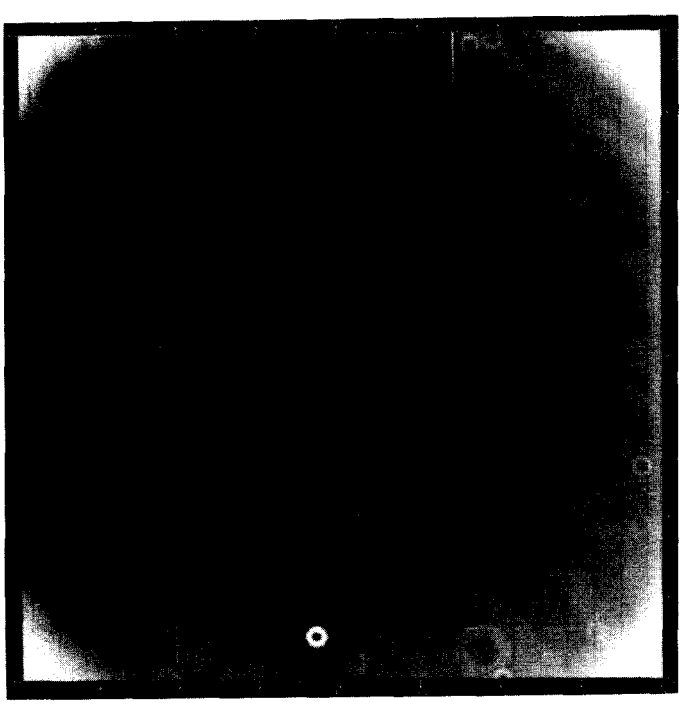

Figure 3-33. Slope term image for 8890 A filter, gain state 2. Slope range = 529.3 - 570.9

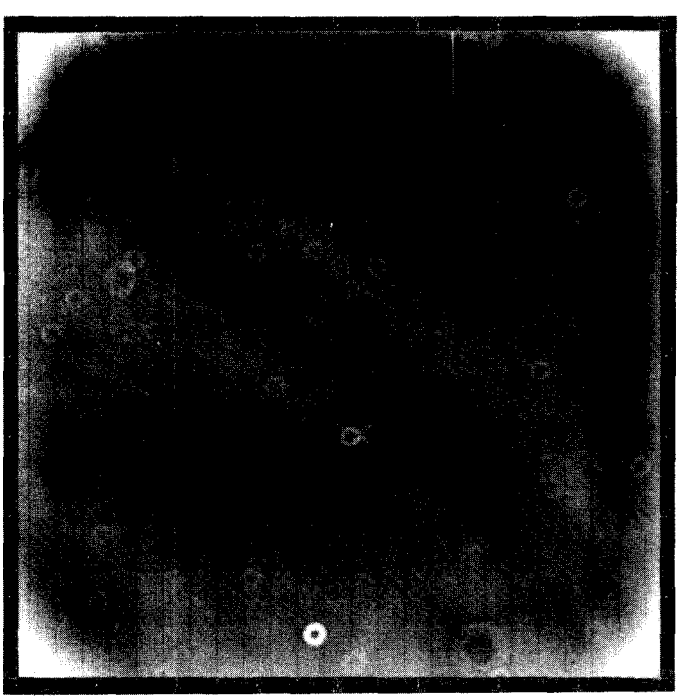

Figure 3-34. Slope term image for >9680 A filter, gain state 2. Slope range = 430.8 - 460.2

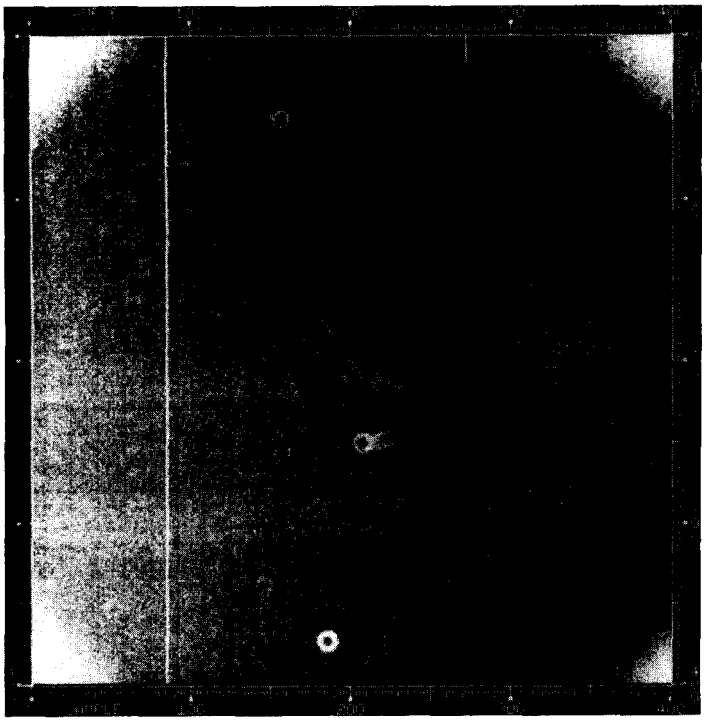

Figure 3-35. Slope term image Green filter, summation mode, gain state 4. Slope range = 1.817 - 1.930

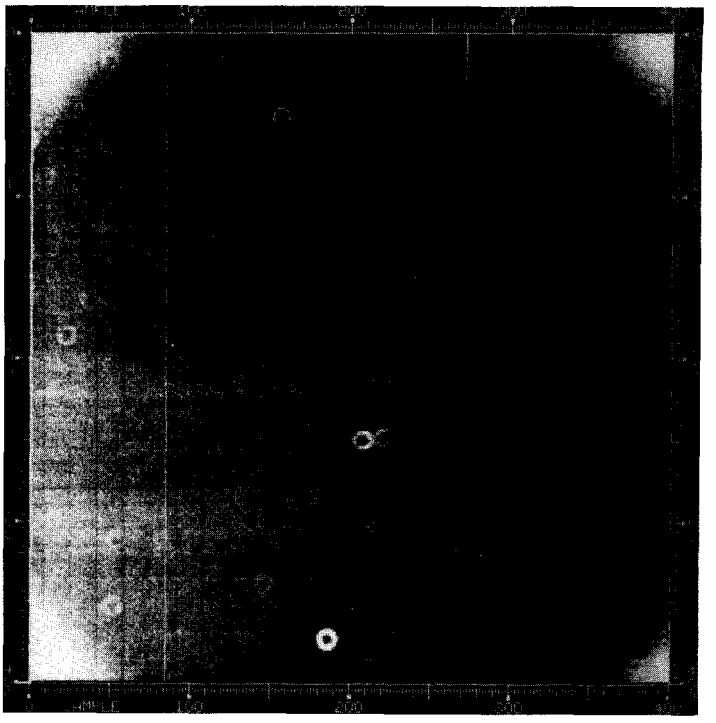

Figure 3-36. Slope term image Green filter, summation mode, gain state 3. Slope range = 8.829 - 9.341

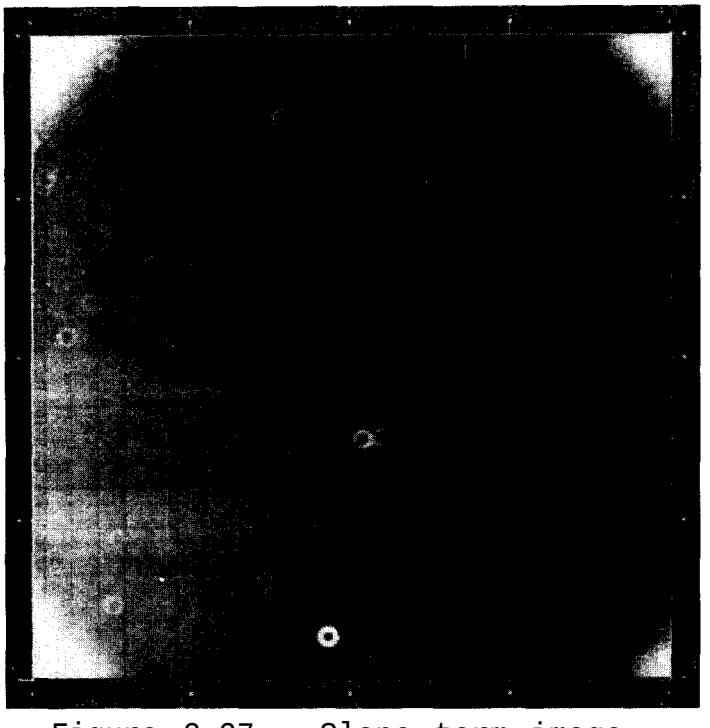

Figure 3-37. Slope term image Green filter, summation mode, gain state 2. Slope range = 17.98 - 18.98

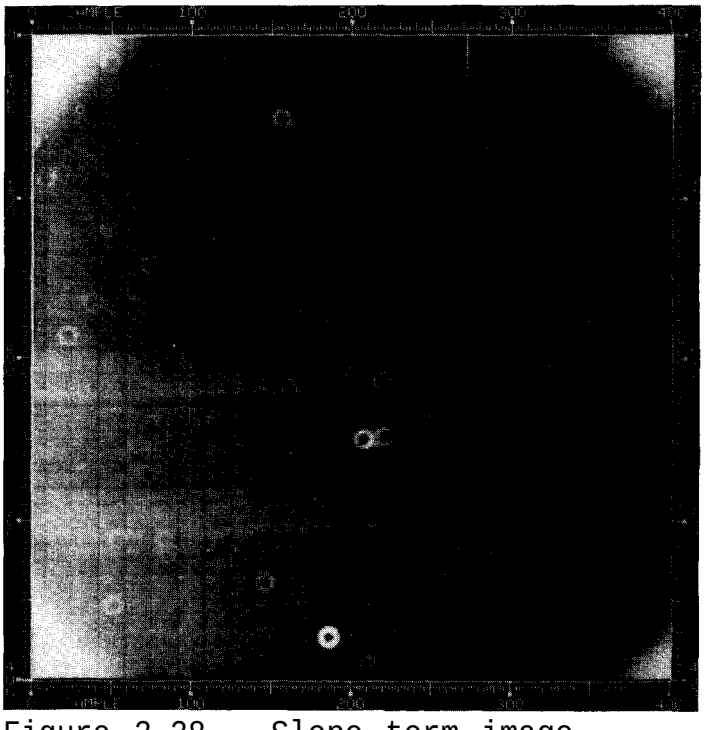

Figure 3-38. Slope term image Green filter, summation mode, gain state 1. Slope range = 87.27 - 92.25

below each picture. Figures 3-39 through 3-46 show contrast-enhanced pictures of the computed offset terms for various gain states, frame times and use of the summation mode. These frames can be compared to actual zero-exposure images in Section III.D below.

Figures 3-47 through 3-70 show several examples of flat field images before and after calibration by the program GALSOS using the GALGEN-produced calibration files. Various exposure levels, gain states, filters and use of the summation mode are included. Note that the calibration totally corrects for the dust speck "donuts", the corner vignetting and the step-and-repeat pattern, leaving an extremely flat field. The remaining random noise level is discussed in Section III.E below. The range of DN values in the resulting images is listed below each picture.

Calibrated flat-field images with low signal levels in the highest gain state (see Figures 3-54 and 3-68) show selected columns that are less well-calibrated than the average (columns around 170, 198 and 610, for example). These apparent non-linearities do not appear for signal levels above 2500e-. Since, except for column ‘170, these columns are not classified as blemishes, the maximum departures from linear response must be less than 3 DN and in most cases are only about 1 DN.

The GALGEN slope files for light transfer data sets acquired in different gain states through the same filter at the same light cannon setting were ratioed to determine gain ratios. The results are displayed in Figures 3-71 through 3-74 and tabulated in Table 3-11. The standard deviations are derived over the array of pixels. The variations are primarily due to random errors in the slope determinations resulting from the noise inherent in the original calibration images. These slope errors range from about 0.5% to 1% as the gain increases in the full-resolution mode and from about 0.5% to about 2% as the gain increases in the summation mode.

Table 3-11. Spatial Variations in Gain Ratios

Gain Ratio	Filter	Mean	Standard Deviation Across Array (%)
4:1	8890 A	4.812	0.52
10:1	8890 A	9.707	0.50
10:1 summation	green	9.886	0.41
gain 4/gain 1 sum	green	9.820	0.37

The slope files for gain state 2 were also ratioed for each filter to that of the green filter. The results are displayed in Figures 3-75 through 3-81. The variability across the array is given in Table 3-12 along with the average filter factors with respect to green. The variations are due primarily to variations in the CCD quantum efficiency as a function of wavelength at different locations across the array.

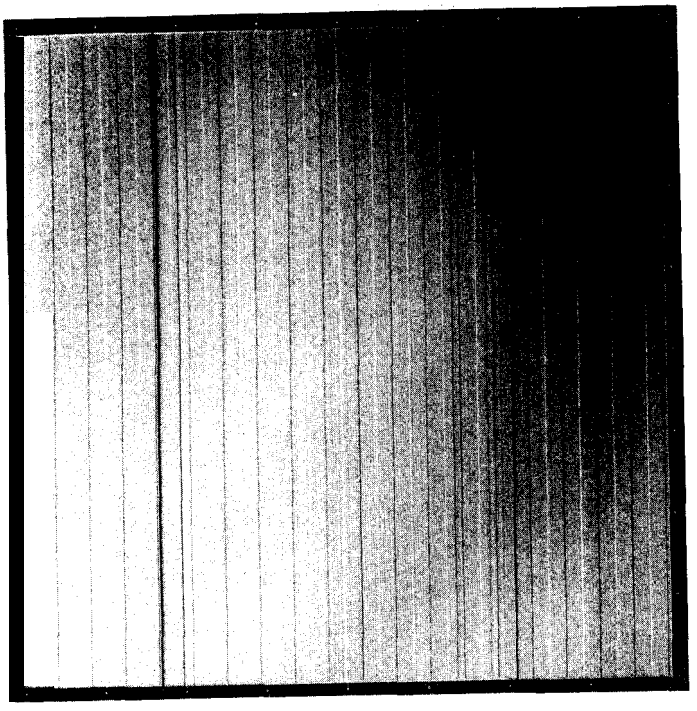

Figure 3-39. Offset term image gain state 4.
DN range = 6.88 - 9.91

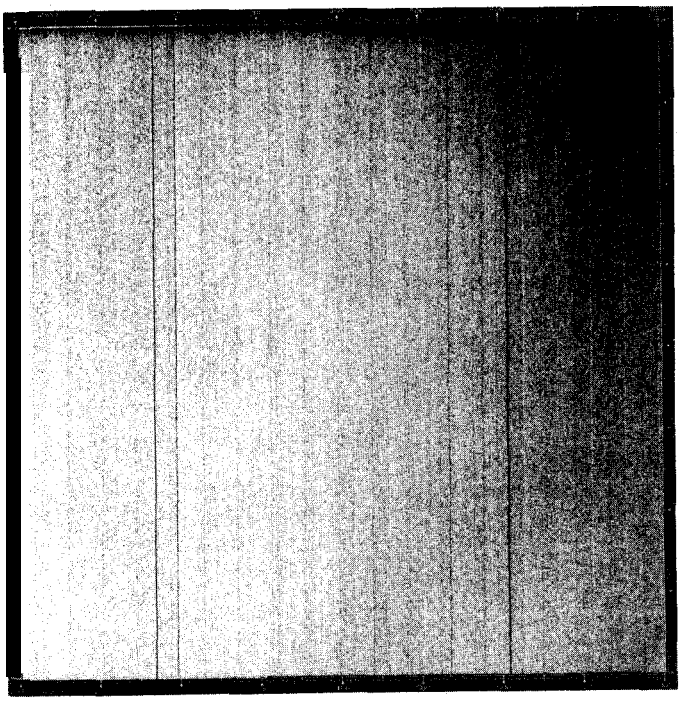

Figure 3-40. Offset term image gain state 3.
DN range = 2.80 - 3.84

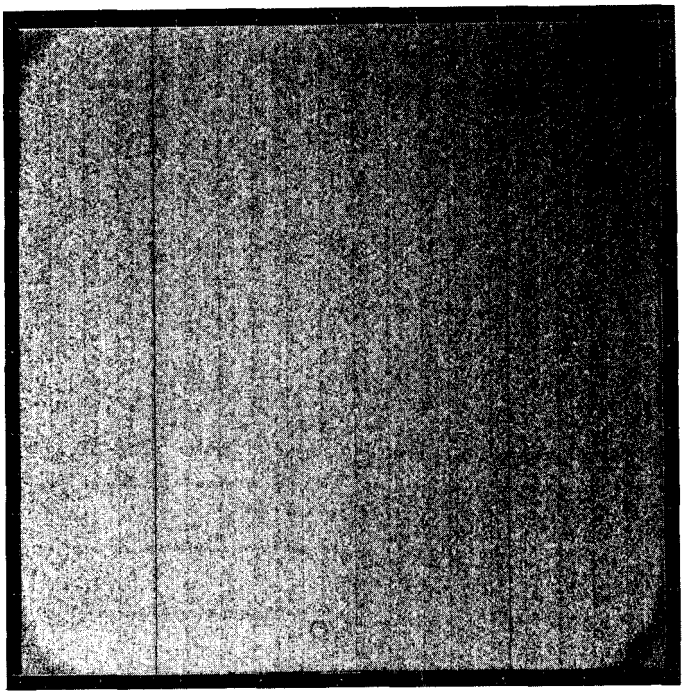

Figure 3-41. Offset term image gain state 2.
DN range = 2.48 - 3.10

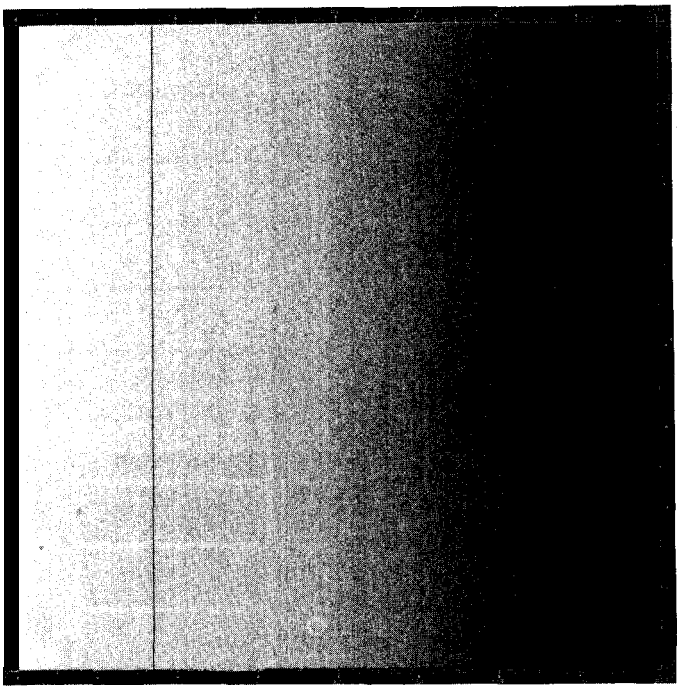

Figure 3-42. Offset term image gain state 2, inverted.
DN range = 3.78 - 4.95

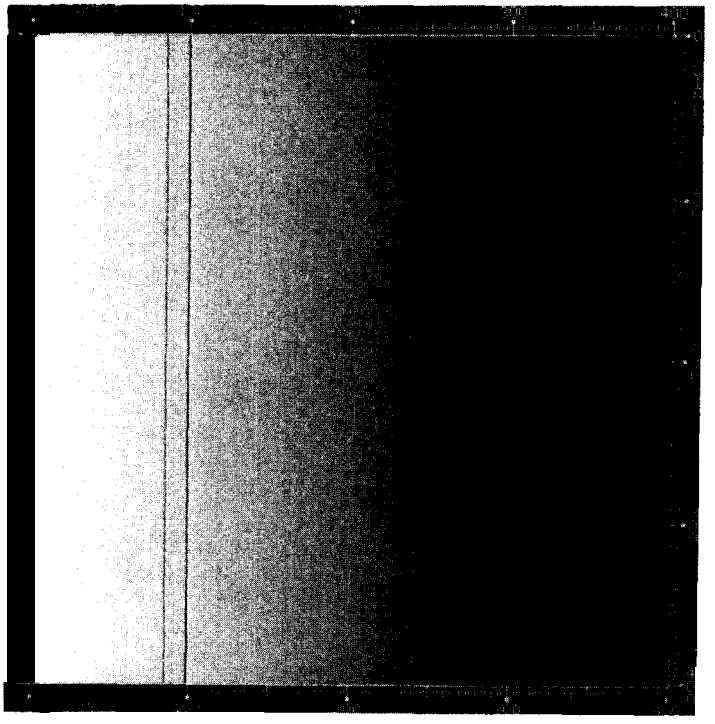

Figure 3-43. Offset term imaqe gain state 4, summation: DN range = 13.03 - 24.05

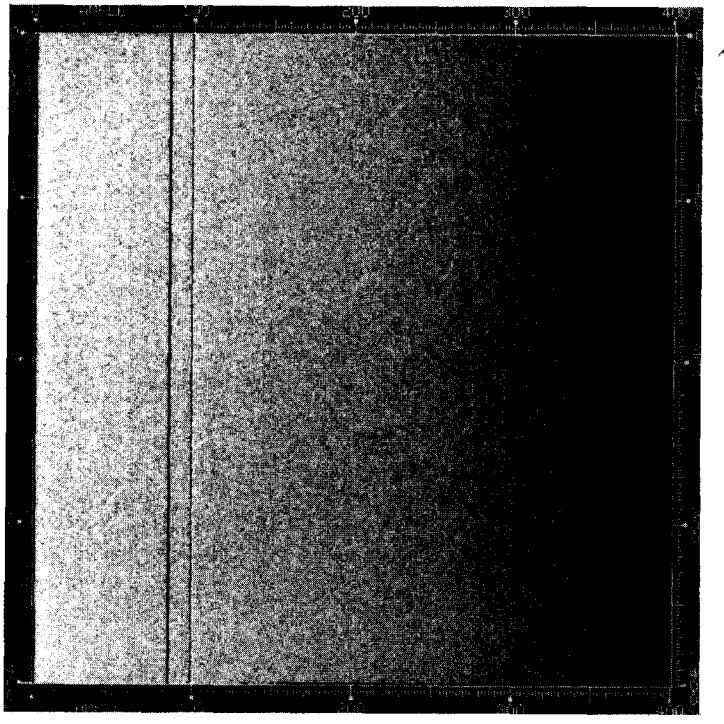

Figure 3-44. Offset term image gain state 2, summation. DN range = 3.06 - 4.45

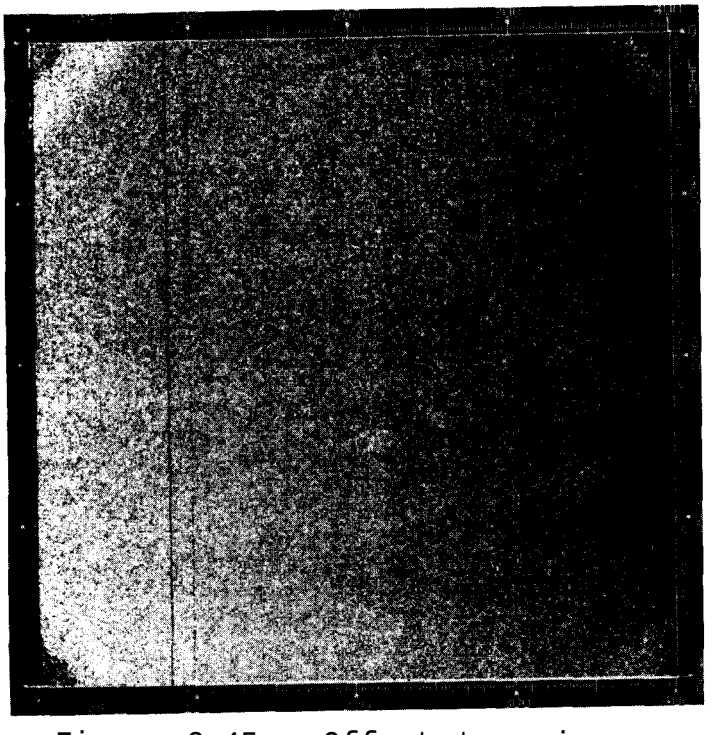

Figure 3-45. Offset term image gain state 1, summation. DN range = 2.31 - 2.88

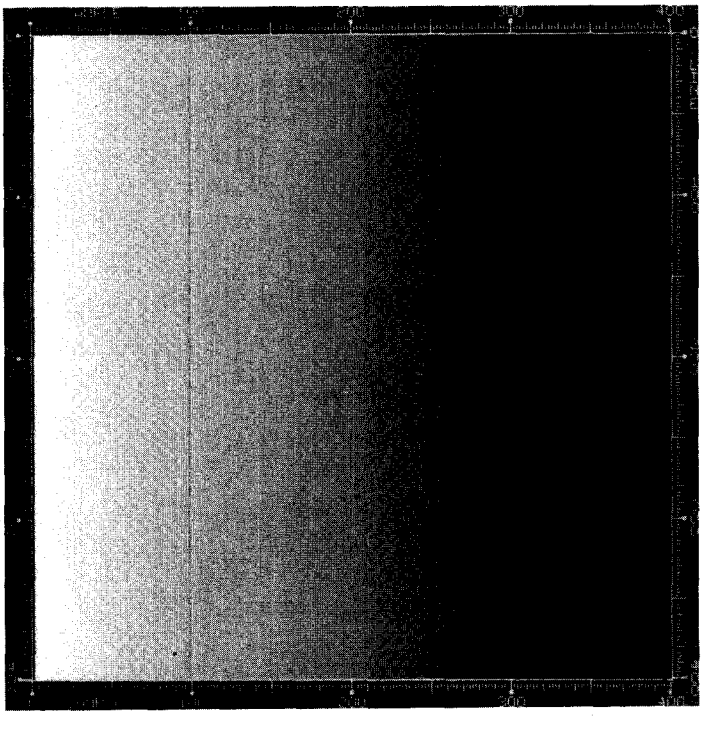

Figure 3-46. Offset term image gain state 4, inverted, summation mode. DN range = 84.06 - 126.45

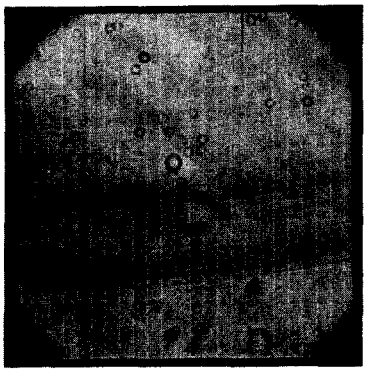

Figure 3-47. Raw flat-field image, gain state 2, clear filter.
DN range = 101 - 107

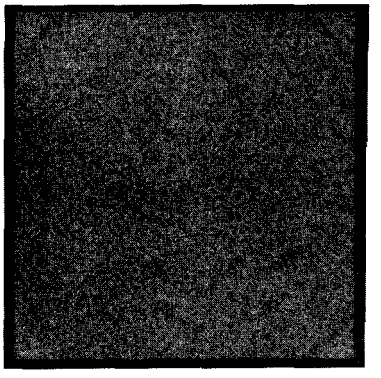

Figure 3-48. Calibrated flat-field image, gain state 2, clear filter.
range = 40.84 - 41.97

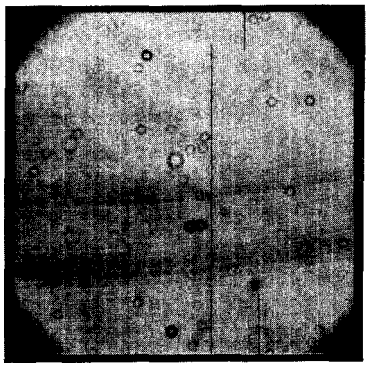

Figure 3-49. Raw flat-field image, gain state 2, clear filter.
DN range = 199 - 211

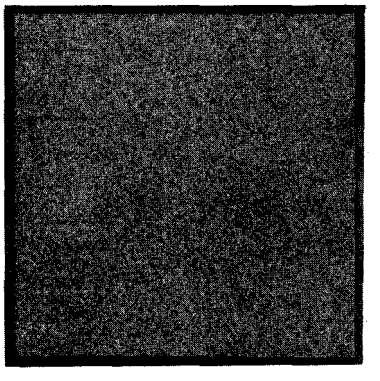

Figure 3-50. Calibrated flat-field image, gain state 2, clear filter.
range = 41.15 - 41.82

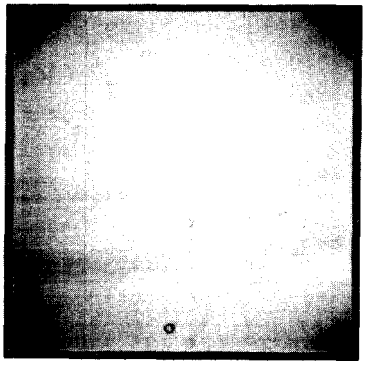

Figure 3-51. Raw flat-field image, gain state 3, violet filter.
DN range = 99 - 113

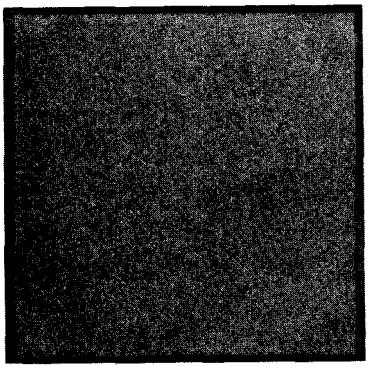

Figure 3-52. Calibrated flat-field image, gain state 3, violet filter.
range = 631.1 - 654.8

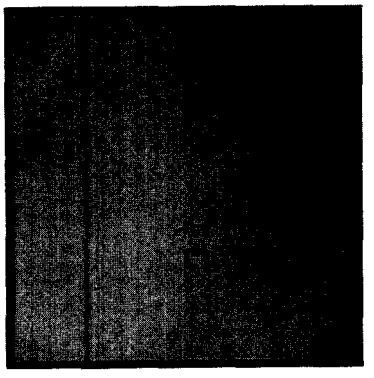

Figure 3-53. Raw flat-field image, gain state 4, >9680 A filter. DN range = 18 - 24

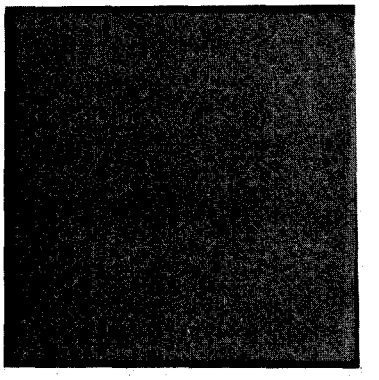

Figure 3-54. Calibrated flat-field image, gain state 4, >9680 A filter. range = 1461 - 1980

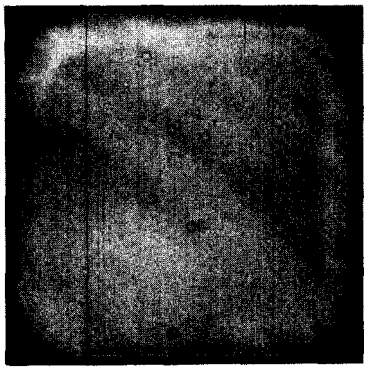

Figure 3-55. Raw flat-field image, gain state 4, >9680 A filter. DN range = 100 - 115

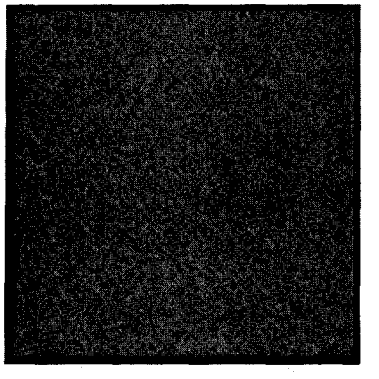

Figure 3-56. Calibrated flat-field image, gain state 4, >9680 A filter. range = 1650 - 1785

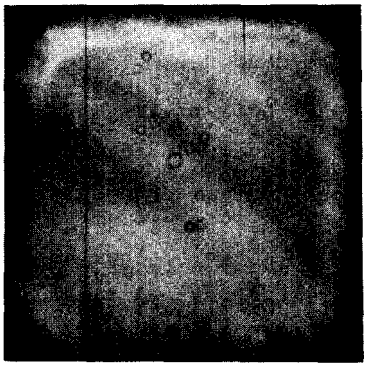

Figure 3-57. Raw flat-field image, gain state 4, >9680 A filter. DN range = 201 - 218

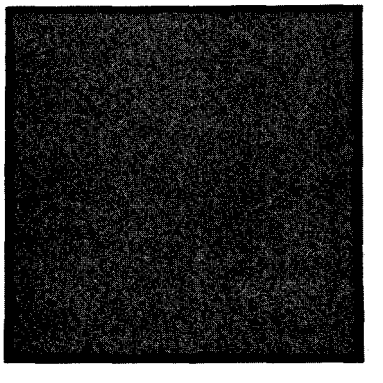

Figure 3-58. Calibrated flat-field image, gain state 4, >9680 A filter. range = 1676 - 1759

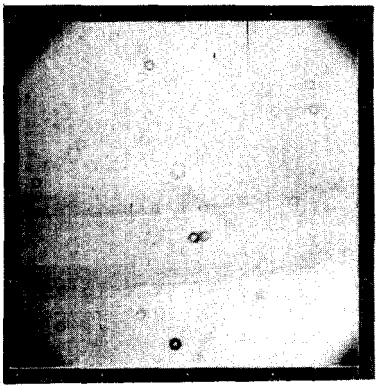

Figure 3-59. Raw flat-field image, gain 1, summation mode, green filter. DN range = 178 - 190

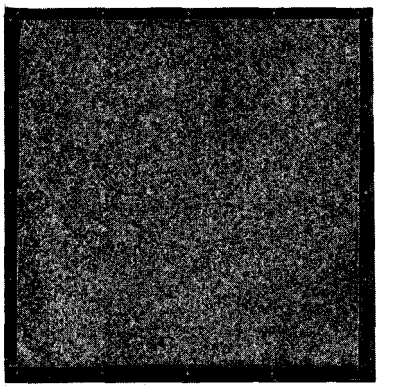

Figure 3-60. Calibrated flat-field image, gain 1, summation, green filter. range = 1270 - 1283

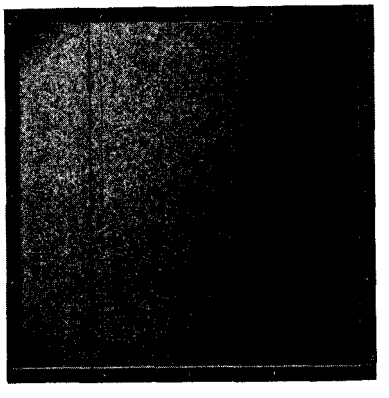

Figure 3-61. Raw flat-field image, gain 2, summation mode, green filter. DN range = 12 - 15

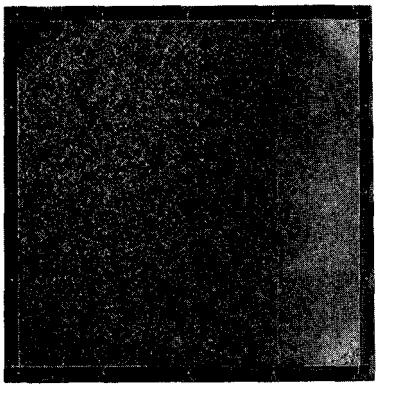

Figure 3-62. Calibrated flat-field image, gain 2, summation, green filter. range = 215.0 - 261.9

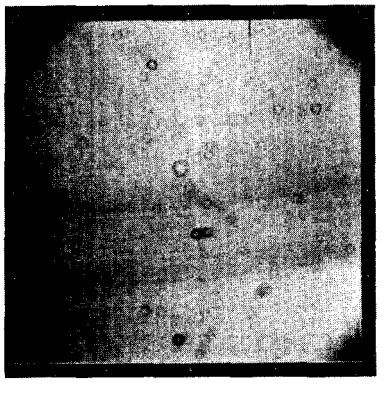

Figure 3-63. Raw flat-field image, gain 2, summation mode, green filter. DN range = 164 - 175

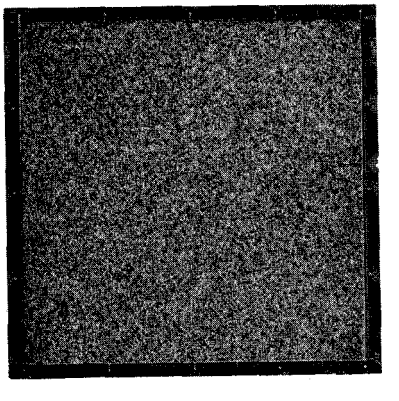

Figure 3-64. Calibrated flat-field image, gain 2, summat ion, green filter. range = 236.9 - 241.7

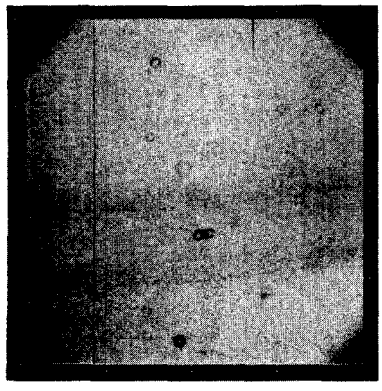

Figure 3-65. Raw flat-field image, gain 3, summation mode, green filter. DN range = 168 - 180

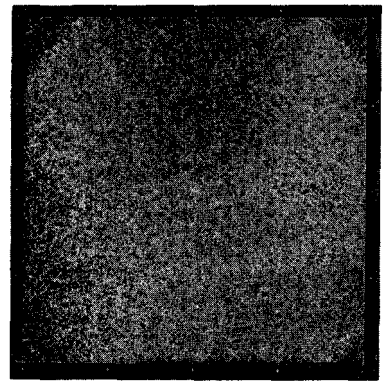

Figure 3-66. Calibrated flat-field image, gain 3, summation, green filter. range = 236.0 - 243.0

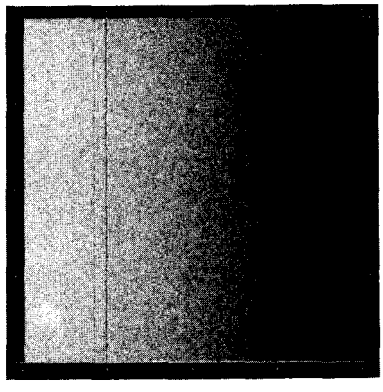

Figure 3-67. Raw flat-field image, gain 4, summation mode, green filter. DN range = 23 - 38

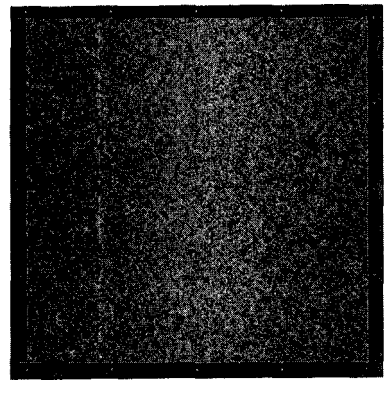

Figure 3-68. Calibrated flat-field image, gain 4, summation, green filter. range = 13.78 - 25.66

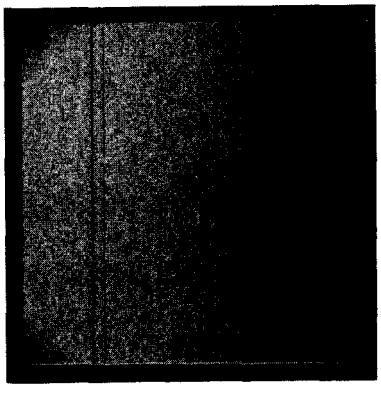

Figure 3-69. Raw flat-field image, gain 4, summation mode, green filter. DN range = 111 - 129

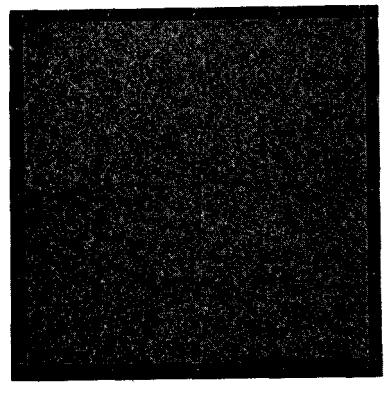

Figure 3-70. Calibrated flat-field image, gain 4, summation, green filter. range = 18.56 - 20.85

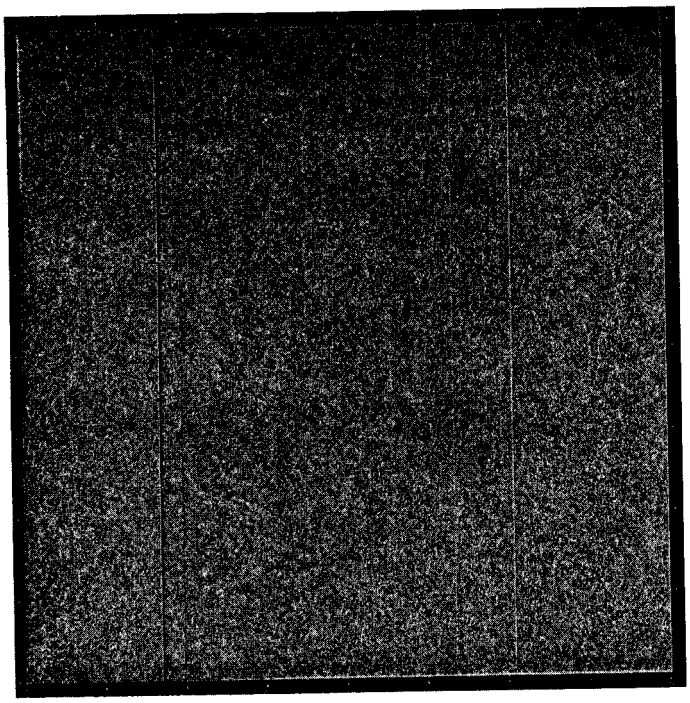

Figure 3-71. Calibrated slope file ratio, gain state 4/3.

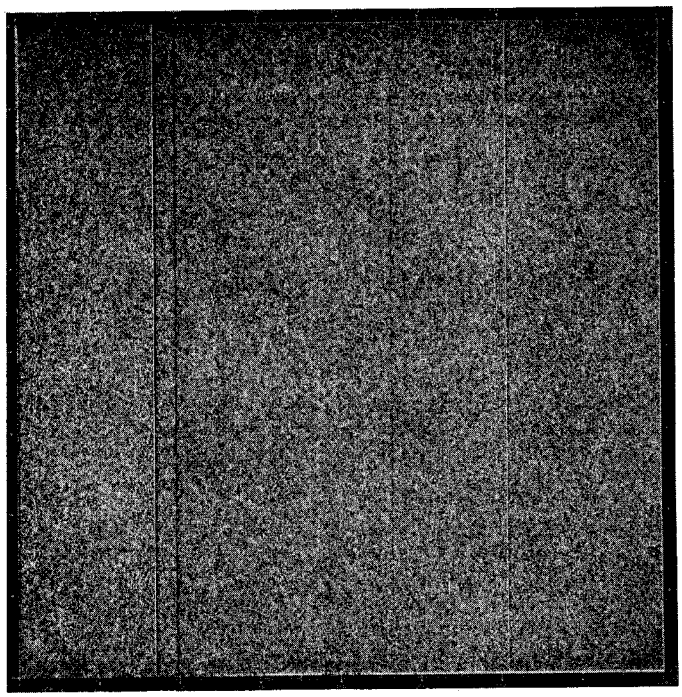

Figure 3-72. Calibrated slope file ratio, gain state 4/2.

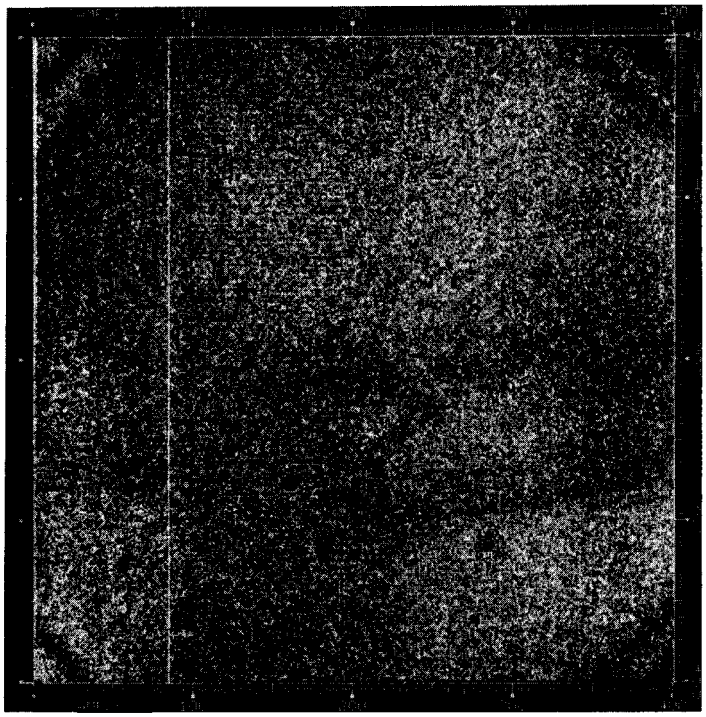

Figure 3-73. Calibrated slope file ratio, summation mode, gain state 3/1.

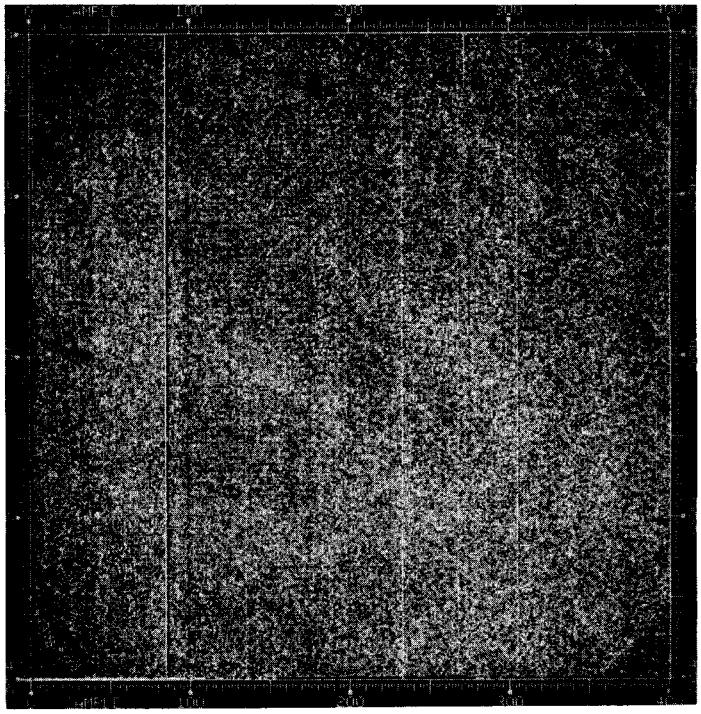

Figure 3-74. Calibrated slope file ratio, normal gain 4/summation mode gain 1.

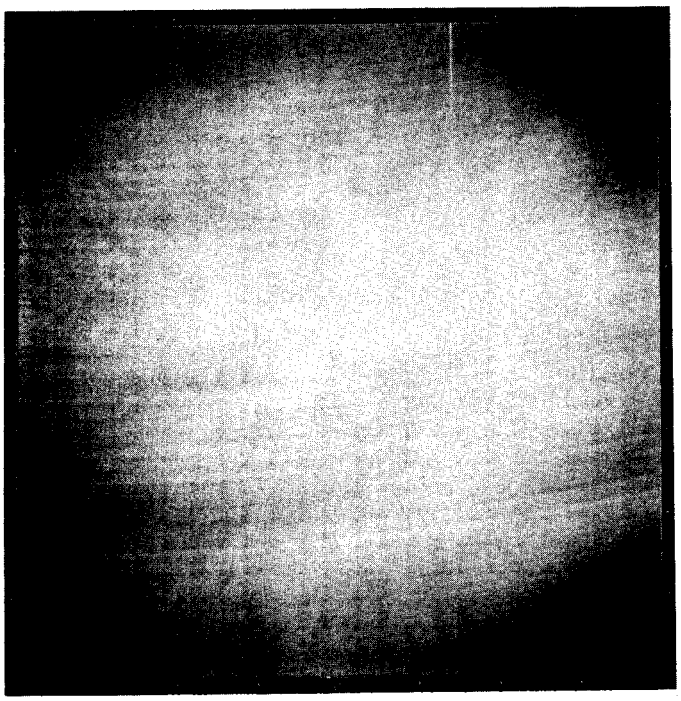

Figure 3-75. Calibrated slope file ratio, green\violet

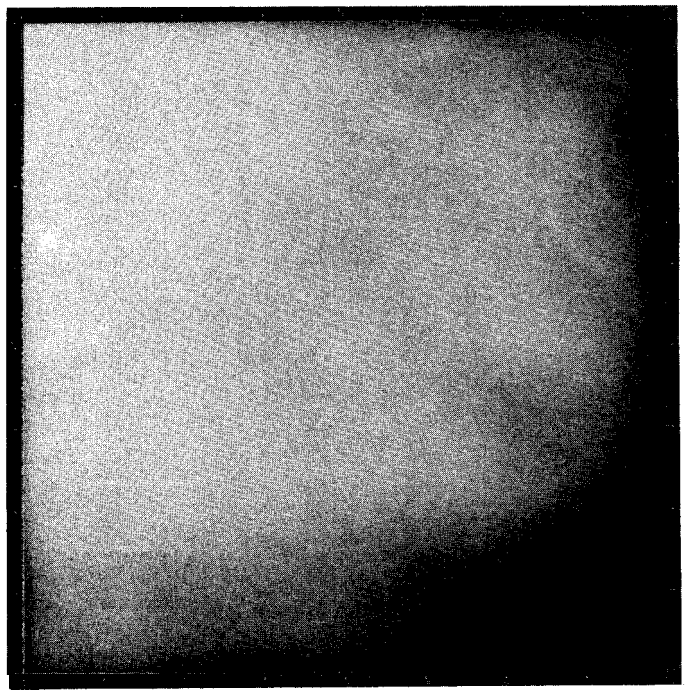

Figure 3-76. Calibrated slope file ratio, green/red

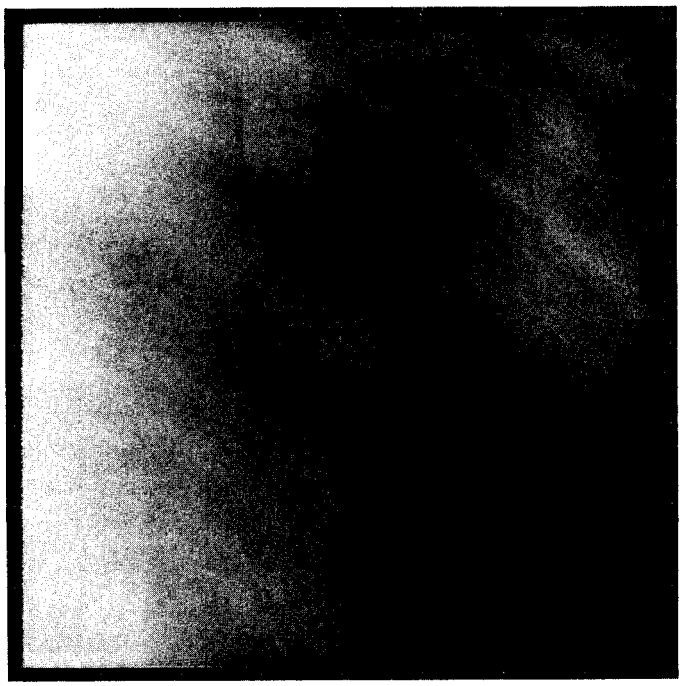

Figure 3-77. Calibrated slope file ratio, green/clear

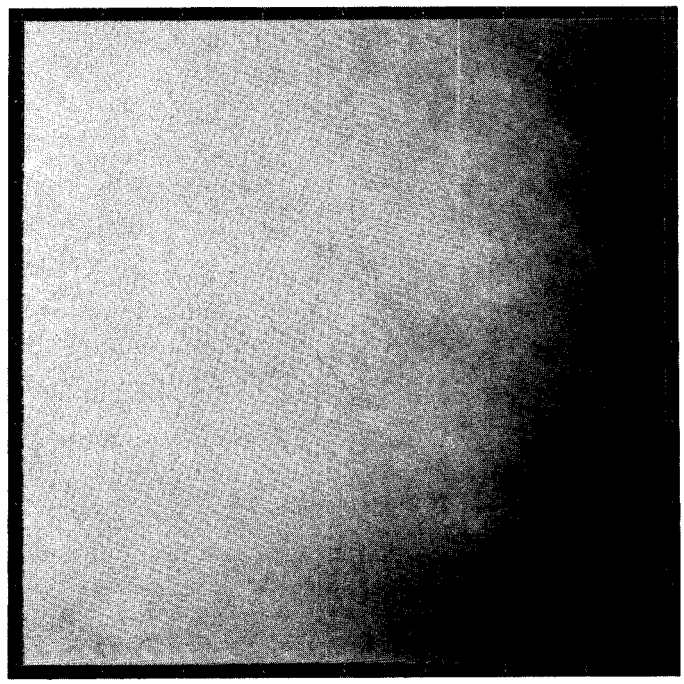

Figure 3-78. Calibrated slope file ratio, green/7270 A

Figure 3-79. Calibrated slope file ratio, green/7560 A

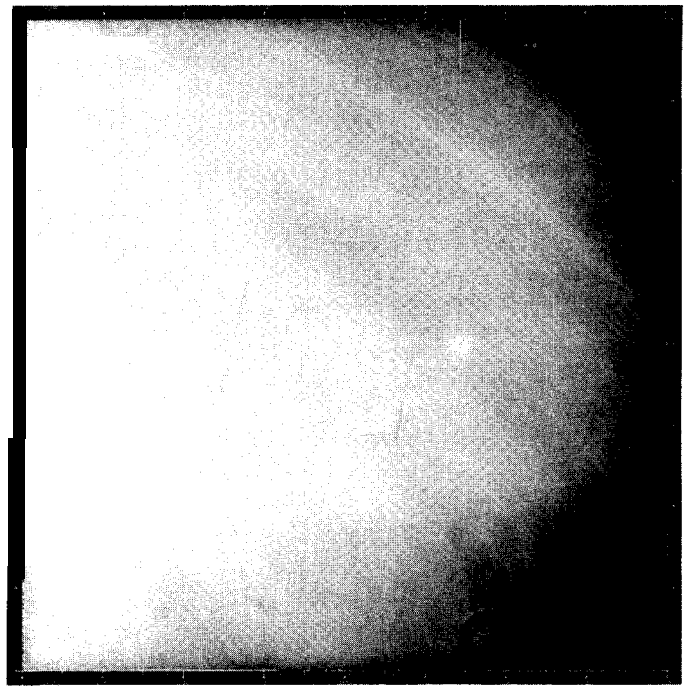

Figure 3-80. Calibrated slope file ratio, green/8890 A

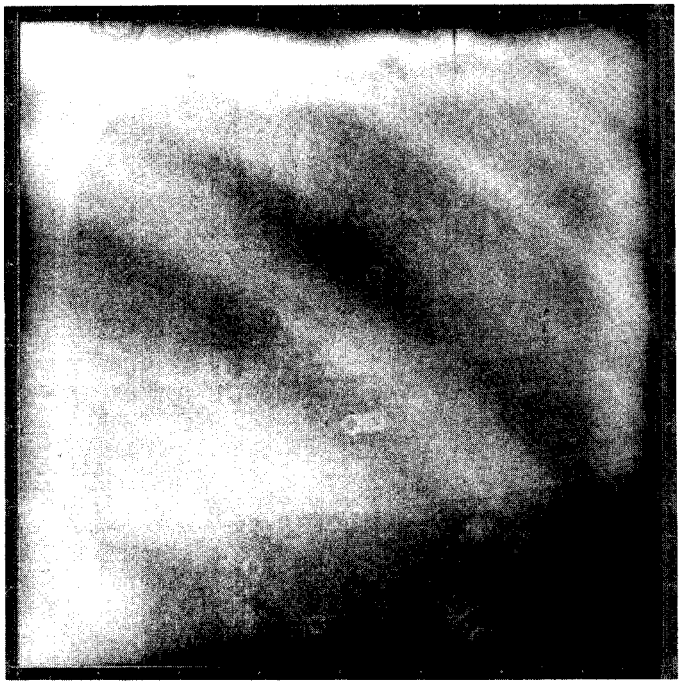

Figure 3-81. Calibrated slope file ratio, green/>9680 A

Table 3-12. Spatial Variation in Filter Factors

Filter	Filter Factor with Respect to Green Filter	Standard Deviation in Filter Factor Across Array
Clear	0.0805	0.00057 (0.71 %)
Red	0.4336	0.0046 (1.07 %)
Violet	27.63	0.49 (1.77 %)
7560 A	1.743	0.0127 (0.73 %)
>9680 A	4.788	0.051 (1.06 %)
7270 A	3.470	0.057 (1.65 %)
8890 A	5.868	0.094 (1.60 %)

Figures 3-82 through 3-95 display the array of maximum DN errors and rms DN errors produced by GALGEN for each combination of gain state and summation mode available. No significant differences with filter position were evident. The pixels having unacceptably nonlinear fits as defined by their residual errors are primarily concentrated in lines 1, 2, 799 and 800 and in columns 1 and 2 of the CCD array. Column 170 also exhibits unacceptably nonlinear behavior in gain state 4.

Figures 3-96 throuqh 3-102 show the locations of all pixels defined as blemishes by BLEMGEN for each combination of gain state and summation mode. Again, no variation with filter position was observed. Most blemishes are due to excessive charge

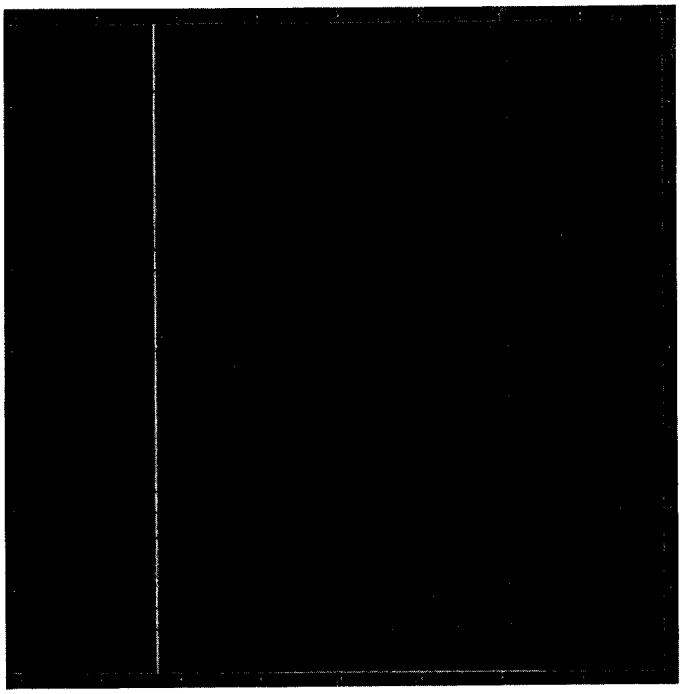

Figure 3-82. Maximum DN errors produced by GALGEN for gain state 4, normal mode.

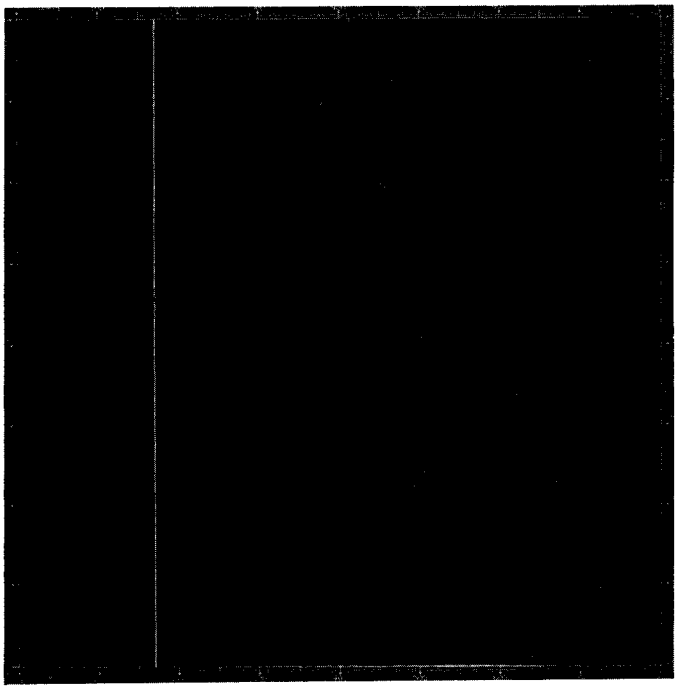

Figure 3-83. r.m.s. errors produced by GALGEN for gain state 4, normal mode

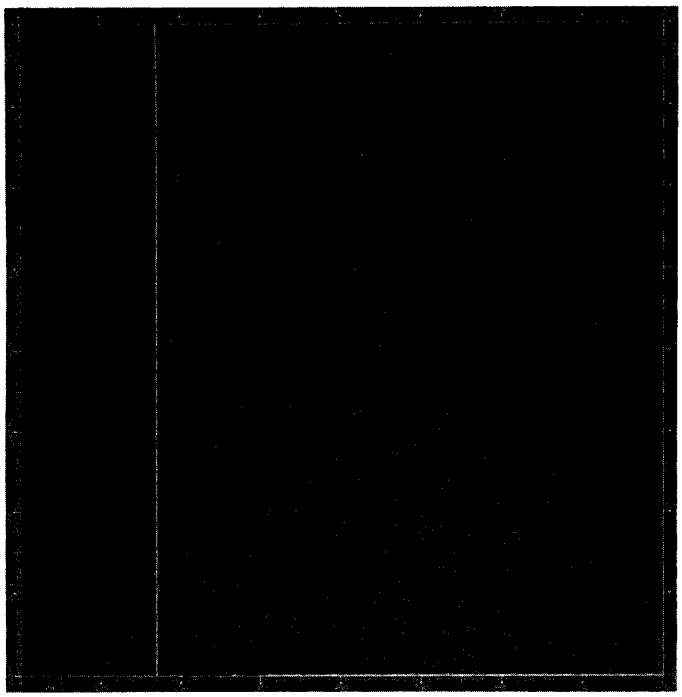

Figure 3-84. Maximum DN errors produced by GALGEN for gain state 3, normal mode.

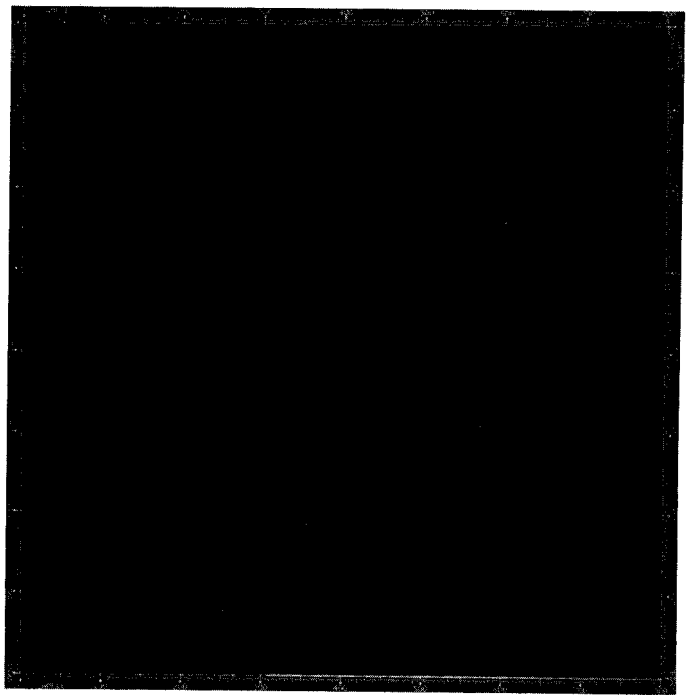

Figure 3-85. r.m.s. errors produced by GALGEN for gain state 3, normal mode

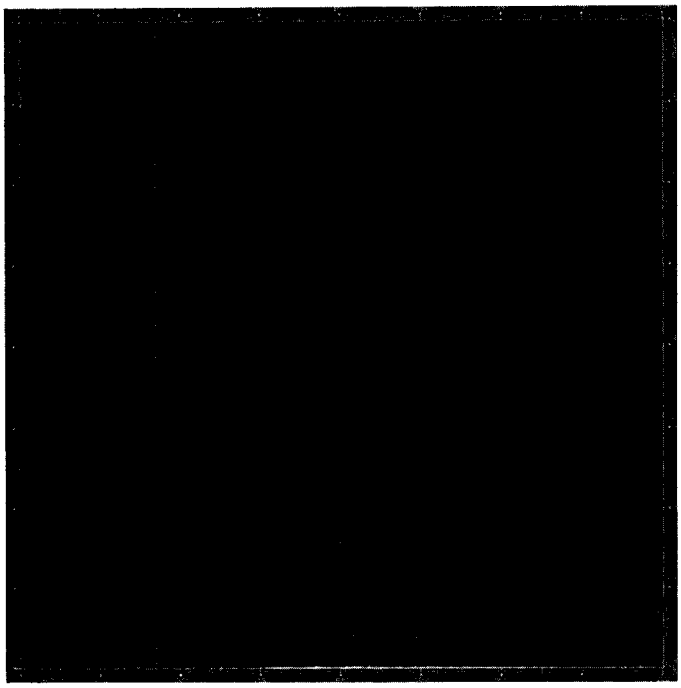

Figure 3-86. Maximum DN errors produced by GALGEN for gain state 2, normal mode.

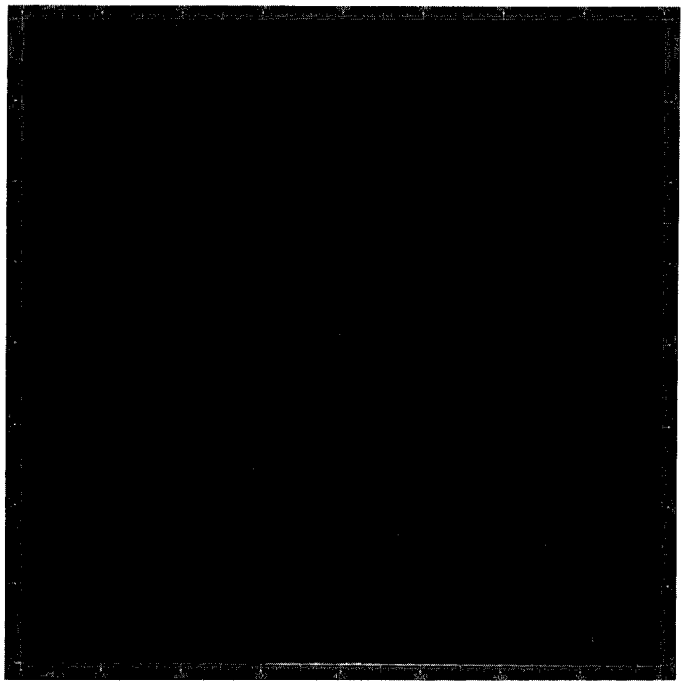

Figure 3-87. r.m.s. errors produced by GALGEN for gain state 2, normal mode

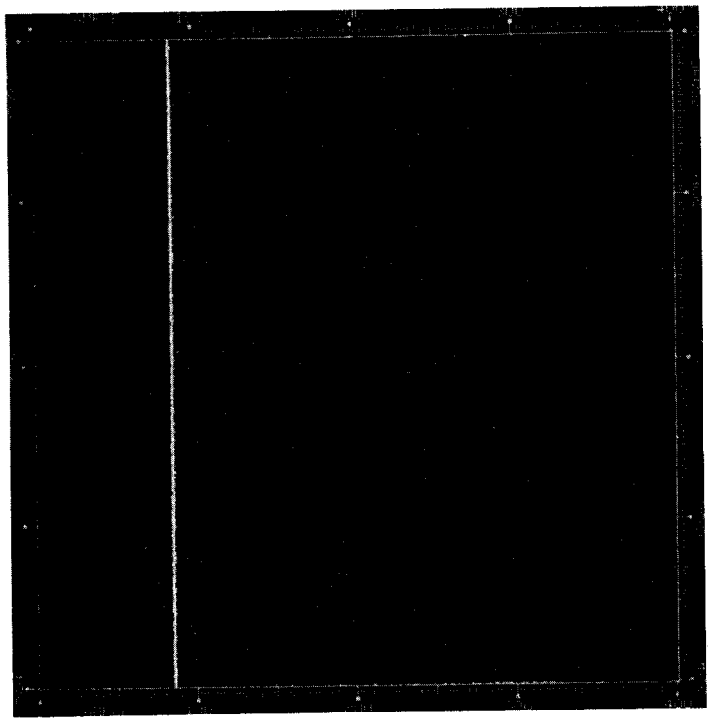

Figure 3-88. Maximum DN errors produced by GALGEN for gain state 4, summation mode.

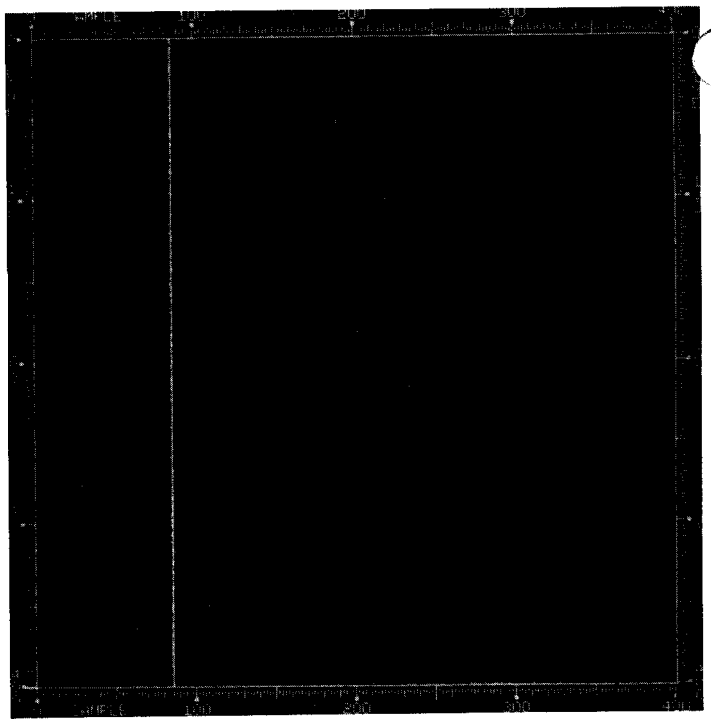

Figure 3-89. r.m.s. errors produced by GALGEN for gain 4, summation mode.

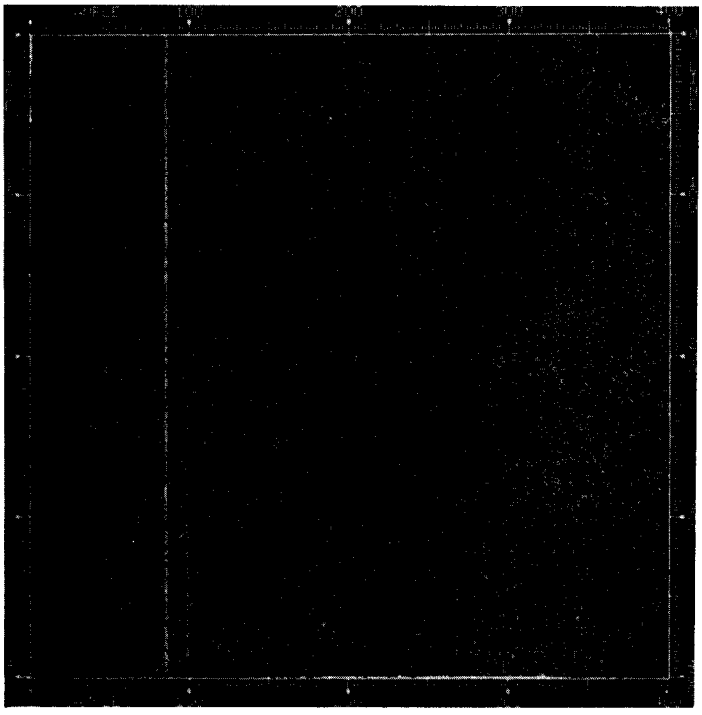

Figure 3-90. Maximum DN errors produced by GALGEN for gain state 3, summation mode.

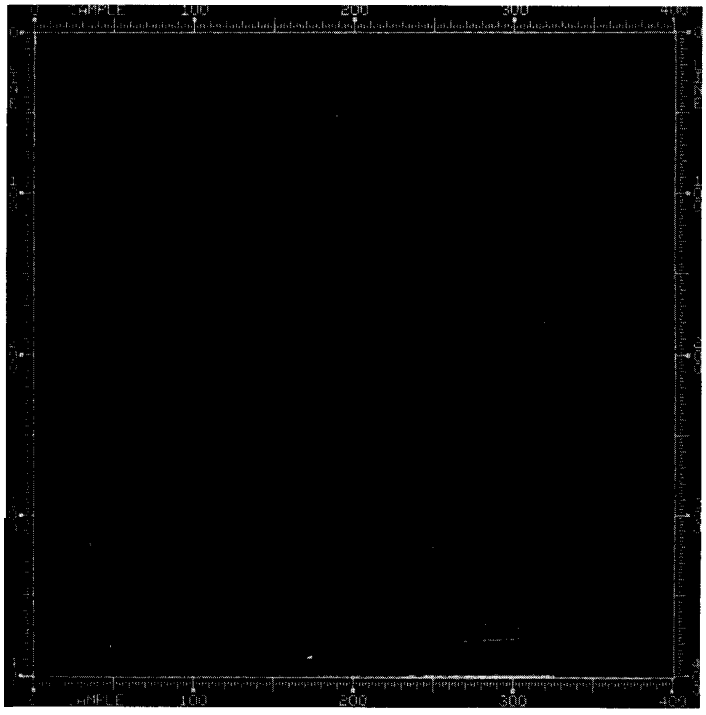

Figure 3-91. r.m.s. errors produced by GALGEN for gain 3, summation mode.

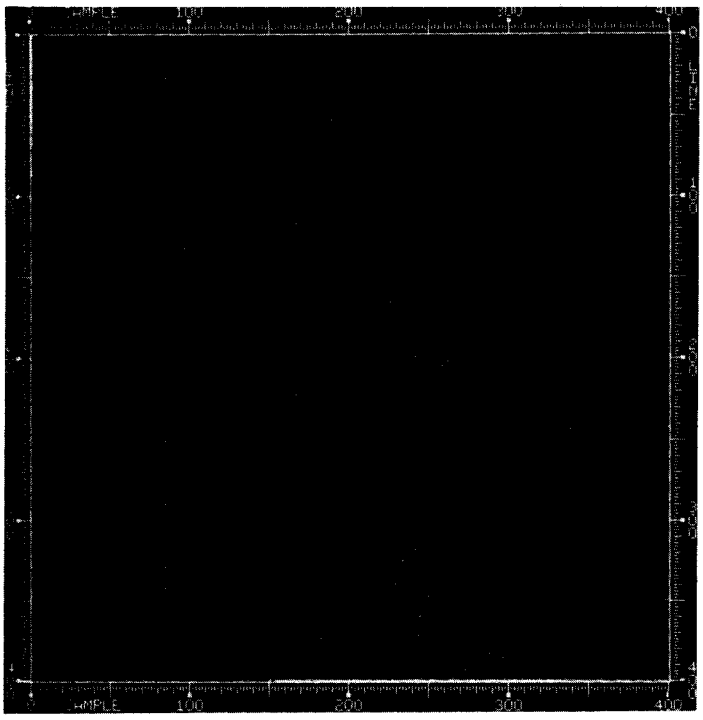

Figure 3-92. Maximum DN errors produced by GALGEN for gain state 2, summation mode.

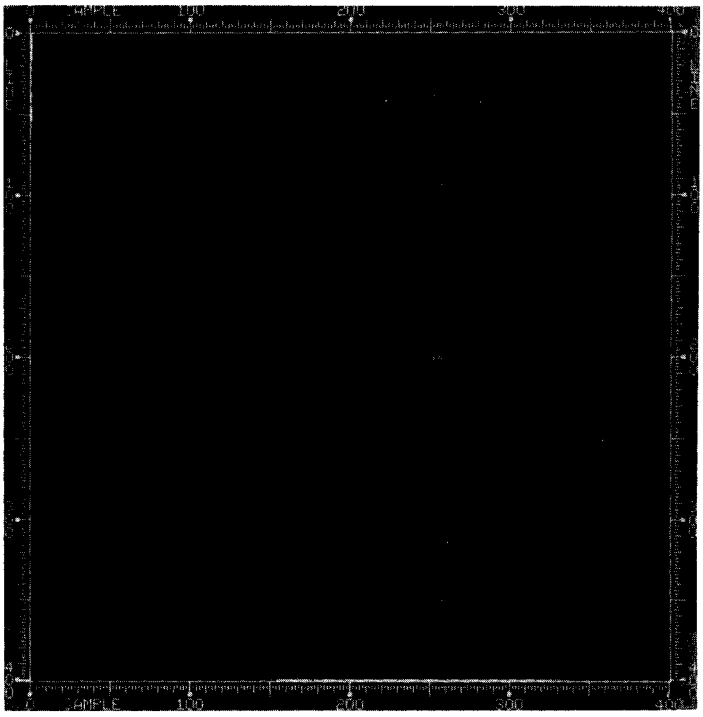

Figure 3-93. r.m.s. errors produced by GALGEN for gain 2, summation mode.

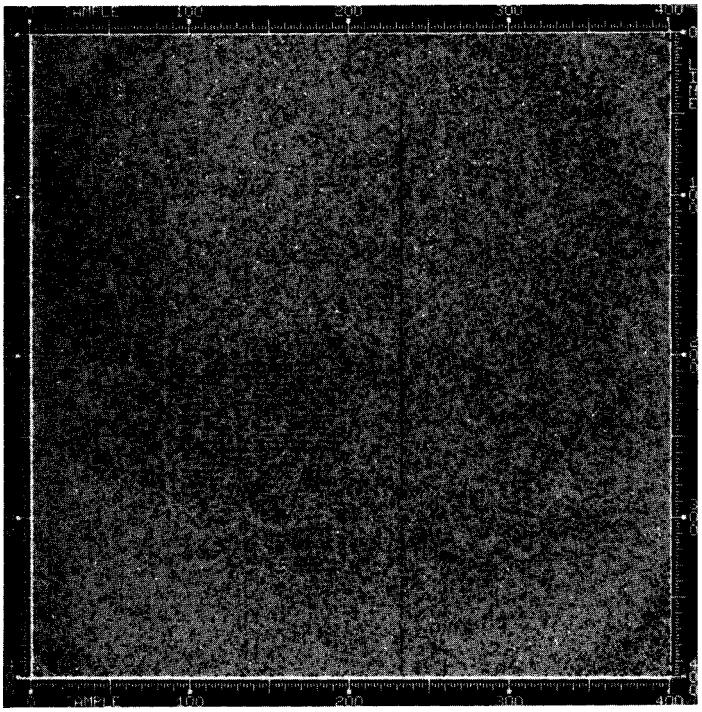

Figure 3-94. Maximum DN errors produced by GALGEN for gain state 1, summation mode.

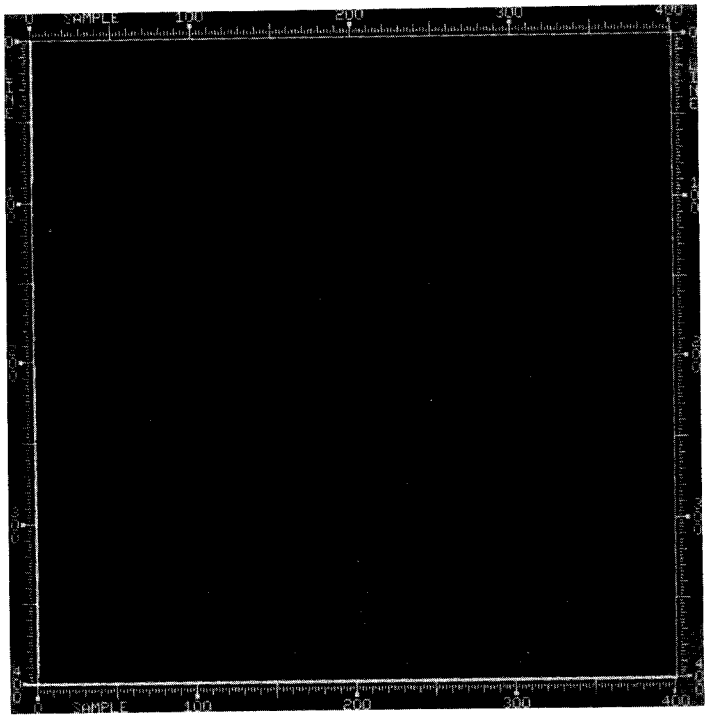

Figure 3-95. r.m.s. errors produced by GALGEN for gain 1, summation mode.

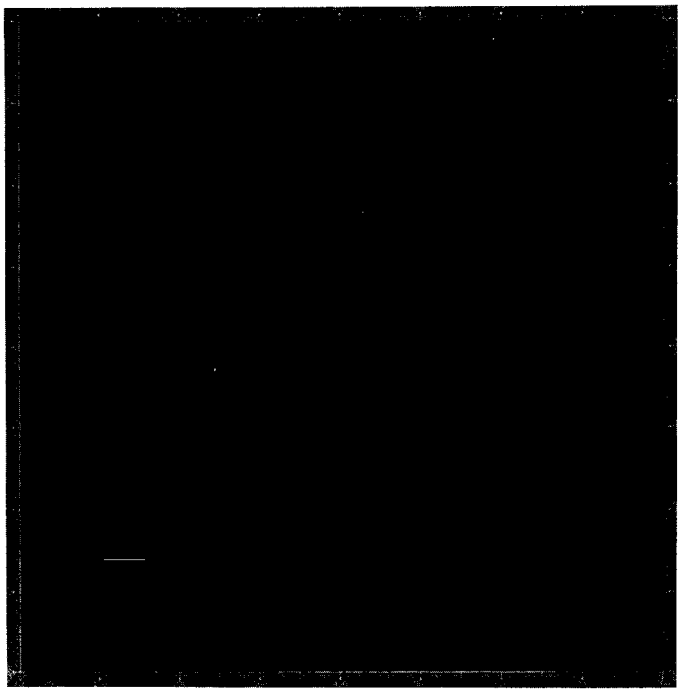

Figure 3-96. Blemish location image for gain state 4.

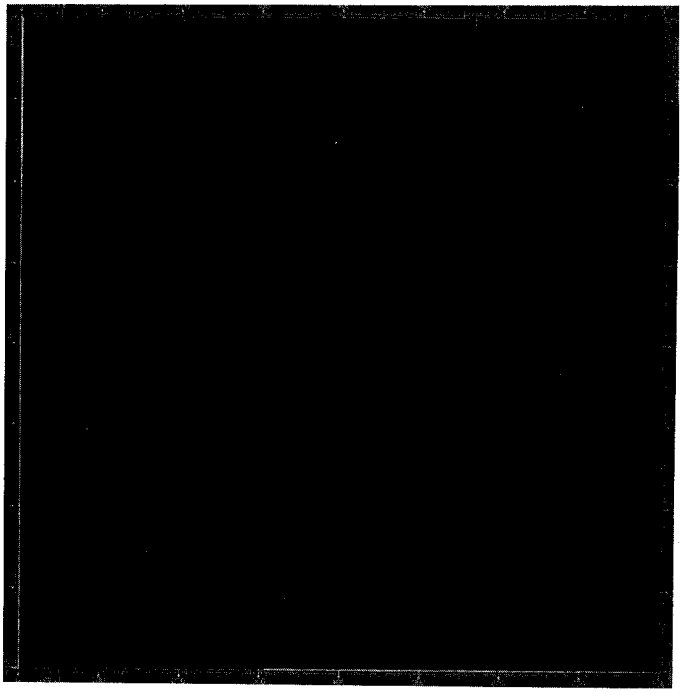

Figure 3-97. Blemish location image for gain state 3.

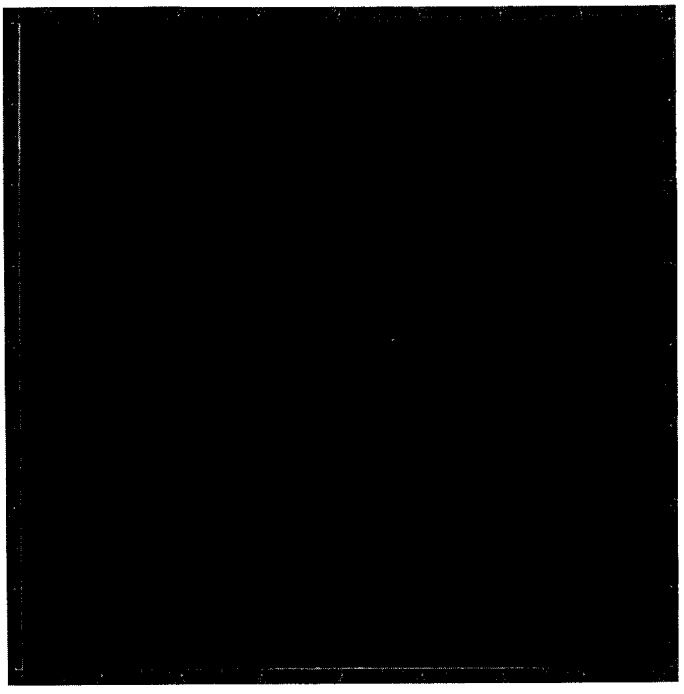

Figure 3-98. Blemish location image for gain state 2.

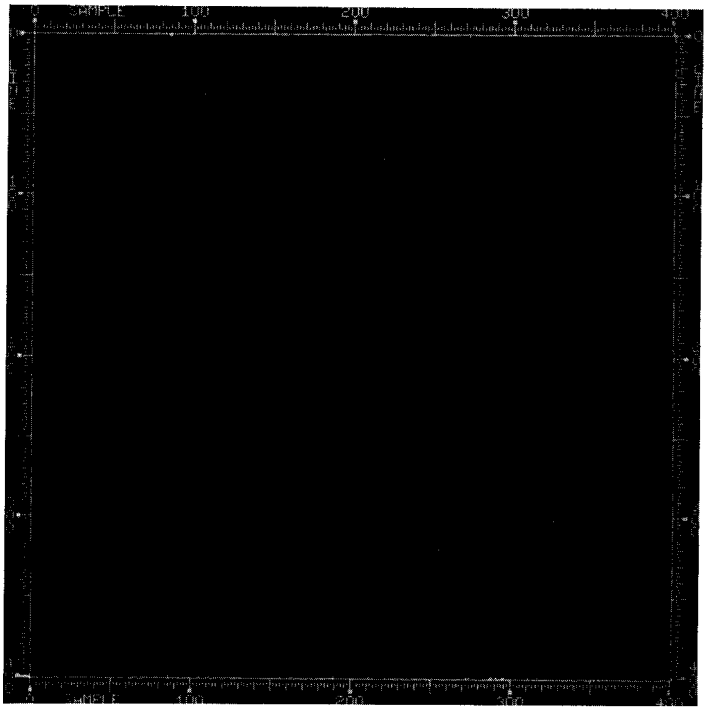

Figure 3-99. Blemish location image for gain state 4, summation mode.

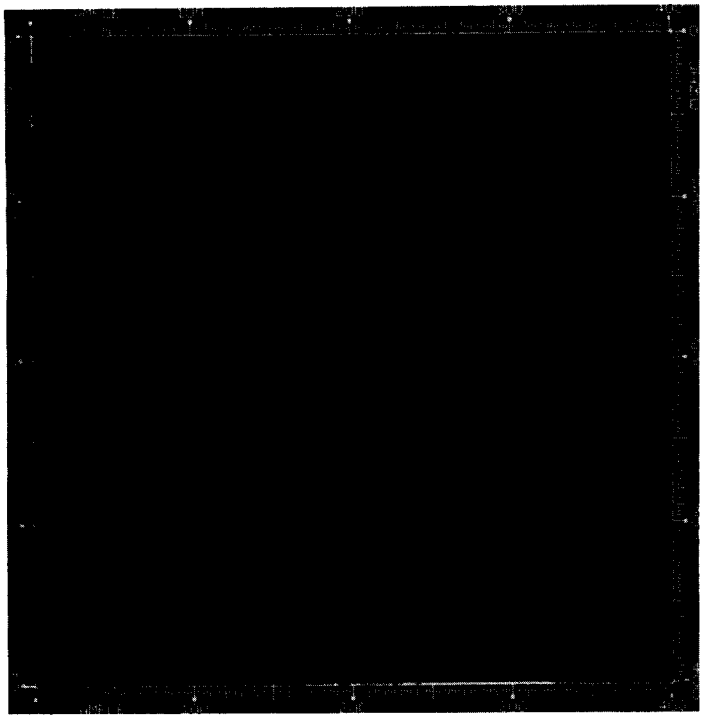

Figure 3-100. Blemish location image for gain state 3, summation mode.

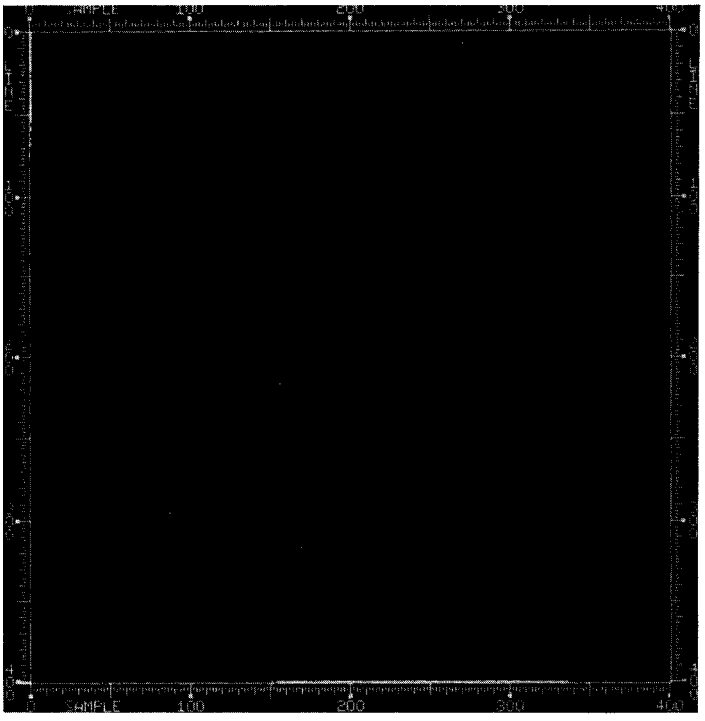

Figure 3-101. Blemish location for gain state 2, summation mode.

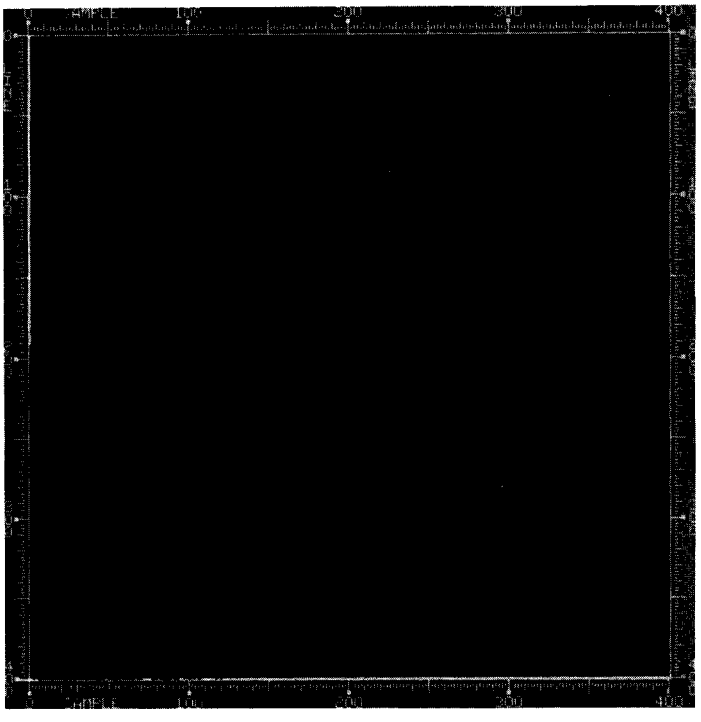

Figure 3-102. Blemish location image for gain state 2, summation mode.

collection in pixels located along the edge of the CCD array. In gain state 4 in the full-resolution mode, column 170 is classified as a blemish because of its nonlinear response, and in gain states 1 and 2, several columns exhibit low-full-well response.

Accurate determinations of the threshold saturation levels of the low-full-well pixels were obtained by examining pixel listings of various flat-field frames in the area of each low-full-well pixel at signal levels near and slightly above those pixels' saturation points. Table 3-13 lists the low-full-well pixel locations and the maximum charge level they will reliably transfer. The blemish files have been edited to incorporate these more accurate saturation thresholds. Figures 3-103 through 3-105 show a set of flat-field images acquired at signal levels from about 1/2 to the mean full-well level for the CCD. The locations of the low-full-well pixels are obvious. No saturation is observed in any of the gain states at less than 255 DN.

Table 3-13. Low-full-well Pixel Characteristics

gain state 2				summation gain state 1			
column	row	e-	1989 DN	column	row	e- (#)	1989 DN
96	389	90000	219	48	195	90000	241
269	420	62000	153	135	211	62000	169
351	679	88000	215	176	340	88000	237
466	75	32000	80(*)	233	38	37000	101
520	668	78000	191	260	334	82000	220
578	659	64000	156	289	330	67000	180
594	696	70000	172	297	348	71000	192
673	743	83000	204	337	372	82000	220
790	754	80000	195	395	377	84000	226

(*) 161 DN in gain state 3
(#) e- per original unsummed pixel

As was noted in Section III.B.5, the SSI spectral response varies with temperature. GALGEN files have been produced only for the expected flight temperature, +8°C. Light transfer data sets exist at -l0°c and +18°c as well; should the SSI temperature in flight differ significantly from that expected, revised calibration files will have to be produced.

co Spectral Response Math Model

The predicted SSI response to the light cannon sources during calibration as computed from the component-level spectral curves for the sensor, optics, filters, and light sources did not match the actual SSI response observed in the calibration images themselves and given in Table 3-7. Therefore, in order to create an SSI spectral response math model that more nearly matched the measured instrument performance, adjustments were

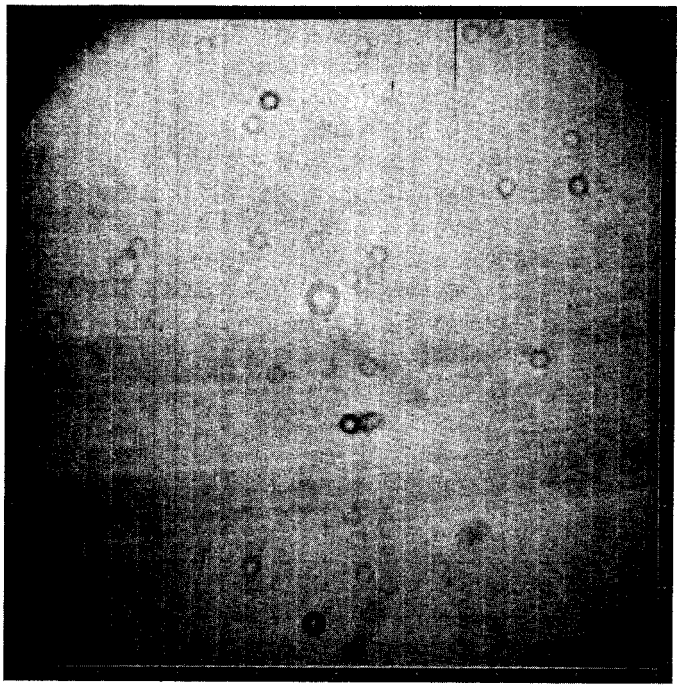

Figure 3-103. Flat-field image, gain state 2, mean DN = 118.

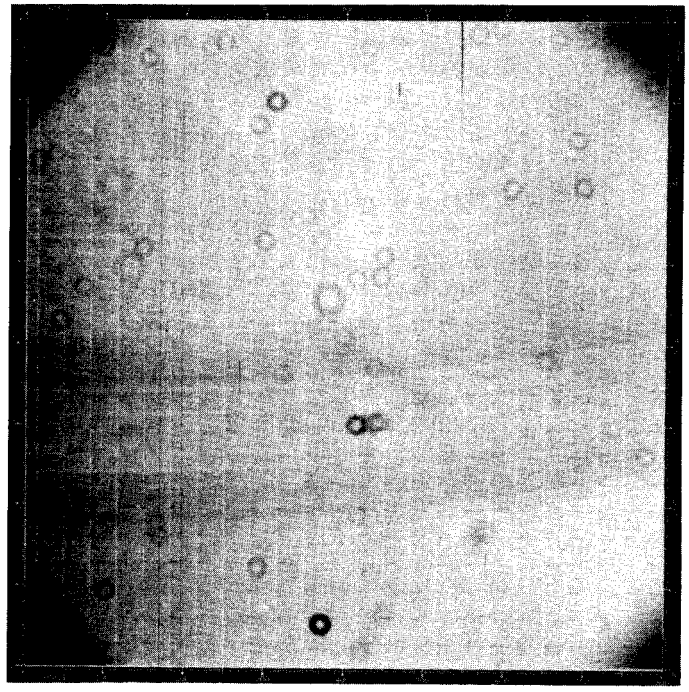

Figure 3-104. Flat-field image, gain state 2, mean DN = 180.

/---

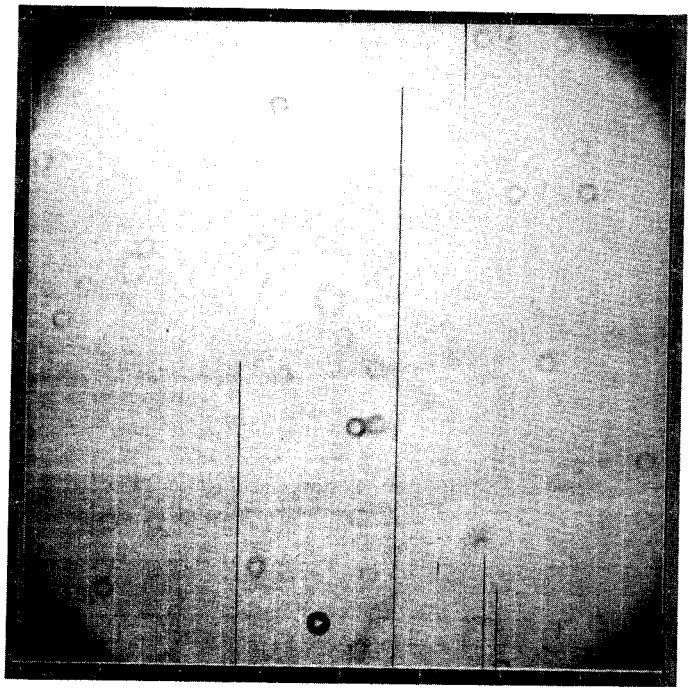

Figure 3-105. Flat-field image, gain state 2, mean DN = 233.

made to the component level data. A weighted-least-squares fit to the calibration data was derived by changing slightly the CCD spectral QE curve shape and scale, the optics spectral transmission curve scale and central wavelength, the filter transmission curves scales and central wavelengths, and the light source spectral radiance curves shape and scale as well as adjusting the conversion factor from e^- to DN slightly. Held constant at their component-level values were the widths of the filter bandpasses and the spectral transmission of the thermal vacuum chamber window. The calibration data that were matched consisted of the SSI response in each of the 8 SSI filters to the tungsten and xenon light cannons, to each of the spectral bandpass target filters in the MVM collimator, and to 43 selected squares of the color target in the MVM collimator. Although the bandpass filter targets and color targets have fairly large uncertainties in their spectral radiances since they were not as well calibrated as the light cannons, the use of the additional different color spectra they provide helps to constrain the least-squares solution.

Table 3-14 gives the ratio of the SSI response to the tungsten light cannon as computed using the SSI spectral response math model to that actually observed in the calibration data for both the original component-level spectral curves and for the adjusted curves resulting from the least-squares fit. With the adjustments, the SSI spectral response math model yields results that match the calibration results to within 1%.

Table 3-14. Computed/Actual Response to Light Cannons

Filter	Component Model	New Spectral Response Model
Clear	1.07	0.989
Violet	1.06	1.000
Green	0.94	1.003
Red	0.87	1.003
7270 A	1.10	0.997
7560 A	0.98	1.008
8890 A	1.07	1.004
>9680 A	1.11	1.002
Violet (xenon)	1.06	0.999

Figures 3-106 through 3-112 compare the component-level spectral curves for the CCD QE, optics transmission, filter transmission, the light source radiances,and the overall system spectral response to the adjusted curves from the least-squares fit. The adjusted values for the overall system response are also provided in tabular form in Table 3-15. The CCD QE had to be increased by about 15% in the visible and decreased by about 10% beyond 800 nm It is not unrealistic that the component-level calibration of the absolute QE could have been in error by this amount. Several of the filter transmission curves had to be changed noticeably - transmission increased by 8% to 10% for the red and 8890 A filters and decreased 9% to 10% for the clear and

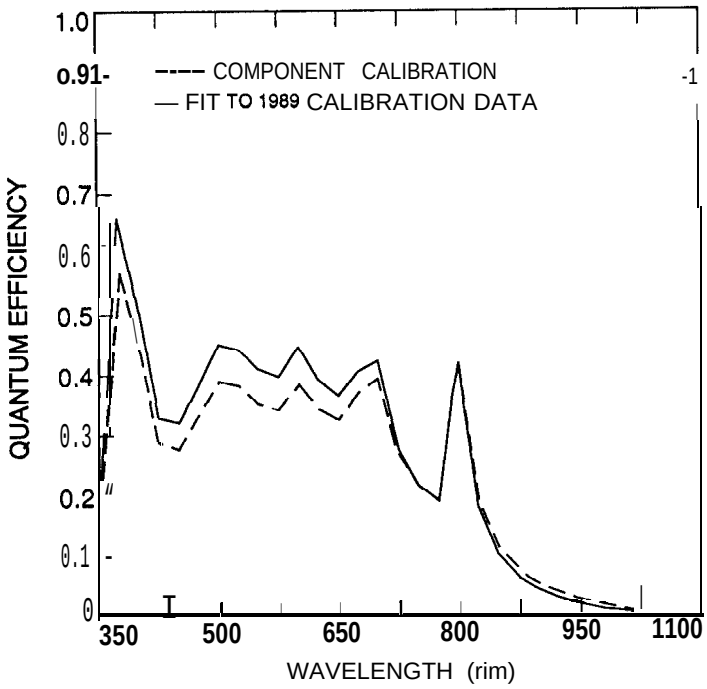

Figure 3-106. CCD quantum efficiency component-level data before and after adjustment for best fit to 1989 instrument calibration data.

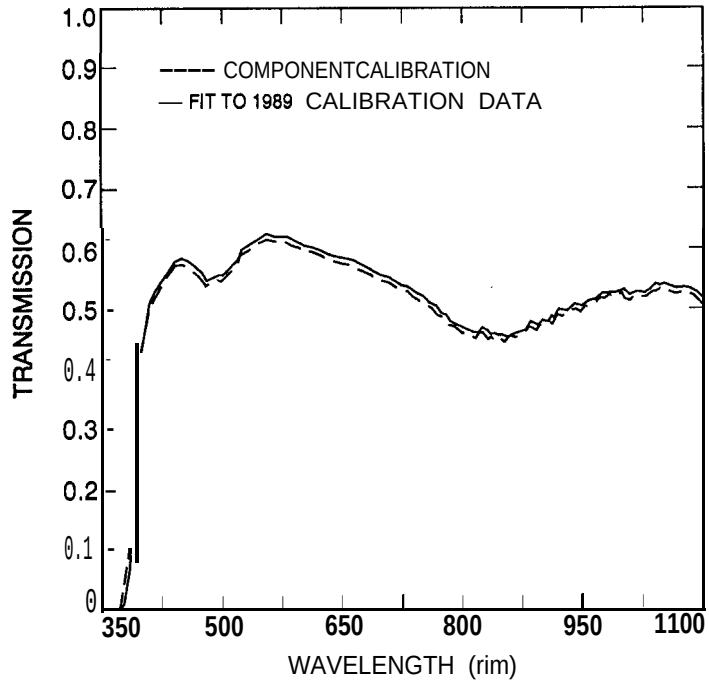

Figure 3-107. SSI optics transmission component-level data before and after adjustment for best fit to 1989 instrument calibration data.

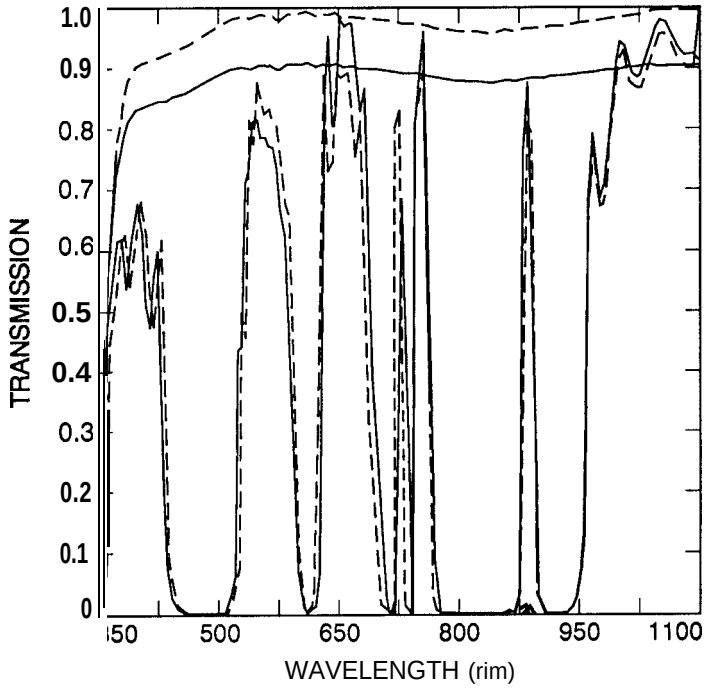

Figure 3-108. SSI filter transmission component-level data before and after adjustment for best fit to 1989 instrument calibration data.

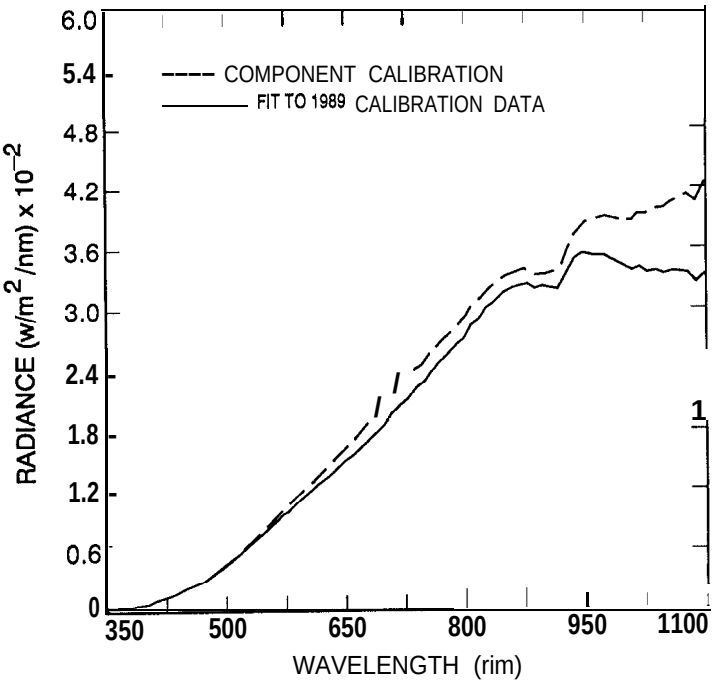

Figure 3-109. Tungsten light cannon spectral radiance component-level data before and after adjustment for best fit to 1989 instrument calibration data.

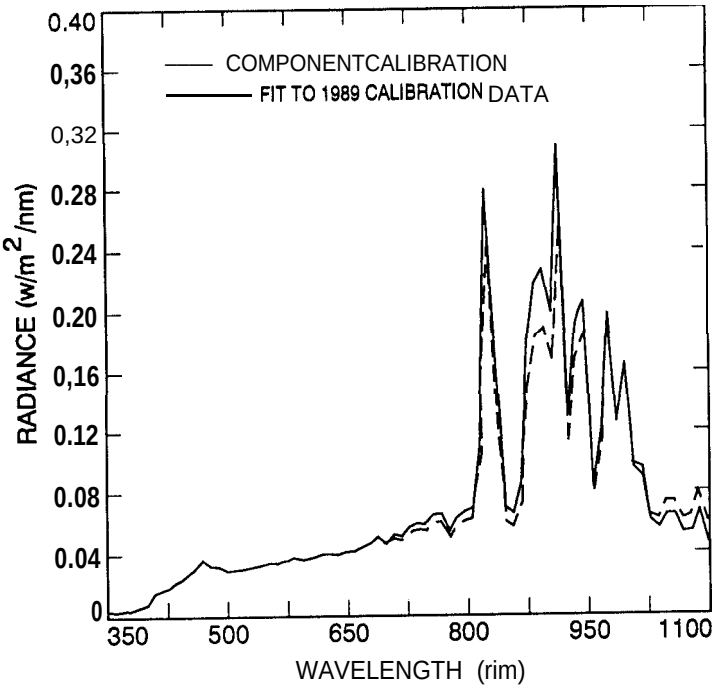

Figure 3-110. Xenon light cannon spectral radiance component-level data before and after adjustment for best fit to 1989 instrument calibration data.

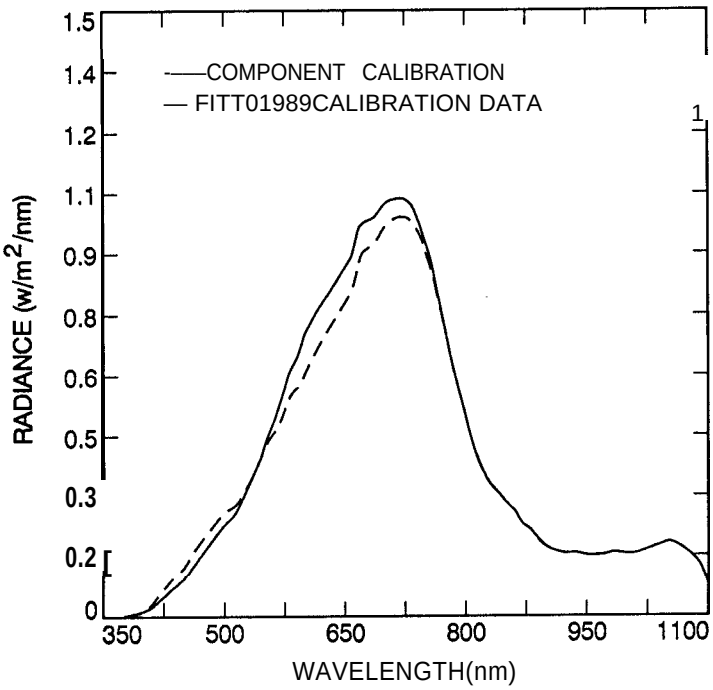

Figure 3-111. MVM collimator spectral radiance component-level data before and after adjustment for best fit to 1989 instrument calibration data.

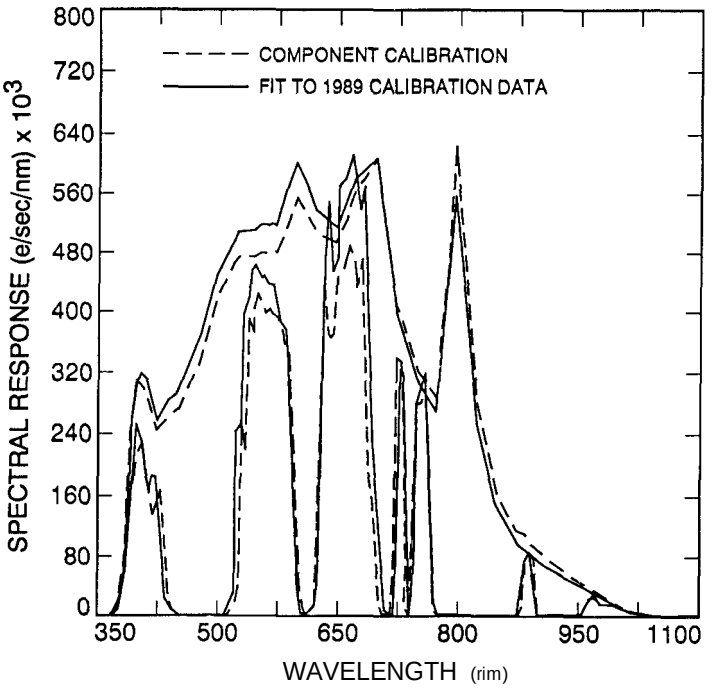

Figure 3-112. SSI spectral response from component-level data before and after adjustment for best fit to 1989 instrument calibration data.

Table 3-15. SSI subsystem spectral response adjusted for-best fit to 1989 instrument calibration data (e^-/sec/nm x 10^3)

wvl (nm)	filter none	clear	violet	green	red	7270A	7560A	8890A	9680A
350	.0000	.0000	.0000	.0000	.0000	.0000	.0000	.0000	.0000
355	.0000	.0000	.0000	.0000	.0000	.0000	.0000	.0000	.0000
360	.0000	.0000	.0000	.0000	.0000	.0000	.0000	.0000	.0000
365	.0000	.0000	.0000	.0000	.0000	.0000	.0000	.0000	.0000
370	.0000	.0000	.0000	.0000	.0000	.0000	.0000	.0000	.0000
375	9.151	6.508	5.648	.0000	.0000	.0000	.0000	.0000	.0000
380	46.40	34.84	28.83	.0023	.0000	.0000	.0000	.0000	.0000
385	104.8	82.55	56.37	.0063	.0000	.0000	.0000	.0000	.0000
390	217.3	175.6	124.9	.0283	.0000	.0000	.0000	.0000	.0000
395	315.8	258.7	200.3	.0190	.0000	.0000	.0000	.0000	.0000
400	367.6	305.0	249.9	.0147	.0000	.0000	.0000	.0000	.0000
405	383.6	319.2	239.3	.0192	.0000	.0000	.0000	.0000	.0000
410	374.2	312.2	191.9	.0524	.0000	.0000	.0000	.0000	.0000
415	356.2	298.1	167.7	.2849	.0000	.0000	.0000	.0000	.0000
420	332.3	278.8	185.5	.0731	.0000	.0000	.0000	.0000	.0000
425	308.7	260.1	185.6	.0031	.0000	.0000	.0000	.0000	.0000
430	317.9	268.6	71.57	.0000	.0000	.0000	.0000	.0000	.0000

Table 3-15 (continued)

wvl (nm)	filter								
	none	clear	violet	green	red	7270A	7560A	8890A	9680A
435	325.6	275.6	23.25	.0000	.0000	.0000	.0000	.0000	.0000
440	333.2	283.2	8.802	.0000	.0000	.0000	.0000	.0000	.0000
445	337.5	288.0	3.820	.0000	.0000	.0000	.0000	.0000	.0000
450	340.3	291.0	1.613	.0000	.0000	.0000	.0000	.0000	.0000
455	356.4	305.5	.7129	.0000	.0000	.0000	.0000	.0000	.0000
460	371.0	318.5	.1002	.0000	.0000	.0000	.0000	.0000	.0000
465	385.9	332.7	.1042	.0000	.0000	.0000	.0000	.0000	.0000
470	400.9	347.0	.1082	.0000	.0000	.0000	.0000	.0000	.0000
475	413.9	359.8	.1118	.0000	.0000	.0000	.0000	.0000	.0000
480	424.7	370.8	.1147	.0000	.0000	.0000	.0000	.0000	.0000
485	445.6	391.1	.1203	.0000	.0000	.0000	.0000	.0000	.0000
490	466.6	411.3	.1213	.0000	.0000	.0000	.0000	.0000	.0000
495	489.9	433.9	.0588	.0000	.0000	.0000	.0000	.0000	.0000
500	509.2	452.1	.0407	.0000	.0000	.0000	.0000	.0000	.0000
505	517.4	461.7	.0259	.0000	.0000	.0000	.0000	.0000	.0000
510	527.0	472.2	.0158	5.391	.0000	.0000	.0000	.0000	.0000
515	536.5	482.0	.0161	20.11	.0000	.0000	.0000	.0000	.0000
520	548.6	493.9	.0055	35.30	.0000	.0000	.0000	.0000	.0000
525	564.3	509.1	.0056	245.3	.0000	.0000	.0000	.0000	.0000
530	566.0	511.5	.0057	252.5	.0000	.0000	.0000	.0000	.0000
535	567.3	512.2	.0057	402.1	.0000	.0000	.0000	.0000	.0000
540	567.1	511.5	.0170	418.8	.0000	.0000	.0000	.0000	.0000
545	567.5	511.6	.0284	461.6	.0000	.0000	.0000	.0000	.0000
550	568.1	514.1	.0682	463.8	.0000	.0000	.0000	.0000	.0000
555	572.8	519.4	.1317	449.4	.0000	.0000	.0000	oooo	.0000
560	573.7	520.4	.1950	450.8	.0000	.0000	.0000	.0000	.0000
565	573.7	519.7	.2123	442.2	.0000	.0000	.0000	.0000	.0000
570	574.7	521.2	.1264	441.2	.0000	.0000	.0000	.0000	.0000
575	576.3	519.7	.0576	420.4	.0000	.0000	.0000	.0000	.0000
580	595.4	536.4	.0179	393.5	.0000	.0000	.0000	.0000	.0000
585	612.8	555.3	.0061	382.2	.0000	.0000	.0000	.0000	.0000
590	630.5	573.3	.0063	271.7	.0000	.0000	.0000	.0000	.0000
595	647.3	588.2	.0065	138.9	.0000	.0000	.0000	.0000	.0000
600	664.4	604.2	.0066	43.73	.0000	.0000	.0000	.0000	.0000
605	650.3	591.4	.0065	5.996	.1756	.0000	.0000	.0000	.0000
610	637.6	580.7	.0064	.2423	2.053	.0000	.0000	.0000	.0000
615	623.8	569.3	.0062	.2870	7.105	.0000	.0000	.0000	.0000
620	610.3	555.2	.0061	.0610	11.05	.0000	.0000	.0000	.0000
625	595.5	540.0	.0060	.0000	41.67	.0000	.0000	.0000	.0000
630	588.3	534.6	.0059	.0000	196.0	.0000	.0000	.0000	.0000
635	583.0	530.7	.0058	.0000	475.6	.0000	.0000	.0000	.0000
640	576.6	524.7	.0058	.0000	552.2	.0000	.0000	.0000	.0000
645	570.8	518.8	.0057	.0000	458.8	.0000	.0000	.0000	.0000
650	565.6	515.6	.0057	.0000	473.7	.0000	.0000	.0000	.0000
655	581.9	528.3	.0058	.0000	573.3	.0000	.0000	oooo	.0000
660	598.8	541.9	.0180	.0000	581.8	.0000	.0000	.0000	.0000
665	613.5	555.7	.0430	.0000	599.3	.0000	.0000	.0000	.0000
670	628.0	569.3	.0879	.0000	614.6	.0000	.0000	.0063	.0000
675	642.7	581.9	.1735	.0000	587.2	.0000	.0000	.0064	.0000
680	649.4	587.0	.2922	.0000	539.4	.0065	.0000	.0065	.0000
685	657.0	593.9	.4008	.0000	572.4	.0066	.0000	.0066	.0000

Table 3-15 (continued)

wvl(nm)	filter none	clear	violet	green	red	7270A	7560A	8890A	9680A
690	663.6	599.8	.4579	.0000	459.9	.0066	.0000	.0066	.0000
695	669.0	604.6	.4616	.0000	230.9	.0067	.0000	.0067	.0067
700	675.6	610.1	.4324	.0000	164.0	.0135	.0000	.0135	.0135
705	632.2	570.8	.3287	.0000	61.50	.0253	.0000	.0190	.0063
710	587.2	529.6	.2466	.0000	10.08	.0352	.0000	.0117	.0000
715	542.1	488.4	.1843	.0000	2.629	.0434	.0000	.0054	.0163
720	495.8	446.3	.1339	.0000	1.507	2.494	.0000	.0099	.0248
725	449.8	404.4	.0945	.0000	1.332	96.59	.0000	.0135	.0045
730	431.6	387.3	.0734	.0000	1.144	327.1	.0000	.0086	.0000
735	412.1	369.1	.1071	.0000	.0041	237.1	1.154	.0041	.0041
740	391.4	350.6	.0861	.0000	.0352	6.897	4.513	.0000	.0078
745	372.4	333.5	.0670	.0000	.0298	.3687	70.05	.0000	.0037
750	353.0	315.9	.0494	.0000	.2118	.2436	281.0	.0000	.0035
755	343.4	307.2	.0481	.0000	.2095	.0172	304.7	.0000	.0034
760	334.0	298.2	.0401	.0000	.2372	.0100	323.2	.0000	.0033
765	326.1	290.8	.0587	.0261	.2315	.0098	220.1	.0000	.0033
770	315.8	281.1	.0505	.0063	.1800	.0063	30.46	.0000	.0032
775	304.7	270.9	.0305	.0000	.1280	.0030	2.480	.0000	.0000
780	375.3	333.3	.0375	.0375	.1388	.0000	1.235	.0000	.0000
785	439.5	389.6	.0527	.0088	.1450	.0000	.5494	.0000	.0000
790	508.5	450.3	.0661	.1119	.1729	.0000	.2898	.0000	.0000
795	576.6	510.6	.0923	.2191	.2422	.0000	.2076	.0000	.0000
800	642.5	568.4	.1092	.2506	.3341	.0064	1992	.0000	.0000
805	570.8	504.6	.1142	.1598	.2854	.0114	.0856	.0000	.0057
810	498.2	440.3	.1096	.1295	.2242	.0100	.0797	.0000	.0050
815	427.8	377.8	.1112	.1840	.1968	.0086	.0770	.0000	.0043
820	359.6	317.5	.1043	.1978	.1726	.0072	.0611	.0000	.0072
825	295.4	260.6	.1034	.1270	.1595	.0059	.0502	.0000	.0059
830	269.9	238.3	.1161	.0405	.1917	.0027	.0486	.0000	.0054
835	242.4	213.8	.1164	.0533	.2812	.0000	.0461	.0000	.0048
840	220.1	193.9	.1277	.0484	.4380	.0044	.0418	.0000	.0044
845	196.0	172.6	.1431	.0490	.4214	.0059	.0353	.0020	.0059
850	172.8	152.3	.1521	.0518	.3905	.0052	.0311	.0017	.0052
855	159.8	141.1	.1566	.0511	.5544	.0032	.0304	.0032	.0032
860	149.7	132.5	.1572	.0449	.7051	.0030	.0299	.0090	.0030
865	138.9	123.0	.1500	.0306	1.014	.0014	.0278	.0139	.0014
870	127.8	113.2	.1355	.0345	1.060	.0013	.0256	.1393	.0026
875	116.8	103.2	.1203	.0420	.5219	0012	.0210	5.272	.0070
880	111.5	98.70	.1082	.0469	.2800	.0011	.0190	40.42	.0078
885	107.3	95.02	.0933	.0494	1.359	.0021	.0172	82.78	.0075
890	99.85	88.55	0719	.0499	1.776	.0050	.0140	88.33	.0070
895	93.06	82.74	.0549	.0484	.1619	0056	.0112	44.20	.0195
900	87.83	78.09	.0378	.0457	.0369	.0026	,0088	2.770	.0378
905	83.48	74.23	.0267	.0426	.0167	.0017	.0067	.9534	.0426
910	80.53	71.69	.0185	.0395	.0169	.0008	.0048	.0596	.0548
915	76.08	67.80	.0122	.0350	.0266	.0008	.0030	.0251	.0662
920	73.60	65.70	.0088	.0280	.0206	.0015	.0022	.0088	.0905
925	68.58	61.23	0069	.0192	0075	.0041	.0014	.0062	.1248
930	65.04	58.07	.0065	.0150	.0052	.0111	.0007	.0052	.1841
935	62.25	55.58	.0056	.0118	.0087	.0081	.0000	.0044	.2702
940	58.90	52.64	.0053	.0094	.0094	.0012	.0000	.0035	.5407

Table 3-15 (continued)

wvl (nm)	filter none	clear	violet	green	red	7270A	7560A	8890A	9680A
945	55.13	49.32	.0044	.0099	.0066	.0006	.0000	.0028	1.212
950	51.09	45.75	.0036	.0112	.0061	.0005	.0000	.0026	2.321
955	48.18	43.19	.0034	.0149	.0125	.0005	.0000	.0024	6.401
960	44.73	40.15	.0031	.0183	.0206	.0000	.0000	.0018	16.96
965	41.32	37.15	.0029	.0227	.0223	.0004	.0000	.0017	28.33
970	38.05	34.19	.0027	.0206	.0190	.0004	.0000	.0011	30.31
975	34.62	31.17	.0031	.0177	.0104	.0003	.0000	.0010	25.34
980	31.58	28.47	.0025	.0155	.0069	.0003	.0000	.0006	21.82
985	28.65	25.88	.0026	.0143	.0049	.0000	.0000	.0006	20.47
990	25.21	22.78	.0023	.0124	.0040	.0000	.0000	.0005	19.66
995	22.23	20.11	.0020	.0102	.0040	.0000	.0000	.0004	19.00
1000	19.04	17.21	.0015	.0089	.0038	.0002	.0000	.0002	17.46
1005	16.62	15.06	.0013	.0090	.0035	.0003	.0000	.0002	15.82
1010	14.48	13.14	.0012	.0112	.0036	.0001	.0000	.0000	13.69
1015	12.48	11.34	.0011	.0124	.0036	.0000	.0000	.0000	11.45
1020	10.30	9.371	.0010	.0120	.0032	.0000	.0000	.0000	9.233
1025	8.039	7.313	.0011	.0105	.0024	.0001	.0000	.0000	7.170
1030	7.020	6.396	.0011	.0103	.0017	.0001	.0000	.0000	6.288
1035	5.986	5.455	.0010	.0095	.0008	.0001	.0000	.0000	5.450
1040	4.948	4.510	.0008	.0083	.0003	.0000	.0000	.0000	4.620
1045	3.822	3.486	.0005	.0067	.0004	.0000	.0000	.0000	3.660
1050	2.702	2.459	.0003	.0050	.0005	.0000	.0000	.0000	2.640
1055	2.334	2.124	.0003	.0046	.0005	.0000	.0000	.0000	2.303
1060	1.956	1.780	.0003	.0045	.0004	.0000	.0000	.0001	1.926
1065	1.601	1.458	.0004	.0042	.0004	.0000	.0000	.0000	1.559
1070	1.230	1.120	.0003	.0037	.0003	.0000	.0000	.0000	1.182
1075	.8570	.7801	.0003	.0029	.0002	.0000	.0000	.0000	.8111
1080	.6923	.6301	.0003	.0027	.0003	.0000	.0000	.0000	.6476
1085	.5493	.4995	.0003	.0023	.0004	.0000	.0000	.0000	.5103
1090	.3821	.3475	.0002	.0018	.0005	.0000	.0000	.0000	.3553
1095	.2132	. 1939	.0001	.0011	.0006	.0000	.0000	.0000	.1987
1100	.0707	.0705	.0000	.0004	.0004	.0000	.0000	.0000	.0650

7270 A filters. Central wavelength shifts implied were small - 5 nm or less. The tungsten cannon spectral radiance appeared to be about 8% lower than expected in the red and near-IR , while the xenon cannon radiance appeared to be slightly higher in the near-IR (about 10%) . And finally, the high-gain conversion factor from e^- to DN increased by about 2%.

The SSI spectral response math model that resulted from this study certainly does not represent a unique solution to the problem of fitting the calibration results. However, it is felt to be an improvement over the model that results from simply using the component calibration data unchanged. Therefore, the revised model was used for calculating the conversion factors from source ftL to units of radiance and reflectivity given in Section III.B.5. Until an improved model can be derived, it also will be used for calculating the predicted SSI response to targets imaged in flight.

The availability of three different SSI spectral response models (based on component calibration spectral curves, curves re-adjusted to fit the 1985 system-level calibration data using the assumptions of Sections II.A.7 and III.B.5 regarding calibration of the tungsten light cannon, and curves adjusted to fit the 1989 system-level calibration data) makes possible an evaluation of any SSI absolute sensitivity changes with time for the various filters and/or an evaluation of the uncertainty in the determination of the SSI absolute sensitivity for the various filters. This was done by computing the SSI response to a imaginary source having a fixed, spectrally uniform radiance level using all three math models and comparing the results. Based on the conclusions reached in Section III.B.5 above, the absolute SSI sensitivity in the green filter was assumed not to have changed with time, and the computed SSI responses were all normalized to the mean green filter response. Figure 3-113 plots the ratio of the normalized response for each filter in each model to the mean response values for each filter for the three models. The scatter in these ratios is quite large reaching 8% for the red and clear filters and 22% for the violet filter. The variations in response implied by the three models could represent actual time variability in SSI spectral sensitivity, time-variable errors in the calibration light source spectral calibrations, and/or allowable flexibility in fitting the models to the calibration data sets. Selection of the best spectral response model to use for predicting SSI response to light sources other than the calibration sources is a problem. If ths SSI spectral sensitivity were really unchanging, the best model appears to be that using the component-level spectral curves since it has the least scatter about the mean. If, however, the SSI spectral response is really changing with time, the best model to use is the one that fits the most recent data best, i.e., the 1989 calibration fit. This model has been chosen for current use; however, the uncertainties in the absolute spectral response of the SSI to different scene radiances using this model should be understood to be at about the 10% level for most filters and at about the 20% level for the

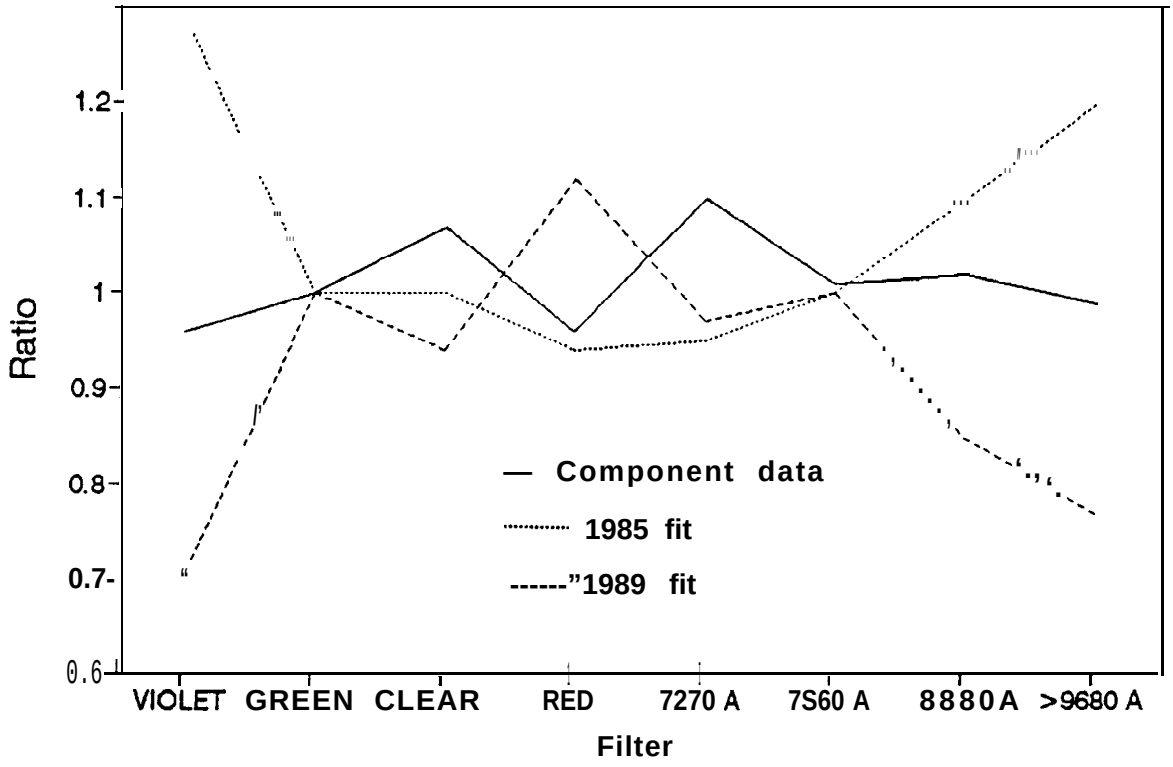

Figure 3-113. Relative SSI spectral response history normalized to the green filter and ratioed to the mean value in each filter

violet and >9680A filters, at least until additional inflight calibration data are acquired and analyzed.

D. Zero-Exposure Offset

Besides the zero-exposure frames taken as part of the various light transfer data sets, additional zero-exposure frames were acquired for the many SSI modes (93 out of a total of 104 possible combinations of frame time, gain state, normal or extended exposure mode, CCD clock voltage level, and use of blemish protection) in which light transfer data were not acquired. These frames were normally obtained at three SSI temperatures. In most cases, multiple frames were acquired in succession for each SSI configuration.

Table 3-16 lists the mean DN level and the standard deviation across the frame for zero-exposure frames acquired in 1989 at the expected flight temperature of +8° C. The CCD clock voltages were normal and blemish protection was not used for these frames. Where multiple frames were available in a given configuration, they were averaged to reduce random noise. Variations in frame time and use of the extended exposure mode have only small effects on the offset level (maximum change with frame

time of 1.3 DN in gain state 4, typical changes of < 0.1 DN in other gains; maximum change with extended exposure mode of 1.1 DN in gain state 4, typical changes of < 0.2 DN in other gains). Changes with gain state and use of the summation mode are more significant.

Table 3-16. Mean DN Level and Standard Deviation for Zero-Exposure Frames Acquired in 1989 at +8° C.

Frame Rate (sec)	Gain State	Mean	Std. Dev.
60 2/3	4	10.07	1.05
	3	3.52	0.51
	2	3.05	0.22
30 1/3	4	9.57	1.05
	3	3.47	0.51
	2	3.03	0.18
8 2/3	4	8.98	0.93
	3	3.76	0.43
	2	3.00	0.04
2 1/3	4	18.78	3.33
	3	5.82	1.08
	2	3.95	0.32
	1	2.84	0.37

Figures 3-114 through 3-123 show contrast-enhanced photographs of averaged zero-exposure frames for various gain states and use of the summation mode. The full-resolution, gain state 4 frames show bright and dark columns spaced 42 pixels apart. These are due to a 2400-Hz coherent noise source and are discussed in more detail in Section III.E. A gradual left-to-right shading pattern is seen in the summation-mode frames. As the gain is decreased, the offset becomes more uniform since the variations become smaller than the DN step size. The pattern of the thermal dark current, which is very small, only becomes apparent when extended exposure frames in gain state 4 are compared to normal frames.

Switching the CCD clock voltages to the inverted level and/or using the blemish protection mode drastically affects the zero-exposure offset because in these modes the amount of thermal dark current and spurious charge generated in the CCD array are greatly increased. In these modes, the use of the extended-exposure mode has very little effect on offset. The frame time selected only makes a difference when the blemish-protection mode is used. Longer readout periods increase the amount of spurious charge generated in this case, and the offset level increases (but this effect is much smaller than that caused by the switch to blemish protection itself). Table 3-17 lists the frame-wide mean offset levels for different frame rates and gain states using the normal exposure mode with the CCD clock voltages at the inverted level and/or blemish protection being used. Note that in gain state 4 in the summation mode, use of the inverted clock voltages in the blemish-protection mode causes the offset level

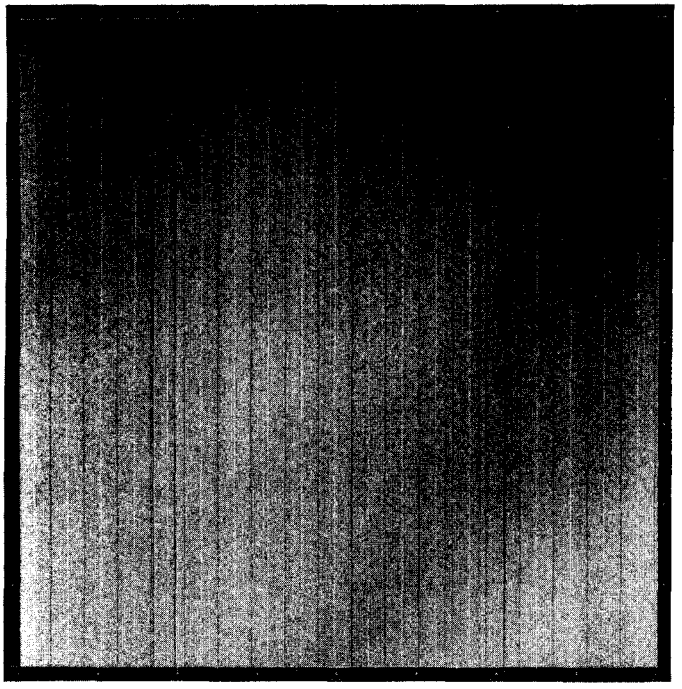

Figure 3-114. Zero-exposure frame, 60 2/3-see frame rate, gain state 4. DN range = 7 - 13

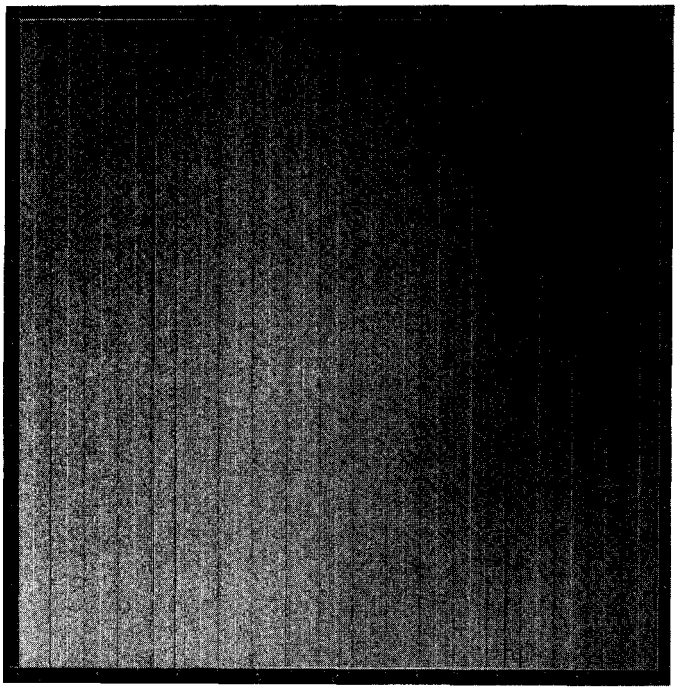

Figure 3-115. Zero-exposure frame, 8 2/3-see frame rate, gain state 4. DN range = 6 - 12

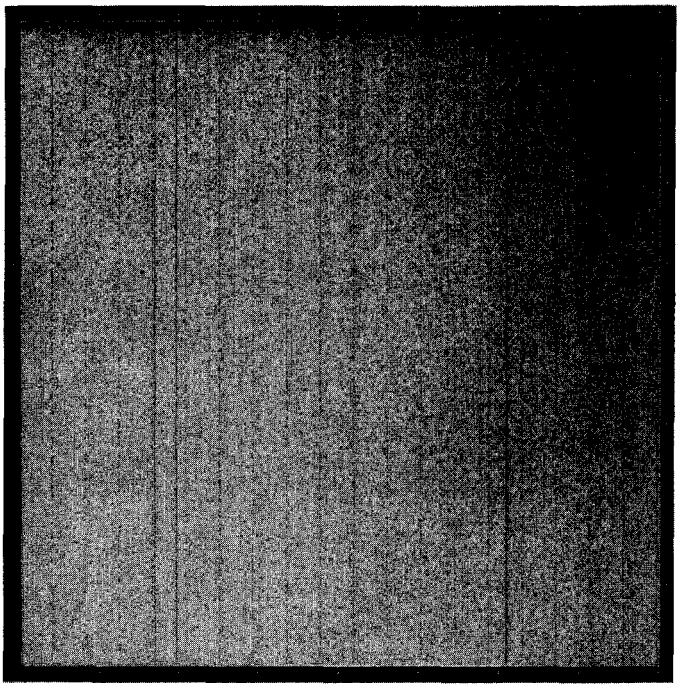

Figure 3-116. Zero-exposure frame, 8 2/3-see frame rate, gain state 3. DN range = 2 - 5

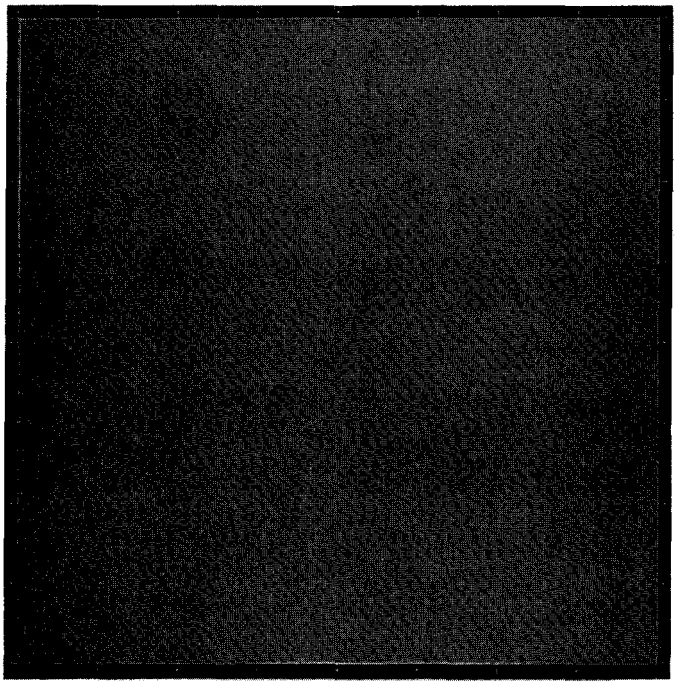

Figure 3-117. Zero-exposure frame, 8 2/3-see frame rate, gain state 2. DN range = 2 - 4

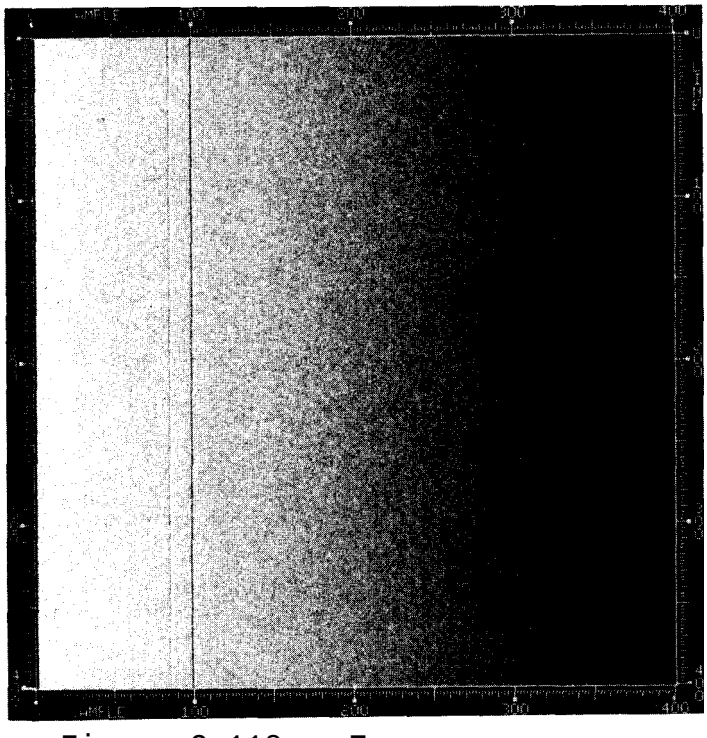

Figure 3-118. Zero-exposure frame, 2 l/3-see frame rate, gain state 4. DN range = 12 - 25

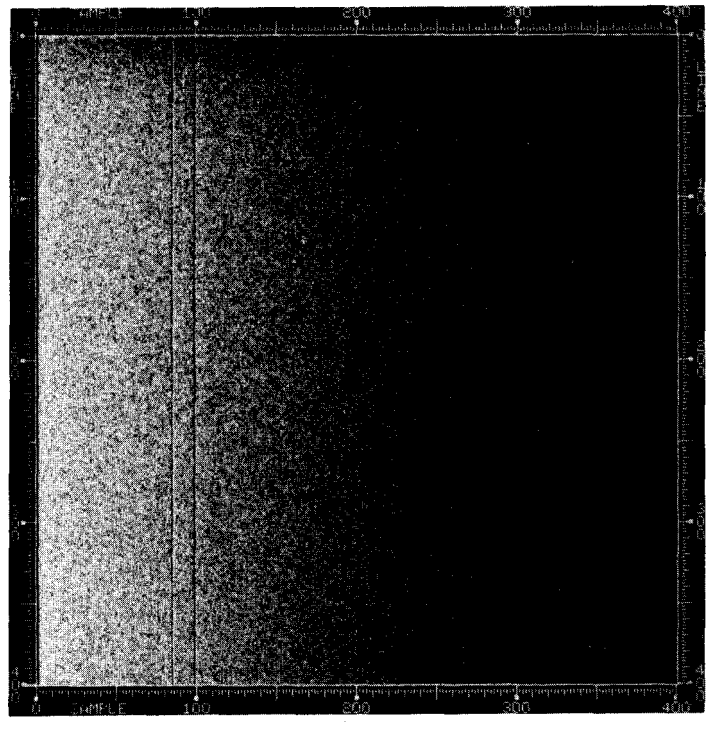

Figure 3-119. Zero-exposure frame, 2 l/3-see frame rate, gain state 3. DN range = 4 - 9

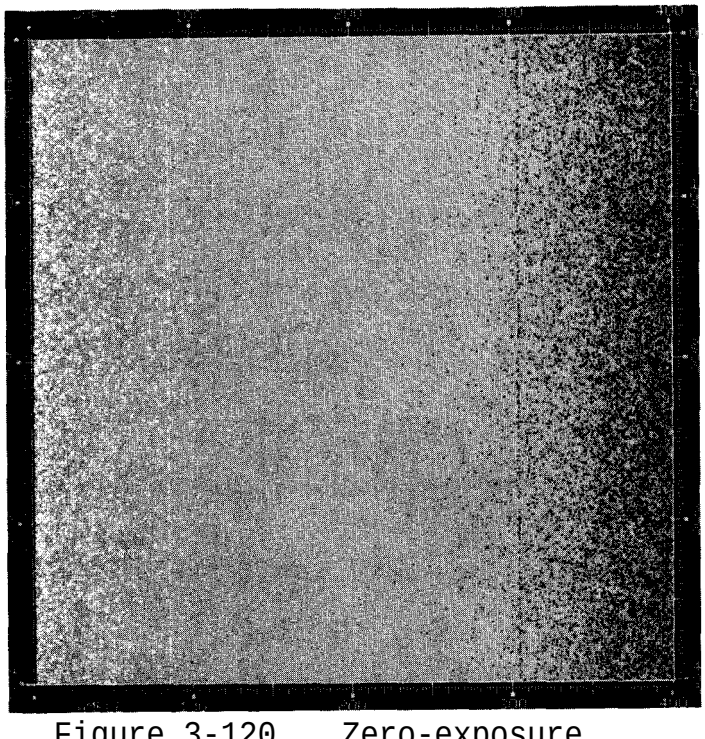

Figure 3-120. Zero-exposure frame, 2 l/3-see frame rate, gain state 2. DN range = 2 - 5

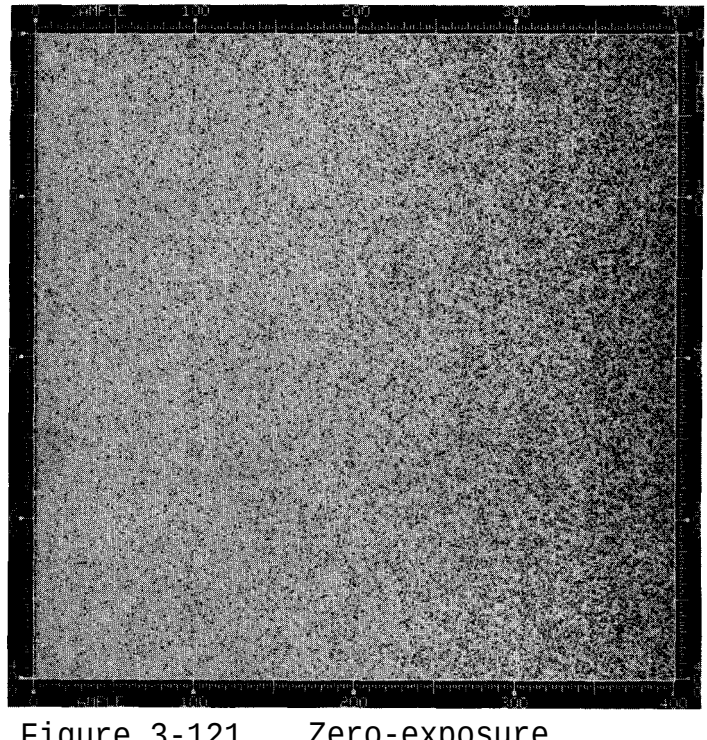

Figure 3-121. Zero-exposure frame, 2 l/3-see frame rate, gain state 1. DN range = 1 - 4

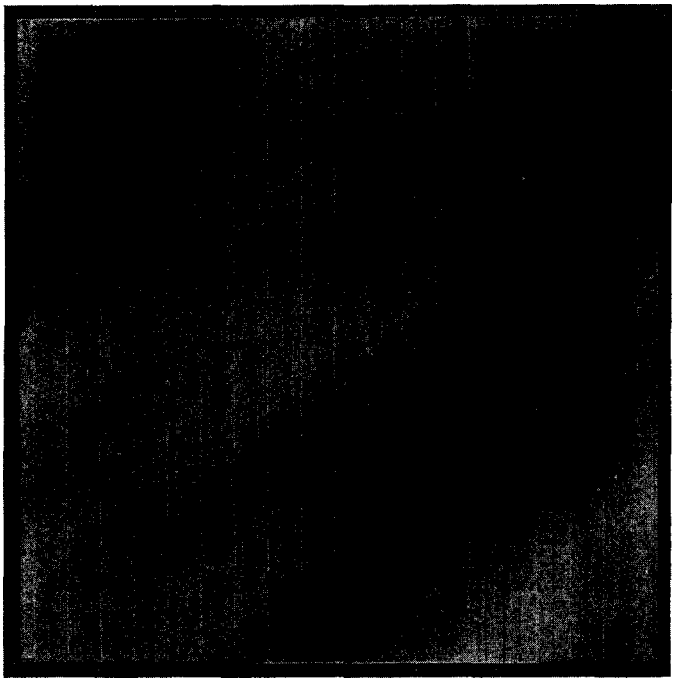

Figure 3-122. Zero-exposure frame, 60 2/3-see rate, gain 4, extended exposure DN range = 9 - 14

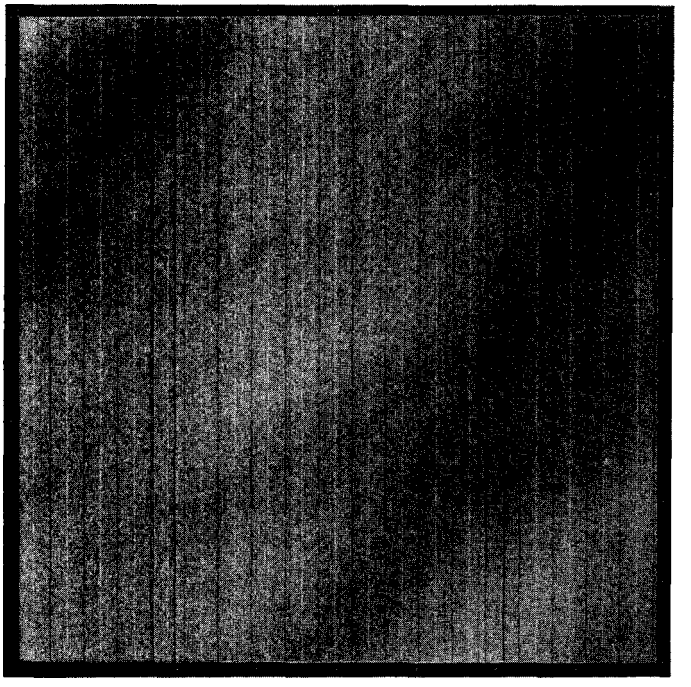

Figure 3-123. Zero-exposure frame, 8 2/3-see rate, gain 4, extended exposure DN range = 7 - 12

Table 3-17. Mean Offsets (DN) with Inverted CCD Clock Voltages (INV) and/or Use of Blemish Protection (BPM).

frame rate (see)	gain state	BPM	INV	INV + BPM
60 2/3	4	23.6	25.9	103.8
	3	6.1	6.3	22.8
	2	4.4	4.7	12.6
30 1/3	4	21.9	24.4	96.9
	3	5.8	6.3	21.6
	2	4.3	4.6	12.0
8 2/3	4	19.1	24.5	85.4
	3	5.5	6.6	19.4
	2	4.0	4.6	10.7
2 1/3	4	61.8	104.1	255.0
	3	14.7	23.6	74.3
	2	8.1	12.5	34.5
	1	5.6	4.5	9.5

to reach 255 DN. Figures 3–124 through 3-126 show contrast-enhanced offset frames in gain state 4 for the 60 2/3-see frame rate with inverted clock voltages and/or blemish protection used. Inverted clock voltages increase spurious charge production

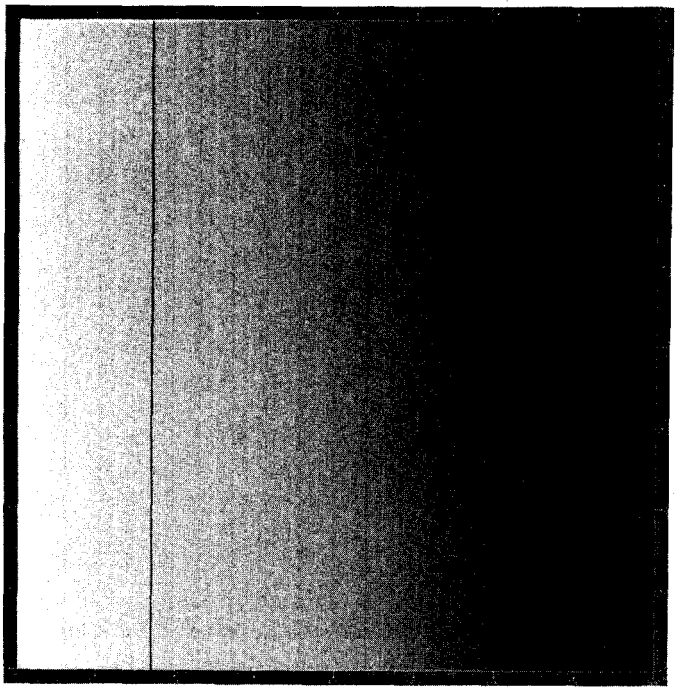

Figure 3-124. Zero-exposure frame, 60 2\3-sec rate, gain 4, inverted clocks. DN range = 19 - 31

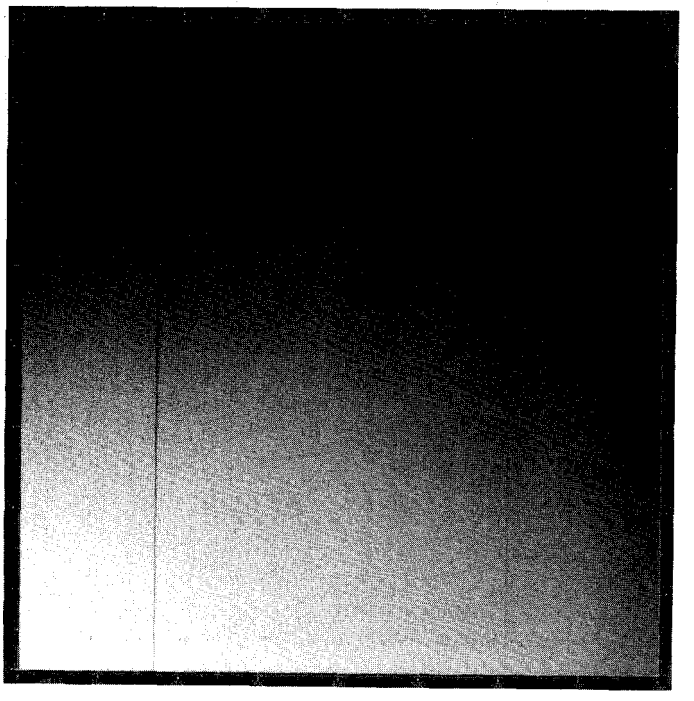

Figure 3-125. Zero-exposure frame, 60 2/3-see rate, blemish protection mode. DN range = 10 - 42

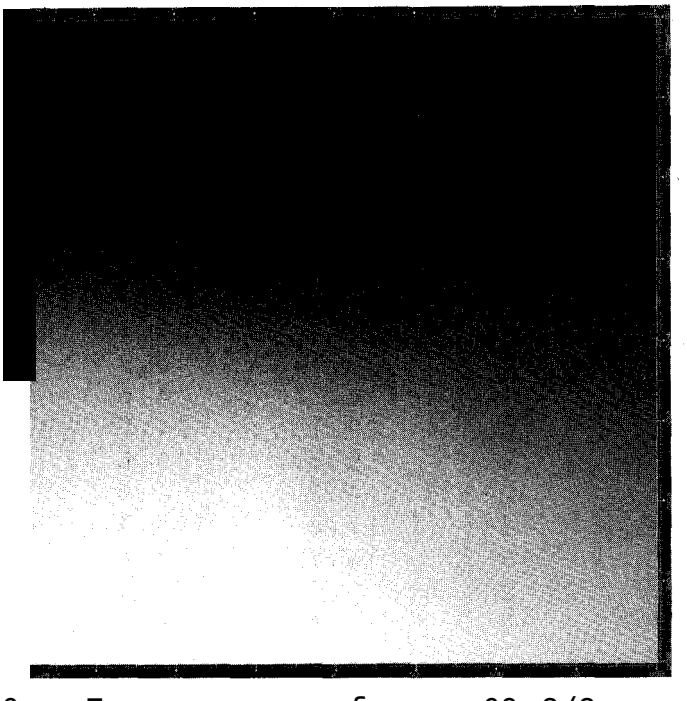

Figure 3-126. Zero-exposure frame, 60 2/3-see rate, gain 4, inverted clocks and blemish protection. DN range = 38 - 188

during CCD readout when the voltages are rapidly switched from the normally positive level to their negative level and back. This introduces a right-to-left shading pattern of spurious charge. In the blemish-protection mode, the CCD clocks are normally held negative during readout, and the charge is shifted by rapidly switching to the positive level and back during readout. While the clocks are negative, thermal dark current is collected in the CCD potential wells much more rapidly than when they are positive. Therefore, thermal dark current buildup is much greater when blemish protection is used, and this introduces an upper-right-to-lower-left shading pattern of dark current charge. In addition, isolated pixels that generate higher-than-average dark current become visible as "dark spikes" in this mode.

Use of the data compressor has no apparent effect on the offset.

Changes in instrument temperature do cause changes in the offset level. Changes over time have also been observed. Figures 3-127 and 3-128 show the offset level in each gain state versus temperature determined four different ways: (a) mean DN over a 50 x 50 pixel area, (b) offset from linear fit to light transfer data for the same 50 x 50 pixel area, (c) mean offset from linear fit to light transfer data for 256 20 x 20 pixel areas spread across the CCD array, and (d) mean offset from GALGEN linear fit to light transfer data. The offset is stable to within about 0.1 DN over periods of up to a few days. The offset level increases with temperature at a rate of roughly 0.01 to 0.02 DN/°C.

The plots in Figures 3-127 and 3-128 compared to the data in Table 3-16 show that the offsets computed from linear fits to the light transfer data are generally lower than the raw zero-exposure DN level by a few tenths of a DN for the data acquired in the 8 2/3-see mode (this is not the case in the summation mode) . This effect can be seen also in the plots of residual errors in the linear fits shown in Figures 3-9 through 3-20. The raw offset data could be in error by between 0.5 and 1 DN due to digitization errors in the SSI analog-to-digital converter (see Section III.E below). However, it is surprising that the mismatch with the linear-fit offsets in all 8 2/3-see cases examined (1989, 1985 and 1984; 3 gain states; 3 temperatures) would have the same sign. It is possible that the SSI response is slightly nonlinear at low signal levels, although the level of error in DN would be expected to decrease as the gain decreases if this were the case, and a previous low-light-level linearity test has shown no evidence of this (in fact, the offset residual in this case has the opposite sign). Nor does low-level nonlinearity explain why the summation-mode offsets derived from the linear fits agree well with the raw zero-exposure offsets. It has been decided that, until this difference is better understood, SSI flight data will be calibrated using the GALGEN linear-fit offsets rather than using averages of zero-exposure frames, at least for those SSI configurations in which light transfer data sets were acquired.

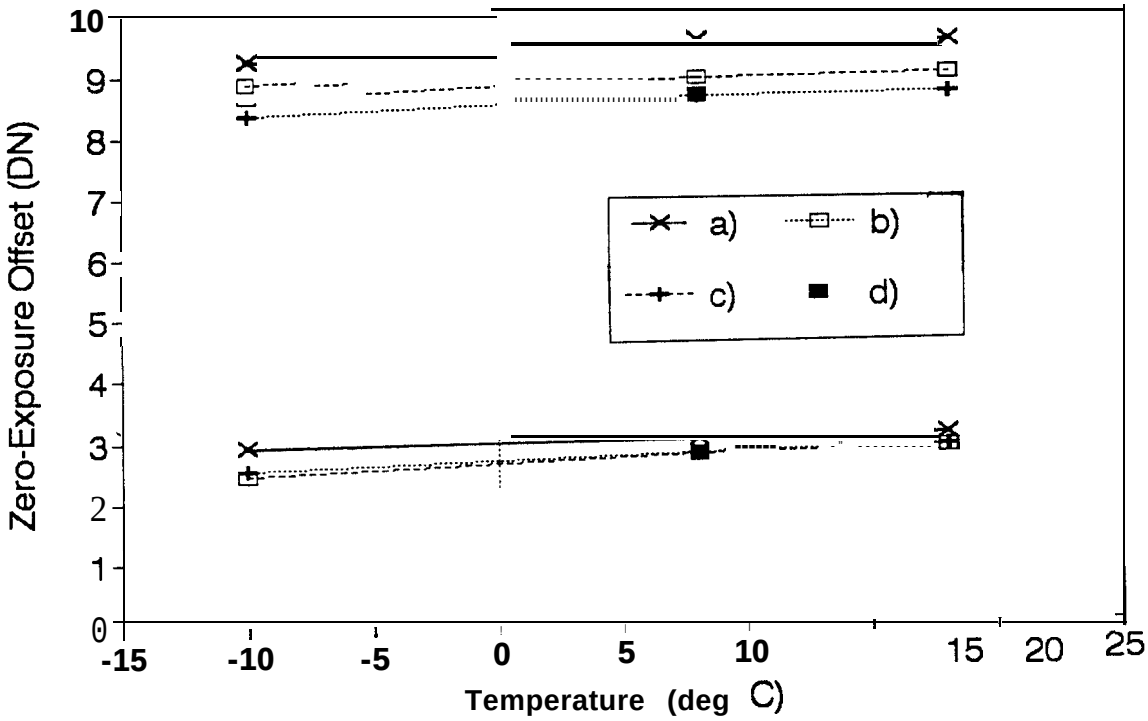

Figure 3-127. SSI offset vs. temperature in gain states 2 and 4 (see text on pg. 67 for symbol definitions)

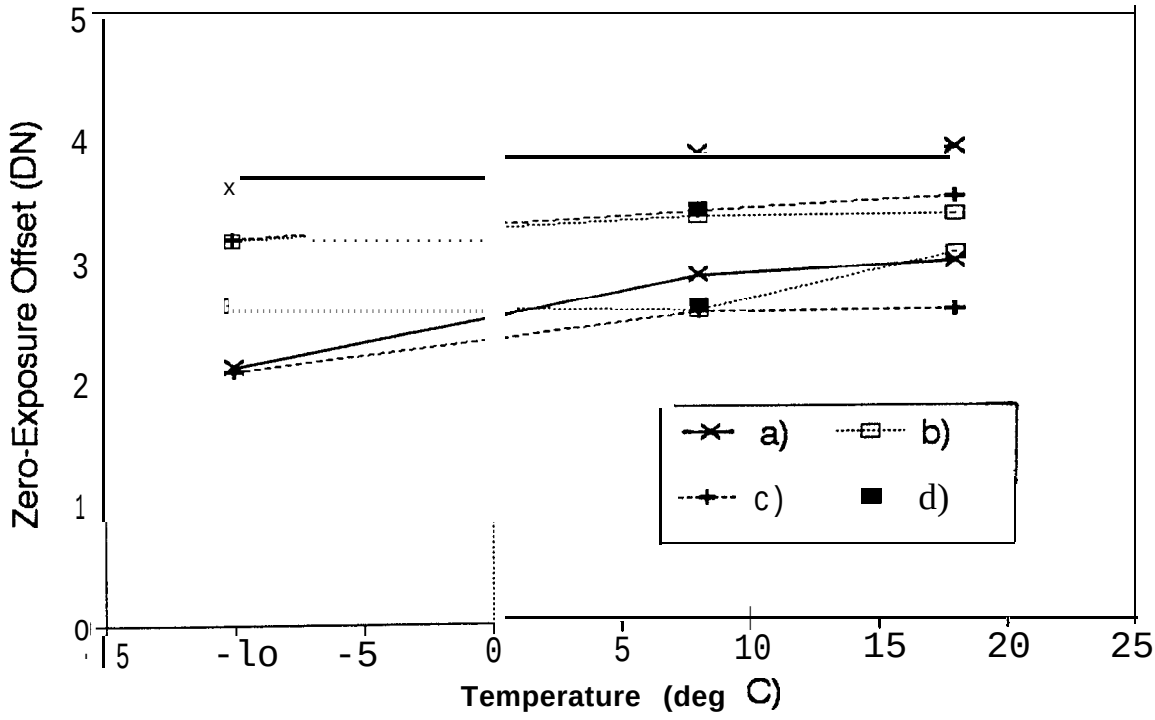

Figure 3-128. SSI offset vs. temperature in gain states 1 (summation mode) and 3 (see text on pg. 67 for symbol definitions)

Comparison of the GALGEN offset files shown in Figures 3-39 through 3-45 to the corresponding zero-exposure frames in Figures 3-115 through 3-121 shows that they match well in their spatial distributions.

E. Noise Characteristics

To study the SSI noise characteristics, the following analyses were performed:

a) Calculation of the system gain constant and noise floor using six light transfer sequences in gain state 4 taken at SSI temperatures of -10°C, +8°C, and +18°C.
b) Random vs. coherent noise statistics were analyzed for uncalibrated frames using 8 2/3-see dark frames at each gain setting in the full-resolution mode (3 cases) at all three temperatures. The same analysis was performed at +8°C on summation-mode dark frames at each gain setting (4 cases) and on compressed dark frames in gain state 2 with the compressor in both the information-preserving and rate-controlled modes.
c) Random vs. coherent noise statistics were determined for radiometrically calibrated dark and flat field frames in each gain state, full-resolution and summation modes, with the data compressor off and on in both rate-controlled and information-preserving modes.
d) Irregularities in the performance of the analog-to-digital converter (ADC) were characterized using selected exposed and dark frames in all gain states in both full-resolution and summation modes.

Calculations of the system noise floor in gain state 4 were provided by algorithms used in the determination of the SSI system gain constant (Section III.B.2). The noise floor was computed over a grid of 100 20x20 pixel areas identical for each light transfer sequence. Areas yielding anomalous results were deleted. Results are given in Table 3-18 where the mean and standard deviation of the noise values over all 20X20 areas are

Table 3-18. 1989 noise floor statistics in gain state 4

Temp °C	Filter	Resolution	Number of Areas	Noise Floor Mean (DN)	Noise Floor Standard Deviation
-10	5600A	Sum Mode	96	1.544	0.146
	Clear	Full Frame	92	0.817	0.051
+8	5600A	Sum Mode	96	1.565	0.134
	Clear	Full Frame	94	0.825	0.045
+18	5600A	Sum Mode	97	1.592	**0.168**
	Clear	Full Frame	93	0.903	0.03

listed. The noise floor increases slightly as temperature increases. Use of the summation mode also raises the noise floor.

Separation of random from coherent (periodic) noise in SSI images employed Fourier analysis techniques, as described in Reference 1. Figures 3-129 through 3-142 show the image data from the noise analysis of raw +8°C dark frame images. Included for each are four sub-images representing the filtered image (a), the two-dimensional Fast-Fourier Transform (b), the coherent noise component (c), and the random noise component (d). Also included are three histograms of the filtered, coherent and random images respectively, and a corresponding one-dimensional power spectrum plot for the coherent noise in the horizontal direction. Table 3-19 lists the statistical information obtained for all raw, filtered, random, and coherent noise images. Referring to the Table, the following trends are apparent:

1. Both random and coherent noise levels increase with increasing gain.
2. In all cases, the standard deviation of the coherent images is significantly lower than that of the random images.
3. The data compressor has no significant effect on noise.

The gain state 4 random noise levels are close to those given in Table 3-18; however, in this case the measured noise level decreases slightly as temperature increases. The random and coherent noise levels remain about the same as in 1985.

Table 3-19. Noise statistics for uncalibrated zero-exposure frames (units are DN)

Temp °C	Gain Mode	Raw mean	Raw dev.	Filtered mean	Filtered dev.	Random mean	Random dev.	Coherent mean	Coherent dev.
-10	10K Full	8.80	1.08	127.49	1.02	127.49	0.98	128.00	0.27
	40K	3.50	0.50	127.50	0.49	127.48	0.49	128.01	0.06
	100K	2.91	0.30	127.51	0.29	127.51	0.29	128.00	0.04
+8	10K	9.09	1.07	127.49	1.00	127.50	0.95	128.00	0.31
	40K	3.74	0.44	127.49	0.43	127.49	0.42	128.00	0.08
	100K	3.01	0.12	127.31	0.12	127.31	0.12	128.00	0.00
+18	10K	9.13	1.02	127.50	0.95	127.50	0.91	128.00	0.27
	40K	3.78	0.42	127.52	0.41	127.53	0.40	128.00	0.07
	100K	3.05	0.22	127.53	0.22	127.50	0.22	128.04	0.02
+8	10K Sum	18.92	2.69	127.50	1.74	127.50	1.68	128.00	0.43
	4 0K	5.72	1.09	127.50	0.85	127.53	0.83	127.97	0.18
	100K	3.98	0.26	127.50	0.25	127.46	0.24	128.04	0.04
	400K	2.79	0.41	127.53	0.40	127.53	0.40	128.00	0.00
	100KFu11,IP	3.01	0.12	127.34	0.12	127.34	0.12	128.00	0.01
	100KFuI1,RC	3.01	0.13	127.36	0.13	127.35	0.13	128.00	0.01

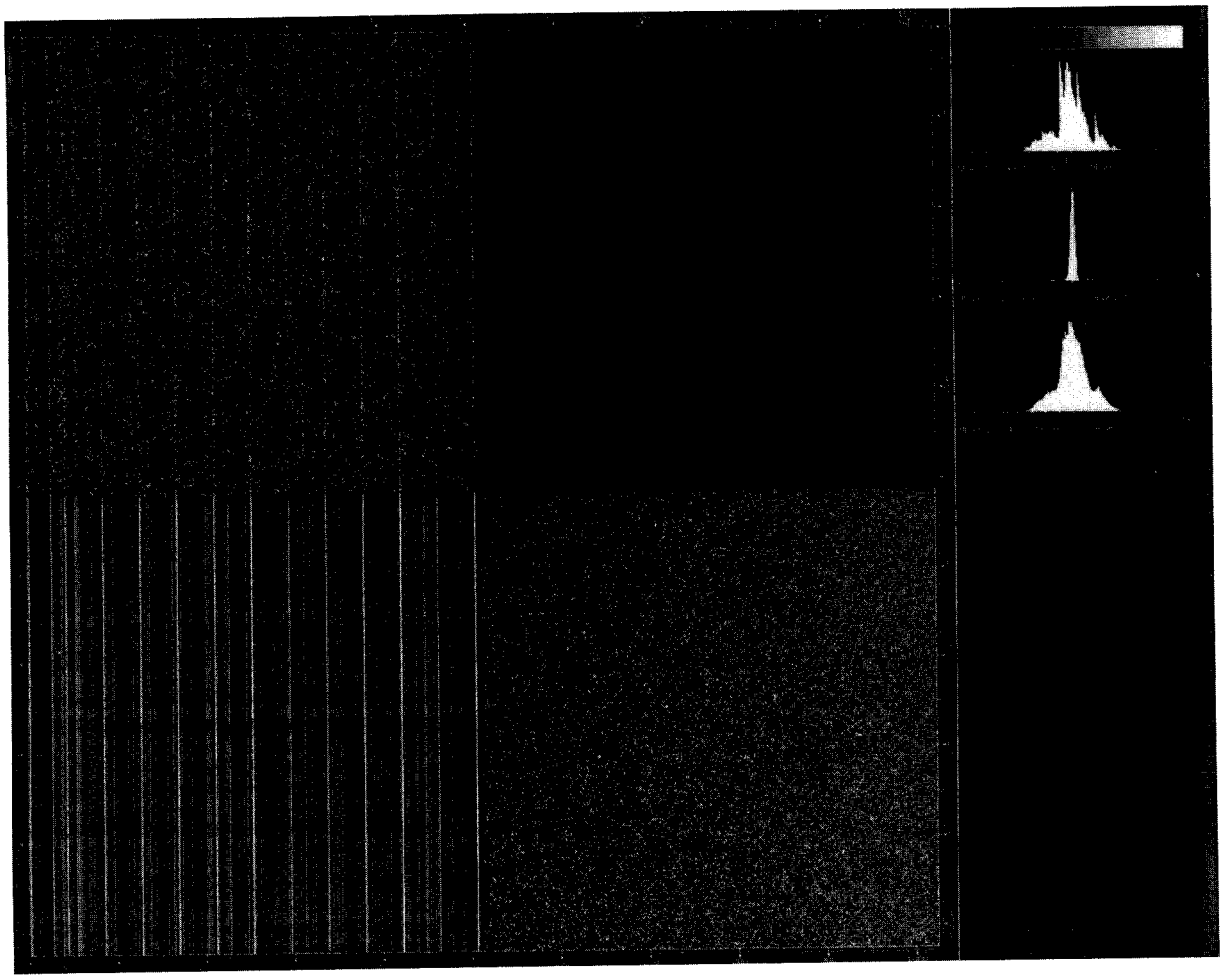

Figure 3-129. Noise analysis data for an uncalibrated dark frame image at 8°C in gain state 4, normal mode.

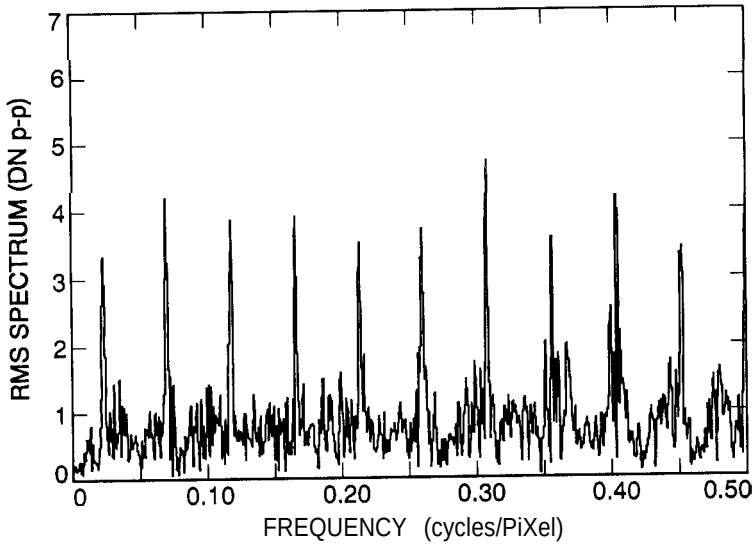

Figure 3-130. One-dimensional power spectrum plot for, the horizontal coherent noise component of the image in Figure 3-129.

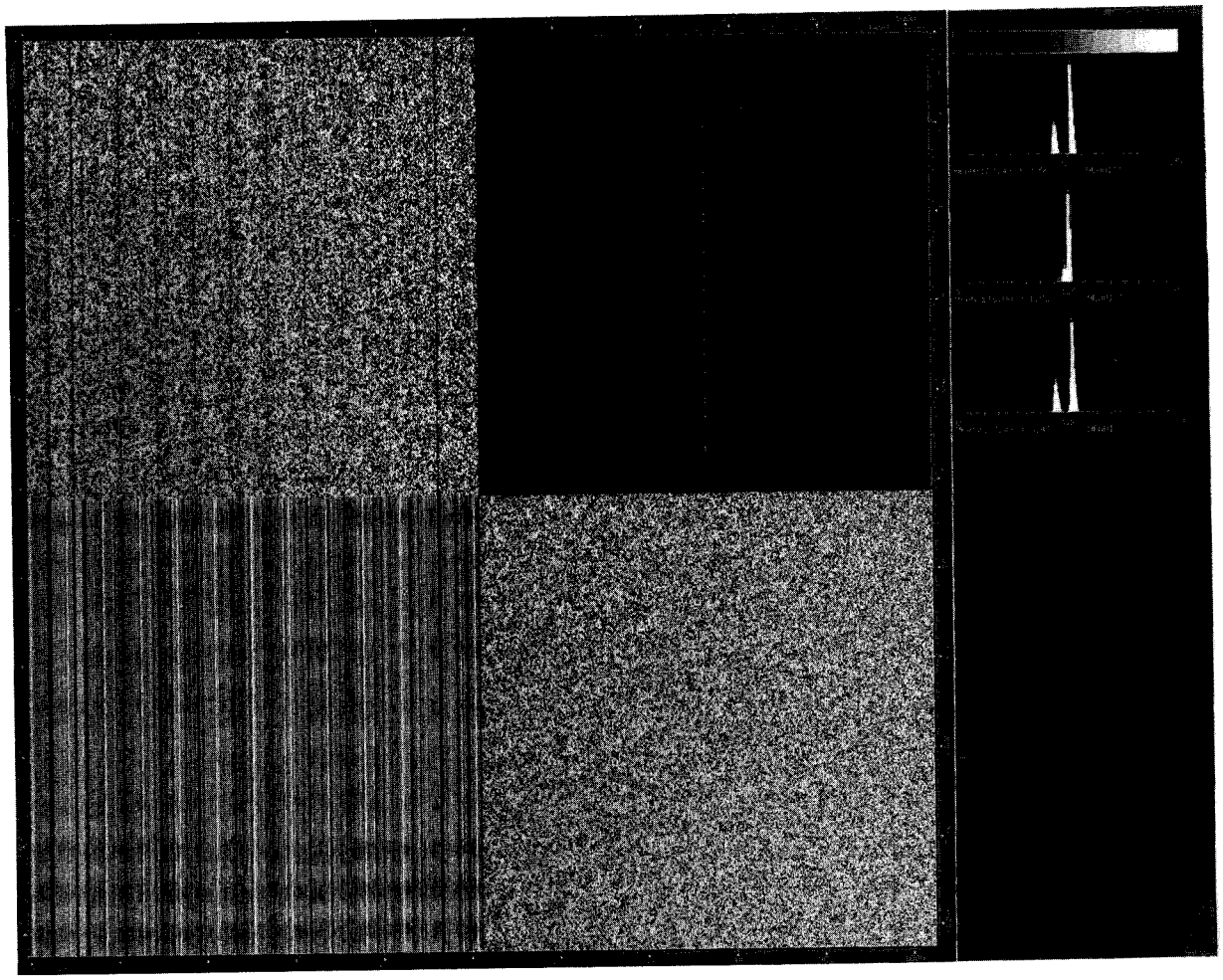

Figur

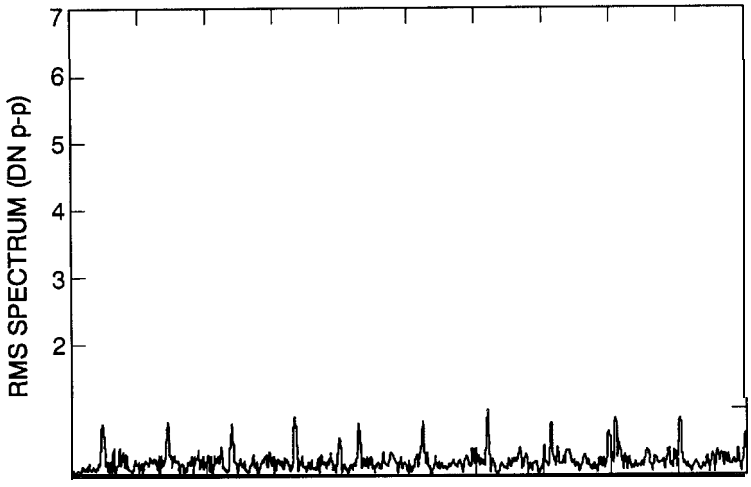

Figure 3-132. One-dimensional power spectrum plot for the horizontal coherent noise component of the image in Figure 3-131.

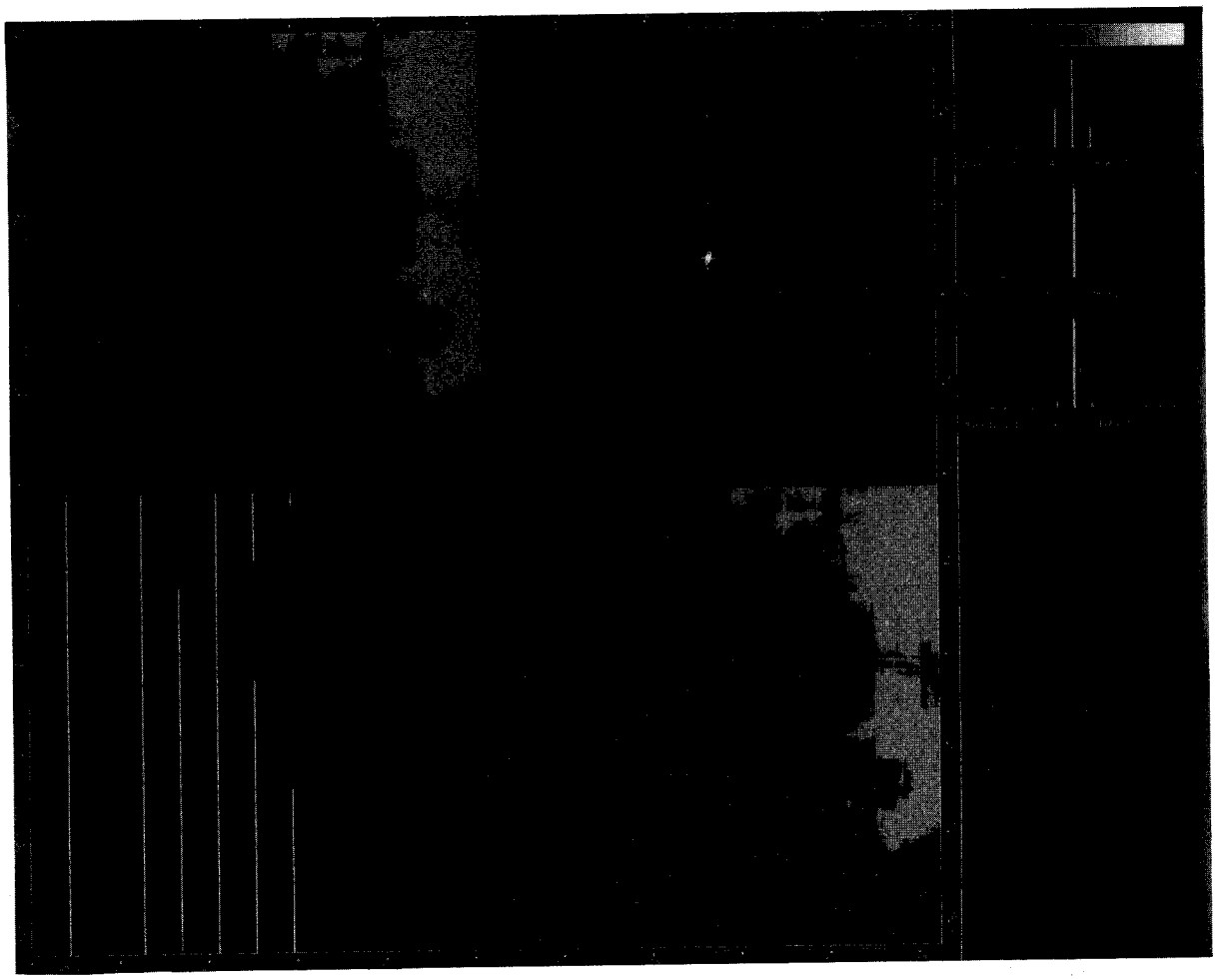

Figure 3-133. Noise analysis data for an uncalibrated dark frame image at 8°C in gain state 2, normal mode.

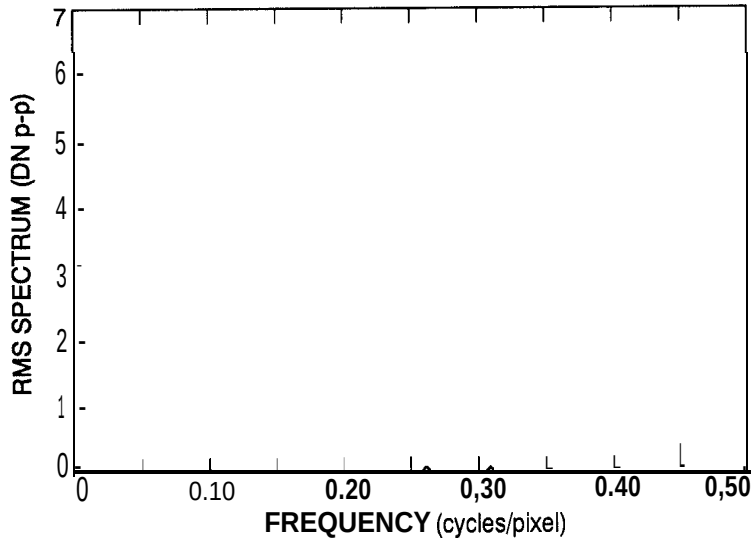

Figure 3-134. One-dimensional power spectrum plot for. the horizontal coherent noise component of the image in Figure 3-133.

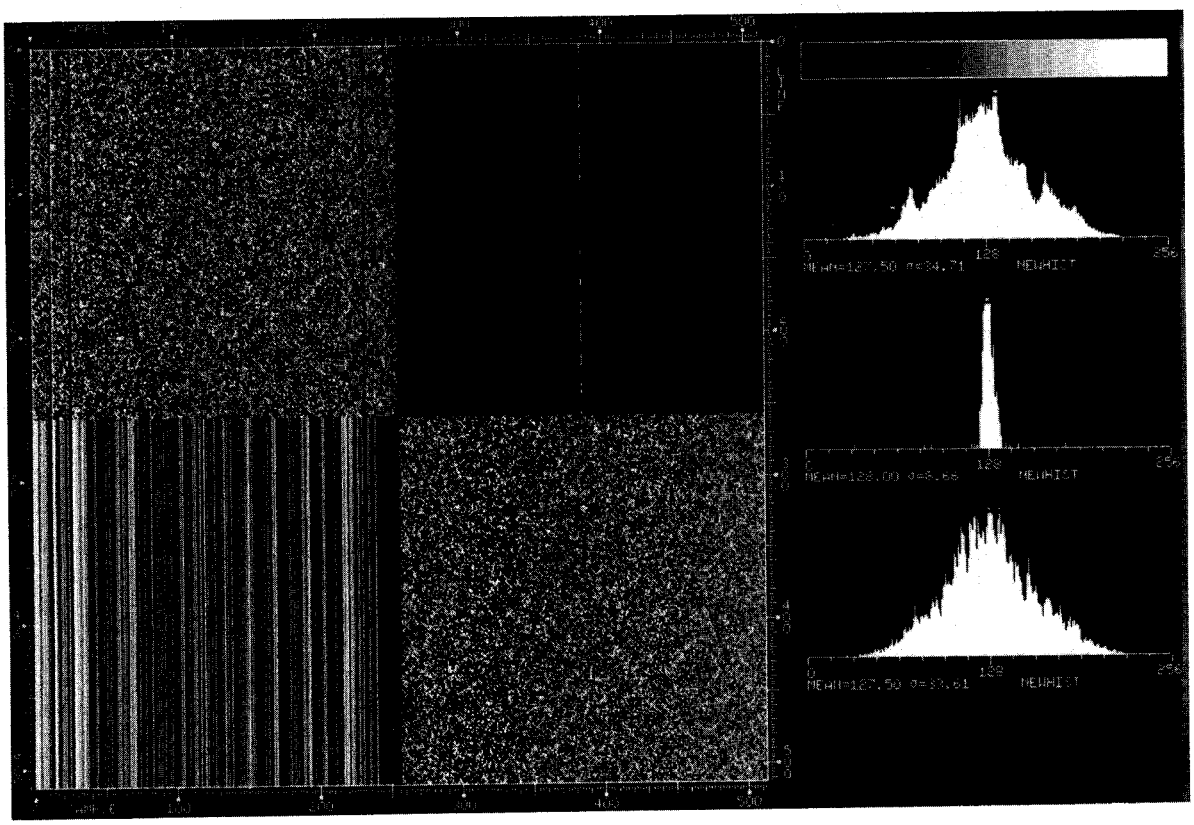

Figure 3-135. Noise analysis data for an uncalibrated dark frame image at 8°C in gain state 4, summation mode.

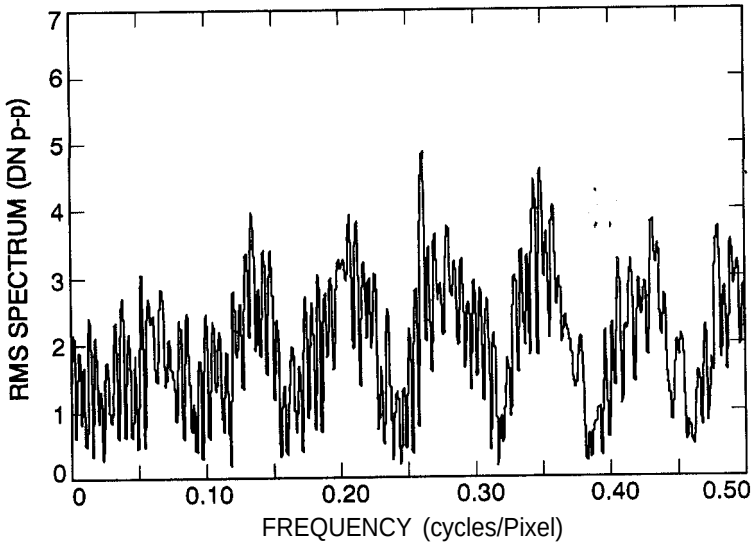

Figure 3-136. One-dimensional power spectrum plot for the horizontal coherent noise component of the image in Figure 3-135.

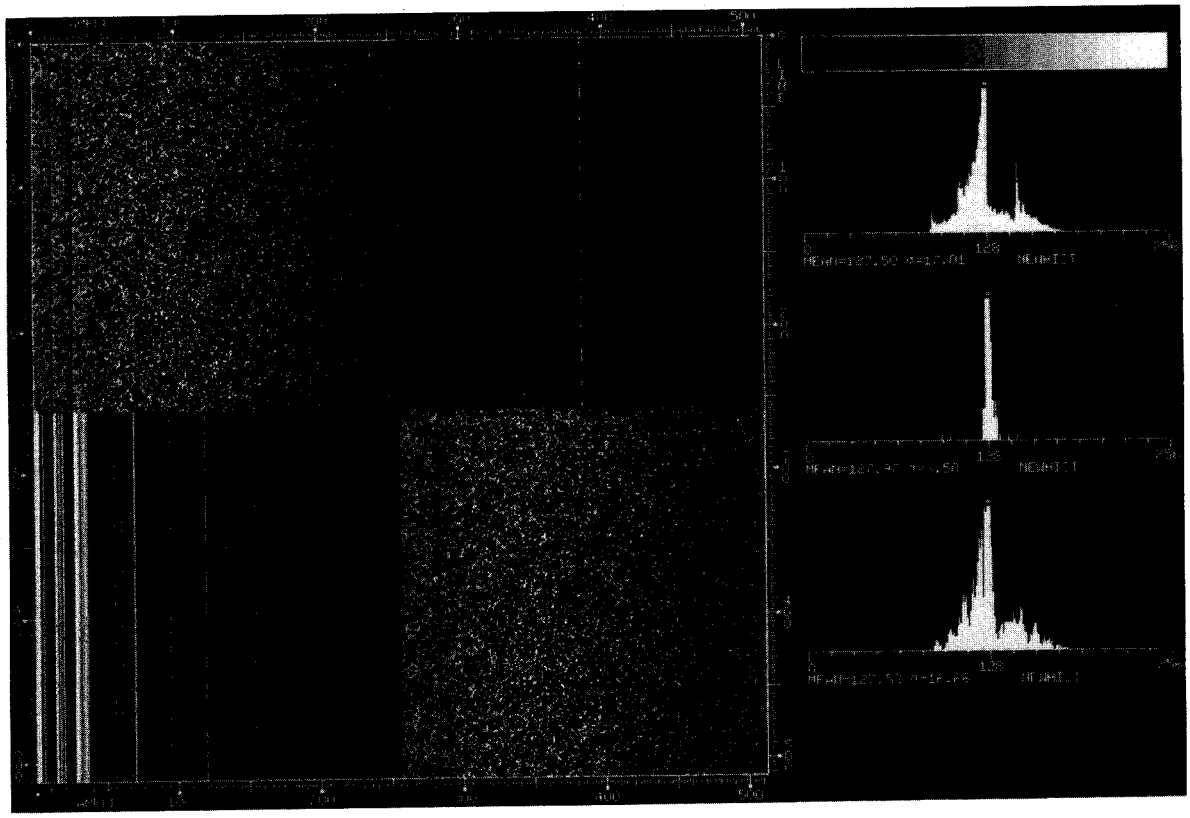

Figure 3-137. Noise analysis data for an uncalibrated dark frame image at 8°C in gain state 3, summation mode.

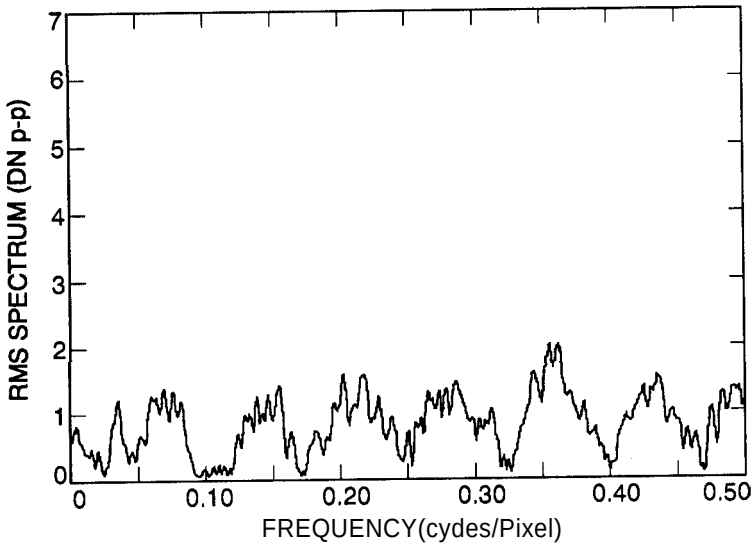

Figure 3-138. One-dimensional power spectrum plot for, the horizontal coherent noise component of the image in Figure 3-137.

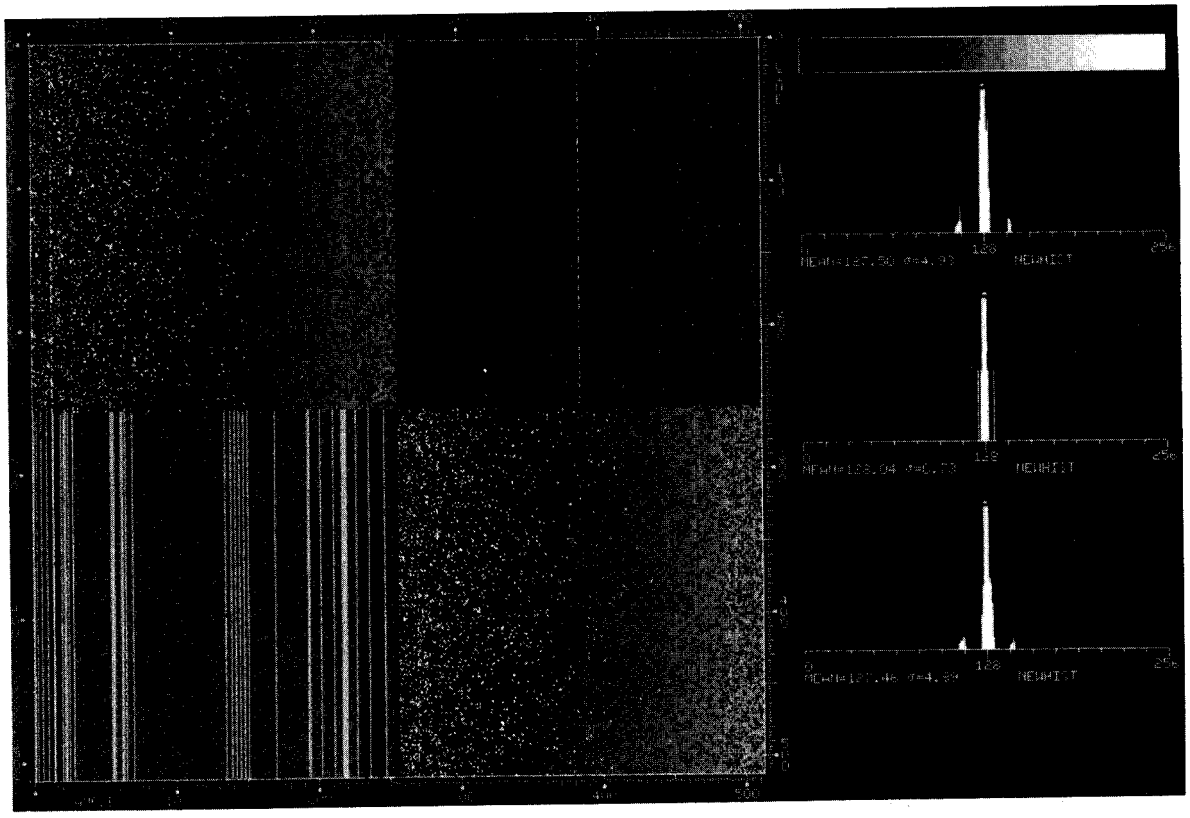

Figure 3-139. Noise analysis data for an uncalibrated dark frame image at 8°C in gain state 2, summation mode.

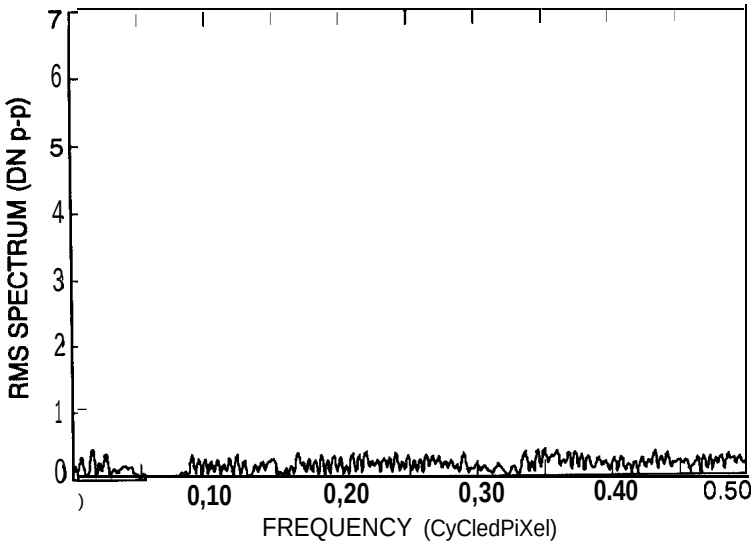

Figure 3-140. One-Dimensional power spectrum plot for, the horizontal coherent noise component of the image in Figure 3-139.

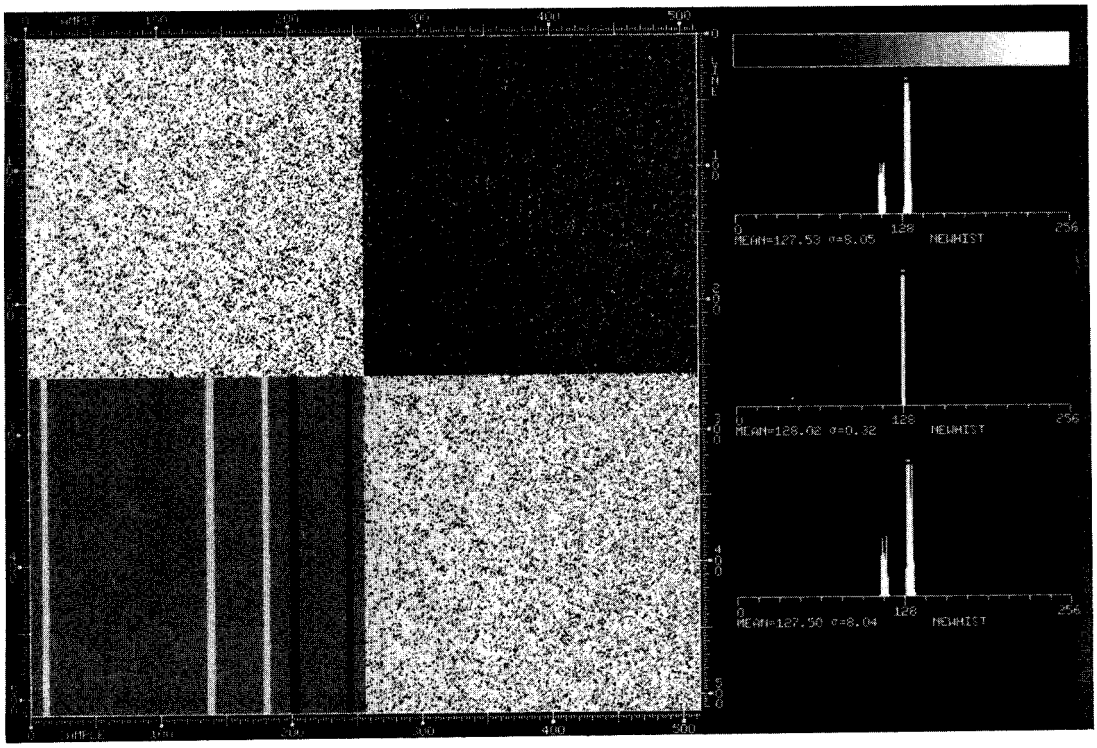

Figure 3-141. Noise analysis data for an uncalibrated dark frame image at 8°C in gain state 1, summation mode.

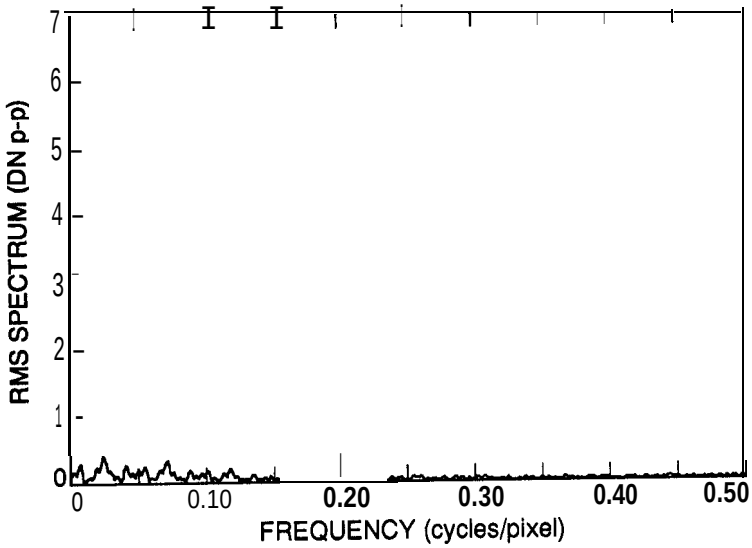

Figure 3-142. One-dimensional power spectrum plot for the horizontal coherent noise component of the image in Figure 3-141.

As was the case in the 1985 data, a prominent coherent signal due to the 2400-Hz power supply is visible as a series of vertical stripes with 42-pixel spacing. This noise component is also visible as the leftmost spike in the horizontal power spectrum plot of the coherent noise image (e.g. , Figure 3-130) with a spatial frequency of 0.0238 cycles/pixel. Harmonics derived from this noise component appear as prominent spikes at spatial frequencies that are integer multiples of the primary frequency, with the odd multiples appearing much more prominently than the even. This effect was consistent through all frames used in the noise analysis study.

A vertical power spectrum plot sometimes reveals the presence of low-amplitude horizontal coherent noise components in the full-resolution images, particularly in the higher gain states. The frequencies of these components were below 8 Hz, and their sources have not been identified.

To evaluate the SSI noise characteristics without the effects of blemishes and CCD spatial sensitivity variations and to study how noise varies with signal level, selected flat-field images were radiometrically calibrated and then analyzed for random and coherent noise levels as described above. Table 3-20 lists the noise statistics for the exposed frames analyzed. In all cases, the amplitude of the coherent noise is only a small fraction of a DN. Figures 3-143 through 3-152 show the noise analysis images for selected frames and corresponding power spectra for the coherent noise components. All full-resolution dark frames show residual uncalibrated 2400-Hz noise as do exposed frames in gain state 4. Well-exposed frames in the lower gain states do not exhibit any residual 2400-Hz noise, although there does remain low-level vertical coherent noise at random spatial frequencies in such frames (e.g., Figure 3-148). The residual coherent noise in the summation mode frames is generally vertical at random spatial frequencies for dark frames and exposed frames in gain states 3 and 4. Exposed summation-mode frames in the lower gain states do not exhibit any vertical coherent noise but do show a pattern of low-level horizontal coherent noise at a frequency matching 60 Hz (Figure 3-150) .

When the noise statistics for exposed frames are analyzed, it appears that the random noise level remaining in flat-field images after calibration is nearly equivalent to the theoretical minimum level expected from a CCD read noise of 31 e- in the full-resolution mode or 44 e- in the summation mode, a quantization error of about 0.36 DN (or 0.64 DN for summation mode in gain states 3 and 4), and the signal shot noise due to photon statistics. There does exist an additional residual uncalibrated noise component that increases linearly with signal level in the proportions shown in Table 3-21. The residual calibration noise in the summation mode in gain states other than 4 was too small to be measured reliably.

Table 3-20. Noise statistics of selected calibrated frames

gain	mode	mean signal (DN)	coherent noise std dev (DN)	random noise std dev (DN)
4	NORM	60	0.16	1.46
4	NORM	110	0.18	1.92
4	NORM	144	0.21	2.16
4	NORM	173	0.28	2.22
4	NORM	213	0.27	2.69
3	NORM	93	0.04	0.87
3	NORM	177	0.09	1.14
3	NORM	225	0.29	1.37
2	NORM	206	0.08	1.08
2	NORM	242	0.08	1.06
4	SUM	71	0.29	2.25
4	SUM	121	0.30	3.14
4	SUM	155	0.26	3.21
4	SUM	222	0.24	3.39
3	SUM	175	0.08	0.93
2	SUM	170	0.03	0.77
1	SUM	185	0.02	0.49

Table 3-21. Noise component due to imperfect calibration as a percentage of mean signal.

gain	summation	residual (%)
10K	none	0.38
4 0K	none	0.27
lOOK	none	0.27
10K	2 x 2	1.00
4 0K	2 x 2	--
100K	2 x 2	--
400K	2 x 2	--

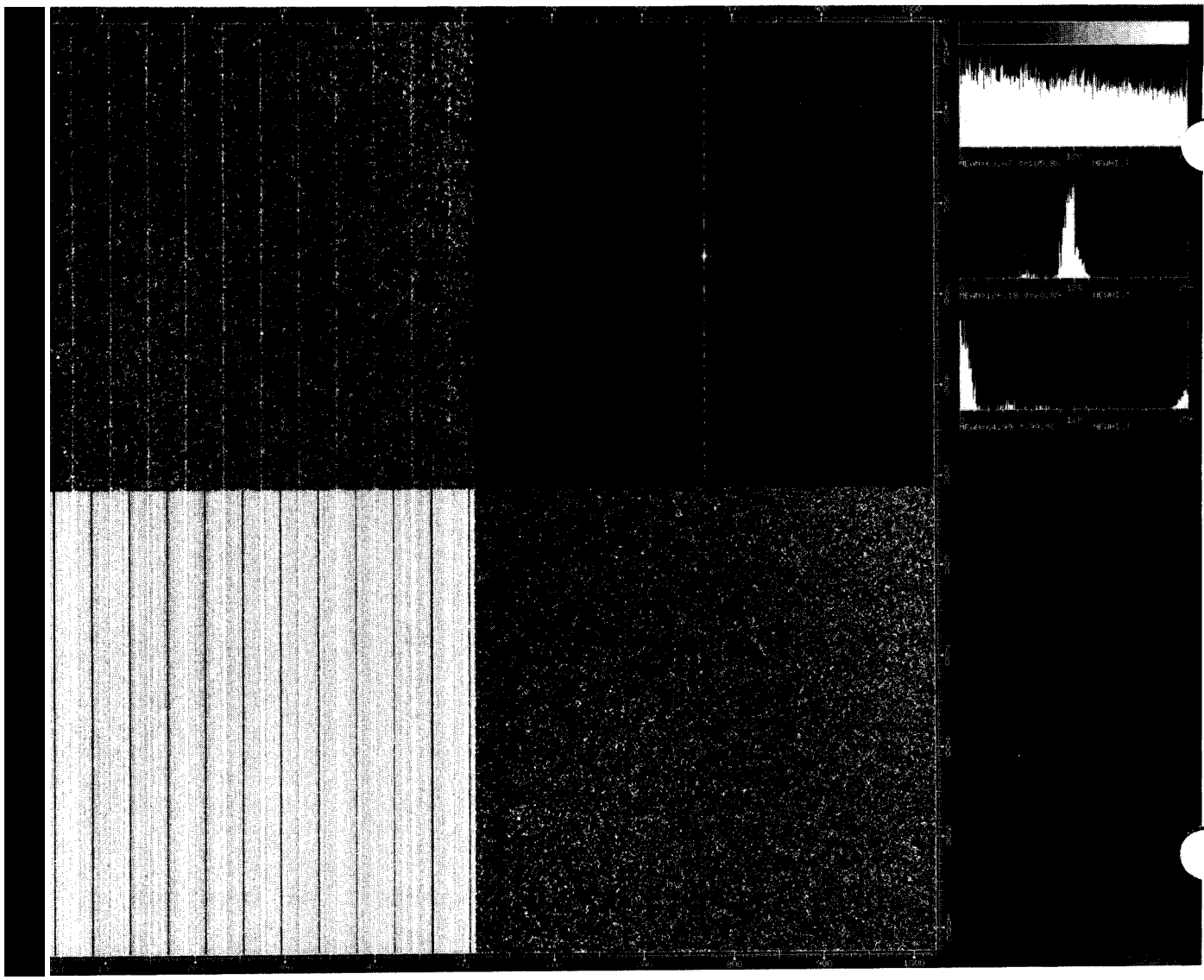

Figure 3-143. Noise analysis data for a radiometrically calibrated dark frame image, 8°C, gain state 4, normal mode.

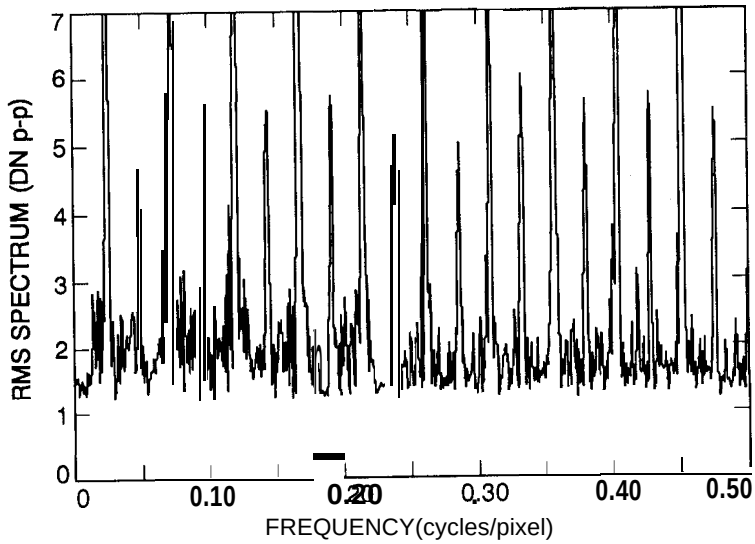

Figure 3-144. One-dimensional power spectrum of the horizontal coherent noise component of the image in Figure 3-143.

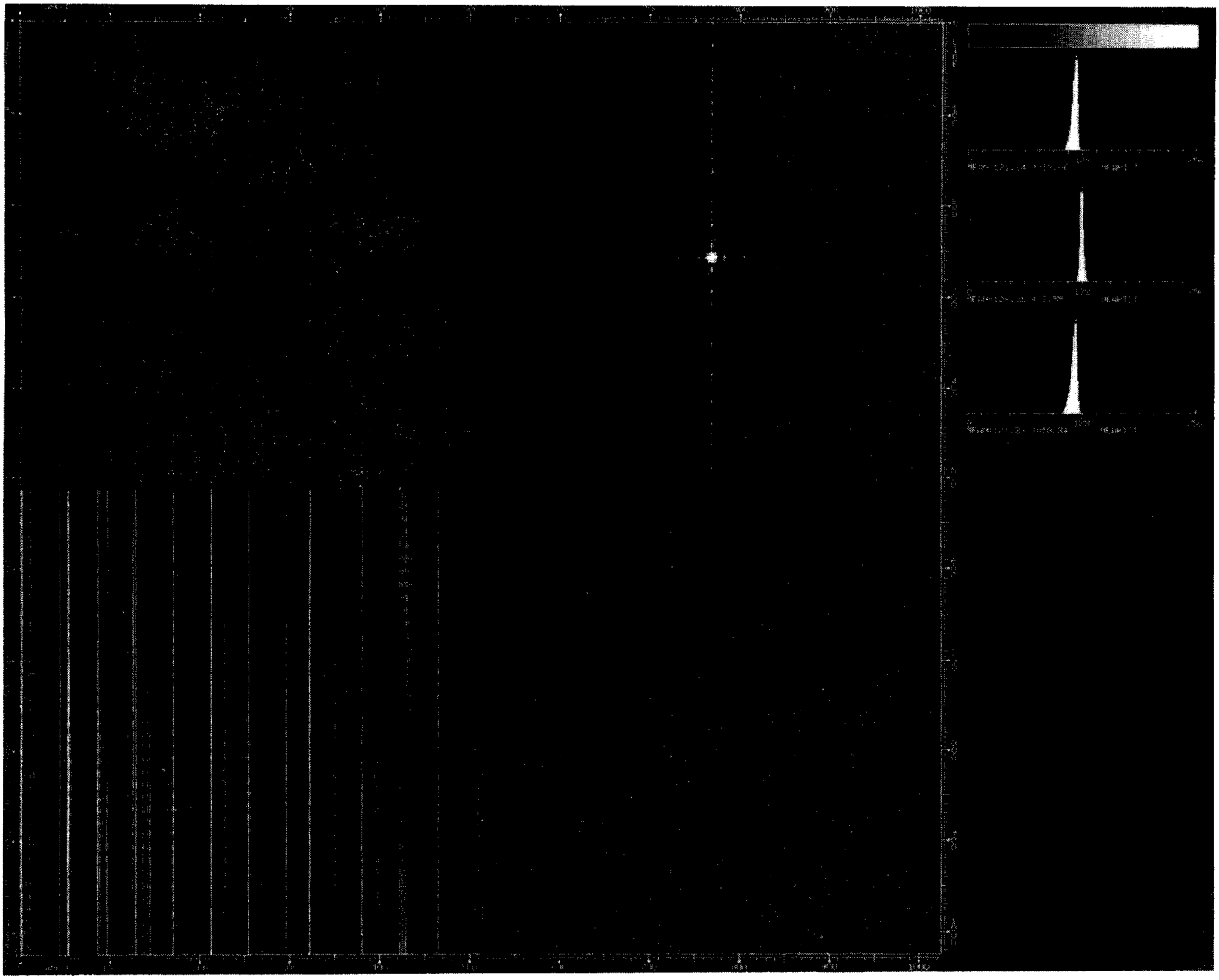

Figure 3-145. Noise analysis data for a radiometrically calibrated dark frame image, 8°C, gain state 2, normal mode.

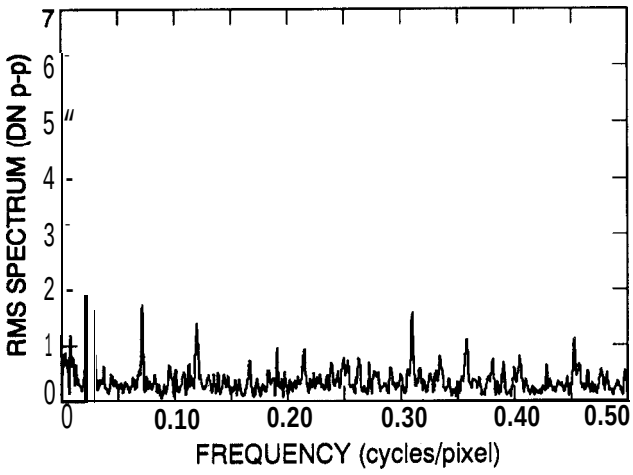

Figure 3-146.
One-dimensional power spectrum of the horizontal coherent noise component of Figure 3-145.

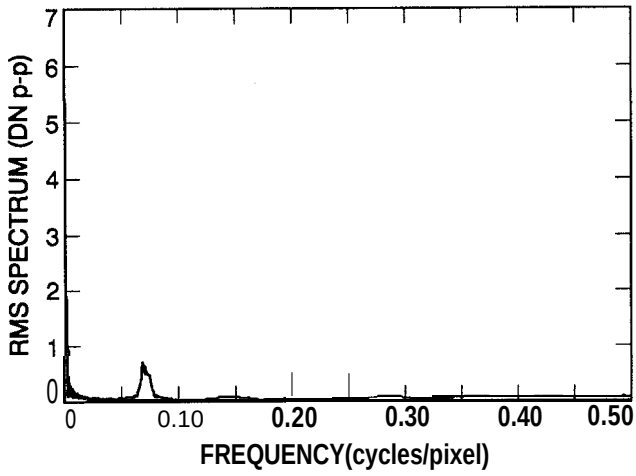

Figure 3-147.
One-dimensional power spectrum of the vertical coherent noise component of Figure 3-145.

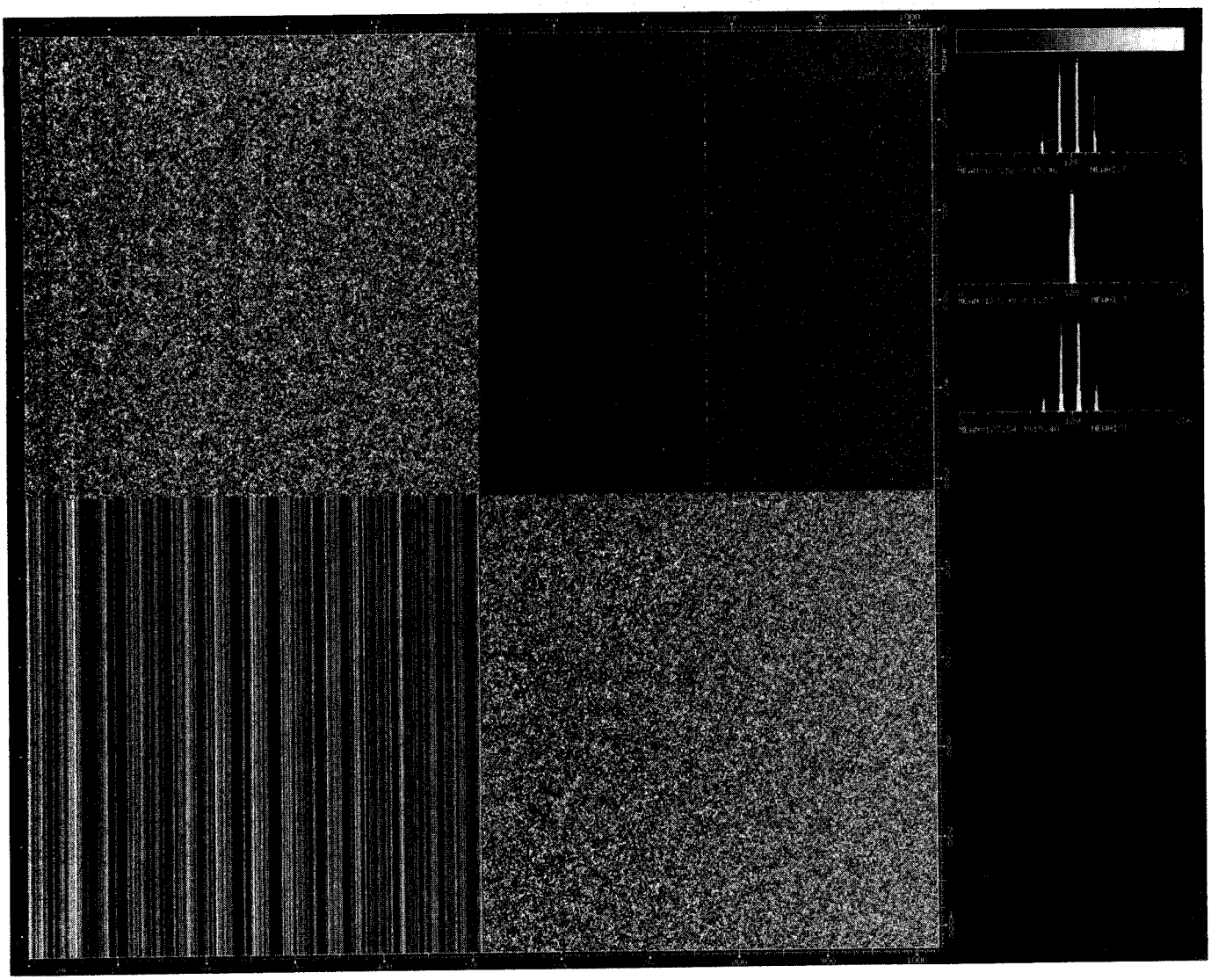

Figure 3-148. Noise analysis data for a radiometrically calibrated exposed frame, 8°C, gain state 2, normal mode.

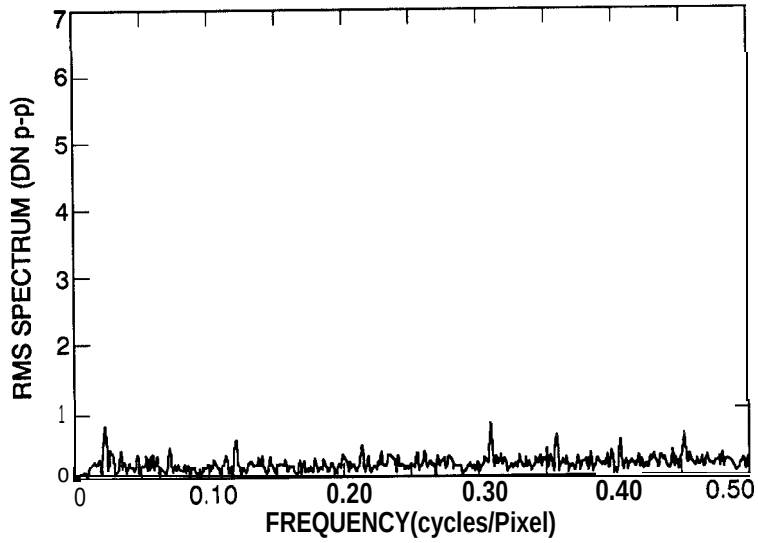

Figure 3-149. One-dimensional power spectrum of the horizontal coherent noise component of the image in Figure 3-148.

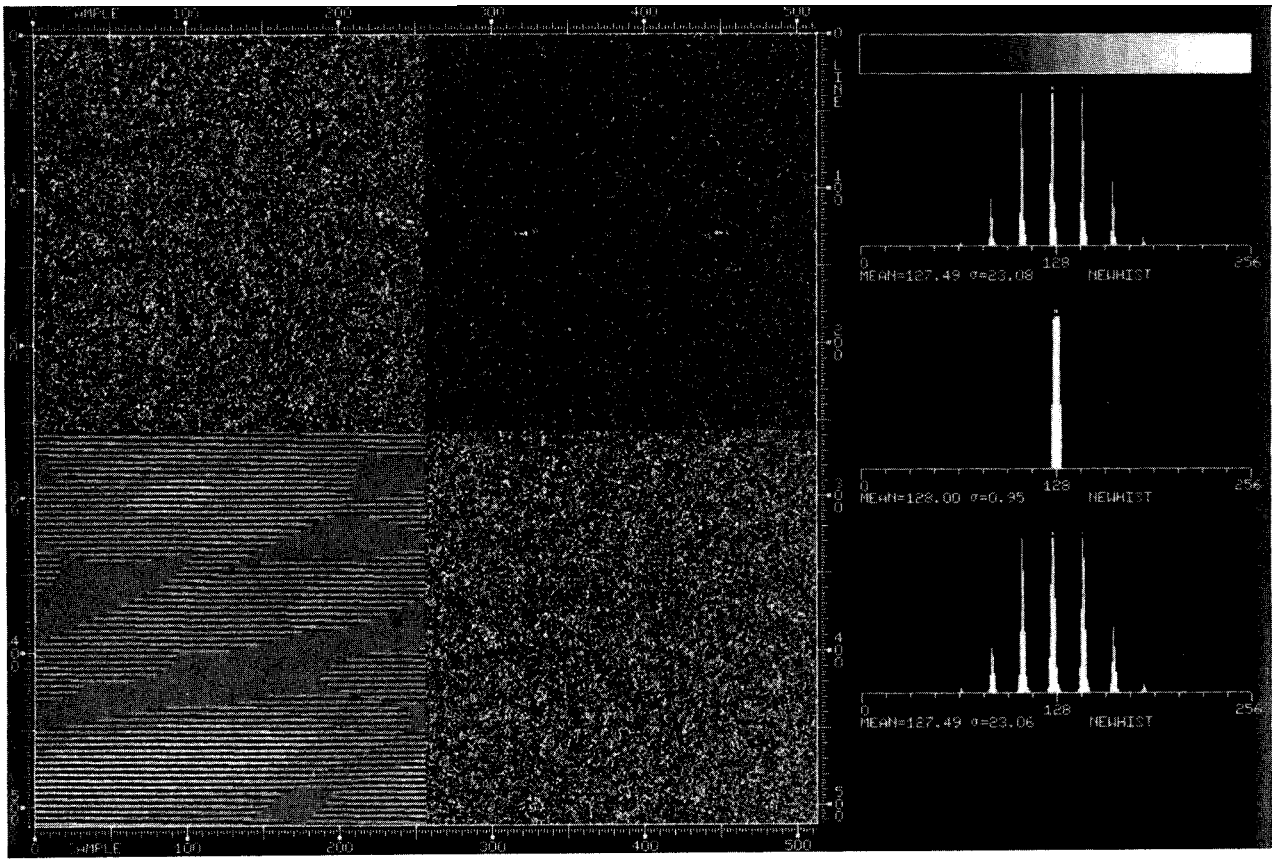

Figure 3-150. Noise analysis data for a radiometrically calibrated exposed frame, 8°C, gain state 2, summation mode.

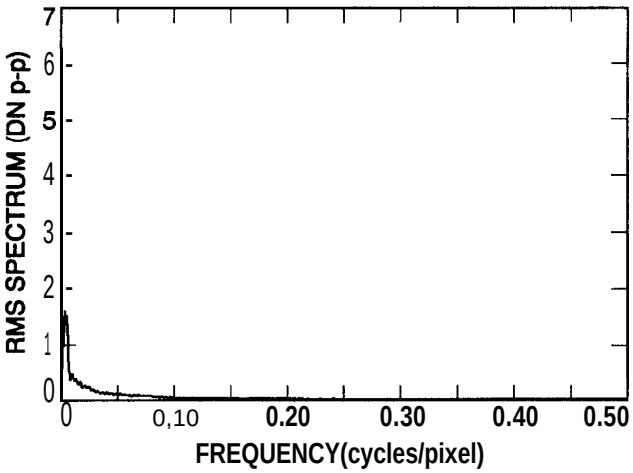

Figure 3-151. One-dimensional power spectrum of the horizontal coherent noise component of Figure 3-150.

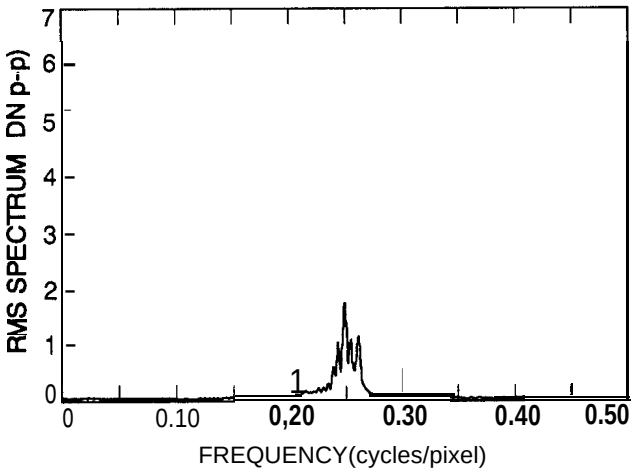

Figure 3-152. One-dimensional power spectrum of the vertical coherent noise component of Figure 3-150.

The level of digitization noise is increased somewhat by unequal bit weighting, i.e., inaccuracies in the operation of the analog-to-digital converter (ADC) that result in DN bins of unequal width. Variations in the DN bin widths may be inferred when the number of pixels in an image with a given DN value deviates from the expected number by more than what would be probable statistically, based on other known noise sources. To obtain a well-defined value for the expected number of pixels for each DN requires images possessing a flat or smoothly varying distribution of signal levels covering a large range of DN values in one image.

The 1989 data set allows for the first time a detailed study of the dependence of uneven bit weighting on gain state, as well as a more comprehensive study of the effect in the summation mode than was possible from earlier data. Examination of the 1989 data showed the following (Reference 2):

1. The magnitude of the uneven bit weighting effects in the full-resolution mode is somewhat greater than was seen in 1985, and comparable to that seen in the smaller 1988 data set.
2. In the summation mode, uneven bit weighting is qualitatively different and larger in magnitude than in the full-resolution mode.
3. In the summation mode, major differences were seen in the pattern of the bit weighting between different gain states. The 10K and 40K gain data matched closely but differed dramatically from the 400K gain state. The small amount of data collected in the 100K gain state appeared similar to the 400K data. In the full-resolution mode, smaller but significant differences were seen between the 10K and 100K gain data.
4. No dependence on frame rate was detected in the full-resolution mode.

Based on these observations, it was decided to generate four separate bit-weighting-corrected DN tables, i.e., for the two imaging modes (full-resolution and summation) and for the high (1OK and 40K) and-the low (1OOK and 400K) gain states.

The general procedure used to correct for uneven bit weighting in both the older and in the recent data was the following. The bin width for each DN in an image was calculated by taking the ratio of the number of pixels with that DN to the number expected for that DN. After this was done to all frames in the data subset being analyzed, a composite bin width table was constructed, using the data from different frames to fill in different parts of the DN scale. In regions of the scale where two or more frames overlap, resulting in multiple independent measurements of a bin width, the bin widths for these frames were averaged. No weighting of the measurements based on counting statistics or other measures of data quality was done in calculating the average; however, statistical checks were performed to see if any of the independent values were outliers (as a result of poor counting statistics, for example) and should be

omitted from the average. When the composite bin width table was complete, a table of DN bin lower and upper bounds and midpoints was built up cumulatively starting at the lowest DN in the table. The entire table was then shifted by a constant fractional-DN offset to bring the midpoints into the closest possible agreement with the nominal DN values. This produced the bit-weighting corrected DN table. For the very highest and lowest DNs, where no usable data exists, nominal values must be assumed.

To calculate bin width it was first necessary to define the number of pixels expected to have a particular DN. For the 1989 analysis an attempt was made to reduce systematic errors by using no more adjacent DNs than necessary to estimate the expected number of pixels for a given DN. A close examination of DN histograms such as that in Figure 3-153 reveals that, if the histogram is viewed as a series of odd-even pairs, the members of each pair seem to deviate equally from the expected number, the surplus of pixels in one of the DNs being balanced by a corresponding deficit in the other. The magnitude and sign of the deviations vary from one pair to another, but almost always the pairwise symmetry holds.

Figure 3-154 shows the pixels/DN distribution when averages of the number of pixels within 2 (or in a few cases 4) adjacent DN levels are used to define bin width for the full-resolution, high-gain data set shown in Figure 3-153. Figure 3-155 shows the composite bin widths obtained by merging the individual frame data to get a broader range of DNs. Figures 3-156 to 3-158 show the derived DN bin widths for the lower gain states and summation mode.

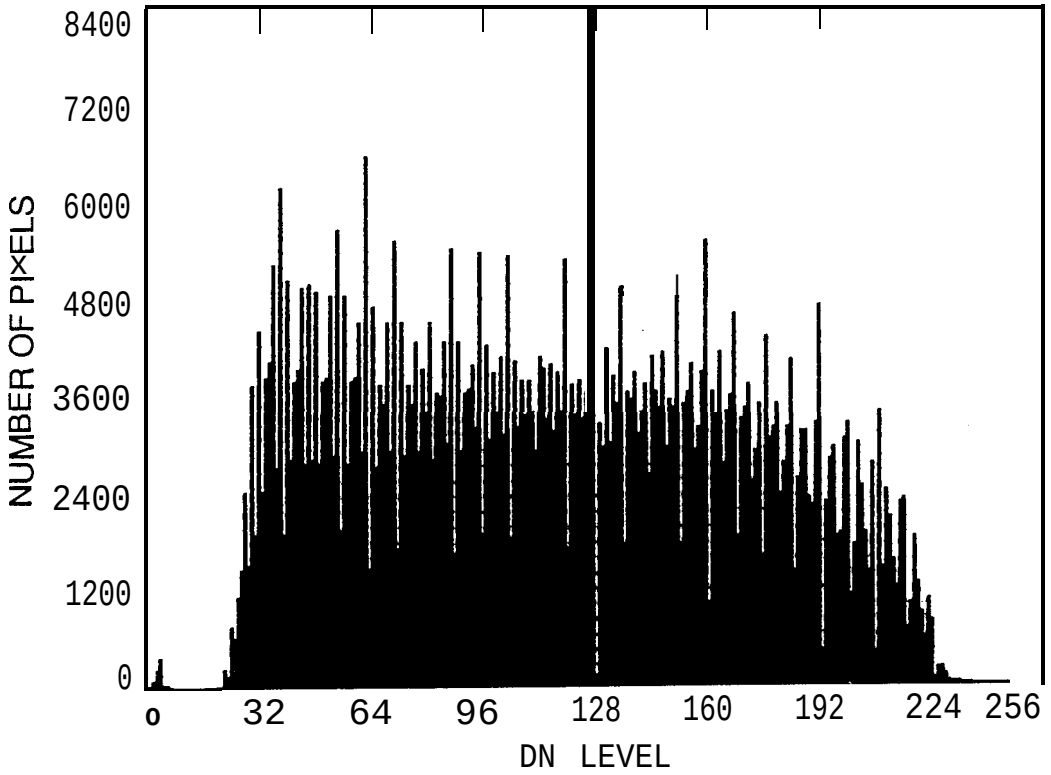

Figure 3-153. Histogram of the DN values in a typical zero-exposure high-gain frame taken to study light leak.

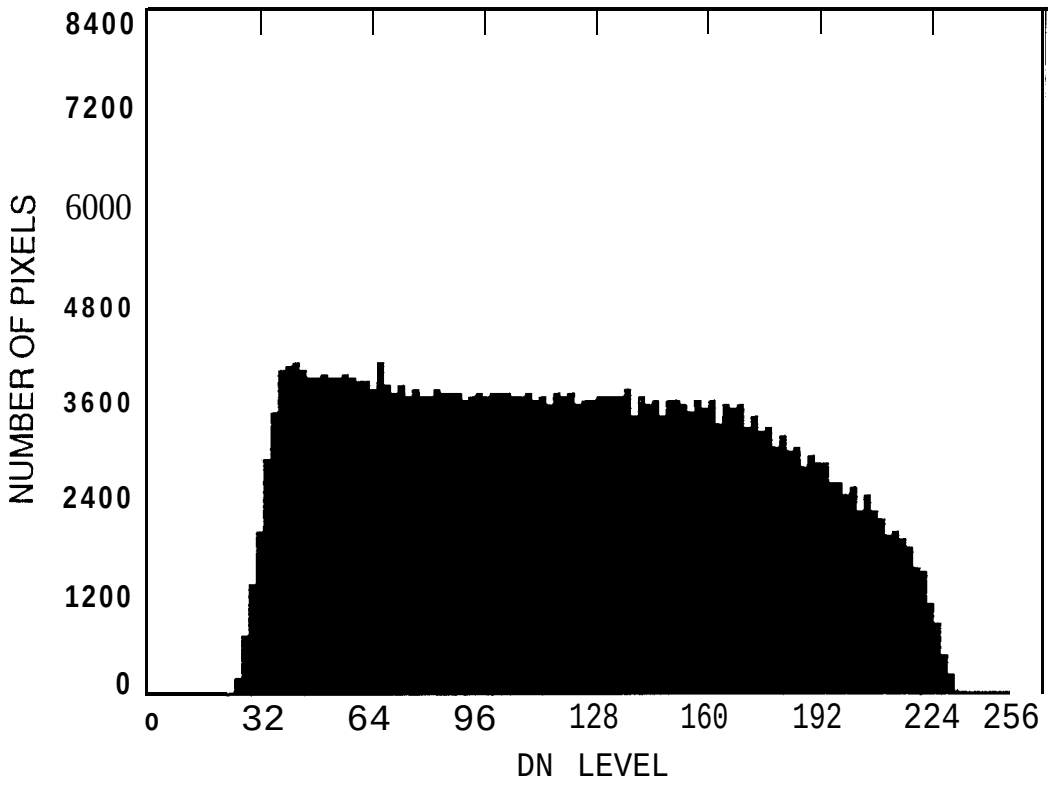

Figure 3-154. Histogram of Fig. 3-153 after 2- or 4-DN averaging

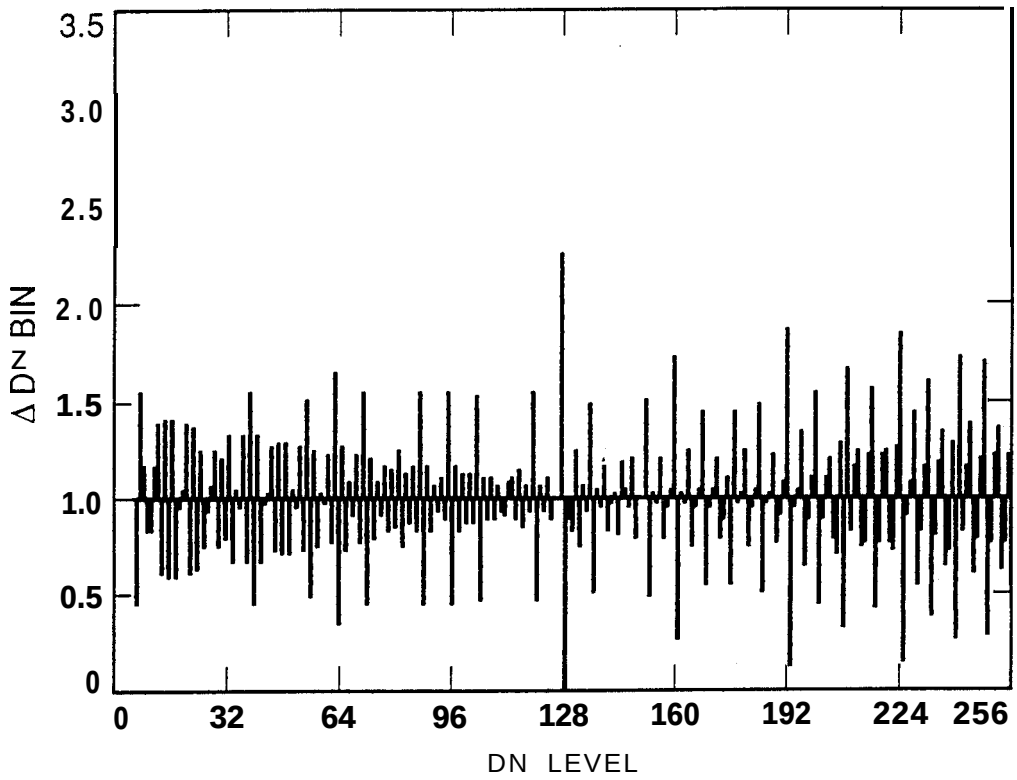

Figure 3-155. DN bin widths for full-resolution mode, high-gain states.

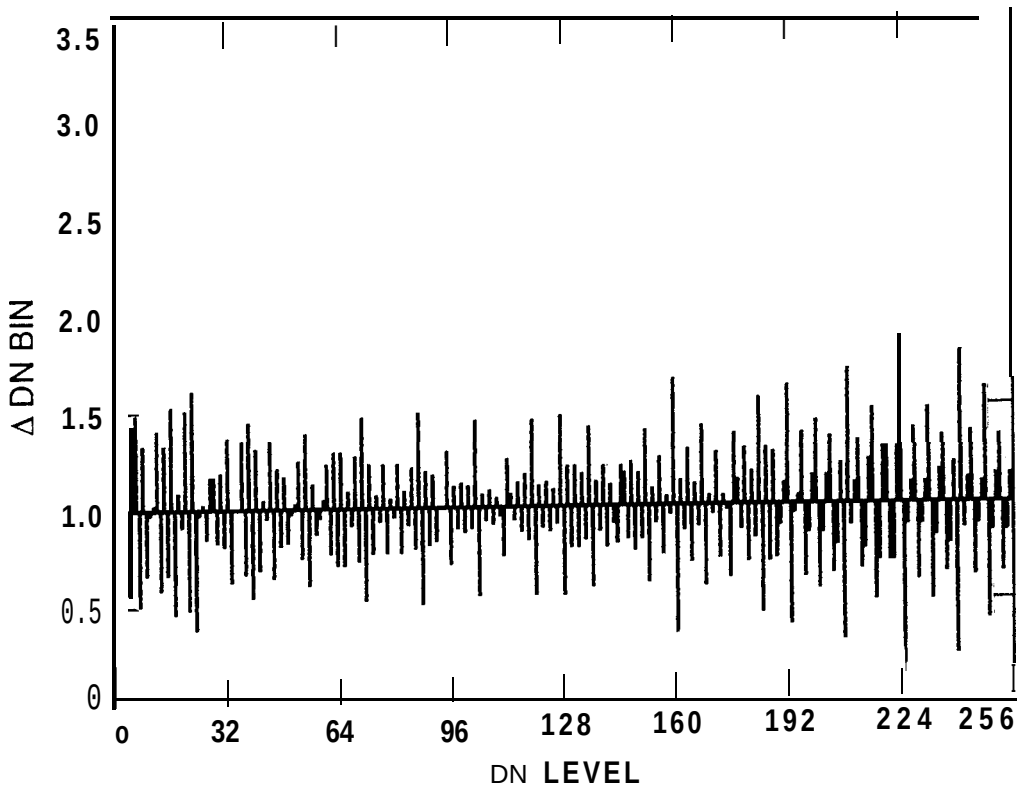

Figure 3-156. DN bin widths for full-resolution mode, low-gain state.

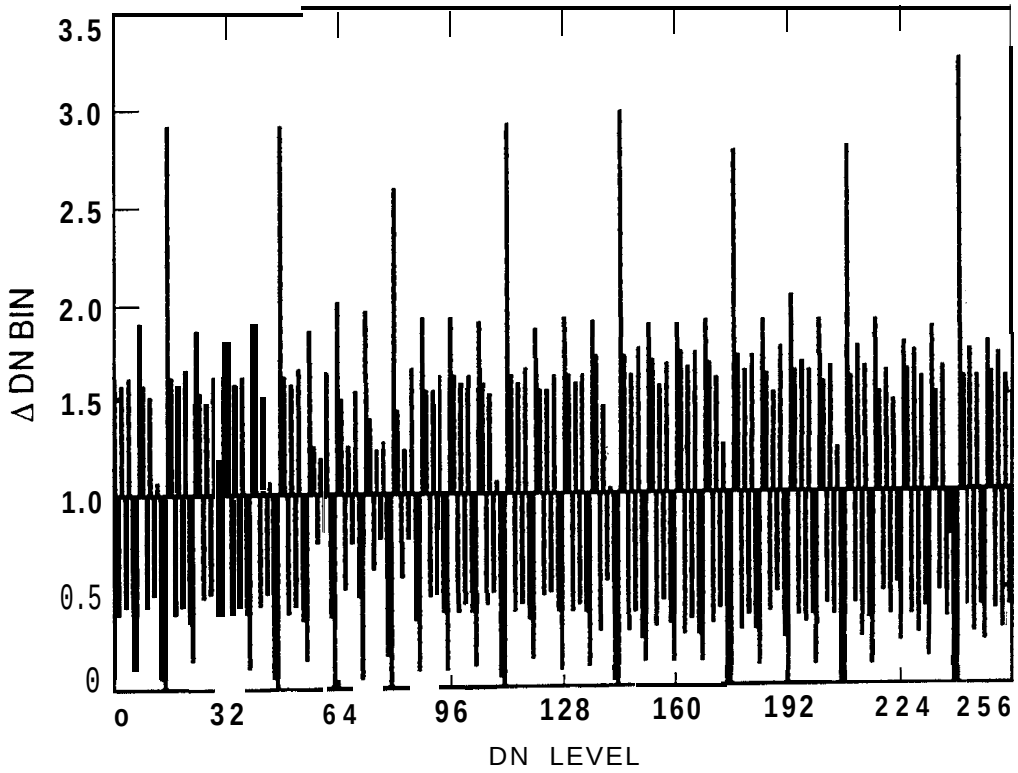

Figure 3-157. DN bin widths for summation mode, high-gain states.

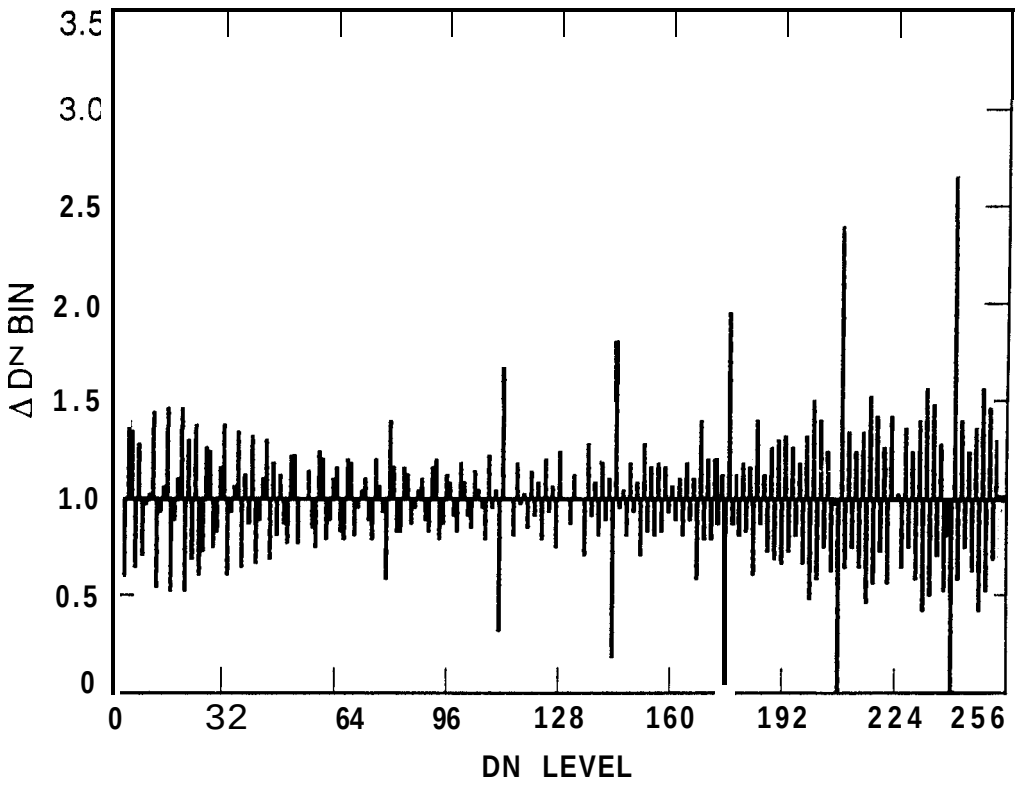

Figure 3-158. DN bin widths for summation mode, low-gain states.

Table 3-22 tabulates the corrected DN values for 10K/40K and 100K/400K for full-resolution mode and summation mode.Figures 3-159 to 3-162 plot the deviation of each corrected DN from its nominal value for the four derived correction tables. Table 3-23 gives the average digitization noise levels for the images used in this study before and after the uneven bit weighting correction is applied. Data taken at the different calibration temperatures show that the uneven bit weighting patterns change with temperature, so if the instrument is operated at an off-nominal temperature in flight,it will be necessary to perform inflight calibrations to correct for this effect.

Table 3-22. DN values corrected for uneven bit weighting based on analysis of 1989 SSI calibration data at +8°C.

	corrected DN			
nominal	full-res. mode		summation mode	
DN	10K/40K	100K	10K/40K	l00K/4ooK
0				
1			1.256	
2			2.257	
3			3.235	
4			4.235	
5		4.695	5.262	4.864
6		5.695	6.262	5.864

Table 3-22 (continued).

nominal DN	corrected DN: full-res. mode 10K/40K	full-res. mode 100K	summation mode 10K/40K	summation mode l00K/400K
7		7.141		7.227
8	7.645	8.141	7.518	8.227
9	8.998	9.064	9.239	9.202
10	9.998	10.064	10.239	10.203
11	10.838	10.889	11.206	11.054
12	11.838	11.889	12.206	12.054
13	13.104	13.096	12.990	13.280
14	14.104	14.096	13.545	14.280
15	15.118	15.063	13.571	15.031
16	16.118	16.063	15.016	16.032
17	17.118	17.163	17.257	17.289
18	18.118	18.163	18.257	18.289
19	18.900	18.940	19.244	19.015
20	19.900	19.940	20.244	20.015
21	21.107	21.150	21.284	21.292
22	22.107	22.150	22.284	22.292
23	23.094	23.201	22.536	23.212
24	24.094	24.201	23.536	24.212
25	25.036	24.893	25.221	25.249
26	26.036	25.894	26.221	26.249
27	26.883	26.826	27.215	26.931
28	27.883	27.826	28.215	27.931
29	29.037	28.980	29.264	29.186
30	30.037	29.980	30.264	30.186
31	31.013	30.987	30.513	30.987
32	32.013	31.987	31.513	31.987
33	33.082	33.083	33.259	33.254
34	34.082	34.083	34.260	34.254
35	34.937	34.900	35.238	35.030
36	35.937	35.900	36.238	36.030
37	37.081	37.067	37.265	37.236
38	38.081	38.068	38.265	38.236
39	39.191	39.121	38.520	39.124
40	40.191	40.121	39.521	40.124
41	41.073	41.055	41.242	41.223
42	42.073	42.055	42.242	42.224
43	42.910	42.922	43.209	43.015
44	43.910	43.922	44.209	44.015
45	45.045	45.078	44.993	45.216
46	46.045	46.078	45.548	46.216
47	47.062	47.001	45.574	47.151
48	48.062	48.001	47.019	48.151
49	49.060	48.985	49.260	49.121
50	50.060	49.985	50.260	50.121
51	50.934	50.892	51.247	50.957
52	51.934	51.893	52.247	51.957
53	53.050	53.028	53.287	53.171
54	54.050	54.028	54.287	54.171
55	55.172	55.098	54.539	55.063
56	56.172	56.098	55.539	56.064

Table 3-22 (continued).

nominal DN	corrected DN: full-res. mode 10K/40K	full-res. mode 100K	summation mode 10K/40K	summation mode l00K/400K
57	**57.041**	56.964		57.133
58	58.041	57.964	58.078	58.133
59	58.931	58.890	59.054	58.944
60	59.931	59.890	60.054	59.945
61	61.025	61.022	61.269	61.165
62	62.025	62.022	62.269	62.165
63	63.236	63.048	62.476	63.016
64	64.236	64.048	63.476	64.016
65	65.045	65.045	65.201	65.145
66	66.045	66.045	66.201	66.145
67	66.955	66.944	67.085	66.973
68	67.956	67.944	68.085	67.973
69	69.027	69.041	69.219	69.155
70	70.027	70.041	70.219	70.155
71	71.190	71.138	70.492	71.051
72	72.190	72.138	71.492	72.051
73	73.018	73.022	73.154	73.121
74	74.018	74.022	74.154	74.121
75	74.956	74.943	75.069	74.971
76	75.956	75.943	76.069	75.971
77	77.003	77.015	77.095	77.097
78	78.004	78.015	77.815	78.097
79	78.993	78.933	77.907	78.866
80	79.993	79.933	79.187	79.866
81	81.040	81.024	81.173	81.147
82	82.040	82.025	82.173	82.147
83	82.984	82.955	83.076	82.988
84	83.984	83.956	84.076	83.988
85	84.999	85.015	85.284	85.132
86	85.999	86.016	86.284	86.132
87	87.190	87.154	86.518	87.049
88	88.190	88.154	87.518	88.049
89	88.998	89.007	89.225	89.115
90	89.998	90.007	90.225	90.115
91	90.954	90.997	91.219	90.987
92	91.954	91.998	92.219	91.987
93	92.970	92.914	93.268	93.169
94	93.970	93.914	94.268	94.169
95	95.195	95.057	94.517	95.011
96	96.195	96.057	95.517	96.011
97	96.999	96.961	97.263	97.107
98	97.999	97.961	98.264	98.107
99	98.983	98.973	99.242	98.985
100	99.983	99.973	100.242	99.985
101	100.980	100.963	101.269	101.114
102	101.980	101.963	102.269	102.114
103	103.178	103.131	102.524	103.001
104	104.178	104.131	103.525	104.001
105	104.974	104.944	105.246	105.089
106	105.974	105.944	106.246	106.089

Table 3-22 (continued).

nominal DN	corrected DN: full-res. mode 10K/40K	full-res. mode 100K	summation mode 10K/40K	summation mode l00K/400K
107	106.974	106.951		106.965
108	107.974	107.951	108.213	107.966
109	108.949	108.939	108.997	109.052
110	109.949	109.939	109.552	110.052
111	110.880	110.799	109.578	110.740
112	111.880	111.800	111.023	111.740
113	112.972	112.949	113.264	113.070
114	113.972	113.950	114.264	114.070
115	114.992	114.980	115.251	114.980
116	115.992	115.980	116.251	115.981
117	116.956	117.001	117.291	117.063
118	117.956	118.002	118.291	118.064
119	119.186	119.142	118.543	119.009
120	120.186	120.143	119.543	120.010
121	120.948	120.969	121.228	121.033
122	121.948	121.970	122.228	122.034
123	122.975	122.982	123.222	122.974
124	123.975	123.982	124.222	123.975
125	124.921	124.962	125.271	125.045
126	125.921	125.962	126.271	126.045
127	127.541	127.147	126.520	126.956
128	128.674	128.148	127.520	127.956
129	129.137	129.024	129.266	129.075
130	130.003	130.024	130.267	130.075
131	131.037	131.023	131.245	131.015
132	132.037	132.023	132.245	132.016
133	132.951	133.006	133.272	133.081
134	133.951	134.006	134.272	134.081
135	135.161	135.125	134.527	134.940
136	136.161	136.125	135.528	135.940
137	136.938	136.986	137.318	137.043
138	137.938	137.986	138.318	138.044
139	139.005	139.021	139.186	138.986
140	140.005	140.021	140.186	139.986
141	140.906	140.969	140.980	141.031
142	141.906	141.969	141.509	142.031
143	142.826	142.830	141.528	142.682
144	143.826	143.831	142.999	143.682
145	144.942	145.002	145.321	145.065
146	145.942	146.003	146.321	146.066
147	147.024	147.037	147.270	146.995
148	148.024	148.037	148.270	147.995
149	148.922	149.011	149.337	149.049
150	149.922	150.011	150.337	150.050
151	151.166	151.118	150.543	150.946
152	152.166	152.118	151.543	151.946
153	152.929	152.971	153.309	153.006
154	153.929	153.971	154.309	154.006
155	155.018	155.050	155.242	154.994
156	156.018	156.050	156.242	155.994

Table 3-22 (continued).

nominal DN	corrected DN: full-res. mode 10K/40K	full-res. mode 100K	summation mode 10K/40K	summation mode l00K/400K
157	**156.900**	156.953	.	157.003
158	157.900	157.953	158.297	158.003
159	159.281	159.252	158.540	159.053
160	160.281	160.252	159.540	160.053
161	160.934	160.993	161.327	161.038
162	161.935	161.994	162.327	162.038
163	163.042	163.071	163.293	162.999
164	164.042	164.071	164.293	164.000
165	164.902	164.980	165.334	165.034
166	165.902	165.981	166.334	166.034
167	167.140	167.138	166.535	166.888
168	168.140	168.139	167.535	167.888
169	168.901	168.958	169.300	168.988
170	169.901	169.958	170.300	169.988
171	171.017	171.063	171.263	170.988
172	172.017	172.063	172.263	171.988
173	172.874	172.950	173.089	173.027
174	173.874	173.950	173.717	174.027
175	174.702	174.753	173.726	174.615
176	175.702	175.753	175.098	175.615
177	176.915	176.996	177.316	177.027
178	177.915	177.996	178.316	178.028
179	179.041	179.078	179.276	179.001
180	180.041	180.078	180.276	180.001
181	180.902	181.014	181.322	181.013
182	181.902	182.014	182.322	182.013
183	183.163	183.211	182.527	182.896
184	184.163	184.212	183.527	183.896
185	184.914	185.077	185.274	185.036
186	185.914	186.077	186.274	186.036
187	187.036	187.065	187.216	186.963
188	188.036	188.065	188.216	187.963
189	188.882	188.893	189.337	188.946
190	189.883	189.893	190.337	189.946
191	191.355	191.236	190.474	190.932
192	192.355	192.236	191.474	191.932
193	192.906	192.917	193.277	192.963
194	193.906	193.917	194.277	193.963
195	195.090	195.122	195.298	195.007
196	196.090	196.122	196.299	196.007
197	196.871	196.866	197.282	196.932
198	197.871	197.866	198.283	197.932
199	199.192	199.151	198.535	198.840
200	200.192	200.151	199.536	199.840
201	200.870	200.868	201.255	200.892
202	201.870	201.868	202.255	201.892
203	203.028	203.105	203.289	202.974
204	204.028	204.105	204.289	203.974
205	204.788	204.836	205.085	204.910
206	205.788	205.836	205.708	205.720

Table 3-22 (continued).

nominal DN	corrected DN: full-res. mode 10K/40K	full-res. mode 100K	summation mode 10K/40K	summation mode l00K/400K
207	206.593	206.597	**205.719**	206.215
208	207.593	207.597	207.097	207.406
209	208.841	208.885	209.260	208.926
210	209.841	209.885	210.260	209.926
211	211.043	211.097	211.346	210.974
212	212.043	212.097	212.346	211.974
213	212.813	212.824	213.296	212.923
214	213.813	213.824	214.296	213.923
215	215.208	215.178	214.536	214.833
216	216.209	216.178	215.537	215.833
217	216.821	216.800	217.225	216.881
218	217.821	217.800	218.225	217.881
219	219.041	219.079	219.289	218.965
220	220.042	220.079	220.289	219.965
221	220.800	220.803	221.203	220.883
222	221.800	221.803	222.203	221.883
223	223.349	223.371	222.601	223.089
224	224.349	224.371	223.601	224.089
225	224.885	224.887	225.283	224.919
226	225.885	225.887	226.283	225.919
227	227.146	227.126	227.333	226.971
228	228.146	228.126	228.333	227.971
229	228.849	228.885	229.266	228.893
230	229.849	229.885	230.266	229.893
231	231.231	231.180	230.557	230.812
232	232.231	232.180	231.557	231.812
233	232.837	232.854	233.231	232.853
234	233.837	233.854	234.231	233.853
235	235.100	235.106	235.293	234.951
236	236.100	236.106	236.293	235.951
237	236.794	236.838	236.871	236.868
238	237.794	237.838	237.268	237.548
239	238.571	238.561	237.271	237.954
240	239.571	239.561	238.874	239.274
241	240.851	240.883	241.271	240.889
242	241.851	241.883	242.271	241.889
243	243.119	243.119	243.332	242.974
244	244.119	244.119	244.332	243.974
245	244.829	244.886	245.267	244.917
246	245.829	245.886	246.267	245.917
247	247.280	247.230	246.598	246.812
248	248.280	248.230	247.598	247.812
249	248.822	248.870	249.277	248.865
250	249.822	249.870	250.277	249.865
251	251.113	251.111	251.330	250.940
252	252.113	252.111	252.330	251.940
253	252.823	252.868	253.271	
254	253.823	253.868	254.271	
255			254.530	

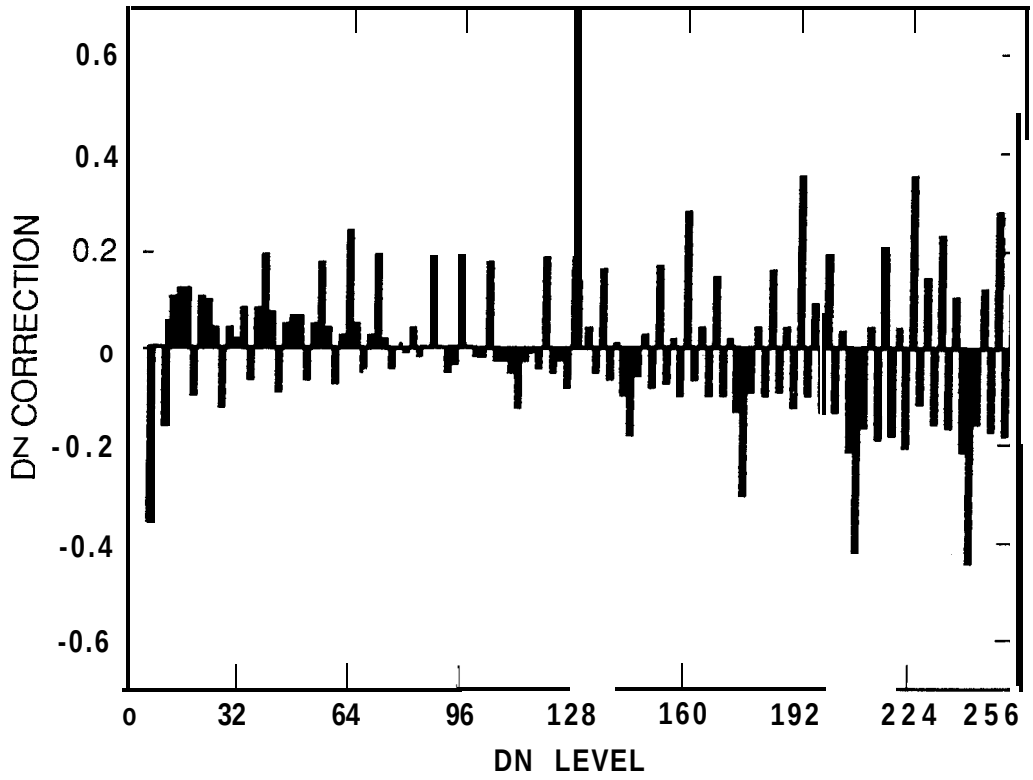

Figure 3-159. DN correction for full-resolution mode, high-gain state.

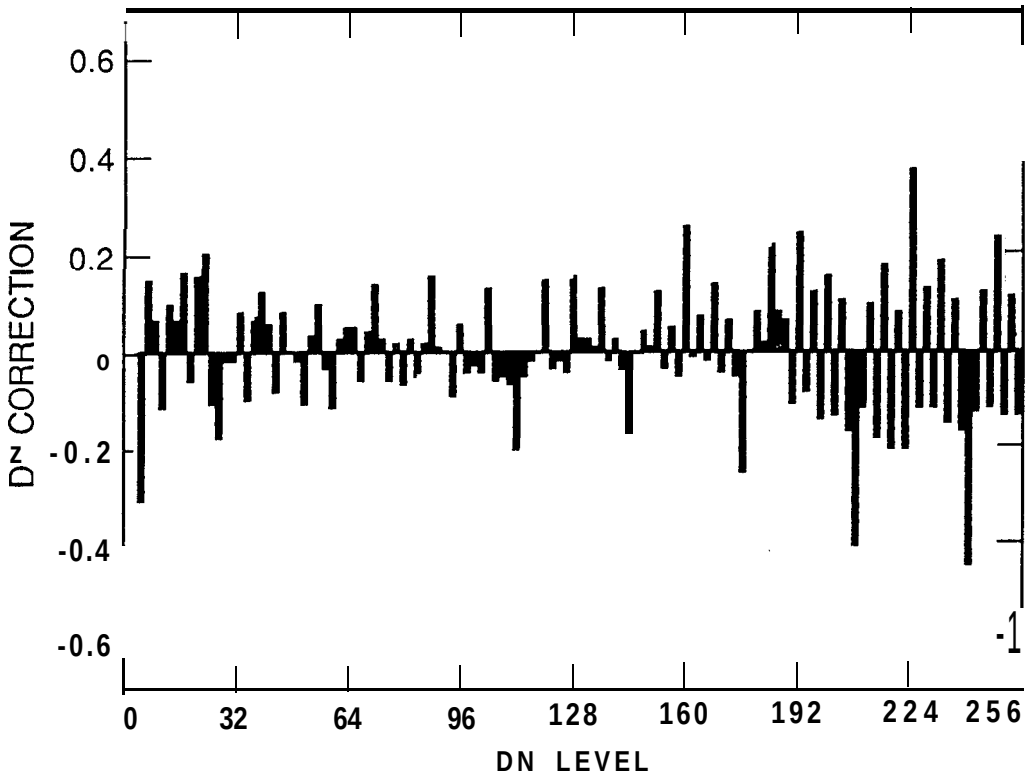

Figure 3-160. DN correction for full-resolution, low gain states.

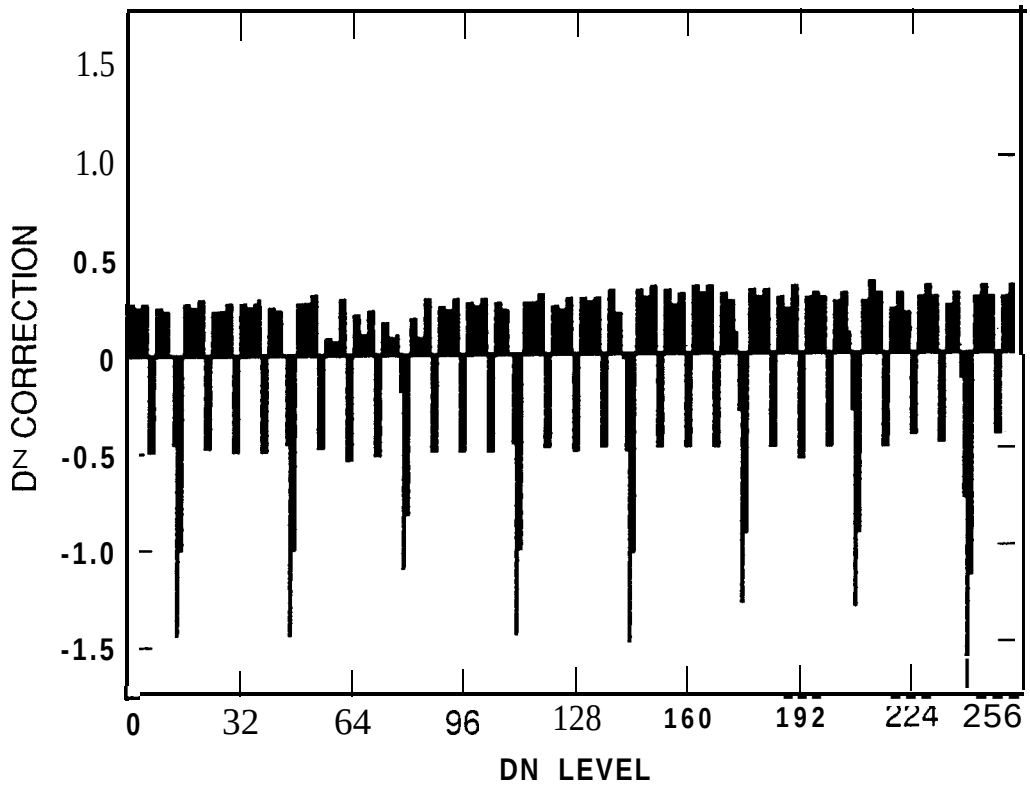

Figure 3-161. DN correction for full-resolution mode, high-gain state.

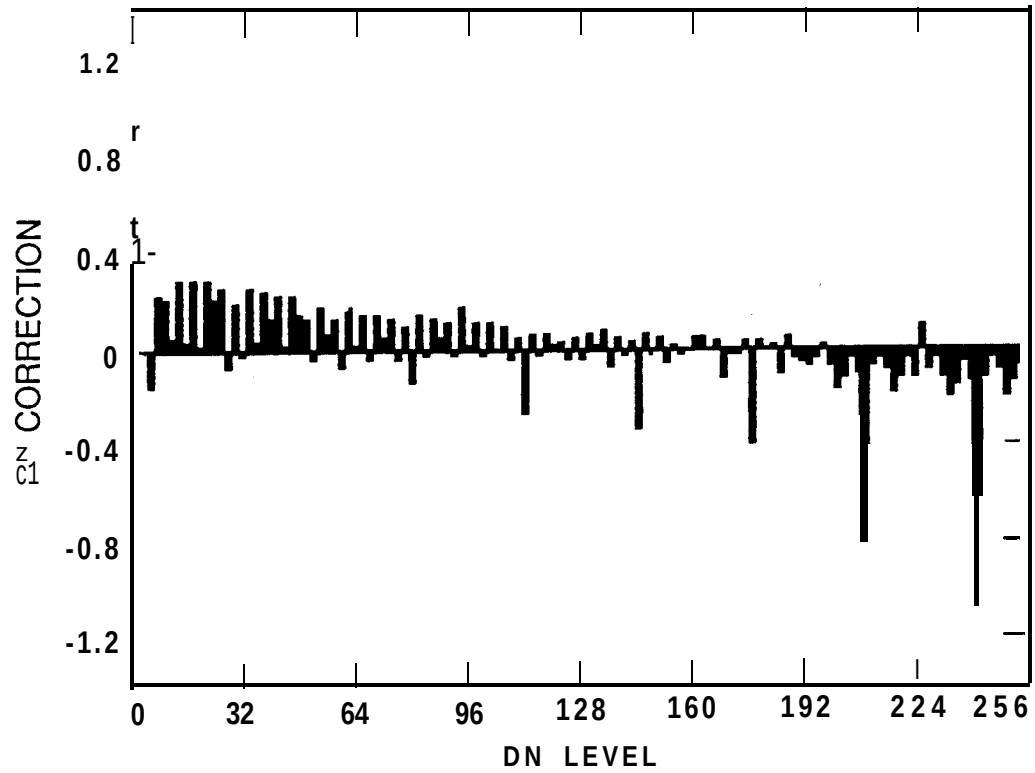

Figure 3-162. DN correction for summation mode, low-gain states.

Table 3-23. Digitization noise in 1989 SSI calibration data before and after correcting for uneven bit weighting.

	digitization noise (DN)							
	full-resolution mode				summation mode			
	l0K/40K		100K		l0K/40K		l00K/400K	
DN range	before corr.	after corr.	before corr.	after corr.	before corr.	after corr.	before corr.	after corr.
7 - 3 2	.354	.327	.356	.337	.661	.495	.349	.326
33 - 64	.343	.331	.325	.316	.628	.476	.323	.308
65 - 96	.330	.320	.320	.313	.565	.443	.313	.301
97 - 128	.378	.342	.320	.309	.634	.480	.319	.307
129 - 160	.339	.318	.329	.317	.657	.494	.327	.314
161 - 192	.360	.329	.344	.324	.648	.495	.347	.332
193 - 224	.393	.346	.395	.346	.622	.478	.401	.370
225 - 252	.402	.350	.382	.339	.704	.514	.449	.404
7 - 252	.364	.333	.348	.325	.636	.482	.368	.334

F. Color Reconstruction

The approach adopted for color reconstruction of SSI images was described in Reference 1. The reconstruction method is somewhat different for image display on a CRT and display on a photographic print. The analysis discussed here was done using color test target images from the 1985 SSI calibration data set converted to radiometric units using the results of the 1985 SSI calibration. Using the old 1985 data should be sufficient to validate the color reconstruction techniques that have been developed. Parameter values to be used for color reconstruction of flight data will be updated using the latest available SSI pre-launch or inflight calibration results.

For display on a CRT, the proper relative DNs to apply to each channel are given by

$$[\ DN^{g}\ ] = [\ K\ ]^{-1}[\ x\ ]^{-1}[\ M\ ]\ [\ R\ ]$$

where

[x] is a 3 x 3 matrix of CIE tristimulus values for the color output by each of the three individual display channels

[K] is a 3 x 3 diagonal matrix of constant factors that determine the color balance between the three channels of the CRT

[M] is a 3 x n transformation matrix corresponding to the n separately filtered SSI input images

[R] is a n x 1 matrix of reflectivity values for the n SSI filtered images.

Calibrations of the MIPL color CRT used to display color reconstruction test images have yielded values of g between 2.1 and 2.8 at various times. The value measured immediately after recalibration of the monitor was 2.25. This value was used in the color reconstruction tests discussed below.

Calibration images of the color test target acquired through the violet, green, and red filters were calibrated into radiance units and input to the matrix [R]. A color reconstructed image was generated and displayed on the MIPL color CRT. Measurements were then made of the chromaticity values of selected color squares in the test image as displayed on the monitor. These values were compared with the expected values calculated using the previously measured spectral radiance of the MVM collimator viewed through the thermal vacuum chamber window and the spectral transmittance of the test target squares themselves. Three of the squares selected fell completely within the color space detectable by the SSI and displayable by the CRT. Two other squares were selected that represented the brightest red and nearly the brightest green squares in the target. These two squares fall outside of the capabilities of the CRT to display accurately; however, it is still desirable that the color reconstruction technique result in highly saturated colors of nearly the correct hue for such squares. Table 3-24 lists the expected and actual chromaticity coordinates of the five selected color target squares. The relative luminance are also listed normalized to that of square 5/7. The chromaticity coordinates are plotted on the standard CIE chromaticity diagram in Figure 3-163. The actual chromaticity coordinates match those expected reasonably well for the three squares whose colors should have been detectable and displayable (5/7, 7/6, and 11/7). Their relative luminance are also well reproduced. The chromaticity coordinates for the other two squares also match those expected fairly well, although the green square is less saturated than it should be. The relative luminance values are also quite a bit less than they should be relative to those of the other three squares.

Table 3-24. Color target chromaticity coordinates (x,y) and relative luminance (Y) comparison (expected vs. reconstructed) for a CRT displayed image

	Expected			Measured		
Square	x	y	Y	x	y	Y
	.271		1.0	.252		1.0
7/6	.453	.323	0.99	.434	.295	1.0
11/7	.382	.349	0.86	.363	.306	0.81
1/3	.696	.302	4.74	.642	.319	2.17
1/12	.439	.534	4.23	.482	.446	1.51

For display of a reconstructed color image using a photographic print, a much more complicated algorithm is required than for a CRT display. This is so because color photography involves a subtractive process. In Reference 1, an algorithm was

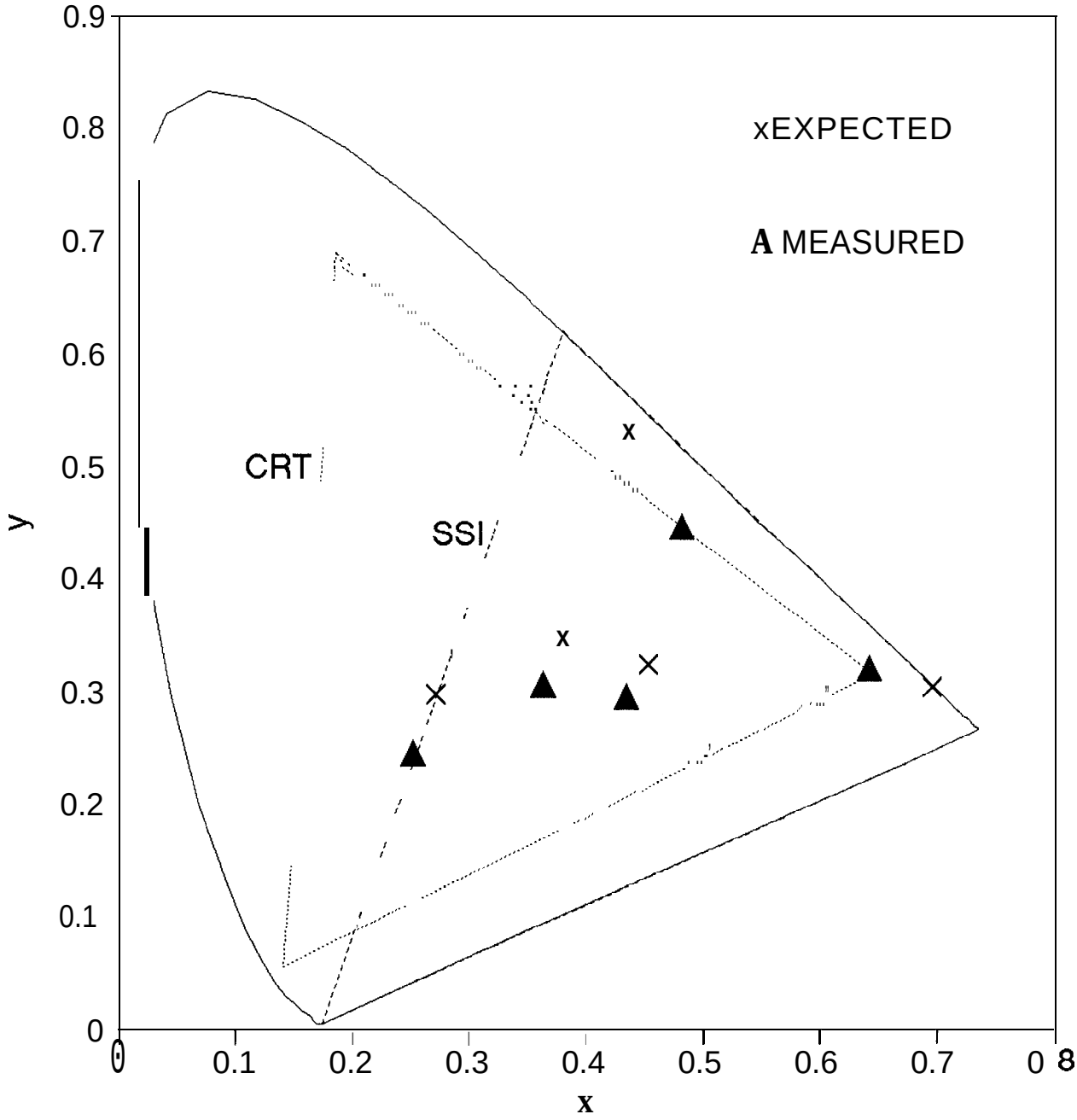

Figure 3-163. Standard CIE chromaticity diagram showing the expected and measured chromaticity coordinates for radiance of five selected color squares from the SSI color test target.

developed under the assumptions that the process is additive and print reflectivity is linear with DN. Both these assumptions are known to be incorrect. Therefore, a revised algorithm was developed and is described below.

Discussions with MIPL and the JPL Photolab indicate that the adopted goal of the JPL film recording/photoprocessing procedure is to achieve a transmission density on the color negative in each channel that is linear with input DN. This process then results in a color print having reflectance densities that are also nearly linear with input DN. Thus for color processing, the traditional linear D vs. log E characteristic used in black-and-white processing (D = density, where density = -log(t), t = negative transmission or print reflectivity; E = exposure, which is proportional to input DN) has been replaced by a linear D vs. E characteristic for each color channel. In order to be able to produce a color print that acceptably approximates the "natural" colors in the original scene, we must be able to produce print reflectivities that are linear with the original scene reflectance at a given wavelength. This can most easily be done by doing a transformation from DNs that are proportional to scene reflectance to DNs that are proportional to log(reflectance) prior to sending them to the film recorder.

The actual transformation is slightly more complicated than this, however, because the minimum reflectivity of a photographic print is only about 2% rather than zero, and the maximum is only about 75% rather than 100%. Therefore, even though we can compute calibrated scene reflectivities on a scale of O to 1, the best that we can produce on a print is a mapping of scene reflectivities, r, to print reflectivities, R, of something like

$$R = k \times r + B = A \times D N + B ,$$

where DN is a value proportional to the actual scene reflectivity, and B is the minimum print reflectivity. With respect to the DN value input to the film recorder, DN , however, the resulting print reflectivity will be approximated by

$$R = l0^{aDN^{*}-b} .$$

If we define the maximum print reflectivity to be C and assume an 8-bit scale, we can derive

$$DN^{*} = \frac{255 \log [(C-B)DN/(255B) + 1]}{\log (C/B)}$$

for the mapping from DN proportional to scene reflectivity to DN* to send to the film recorder. This mapping can be different for each color channel since B and C can differ for different channels.

The discussion above addresses the relationship between print reflectivity and input DN to the film recorder; however, it does not address the remaining problem that the color

photographic process is actually subtractive rather than additive. In practice, for any color that requires non-zero DNs from more than one channel, errors will be introduced because of "cross talk" between the channels, i.e., the print reflectance at the wavelength of one channel will be affected by the amount of reflectance reproduced at the wavelength of another channel. The following discussion outlines a "natural" color reconstruction algorithm for photographic prints that includes an approximate first-order compensation for channel "cross talk" effects.

The photographic print produces colors by subtracting (i.e., absorbing) varying amounts of the light incident upon it at each wavelength and reflecting the rest to the observer. For example, absorption of red light occurs in one layer of the photographic emulsion (allowing cyan to be reflected), subtraction of green light in another (allowing reflection of magenta), and subtraction of blue light in a third (allowing reflection of yellow). The amount of absorption increases with the amount of light exposure supplied to each layer during the printing process. If the wavelengths of light absorbed in each emulsion layer were totally independent of those absorbed in the other layers, we could express the reflectivity of the color print at any wavelength, W, in terms of the DN applied to the channel that exposes the relevant absorbing layer by

$$R_w = 10^{xwDN^*-y}$$

as discussed above for the JPL photo processing procedure. The maximum reflectivity results when DN = 255. Thus,

$$R_w = R_{w_{max}} \times 10^{Xw(DN^*-255)}.$$

Unfortunately, the wavelengths absorbed by each layer are not totally independent; each layer in fact absorbs some light at all wavelengths. Therefore, the reflectivity at any wavelength is more properly given according to Beer's law by

$$Rw = Rwmax\ (^{10xwr(DNr^*-255)})\ (^{10xwg(DNg^*-255)}, (10xwb(DNb^{*-255}),$$

$$= Rw\ max\ (10^{xwrDNr^*+xwgDNg^*+xwbDNb^*\ -255(Xwr+Xwg+Xwb)}),$$

where the subscripts indicate the red, green, and blue channels of the film recorder and the x's apply at wavelength w.

Since what is really desired for "natural" color reconstruction is to match the tristimulus values of the scene reflectance on the print, we must convert the equation above for print reflectivity to one for print tristimulus values. We have elected to compute this conversion exactly for three standard colors and to use the same conversion for all other colors accepting any errors that might result from this approximation. Recognizing that the tristimulus values of the print reflectance are given by convolutions of the standard color matching functions with the spectral reflectance, we observe that the tristimulus values for a given spectral reflectance can be written as

$$X/X_{max} = 10^{X_{xr}DN_r^* + X_{xg}DN_g} *+ X_{xb}DN_b^* - 255 \; (X_{xr}+X_{xg}+X_{xb})$$

$$Y/Y_{max} = 10^{X_{yr}DN_r^* + X_{yg}DN_g^* + X_{yb}DN_b^* - 255} \; (X_{yr}+X_{yg}+X_{yb})$$

$$Z/Z_{max} = 10^{X_{zr}DN_r^* + X_{zg}DN_g^* + X_{zb}DN_b^* - 255} \; (X_{zr}+X_{zg}+X_{zb})$$

where the nine x's are constants independent of wavelength. These nine constants can be solved for given the three standard colors to match, knowledge of X_{max}, Y_{max} and the values of X, Y, and Z when the DN* 's are all zero.

The solution is as follows:

$$[L] = [x] [DN^*] - 255 [\text{sum } x]$$

where

[L] = 3x3 matrix of log (X/X_{max}), log (Y/Y_{max}), log (Z/Z_{max})
[x] = 3x3 matrix of unknown x's
[DN*] = 3x3 matrix of DN values sent to the film recorder
[sum x] - 3x3 matrix of the sums of the xx's, X_Y's, and X_Z's.

Note that 255 [sum x] is also given by -log $(X_{min}/X_{max})r$ -log (Ymin/Y max) and -log (Z_{min}/Z_{max}) when all DN's are zero. prints have shown that these values are all about 1.25. [x] is then given by

$$[x] = \{[L] + 1.25\} [DN^*]^{-1}.$$

The three standard colors chosen to be matched are white and the magenta and yellow produced when one film recorder channel is supplied with zero DN and the two others have 255 DN. This selection permits a first-order compensation for color channel "cross talk" since two or three layers of emulsion are exposed on the negative and must transmit light on the print. Color test target prints have been generated consisting of squares for which one, two, and three film recorder channels were driven with various DN levels, and the spectral reflectance and tristimulus values of each color square have been measured. The results of these measurements were used to determine the matrix [x] needed to fit the white, magenta, and yellow tristimulus values.

This [x] matrix was then used to determine the DN* to send to the film recorder to match the tristimulus values for any other scene reflectance using

$$[DN^*] = [x]^{-1}\{[L] + 1.25\}.$$

To match the range of reflectance available in a photographic print, it is desirable to scale the scene reflectance tristimulus values prior to computing matrix [L]. This is done as follows. Using the standard definition of chromaticity coordinates (i.e., x = X/(X+Y+Z) and y = Y/(X+Y+Z)), the range of possible colors that can be reproduced on a print is defined. The resulting chromaticity coordinates and the sum Q = X+Y+Z for the cases with 255 DN applied to one, two and three channels were

derived. Figure 3-164 shows these coordinates plotted on a chromaticity diagram along with their Q values. The value of Q gives a measure of the maximum total reflectance possible from the print for the given color. An estimate of the maximum reflectance possible from the print for any intermediate color is made by interpolating between the 7 Q values measured. This interpolation is done by fitting triangular planes in (x, Y, Q) space between the neutral data point and each pair of two "adjacent" colors plotted in Figure 3-164. The desired scaling factor for the scene tristimulus values, T, is computed by comparing the sum $q = T_x+T_Y+T_z$ to Q at the x,y chromaticity coordinates defined by tie scene reflectance tristimulus values, i.e., $x = T_x/(T_x+T_Y+T_z)$ and $y = T_Y/(T_x+T_Y+T_z)$. For each pixel, the quantity $s = Q/q$ is computed. Histograms of s are compiled for the entire frame and for areas of approximately equal colors. These approximately equal color areas are defined to be areas in the x,y plane with dimensions of 0.02 units on a side. The value of parameter S is determined such that either

a) the number of pixels having s > S over the entire frame equals a user-defined percentage of the total pixels (e.g., 10% or 64,000 for a non-summation mode frame),

or b) the number of pixels having s > S in any area of approximately equal color equals a user-defined percentage of the total pixels in the frame (e.g., 1% or 6400 pixels),

is true, but not both. For pixels whose x,y values fall outside

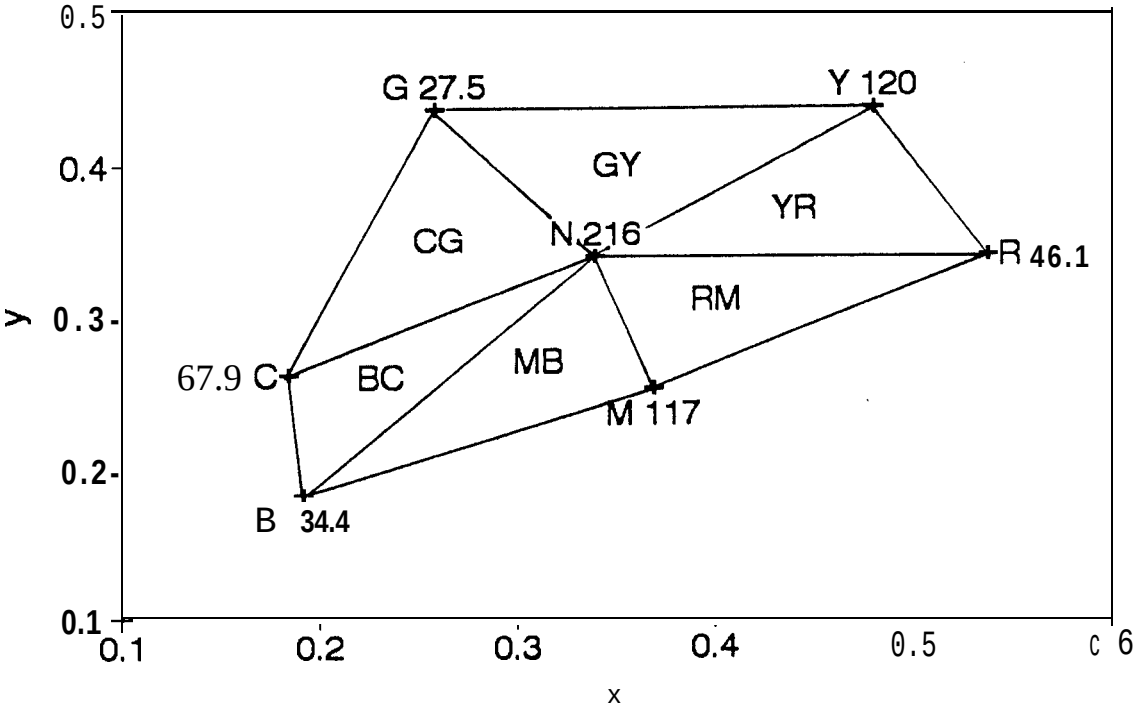

Figure 3-164. Seven-color test print chromaticity coordinates and Q values

of the area outlined in Figure 3-164, the value of Q at the intersection of a line joining (x, y) and the chromaticity coordinates of neutral (.339 ,.339) with the border outlined in the Figure is used in computing s. The value of s in this case is grouped with the histogram for the approximately equal color area containing this intersection point.

The scaled tristimulus matrices for the scene at each pixel are then determined by

$$[t] = [T] \times S.$$

Matrix [L] is calculated for each pixel by

$$[L] = \begin{bmatrix} \log (t_x/x_{max}) \\ \log (t_y/y_{max}) \\ \log (t_z/z_{max}) \end{bmatrix}.$$

The [DN*] calculated from this [L] matrix should require no further scaling; however, DN* values < 0 must be set to O and DN values > 255 must be set to 255.

Figure 3-165 is the best "natural" color reconstruction of the color test target photographed by the SSI in the thermal vacuum chamber using the above algorithm. The tristimulus values of the reflectance from the three color squares selected for determining the conversion from calibrated scene reflectance to tristimulus values (5/7, 7/6, 11/7) as well as the two highly saturated squares (1/3, 1/12) were measured off the print and compared to the expected values. The results are listed in Table 3-25. The agreement is quite good.

Table 3-25. Color target chromaticity coordinates (x,y) and relative reflectance (Y) comparison (expected vs. reconstructed) for a color photographic print

	Expected			Measured		
Square	x	y	Y	x	y	Y
5/7	.284	.302	1.0	.287	.334	1.0
7/6	.471	.323	1.03	.482	.329	1.23
11/7	.398	.350	0.87	.395	.359	0.97
1/3	.698	.301	5.29	.544	.344	2.90
1/12	.445	.529	4.25	.499	.425	7.89

G. Light Leaks

Light leak tests were performed for the 1989 calibration primarily to verify trends established during tests in 1984/1985 of the effectiveness of the closed camera shutter in blocking out light. Fifteen zero exposure frames using high gain (1OK) were acquired: eight through the clear filter for 60 2/3-, 30 1/3-, 8 2/3- and 2 l/3-sec frame rates, plus several frames at 60 2/3-sec through various other filters. These tests were all performed at

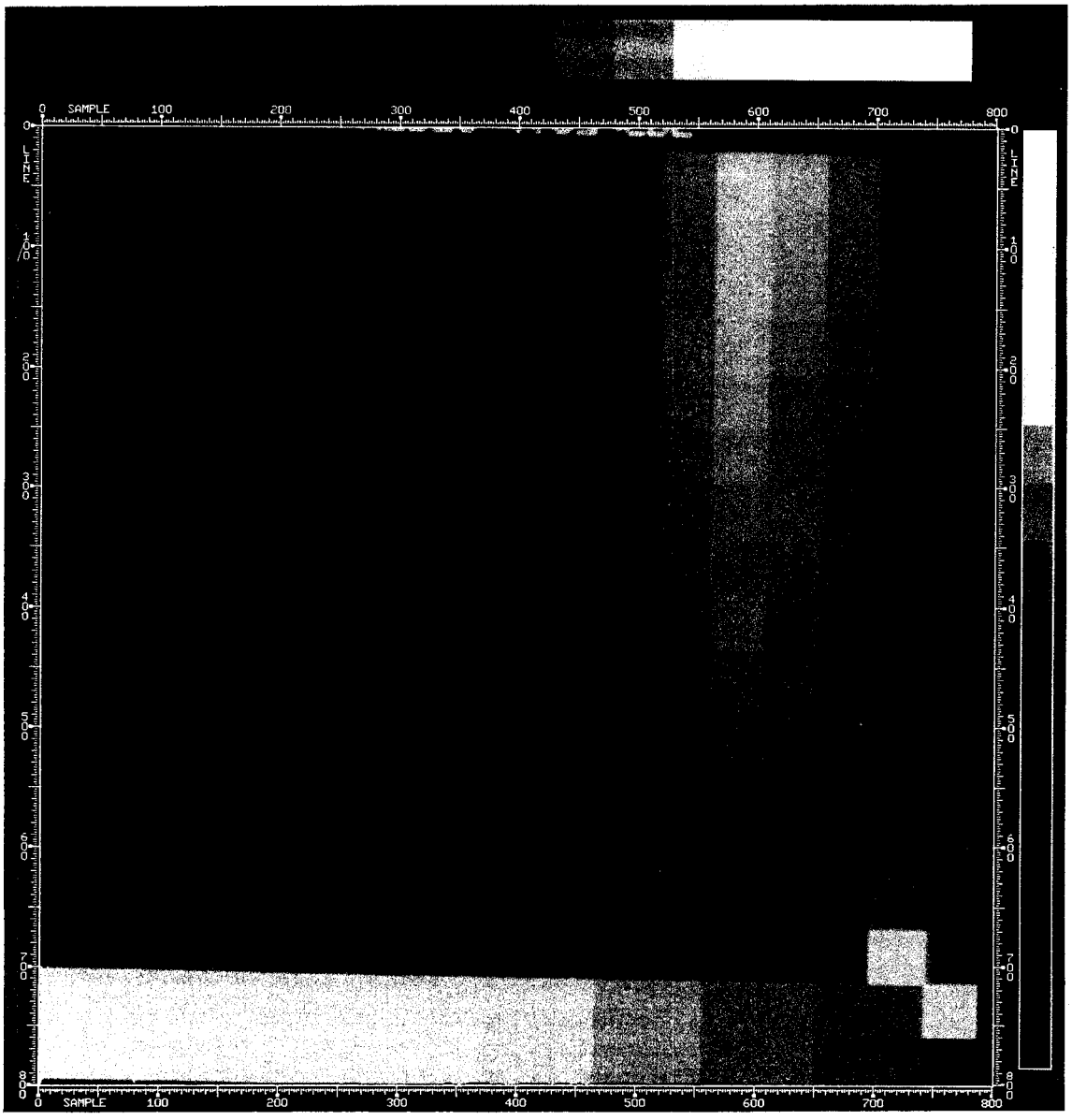

Figure 3-165. “Natural” color reconstruction of color test target illuminated by the MVM collimator and viewed through the thermal vacuum chamber window

three camera operating temperatures; however, only the data acquired at +8°C have been analyzed in detail. No significant differences were observed at other temperatures. Images were recorded both in total darkness and with the SSI viewing the xenon light cannon as a source of high-level illumination. The difference in DN values for the illuminated and non-illuminated frames is a measure of the magnitude of the light leak.

Table 3-26 lists the frames, the average DN after subtraction, and, using the high gain conversion factor of 38.7 e-/DN, the average electron yield. The average DN is converted to equivalent xenon cannon luminance by using a conversion factor of 920 DN/ftL-sec for the clear filter in gain state 4. Average integration times are 27.9 sec in the 60 2/3-sec imaging mode, 14.7 sec in the 30 l/3-sec mode, and 4.6 sec in the 8 2/3-sec mode (maximum integration 'times are approximately twice these values), 2 1/3 sec for the 2 l/3-sec mode, and 4 2/3 sec for the 2 l/3-sec extended mode. The leakage-equivalent luminance divided by the actual luminance of the calibration light source (6200 ftL) yields the fraction of the incident light reaching the detector with the shutter closed.

Table 3-26. Light leak measurements obtained by comparing zero-exposure images made in darkness and with a 6200 ftL calibration light source.

Filter	Frame Rate (sec)	Avg. DN	Avg. e^-	equivalent Luminance (ftL)	Leakage Fraction	Ratio to 1985
Clear	60 2/3	sat.	n/a			
Clear	30 1/3	91.6	3545	0.00677	1.092×10^{-6}	2.70
Clear	8 2/3	27.3	1057	0.00645	1.040×10^{-6}	2.57
Clear	2 1/3	75.8	2933	0.00883	1.424×10^{-6}	n/a
Clear	2 1/3, ext.	140.1	5422	0.00816	1.316×10^{-6}	n/a
7270A	60 2/3	3.2	124	0.00012	2.011×10^{-8}	2.96

The leakage fraction has increased by nearly 3 times compared to that measured in 1985. No explanation for this increase has been generated.

The brightness of Jupiter seen at zero phase is 330 ftL, a factor of -18 lower than the calibration light source, and hence the amount of light reaching the detector would be lower by this factor, as shown in Table 3-27. It can be seen that the amount of light reaching the detector is not insignificant. The variation with filter selection suggests that the leakage is occurring along the optical axis of the instrument, since otherwise no de-

pendence on filter choice would be expected. Viewing Jupiter or its satellites at low phase angles in the high gain state should be avoided when high photometric accuracy is desired. Zero exposure calibration frames of Jupiter and its satellites should be acquired in this configuration, in order to allow subtraction of this effect from the raw data set.

Table 3-27. Expected light reaching the detector from the disk of Jupiter at zero phase in various imaging modes with the shutter closed.

Filter	Frame Rate (sec)	Avg. DN	Avg. e^-	Equivalent Luminance (ftL)
Clear	60 2/3	9.26	358	3.60×10^{-4}
Clear	30 1/3	4.88	189	3.61×10^{-4}
Clear	8 2/3	1.45	56	3.43×10^{-4}
Clear	2 1/3	4.03	156	4.69×10^{-4}
Clear	2 1/3, ext.	7.46	289	4.34×10^{-4}
7270A	60 2/3	0.17	7	6.62×10^{-6}

H. Internal Scattering/Ghosts

Scattered light has been observed in the pre-launch SSI data both with the optics cover off and with the cover on. Pre-launch calibration data with the cover off include knife-edge images (see Sec. II.C) and navigation target images with circular and crescent “planets” acquired in the thermal vacuum chamber at 8°C. A set of horizontal MTF wide-bar images in all 8 filters was acquired in an ambient room-temperature environment with the cover both on and off.

The cover-off knife-edge images were acquired in the 100K gain state through all eight filters. Scattered light is observed extending out beyond 100 pixels from the white/black edge, with the response dropping to less than 5% of the peak signal within the first 25 pixels from the edge in all filters. The edge is defined as the midpoint between the peak and background. Variation in the response wing shape with wavelength is evident. Larger scattering is observed in the shortest and longest wavelengths. These variations are characterized in Table 3-28, where for each filter the ratio of scattered light response to the peak DN is listed for six sampled distances from the edge.

Table 3-28. Scattered light levels as a fraction of the maximum signal

Filter	DN max	Pixels from edge +25	+50	+75	+100	+200	+300
Violet	116	.034	.034	.034	.026	.017	.009
Green	158	.019	.013	.013	.013	.006	.006
Red	228	.026	.022	.018	.018	l 009	.005
Clear	220	.014	.009	.009	.009	.005	.005
7270 A	189	.048	.042	.037	.032	.021	.011
7560 A	227	.035	.031	.026	.026	.013	.004
8890 A	80	.038	.025	.025	.025	.013	.013
>9680 A	79	.050	.025	.025	.025	.013	.013

Figures 3-166 through 3-173 are plots of 50-line averages of horizontal line traces across the knife edges. The background dark current has been removed in these traces.

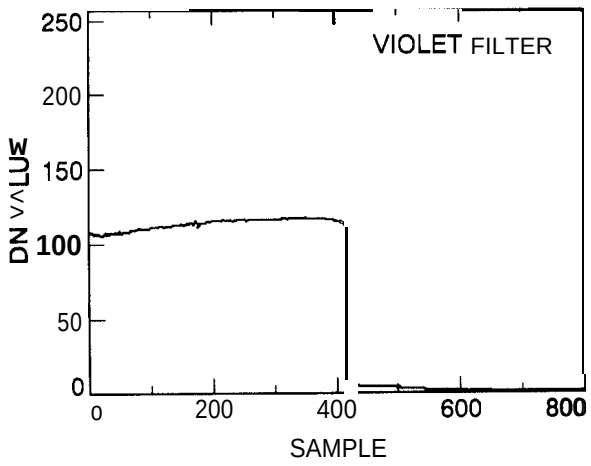

Figure 3-166. Average line trace for knife edge image, violet filter

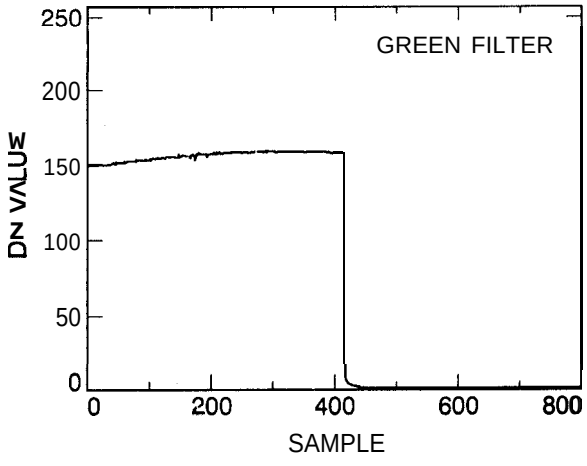

Figure 3-167. Average line trace for knife edge image, green filter

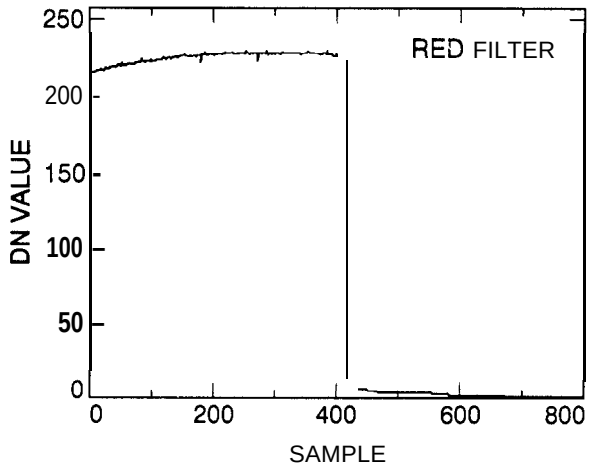

Figure 3-168. Average line trace for knife edge image, red filter

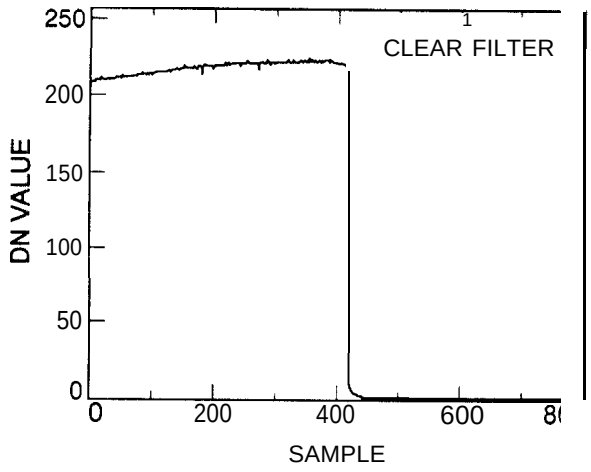

Figure 3-169. Average line trace for knife edge image, clear filter

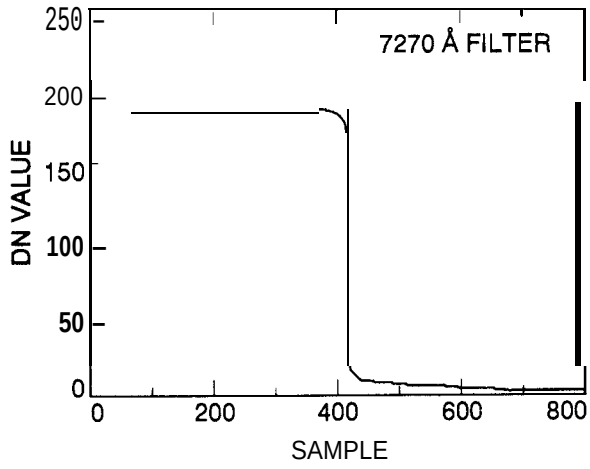

Figure 3-170. Average line trace for knife edge image, 7270 A filter

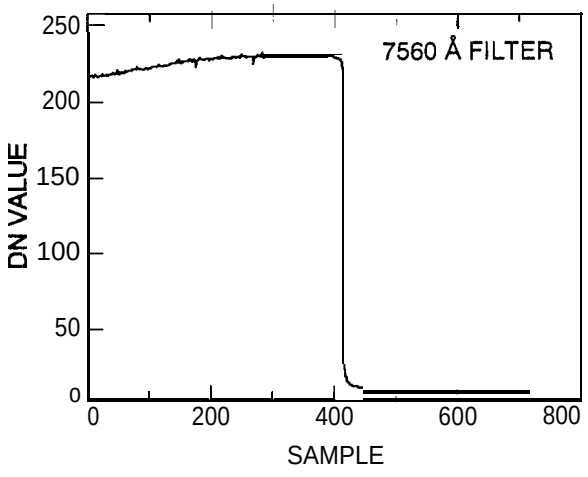

Figure 3-171. Average line trace for knife edge image, 7560 A filter

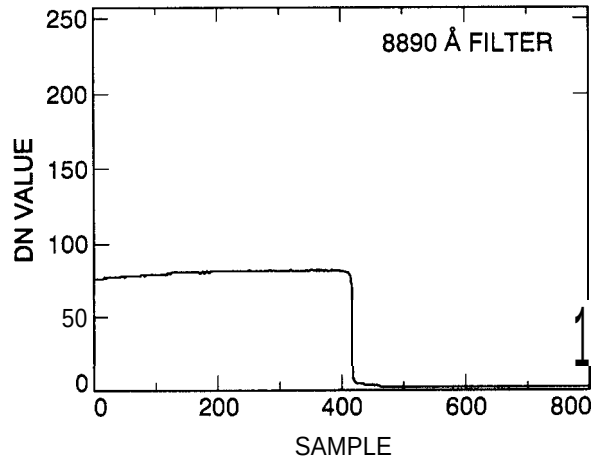

Figure 3-172. Average line trace for knife edge image, 8890 A filter

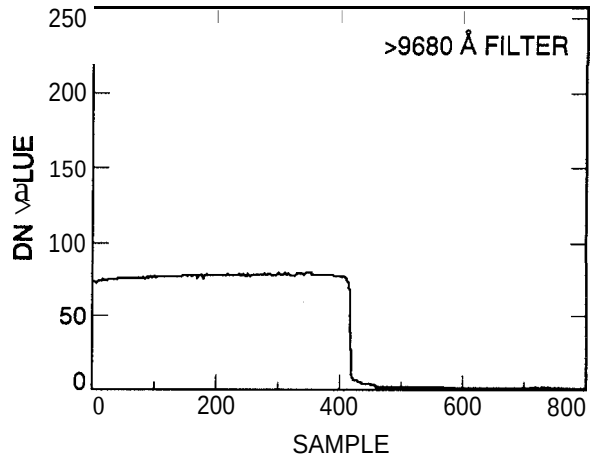

Figure 3-173. Average line trace for knife edge image, >9680 A filter

Images of the navigation target in each filter were also acquired in the thermal vacuum chamber with the cover off. Scattered light is seen at about the 1% level out to 20 pixels from the limb of the largest"planet". Figures 3-174 through 3-181 are examples of horizontal line traces for these images. The peak signal level is cut off in these plots since it exceeds 255 DN in gain state 4. The actual peak signal was targeted to be about 75,000 e-, equivalent to about 1940 DN in gain state 4. Variations in the wing shape as a function of filter are consistent with the knife-edge results. The levels of internal scattered light reported here should be taken as upper limits on the actual SSI scattered light. Some of the scattering seen here may be due to scattering within the MVM collimator or from the thermal vacuum chamber window.

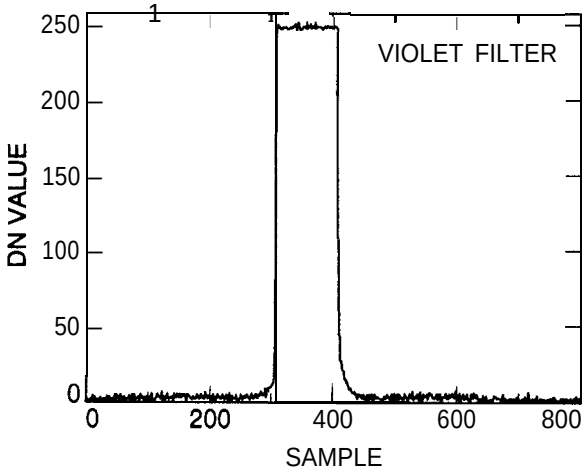

Figure 3-174. Navigation target trace through "Planet", violet filter

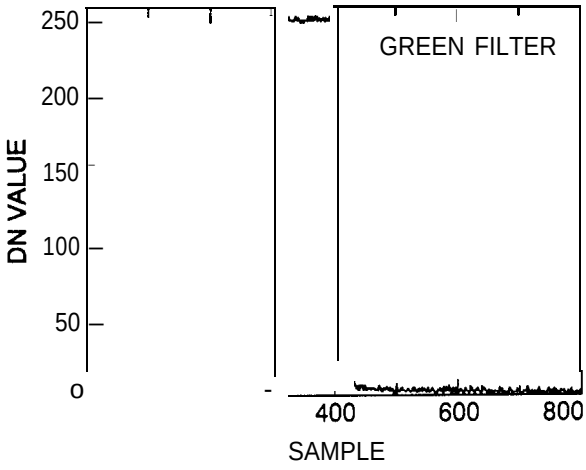

Figure 3-175. Navigation target trace through "Planet", green filter

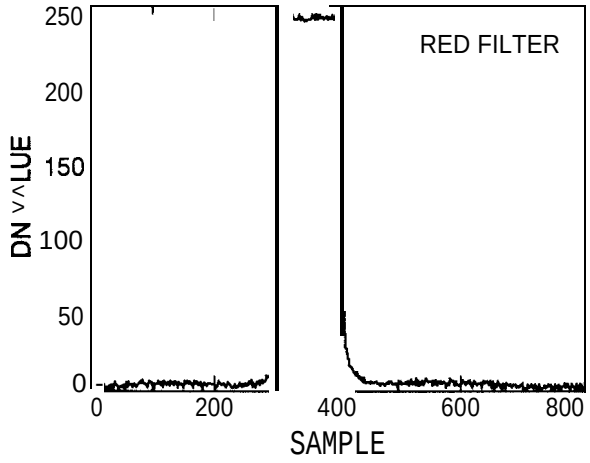

Figure 3-176. Navigation target trace through "Planet", red filter

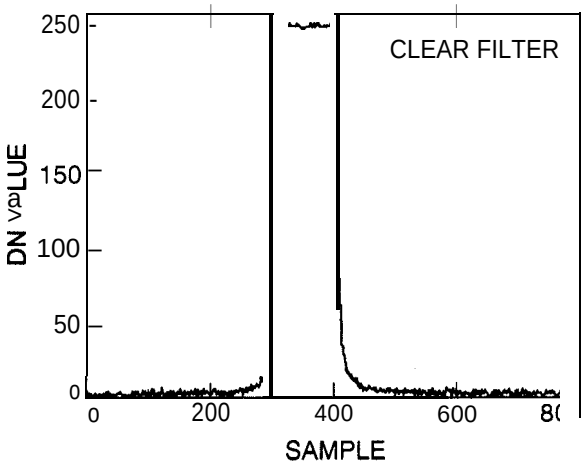

Figure 3-177. Navigation target trace through "Planet", clear filter

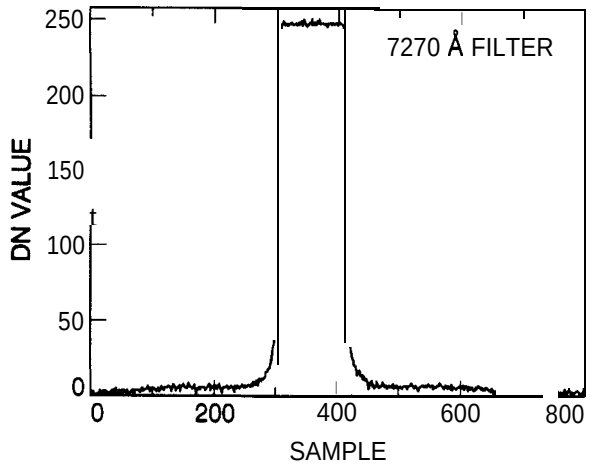

Figure 3-178. Navigation target trace through "planet", 7270 A filter

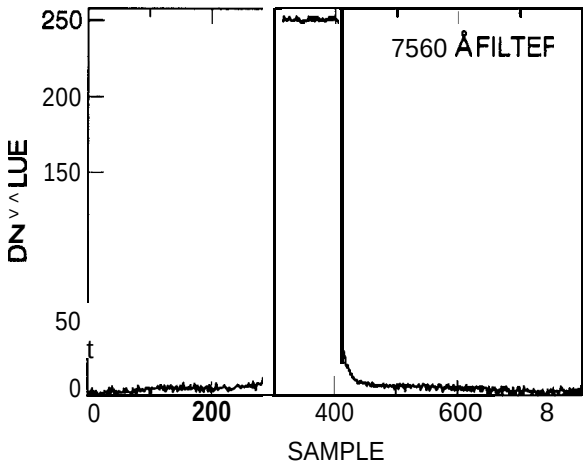

Figure 3-179. Navigation target trace through "planet", 7560 A filter

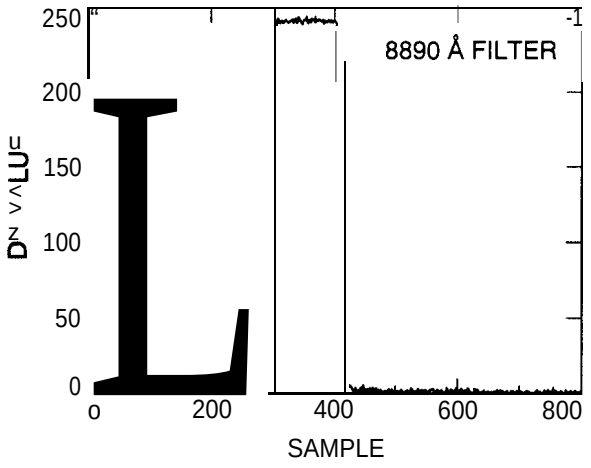

Figure 3-180. Navigation target trace through "Planet", 8890 A filter

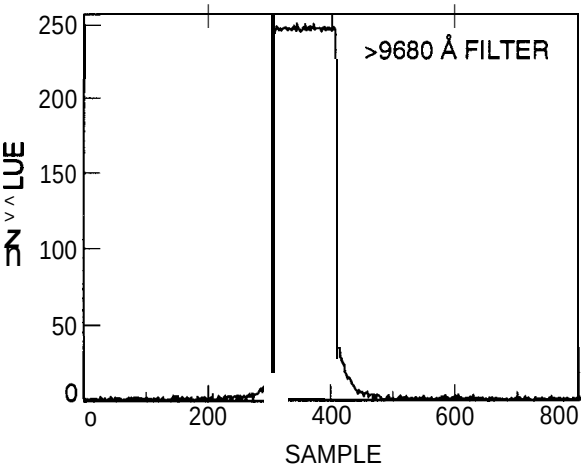

Figure 3-181. Navigation target trace through "Planet", >9680 A filter

Using these data, a model was developed which can be used to predict scattered light from a source of any size and illumination. A unique scattering function was created for each filter that describes the attenuation of the illumination on a single source pixel as a function of distance from the source pixel. The scattered light expected from an individual pixel is obtained by multiplying the attenuation factor (for the distance between that source pixel and the point at which the scattered light is to be predicted) by the illumination at that pixel. To compute the scattered light expected from a complicated illuminated scene, contributions from individual source pixels are summed over the source area.

Construction of the attenuation curves was accomplished by using point spread function approximations derived from MTF data for the distance range between 0 and 2 pixels for each separate filter (see Sec. IV.B) and data from the pre-launch Utah State off-axis calibration for distances beyond approximately 1000 pixels for all ***filters (see*** Reference 1). Intermediate points on these curves were determined as follows. For each filter, a best guess curve was used to predict the scattered light expected in the pre-launch navigation and knife edge calibration images. This was done by mathematically modeling the shapes of the illuminated source areas in the images and then summing the expected scattered light contributions from each illuminated pixel at a particular location in the non-illuminated portion of the frame. It was assumed that the scattering is radially symmetric about each source pixel, and a mean value was used for the illumination over the source areas. The attenuation curve for each filter was then iteratively modified until it correctly predicted scattered light for both navigation target and knife edge frames to within a factor of 2 of the scattered light measured. Therefore, these models should predict scattered light to within a factor of 2 for each filter. The attenuation curves are shown in Figures 3-182 through 3-184. Upon the availability of in-flight scattered light data, it will be possible to refine these rough models.

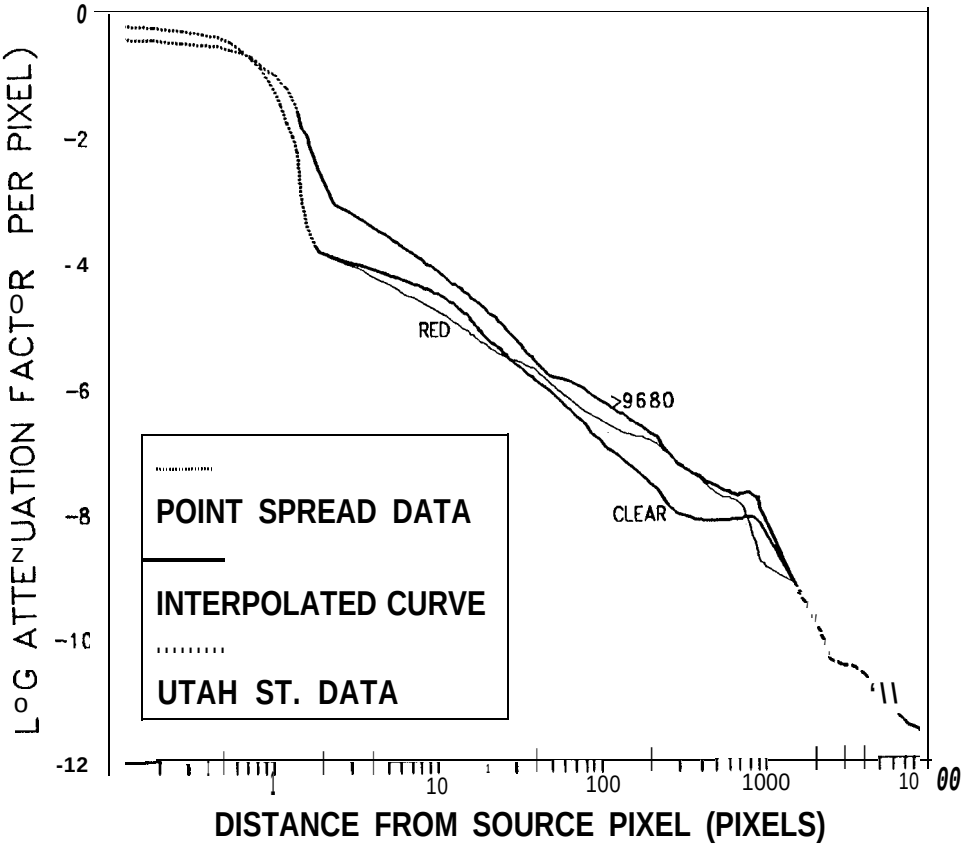

Figure 3-182. Scattered light attenuation models for clear, red, and >9680 A filters

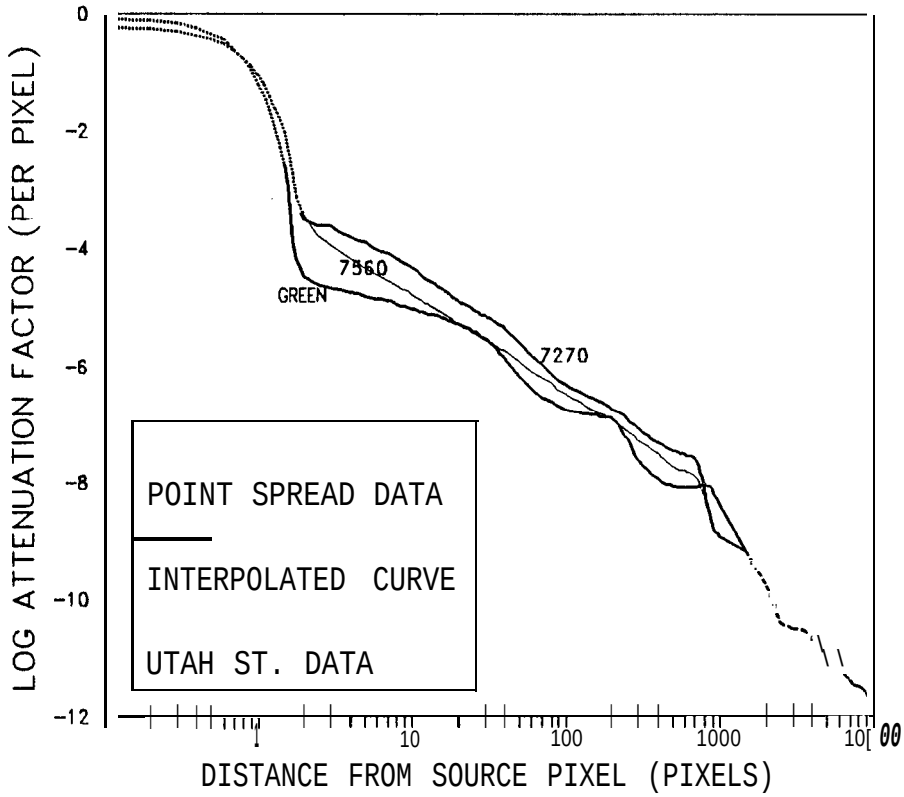

Figure 3-183. Scattered light attenuation models for green, 7270 A, and 7560 A filters

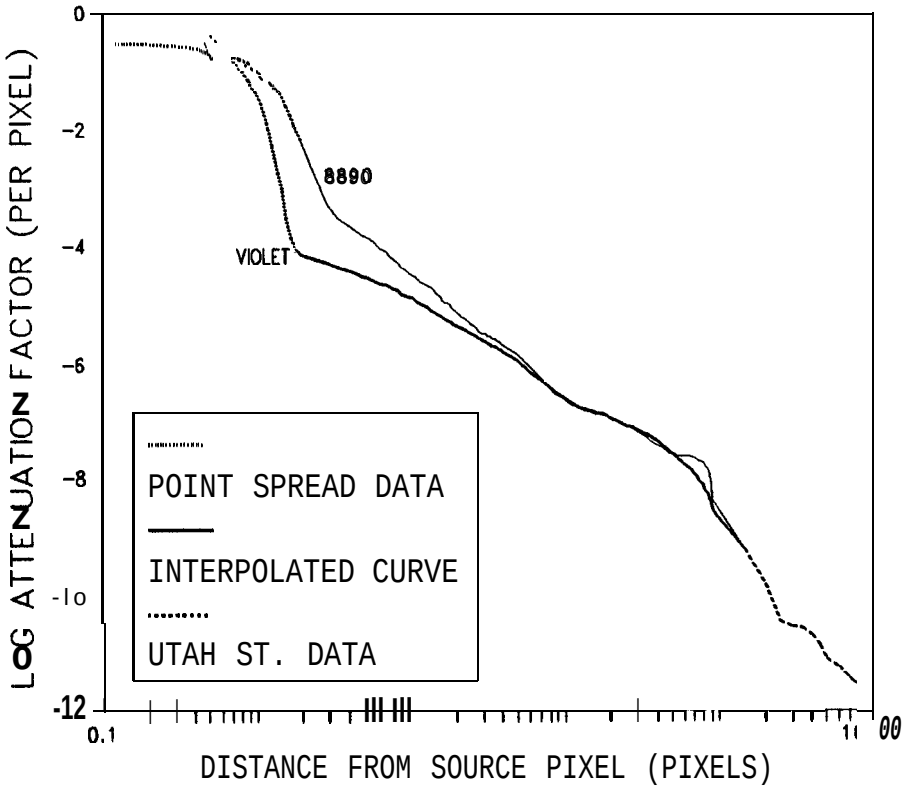

Figure 3-184. Scattered light attenuation models for violet and 8890A filters

Horizontal MTF wide-bar images were acquired through the MVM collimator at room temperature through all eight filters with the optics cover on and with the cover off. This allowed direct measurement of the effects of the optics cover on scattered light. The cover-on images show a 20-25 pixel wide response pedestal within the dark bars just to the left of the right-hand bright edge in the violet and >9680 A filters, and possibly also in green but at a much lower level. Corresponding cover-off images do not exhibit such a pedestal. Figures 3-185 and 3-186 compare the cover-on and cover-off response for the violet and >9680 A filters, respectively, by plotting a 15-line average horizontal trace along the right-hand end of a selected dark bar of the horizontal MTF target. These curves represent the ratio of raw DN to the peak signal. The peak signals in each case have been normalized to 100. Beyond 25 pixels from the bright edge, the cover-on curves match the background of the cover-off curves. However, for both filters, an elevated pedestal is apparent above the background level for approximately 20 to 25 pixels from the edge. The amplitude of increased response appears to be approximately 2% of the peak signal for both filters. Pedestals in the other filters are not apparent in similar line traces.

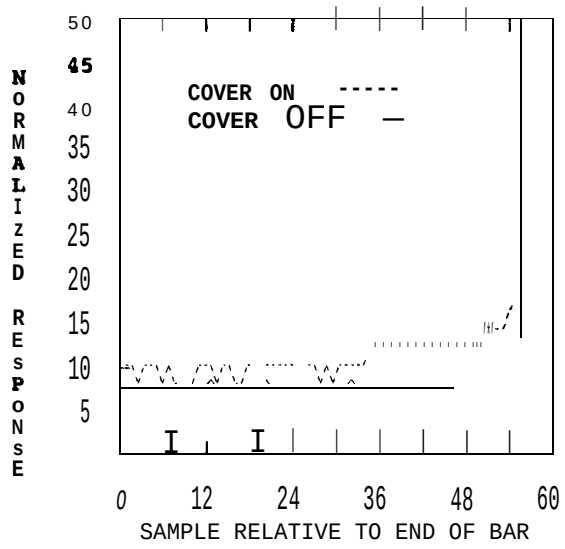

Figure 3-185. MTF bar response - cover on Vs. cover off (violet)

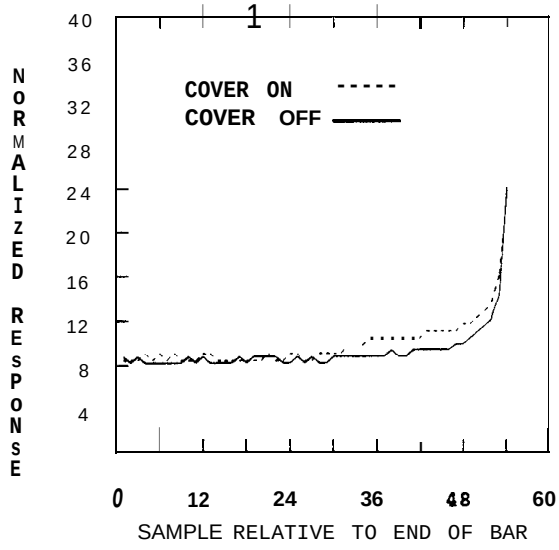

Figure 3-186. MTF bar response - cover on vs. cover off (>9680 A)

The specular reflectance of the CCD and optics cover (Figure 3-187 and Figure 3-188, respectively) are significant in the violet and l-micron regions. From these curves, it would be reasonable to attribute the observed pedestal to an offset ghost image due to specular reflectance between the CCD and the cover that is seen most strongly in the violet and >9680 A filters. Given the CCD and cover spectral reflectance the expected amplitude of a ghost would be about 2% of the primary signal in violet and about 4% at 1 micron. In other filters, the expected ghost amplitude would be about 1%.

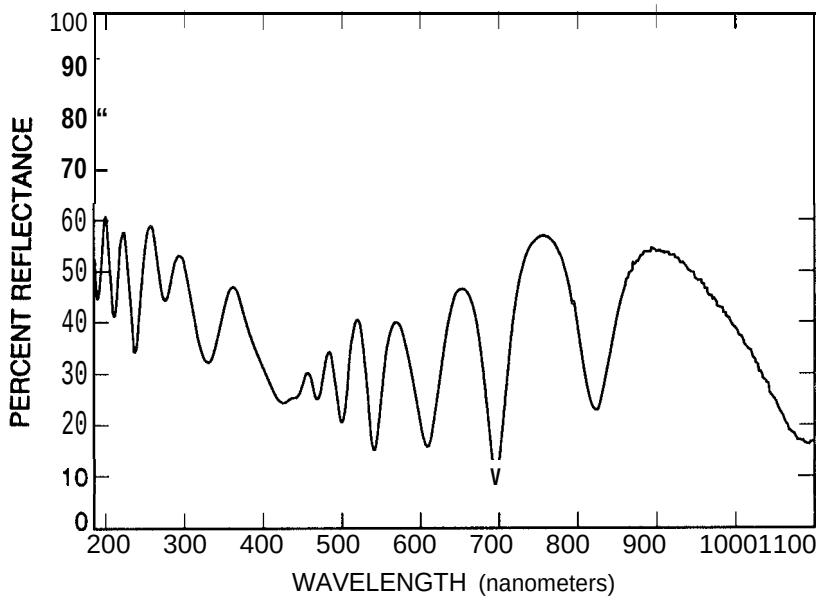

Figure 3-187. Specular reflectance of the CCD

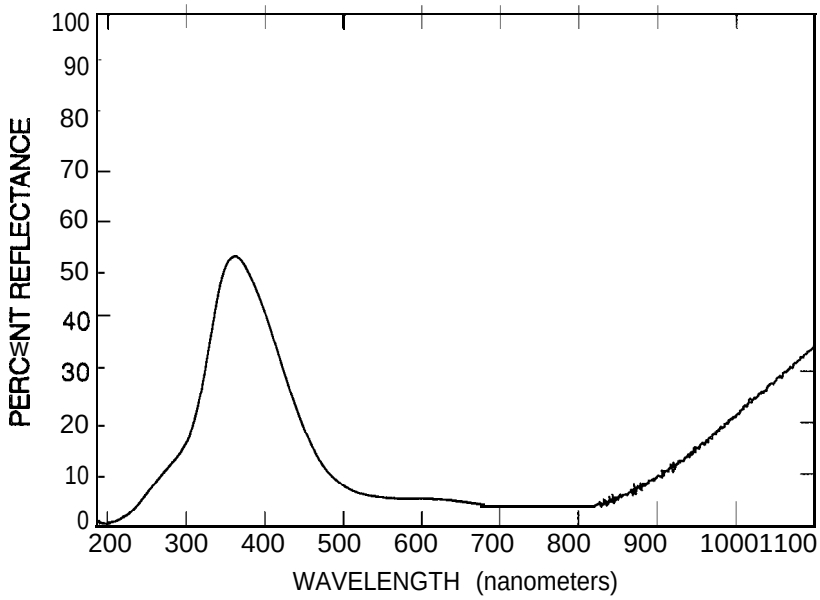

Figure 3-188. Specular reflectance of the optics cover

Section IV - Spatial Resolution

A. MTF

In 1989, wide-bar MTF target images were collected with the camera in the thermal vacuum chamber at the nominal temperature of +8° C. Images were processed and MTF curves obtained for full-resolution-mode images in gain state 2 (100K) of the horizontal bar target through all eight filters and of the vertical bar target through the clear filter. Summation-mode images were also acquired of the target in both orientations through the clear filter in gain state 1 (400K), and in the vertical orientation with the green filter in gain state 4 (10K). The images taken with filters I-7 were l/2-full well exposures, the images through the clear filter were 2/3-full well, and the green summa

tion images were <1/3-full well. Additionally, low signal (<10,000 electrons) level, full-resolution-mode images were also acquired through the green filter in gain state 4 (1OK) of the vertical and horizontal targets at three different exposure settings each.

Data products included photographic prints of images, line traces, and plots of MTF and phase curves as a function of spatial frequency. Plots of MTF amplitude and phase for selected frames are shown in Figures 4-1 through 4-8. The theoretical diffraction-limited SSI MTF, assuming perfect focus and a perfect CCD is shown for comparison for the clear, green, and >9680 A filters in Fiqures 4-1, 4-3, and 4-4. The MTF values at the Nyquist frequency for all images are tabulated in Table 4-1.

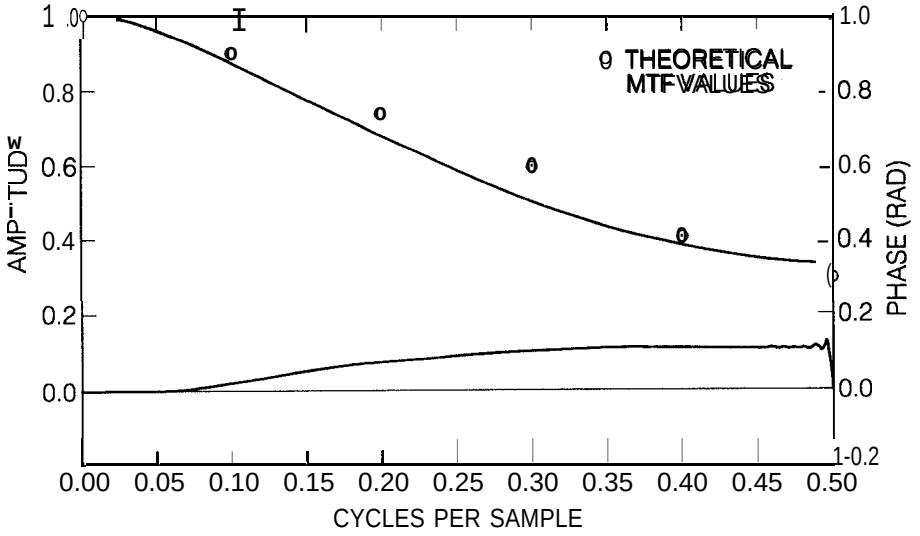

Figure 4-1. Horizontal-bar MTF amplitude and phase from an image through the clear filter with 6 l/4-ms exposure time, gain state 2, normal mode.

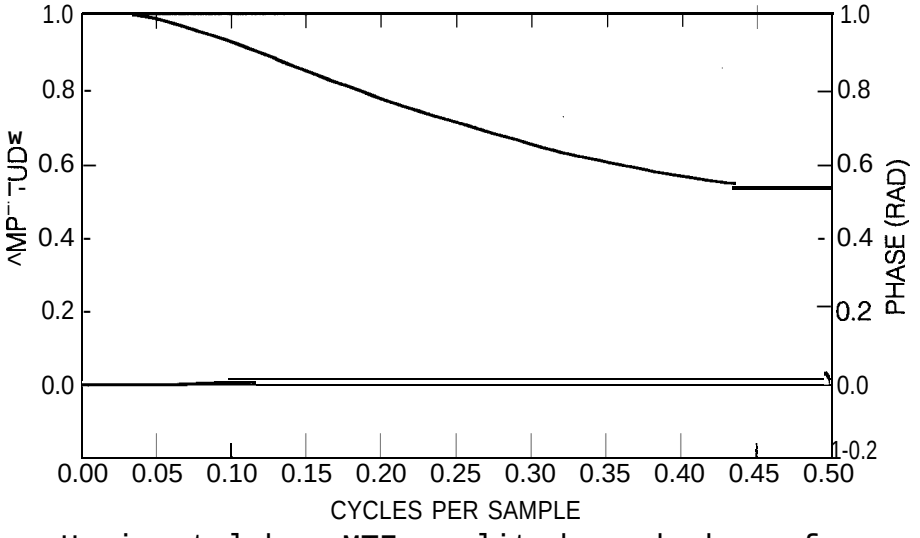

Figure 4-2. Horizontal-bar MTF amplitude and phase from an image through the violet filter with 133 l/3-ms exposure time, gain state 2, normal mode.

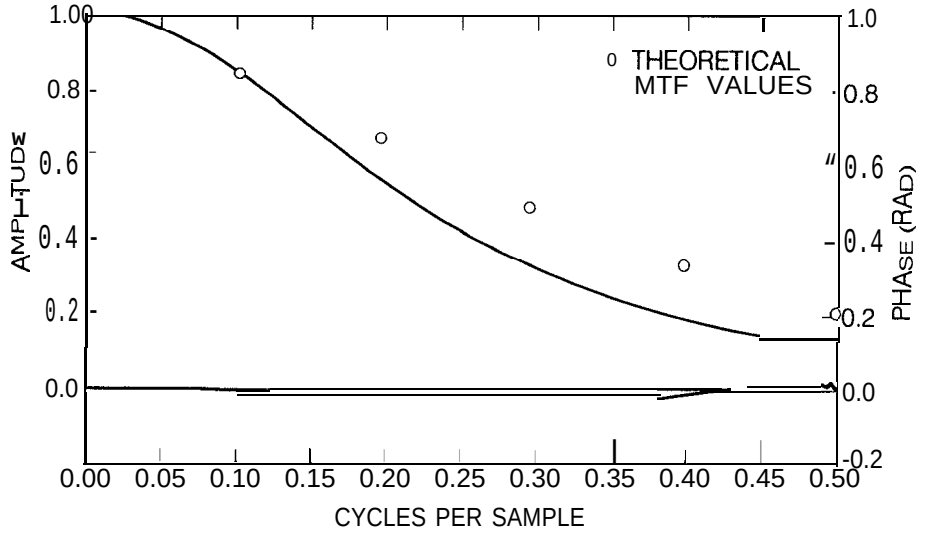

Figure 4-3. Horizontal-bar MTF amplitude and phase, >9680 A filter, 100-ms exposure time, gain state 2, normal mode.

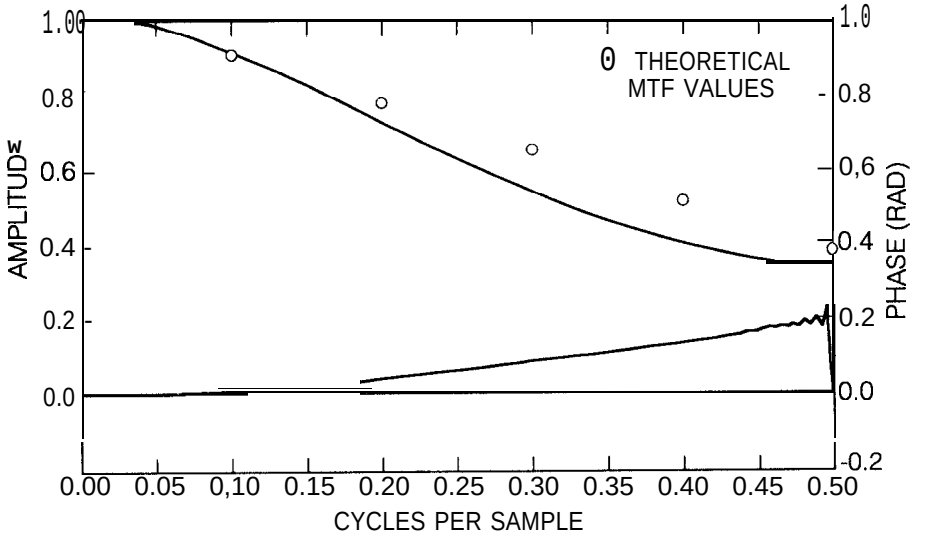

Figure 4-4. Vertical-bar MTF amplitude and phase, green filter, 50-ms exposure time, gain state 4, normal mode.

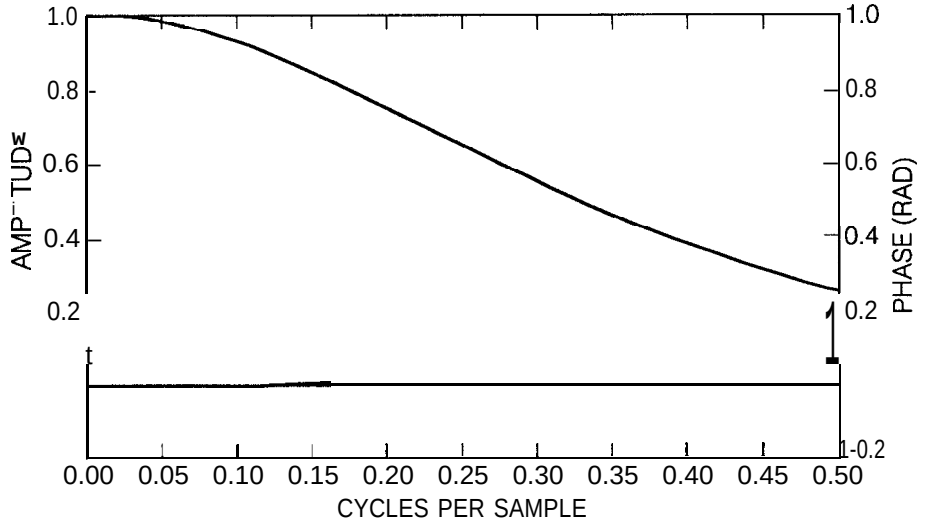

Figure 4-5. Vertical-bar MTF amplitude and phase, green filter, 4 l/6-ms exposure time, gain state 4, normal mode.

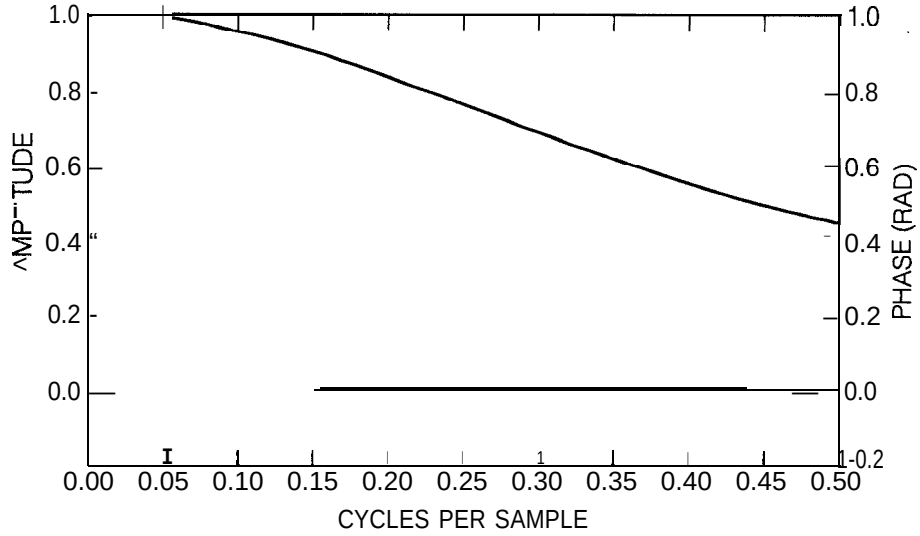

Figure 4-6. Horizontal-bar MTF amplitude and phase, green filter, 4 l/6-ms exposure time, gain state 4, normal mode.

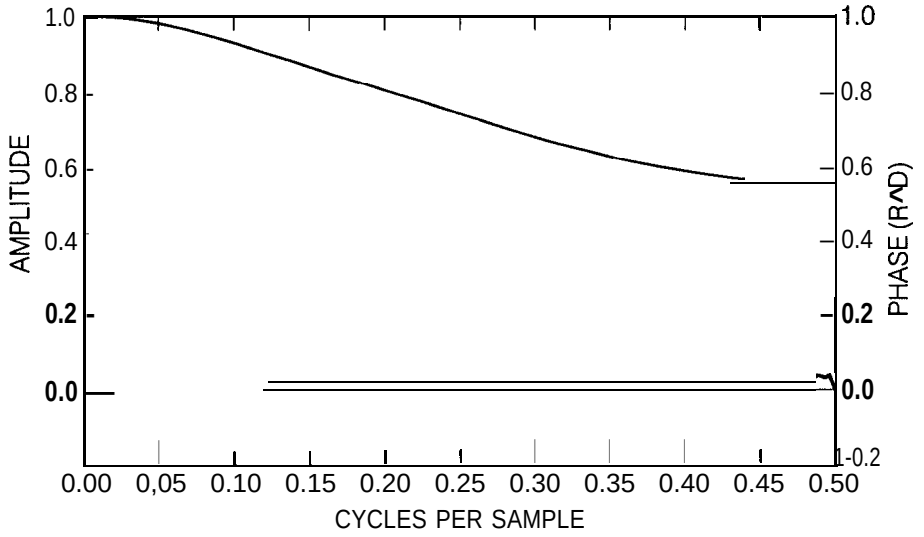

Figure 4-7. Horizontal-bar MTF amplitude and phase, clear filter, 6 l/4-ms exposure time, gain state 1, summation mode.

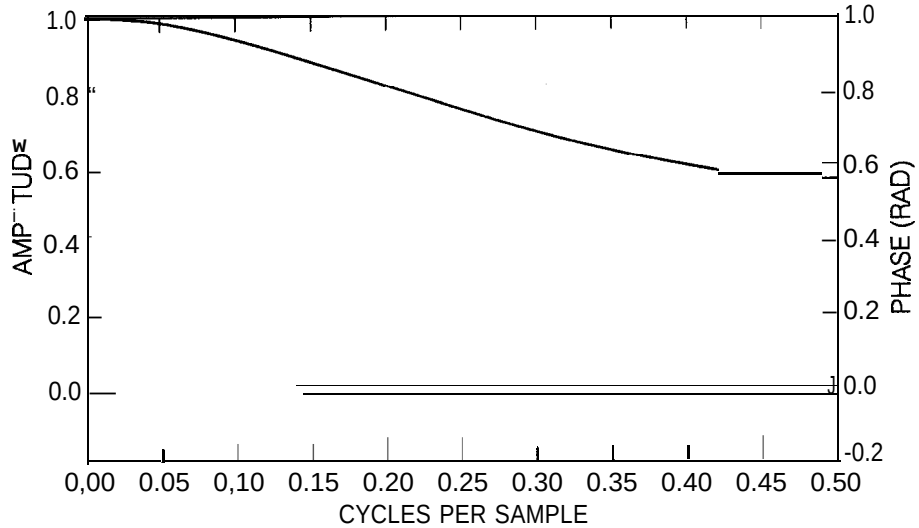

Figure 4-8. Vertical-bar MTF amplitude and phase, clear filter, 6 l/4-ms exposure time, gain state 1, summation mode.

Table 4-1. Modulation Transfer Function at Nyquist frequency for the nominal +8° C data set.

target orient. (V/H)	filter	mode	gain	exposure (msec)	approx. signal level (1000 e-)	MTF at Nyquist
v	clear	NORM	2	6.25	84	0.252
H	clear	NORM	2	6.25	85	0.328
H	violet	NORM	2	133.33	50	0.518
H	green	NORM	2	6.25	68	0.381
H	red	NORM	2	4.16	86	0.309
H	7270 A	NORM	2	16.67	58	0.269
H	7560 A	NORM	2	12.50	71	0.264
H	8890 A	NORM	2	133.33	38	0.077
H	>9680 A	NORM	2	100.00	27	0.129
v	green	NORM	4	50.00	9	0.328
v	green	NORM	4	12.50	2	0.332
v	green	NORM	4	4.16	1	0.256
H	green	NORM	4	50.00	9	0.346
H	green	NORM	4	12.50	2	0.320
H	green	NORM	4	4.16	1	0.450
H	clear	SUM	1	6.25	345	0.544
v	clear	SUM	1	6.25	318	0.556
v	green	SUM	4	4.16	1.3	0.496
v	green	SUM	4	8.33	4.2	0.712

The following observations are noted regarding the effects of signal level, target orientation (horizontal or vertical), filter, and mode (full-resolution or summation) on MTF and phase shift:

a) The effect of low signal levels (<l0,000e-) on MTF was studied only for the green filter. In the full-resolution mode, there is no 'obvious trend in vertical bar or horizontal bar MTF as a function of signal level, but in the summation mode, the vertical bar images show a significant increase in MTF with increasing signal.

b) In the full-resolution mode, horizontal bar MTF is slightly higher than the vertical bar MTF in the clear filter (2/3 full-well) images and moderately higher in the green filter (< 1/3 full-well) images. In summation mode, the MTF is about the same for the vertical and horizontal bar clear filter images.

c) Consistent with earlier data sets, the horizontal-bar MTF degrades with longer wavelength filters. At the Nyquist frequency this degradation amounts to a factor of 4 (as compared to a factor of 2 in the 1985 data) between the violet and >9680 A filters in the +8° data set. The only exception to this trend is the 8890 A filter which has an MTF lower than expected.

d) In the full-resolution mode there is some variation but no definite trend in the vertical bar phase shift with signal level, whereas in the vertical bar summation images, phase shift is larger with increasing exposure. The horizontal bar phase shift does not change significantly with signal level in the full-resolution mode.

e) There is no apparent trend in phase shift in a comparison of the vertical and horizontal bar images in full-resolution-mode. Horizontal and vertical-bar images in summation mode have similar phase shift amplitudes but the signs are opposite.

f) There is no significant effect of the phase shift in the horizontal-bar images with change in filter.

g) MTF in the summation mode is generally worse than in the full-resolution mode at half the summation mode spatial frequency. However, the summation mode has significantly better MTF than full-resolution mode at equivalent cycles/sample.

h) The theoretical MTF calculations tend to be slightly higher than the measured results for the clear, >9680 A, and green filters. Possible reasons for this are addressed below.

The 1989 MTF values at Nyquist frequency are compared with MTF data acquired previously in 1985, 1984, and 1983 in Table 4-2. With the exception of the 1985 data set, the MTF appears to improve with each subsequent data set. A possible explanation for the increased MTF values may have to do with refinement in the calibration technique over the years. In the 1983 and 1984 +10° C data sets, no attempt was made to refocus the collimator. In 1985, for the +8° C data set, the collimator was focused so as to maximize the SSI MTF response under room-temperature ambient conditions. It was assumed that this focus setting would remain optimum even with the SSI cooled to its operating temperature in the thermal vacuum chamber, an assumption that does not seem to have been valid. The 1985 data deviates obviously from the trend of increasing MTF. In 1989 the collimator was refocused at each temperature to maximize the MTF and to compensate for thermally induced focus shifts due to the thermal vacuum chamber window. These values are by far the highest obtained. Accuracy in the MTF measurements can also be affected by other factors in the calibration environment, such as vibration? thus these data represent a lower limit on the resolution obtainable with the SSI.

Table 4-2. Variations in MTF at Nyquist frequency

		1983	1984	1985	1989
clear	H	0.187	0.197	0.072	0.328
clear	V	00112	0.123	0.104	0.252
violet	H	0.261	0.251	0.138	0.518
green	H	0.213	0.192	0.112	0.380
red	H	0.181	0.187	0.090	0.309
7270 A	H	0.101	0.139	0.094	0.269
7450/7560	H	0.107	0.160	0.134	0.264
8890 A	H	0.128	0.128	0.096	0.077
>9680 A	H	0.096	0.091	0.058	0.129

Images of the horizontal-bar target were obtained in 1989 for each filter in gain state 2 at temperatures of -10° C and +18° C, in addition to the +8° C set. This permitted a study of temperature effects on MTF. The temperature-dependence of MTF is illustrated in Table 4-3. As in the 1983 calibration data, MTF improves with shorter wavelength for all temperatures studied. In the 1983 calibration it was also observed that as the temperature departs from nominal, the horizontal-bar MTF decreases at short wavelengths, and increases at longer wavelengths. This trend is also evident in the 1989 data at values which are larger than the measurement uncertainty; in fact, there are larger percent changes in the 1989 Nyquist-frequency data than in the 1983 data.

Table 4-3. Modulation transfer function variability with temperature

	MTF at Nyquist freq.			Percent Change -10° to +8°		Percent Change +8° to +18°	
Filter	-10°	+8°	+18°	Nyq .	Int. *	Nyq.	Int.
violet	0.305	0.518	0.438	+69.84	+43.61	-18.26	-12.63
green	0.316	0.381	0.382	+20.57	+10.94	+0.26	-2.02
red	0.275	0.309	0.311	+12.36	+9.77	+0.65	-0.07
7270 A	0.262	0.269	0.241	+2 .67	-0.85	-11.62	-3.31
7560 A	0.267	0.264	0.238	-1.14	+3.22	-10.92	-5.34
8890 A	0.166	0.077	0.180	-215.58	-49.08	+233.77	+56.60
>9680 A	0.134	0.129	0.130	-3.88	+1.40	+0.76	+1.41

(*) The columns labeled "Int." represent the percent change in the integrated MTF over frequency values from 0.25 to 0.48 cycles per sample.

To study the quality of resolution of the instrument at low light levels, the data also included a set of slant-bar target images through the green filter at eight different exposures in the full-resolution mode and two exposures in the summation mode, and two full-resolution clear filter images in 100K gain state at different exposure levels. Examples of the full-resolution images (contrast enhanced) are shown in Figures 4-9 and 4-10. These data show that the instrument continues to resolve at spatial frequencies of at least 0.4 cycles/sample at the lowest exposure, in which the highest raw DN value in the image is less than 16 DN (approximately 600 e-). This is comparable to the spatial resolution seen in the 1985 slant bar images. In the summation mode (Figure 4-11) , the resolution is slightly degraded with a maximum spatial resolution of 0.3 cycles/sample in both exposures.

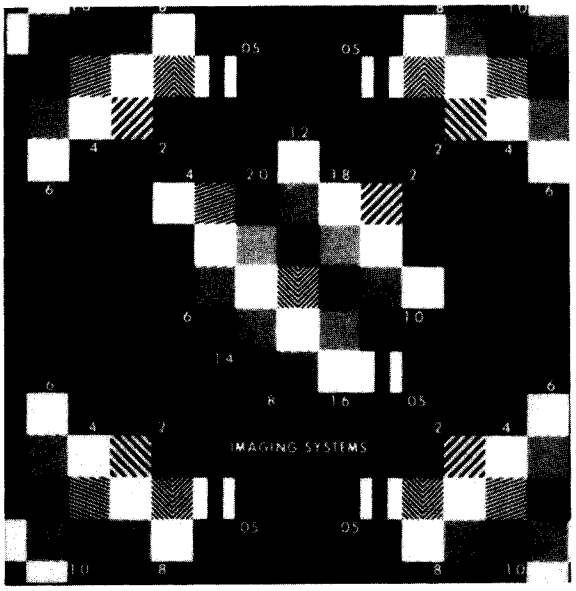

Figure 4-9. Contrast-enhanced full-resolution mode image of the slant-bar target in gain state 4 through the green filter with an exposure time of 50 ms.

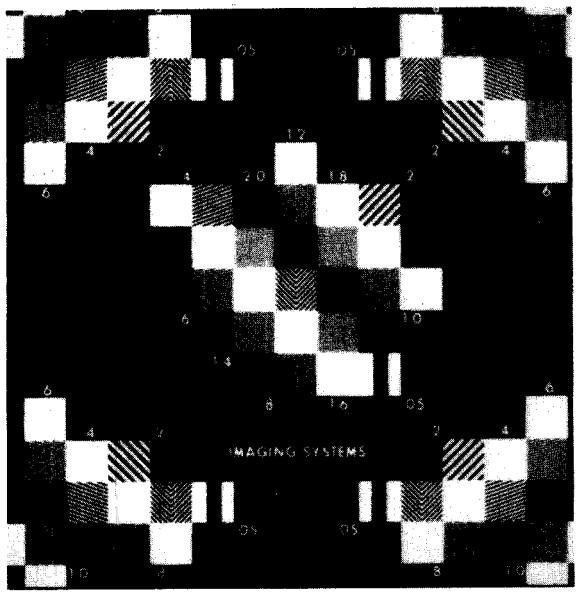

Figure 4-10. Contrast-enhanced full-resolution mode image of the slant-bar target in gain state 4 through the green filter with an exposure time of 4 1/6 ms.

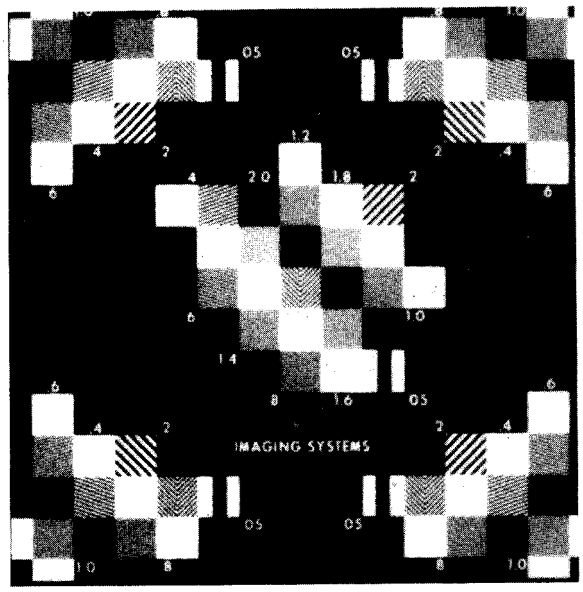

Figure 4-11. Contrast-enhanced summation-mode image of the slant-bar target in gain state 4 through the green filter with an exposure time of 4 1/6 ms.

B. Point Response Function

Images of the point response function target were acquired through the clear filter at five different exposure levels ranging from approximately 1/5 of full well to full well. These images were taken in both the full-resolution and the 2x2 pixel summation modes. The target contains 14 10-micron diameter pinholes that approximate point sources for the SSI.

The mean and standard deviation (sigma) of the DN distribution in both the line and sample directions were calculated for each pinhole in each image. For the full-resolution images, the sigma in the vertical direction ranged between 0.63 and 0.97 with a mean value of 0.78 pixels. In the horizontal direction, sigma ranged between 0.62 and 1.03 with a mean value of 0.86 pixels. The larger mean sigma in the horizontal direction was investigated by plotting the horizontal sigma for each pinhole vs. the sample number of the pinhole image (Figure 4-12). Note that the horizontal sigma value is measurably smaller for samples at 100 than it is for samples at 240 and above. No such variation in sigma is seen in the vertical direction as a function of line

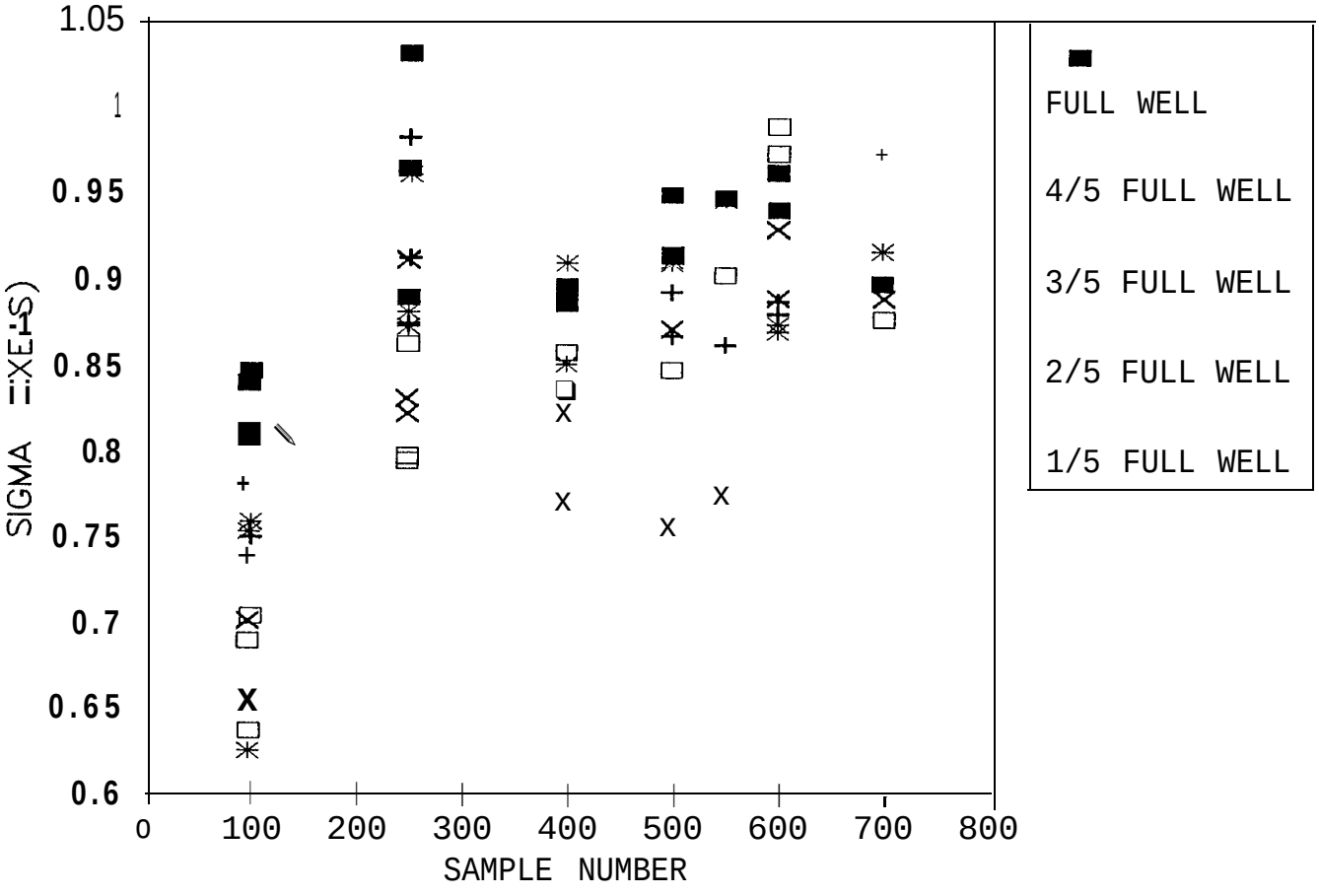

Figure 4-12. Standard deviation in the horizontal charge distribution of pinhole images vs. sample number of pinhole.

number. The symmetry of the point response function was investigated by comparing a sigma calculated using only pixels to the left of (or above) the center of the response profile to one calculated using only pixels to the right (or below) the center. While no asymmetry appeared in the vertical direction, the sigma on the right was significantly larger than that on the left for pinholes imaged ay about sample 240 and above, as illustrated in Figure 4-13. At sample numbers around 100, the horizontal sigma ranged between 0.63 and 0.85 with a mean value of 0.74 pixels, showing good symmetry with the vertical sigma. However, for sample numbers around 240 and above, the horizontal sigma ranged between 0.76 and 1.03 with a mean of 1.00 pixels. These results suggest that some type of charge transfer problem is occurring in the serial register somewhere between sample 100 and sample 240. The anomalous column 170 seen in the flat-field images (see Section III.B.6) may be the location of some type of charge trap that causes the charge distribution to be spread out in the trailing direction as charge is transferred through that location.

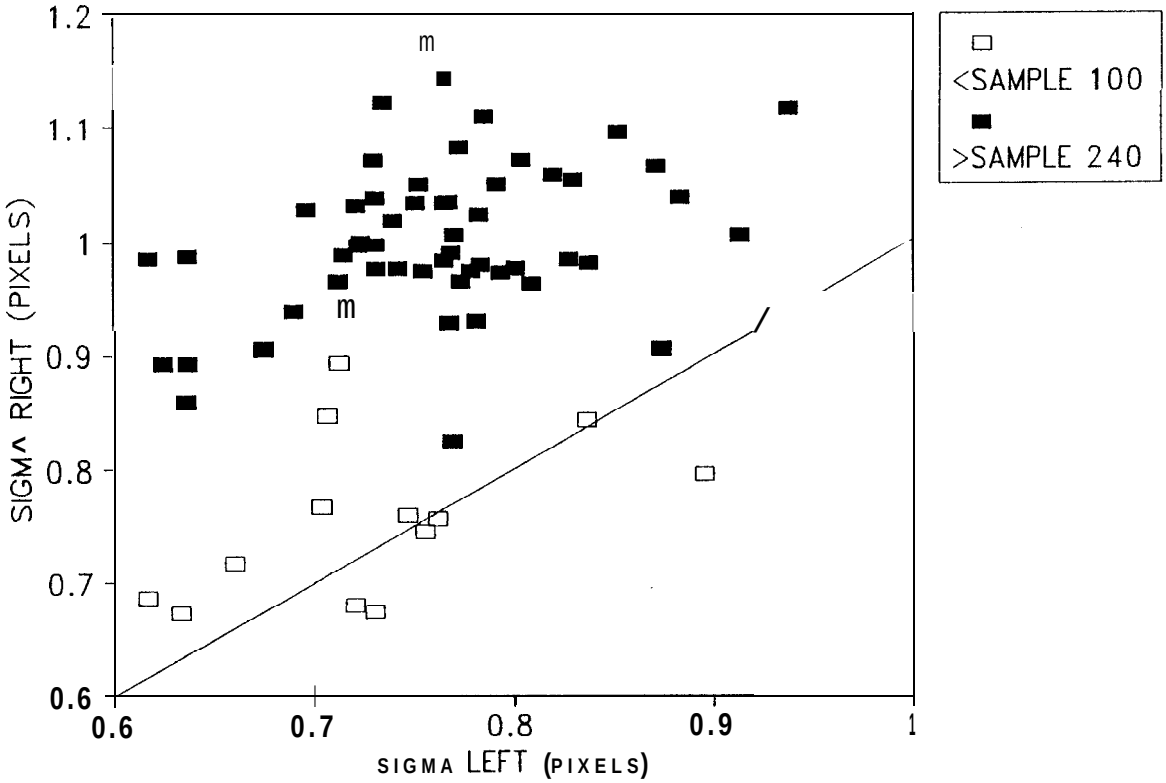

Figure 4-13. Horizontal line spread function symmetry evaluation.

Figure 4-14 shows a plot of the vertical line spread function. The fraction of the total charge in the point image that is contained in each line and summed over all columns is plotted against the position of the line relative to the center of the charge distribution. Note that a line positioned exactly on the

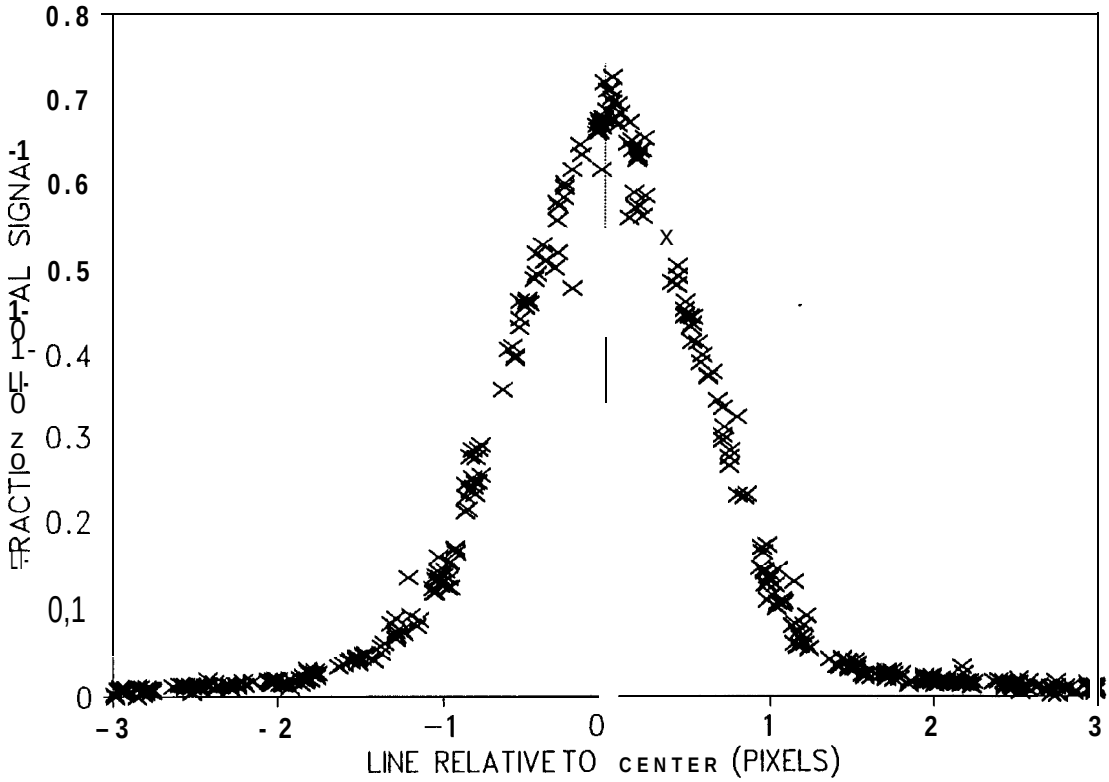

Figure 4-14. Vertical line spread function plotted on a linear scale.

center of the point image will contain about 0.7 of the total charge in the image. Figure 4-15 plots the same data on a log scale so as to allow better visibility into the character of the wings of the line spread function. Beyond two line widths from the center of the image, the signal within a line becomes so low that the measurement becomes corrupted by background noise. Noise at the +1 DN level located in the wings becomes indistinguishable from real signal; therefore, the values plotted beyond two lines from the center probably represent upper limits to the real line spread function. Values of zero cannot be plotted on the log scale; zero values occur for lines as close as 2.8 pixels from the center. An empirical fit to the central core of the vertical line spread function, l(y), is also plotted in Figure 4-15. The equation for this fit is

$$\text{in } l(y) = \ln(.7) - 1.5y^2.$$

Figures 4-16 and 4-17 show similar plots for the horizontal line spread function. The differences between the horizontal line spread function shapes for samples below column 100 and those above column 240 are readily apparent. Above column 240, the function appears asymmetric, with its peak displaced slightly left of the mean and with an elevated wing response to the right of the center. This elevated response contains roughly 1% of the total charge indicating that somewhere between about 500 and 2500 e^- of charge is being deferred. Zero values occur for samples as close as 2.7 pixels from the center except on the right of points above column 240 where zero values are never closer than 4.7

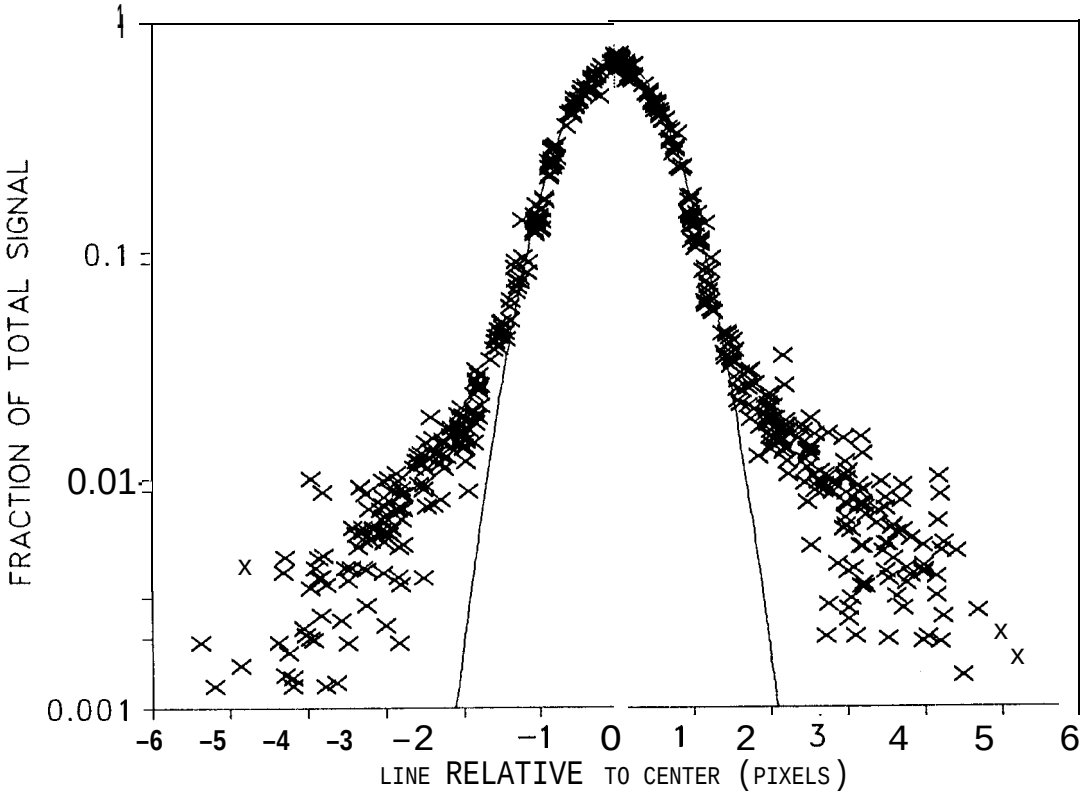

Figure 4-15. Vertical line spread function plotted on a logarithmic scale.

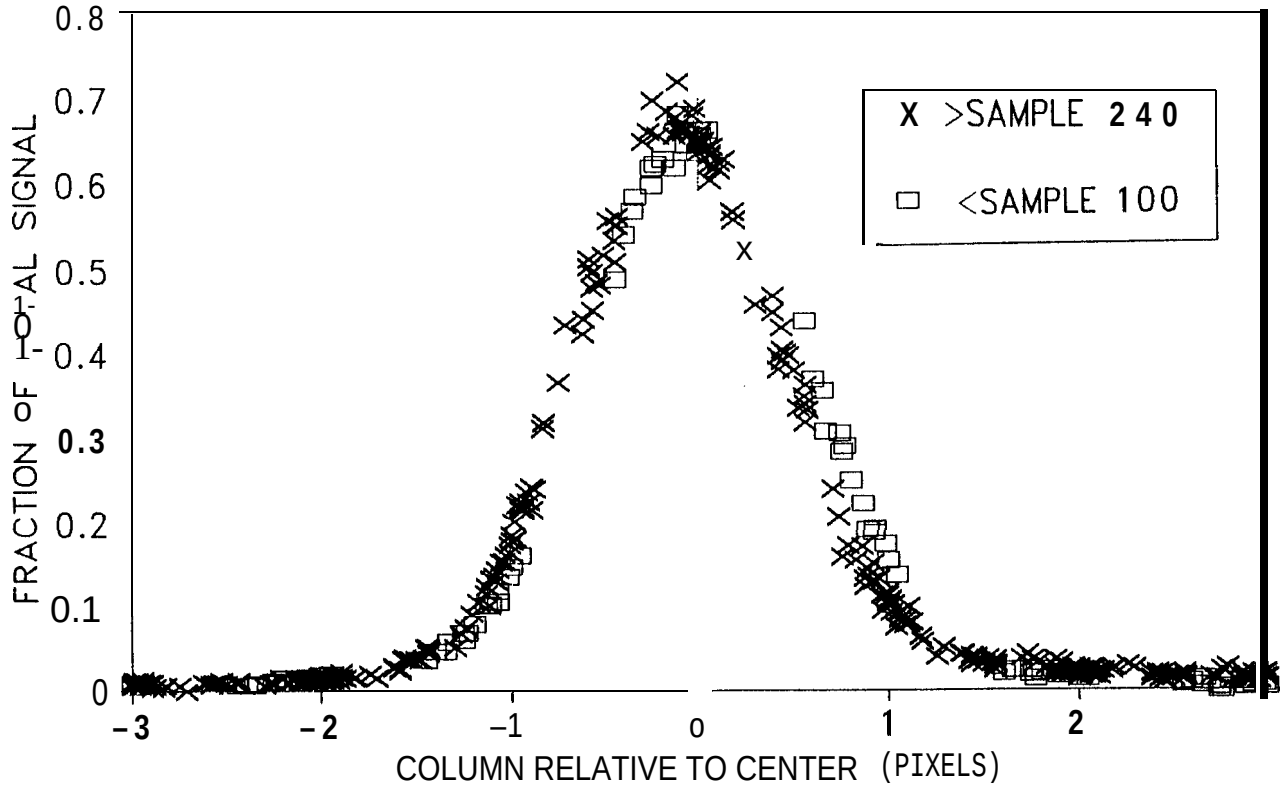

Figure 4-16. Horizontal line spread function plotted on a linear scale.

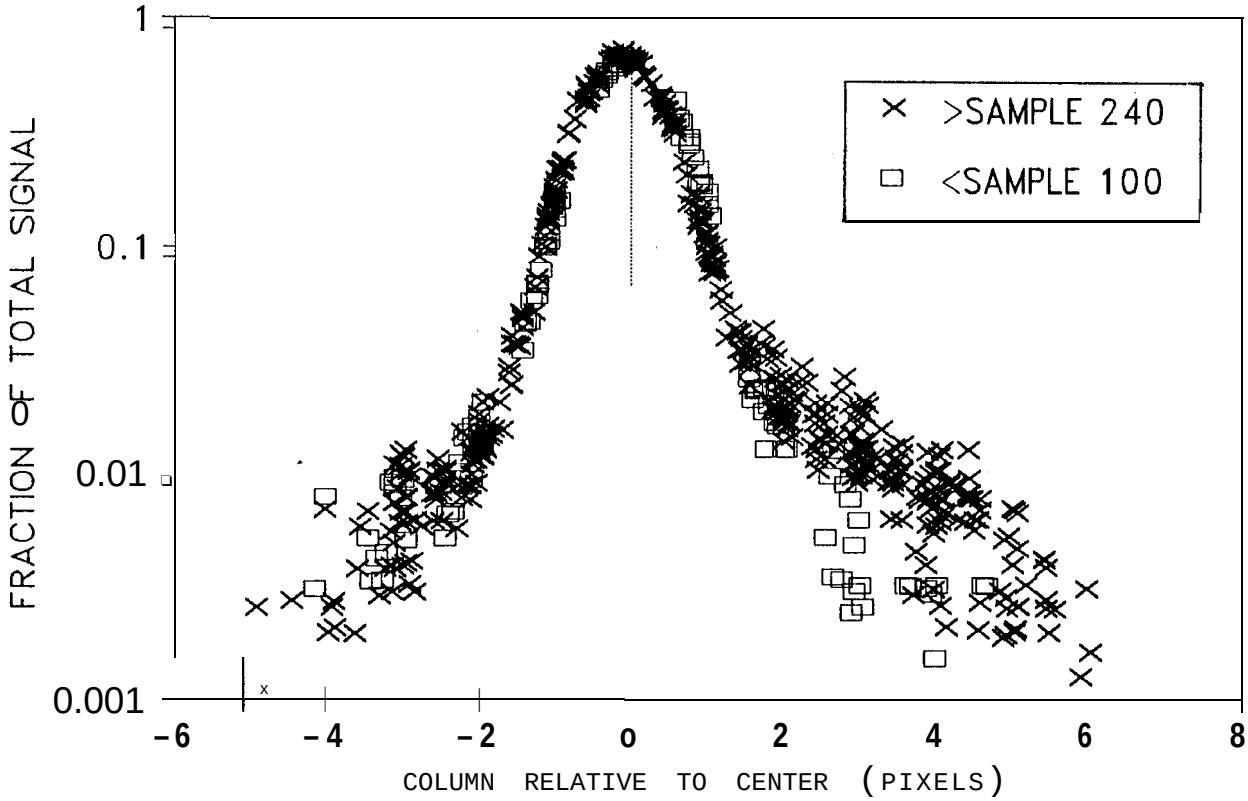

Figure 4-17. Horizontal line spread function plotted on a logarithmic scale.

pixels from the center. The deferred charged must, therefore, be nearly all released within not more than two additional pixel shifts. Figure 4-18 shows the horizontal line spread function

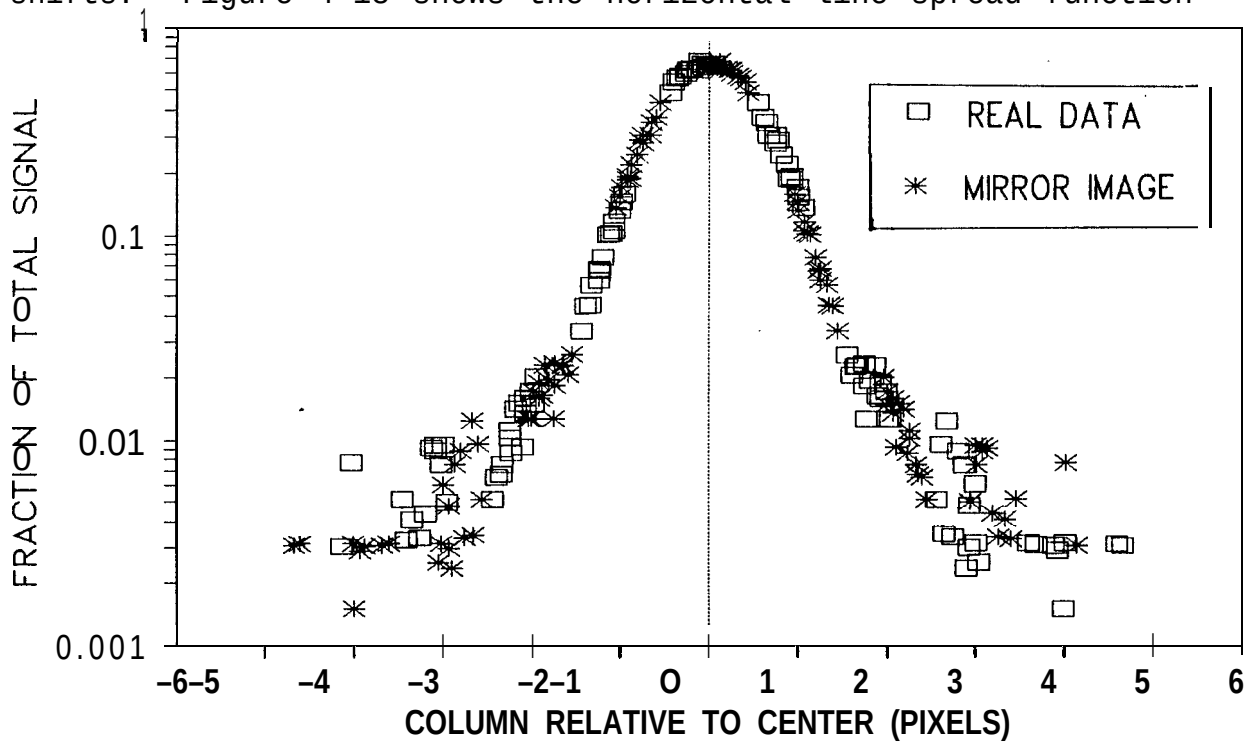

Figure 4-18. Horizontal line spread function based only on points below sample 100 plotted on a logarithmic scale.

based only on points in columns below 100. The real measurements have been mirrored about the mean to generate a continuous curve. This curve shows good symmetry and agrees nicely with the vertical line spread function.

An MTF value can be derived from the empirical fit to the vertical line spread function plotted in Figure 4-15. The MTF at Nyquist frequency determined in this way is 0.20, which is somewhat lower than the value of 0.33 determined for the clear filter using the wide-bar target images and the value of 0.31 predicted theoretically for a diffraction-limited, perfectly focused SSI (Section IV.A). Figure 4-19 plots the theoretically predicted SSI line spread function along with the empirically determined fit to the measured line spread function. The measured function is somewhat wider than the theoretical prediction consistent with the corresponding lower MTF. Since the MTFs determined from wide-bar images are generally consistent with the theoretical predictions, the wider point spread function measured is most likely due to the fact that the pinholes in the target are approaching the geometric size of a pixel.

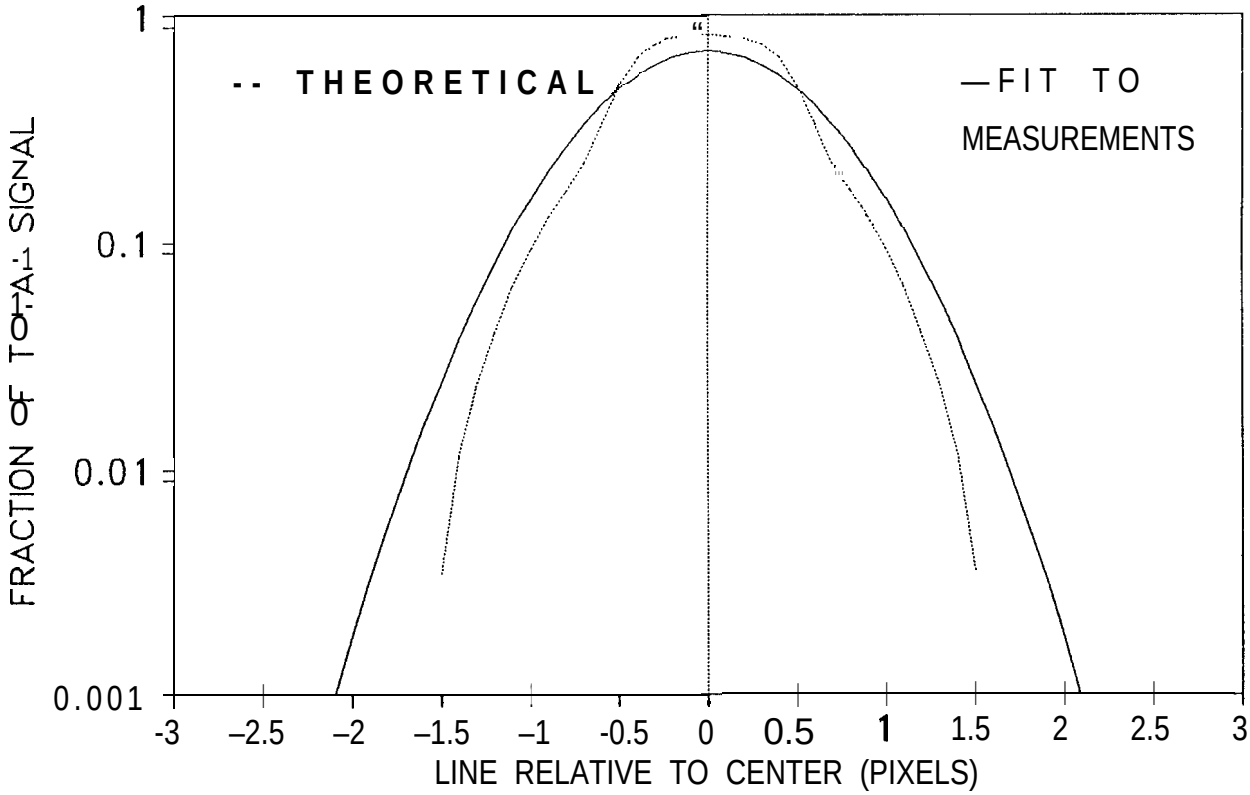

Figure 4-19. Comparison of theoretically predicted and measured line spread functions.

The measured point spread sigmas show a weak trend toward larger values at larger signal levels with the mean value increasing from about 0.70 pixels at 1/5 full-well signals to about 0.84 pixels at full-well (excluding horizontal measurements to

the right of center) . This effect is thought to be simply a result of the higher signal levels bringing more of the pixels in the wings up to the 1 DN detection threshold level rather than a real change in the shape of the point spread function with signal level. No dependence of the calculated sigmas on the exact location of the point image center within a pixel was seen.

For the summation-mode images, the effective pixel size relative to the optical point image is doubled. In addition, a lower gain state was used compared to the same exposure level in the full-resolution mode. These effects served to mask to a great extent the horizontal asymmetry seen in the full-resolution point spread data. No systematic differences were observed in the sigmas computed in any of the four directions. The summation-mode sigmas ranged between 0.25 and 0.69 with a mean value of 0.48 pixels. No variation in the computed sigma value was seen with signal level. Figures 4-20 and 4-21 show plots of the vertical line spread function in the summation mode. Zero values occur for lines as close as 1.2 pixels from the center.

Figures 4-22 and 4-23 show plots of the horizontal line spread function in the summation mode. Here evidence of the charge deferral in the horizontal direction can be seen in the

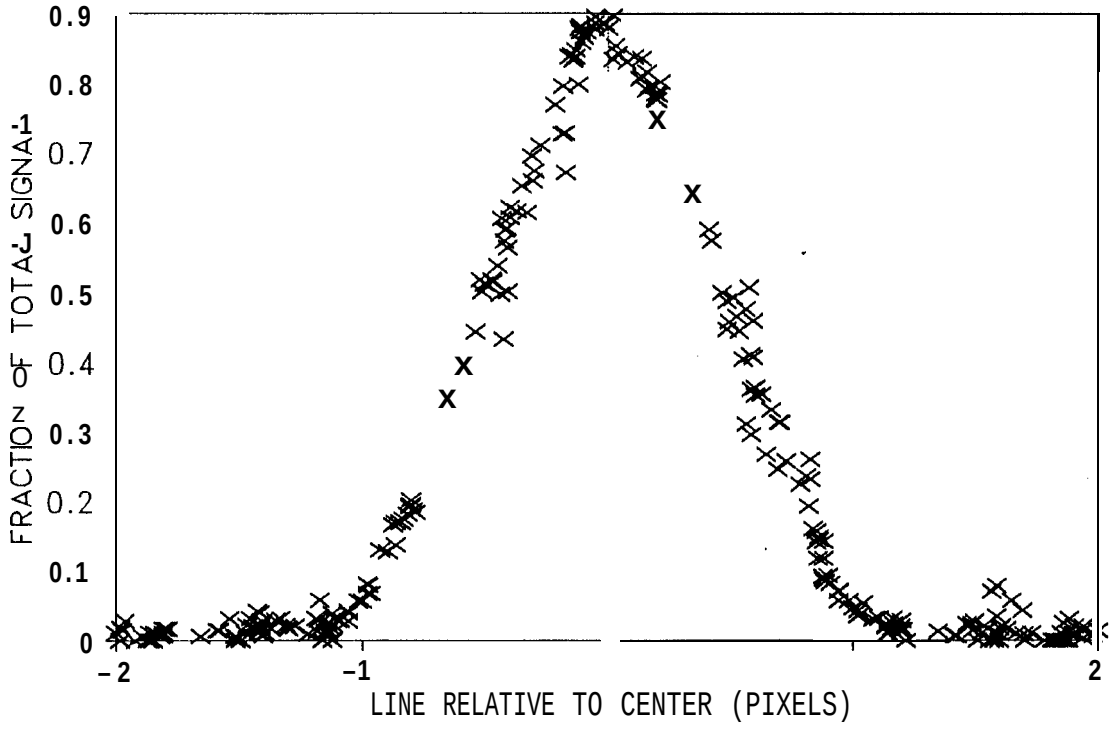

Figure 4-20. Summation-mode vertical line spread function plotted on a linear scale.

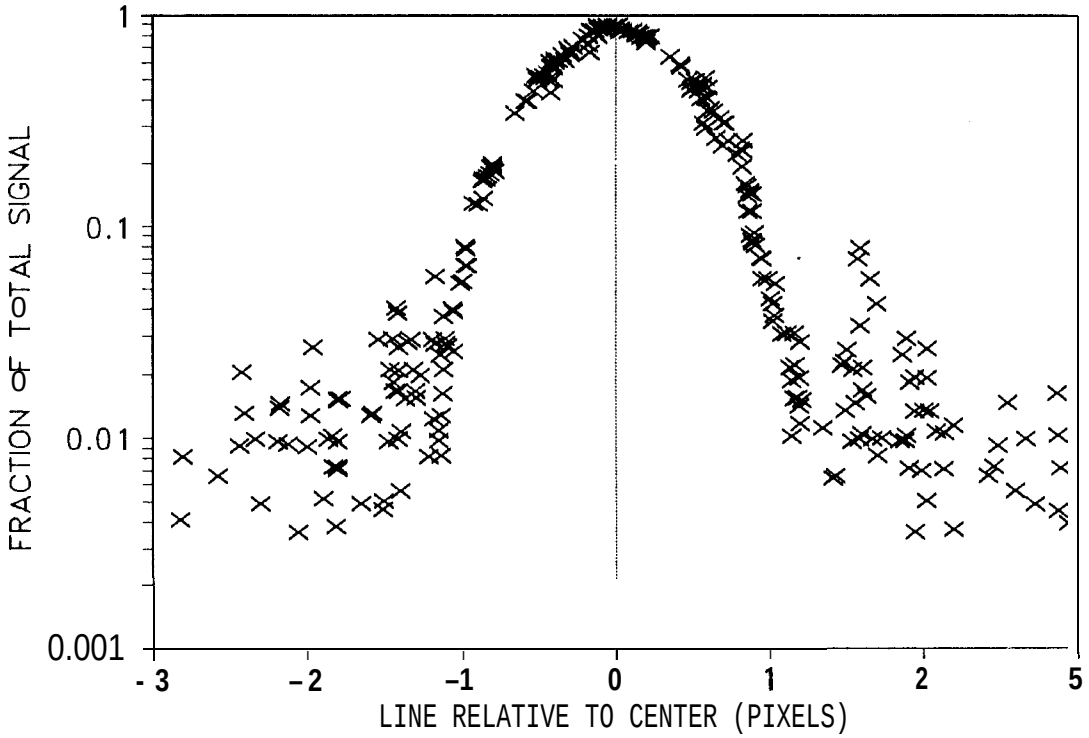

Figure 4-21. Summation-mode vertical line spread function plotted on a logarithmic scale.

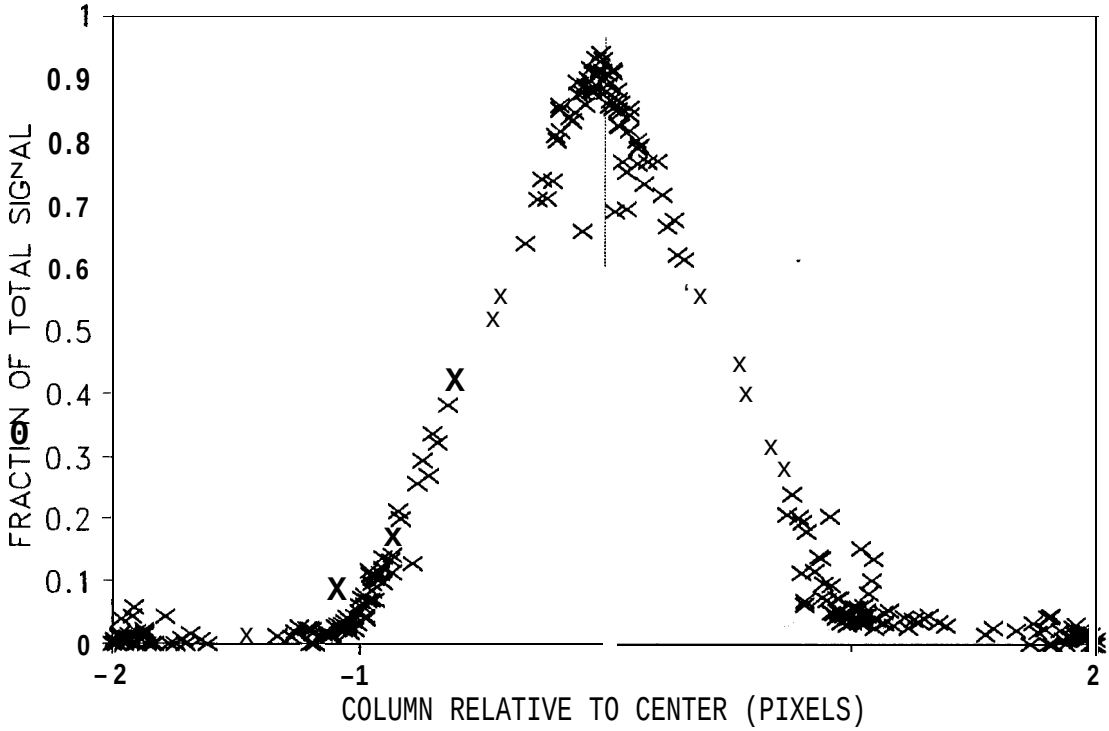

Figure 4-22. Summation-mode horizontal line" spread function plotted on a linear scale.

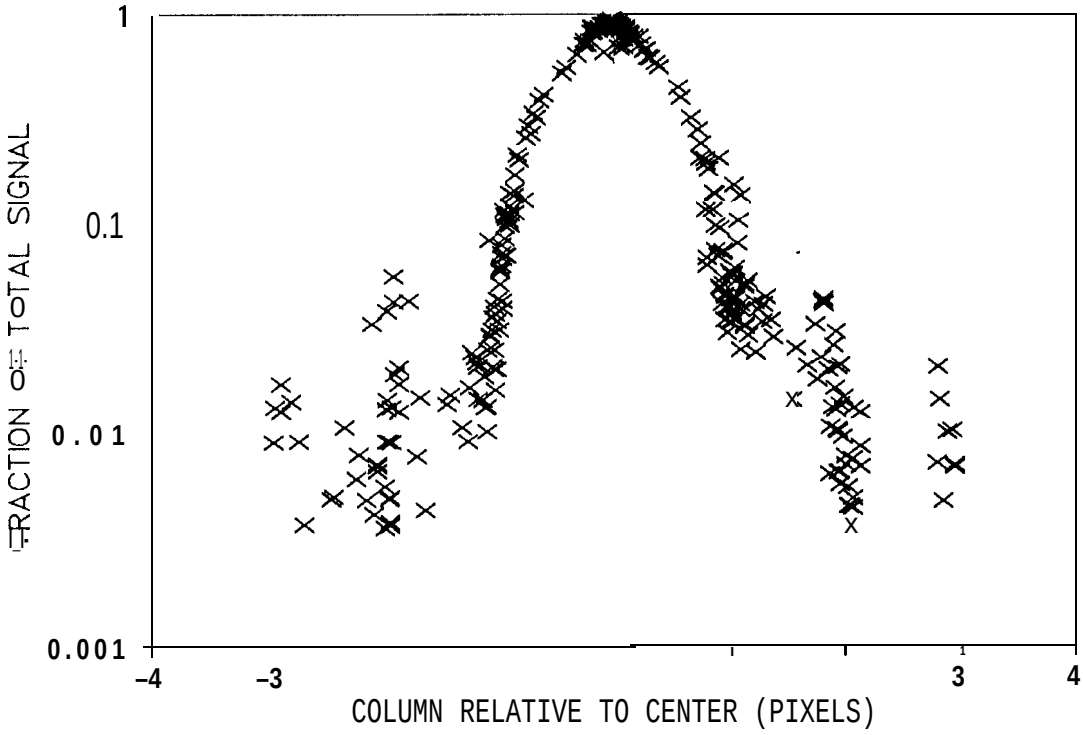

Figure 4-23. Summation-mode horizontal line spread function plotted on a logarithmic scale.

slightly raised charge pedestal to the right of the center in the distribution between pixels 1 and 2. Zero values occur as close as 1.2 columns from the center on the left but only as close as 1.7 columns from the center on the right.

The larger summation-mode pixels result in spatially undersampling the point spread function to a significant degree. As a result, the calculated sigma of any particular point image varies depending on where the center of the distribution falls with respect to the center of a pixel. Figures 4-24 and 4-25 show the dependence of the calculated sigma above and below (and to the left and right of) the mean of the charge distribution as a function of the location of this mean within a pixel. Note that the sigmas are smallest when the mean is near the center of a pixel. In the vertical direction, the sigma above the mean is lowest when the mean lies just below the center of a pixel and the sigma below the mean is lowest when the mean lies just above the center. A similar trend is seen in the horizontal direction.

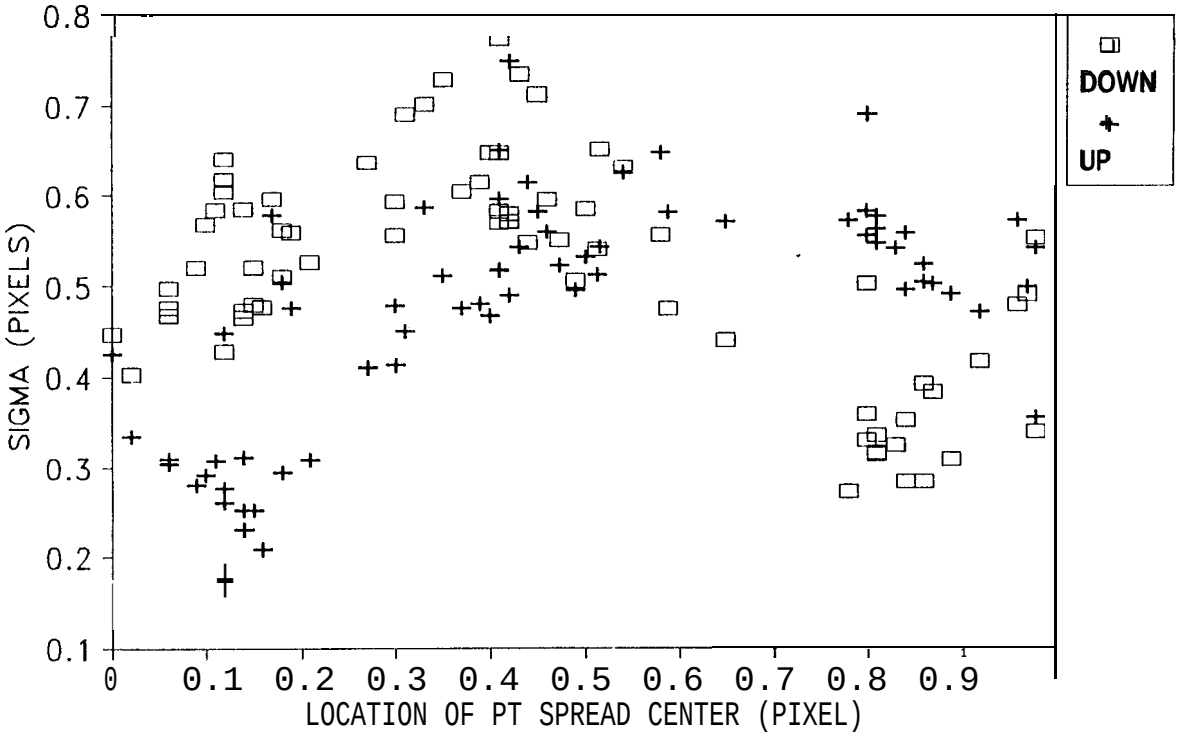

Figure 4-24. Summation-mode vertical point spread function sigmas vs. location of center of charge distribution within a pixel.

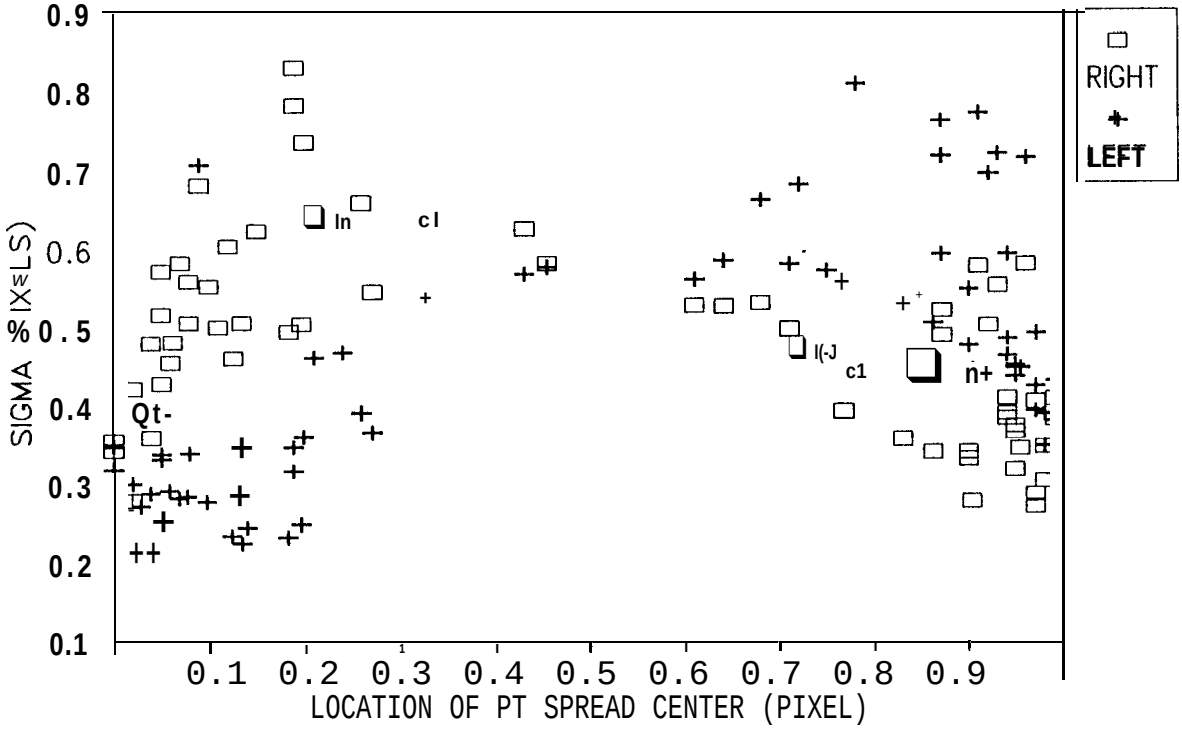

Figure 4-25. Summation-mode horizontal point spread function sigmas vs. location of center of charge distribution within a pixel

Section V - Geometric Distortion

Measurements of SSI geometric distortion through 1987 were reported on in Reference 1. Two sources of distortion were observed then - optical pincushion distortion plus a distortion that occurred within the CCD due to improper charge transfer across the transfer gate. A change was made to the CCD clocking scheme in 1988 in order to eliminate this improper charge transfer effect. Subsequent to this fix, geometric distortion calibrations were conducted at room temperature under ambient conditions and in the thermal vacuum chamber environment. The room temperature tests used both the large Fairchild collimator and the portable MVM collimator while the thermal vacuum chamber tests used only the MVM collimator. Room temperature images were acquired through the Fairchild both with and without the SSI optics cover in place while only cover-on images were analyzed through the MVM collimator. Thermal vacuum chamber images were acquired only with the cover off. The data set also included ambient and thermal vacuum chamber frames for both clear and red filters, normal and inverted CCD clocks, and 100K and 10K gain states.

One change in the analysis technique from that described in Reference 1 is that the target grid intersections are modeled as a perfectly regular orthogonal array rather than using traveling microscope measurements of the target grid intersection locations. It was determined that the random measurement errors in the locations were larger than any departures from perfect regularity and were also larger than the target manufacturer's stated accuracy.

Table 5-1 presents the rms residual geometric distortions and the maximum residual distortion for a best fit in magnification, rotation, and offset. Note that the residuals are much larger for the Fairchild collimator cases. This is so because the MVM collimator, being of the same optical prescription as the SSI telescope, effectively cancels out the pincushion distortion built into the SSI telescope. The Fairchild collimator, however, allows the SSI pincushion distortion to be measured, and this shows up as larger geometric distortion residuals. No significant distortion differences are observed for different filters, CCD clock settings, or the presence of the optics cover. The residual distortion in the Fairchild images is consistent with the theoretical level of pincushion distortion in the SSI optics. This distortion can be modeled to an accuracy of about 0.01 pixel by the following equation:

$$R - r = A r^3$$

where R = actual image distance from the center of the field in pixels

r = ideal image distance from the center of the field in pixels

$A = 6.58 \times 10^{-9}$ for the theoretical distortion.

At the corner of the frame, the distortion equals 1.19 pixels. The linear fit to a perfectly regular grid results in the intersections near the corners lying further from the center of the frame than the fit would predict (by about 0.7 pixels, as seen in Table 5-1) and the intersections midway to the corner lying closer to the center of the frame than the fit would predict.

Table 5-1. Residual geometric distortions in SSI images

Environment	Collimator	rms distortion (pixels)	max distortion (pixels)
Ambient	Fairchild	0.17	0.72
Amient	MVM	0.04	0.20
T/V, 8°C	MVM	0.04	0.22

Figures 5-1 and 5-2 show the residual errors in image space at each grid intersection for grid target images taken through the Fairchild and MVM collimators. The black points indicate the grid intersections for the perfect reference grid while the white points mark the locations of the intersections in the SSI image of the grid target. Displacements have been exaggerated by a factor of 10 to aid in visual interpretation of the residuals.

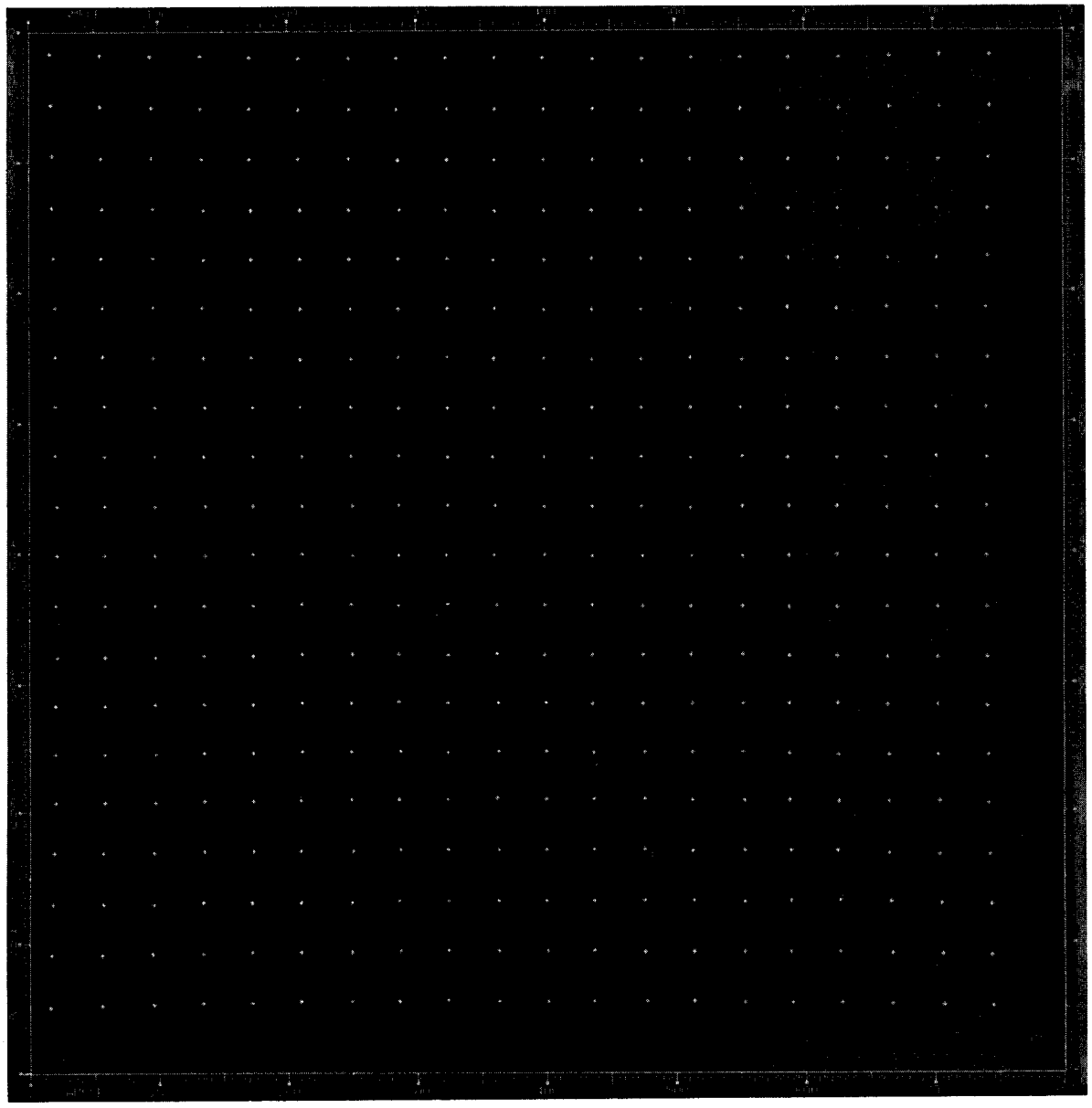

Figure 5-1. Geometric distortion residuals (10x) using the Fairchild collimator showing the SSI pincushion distortion

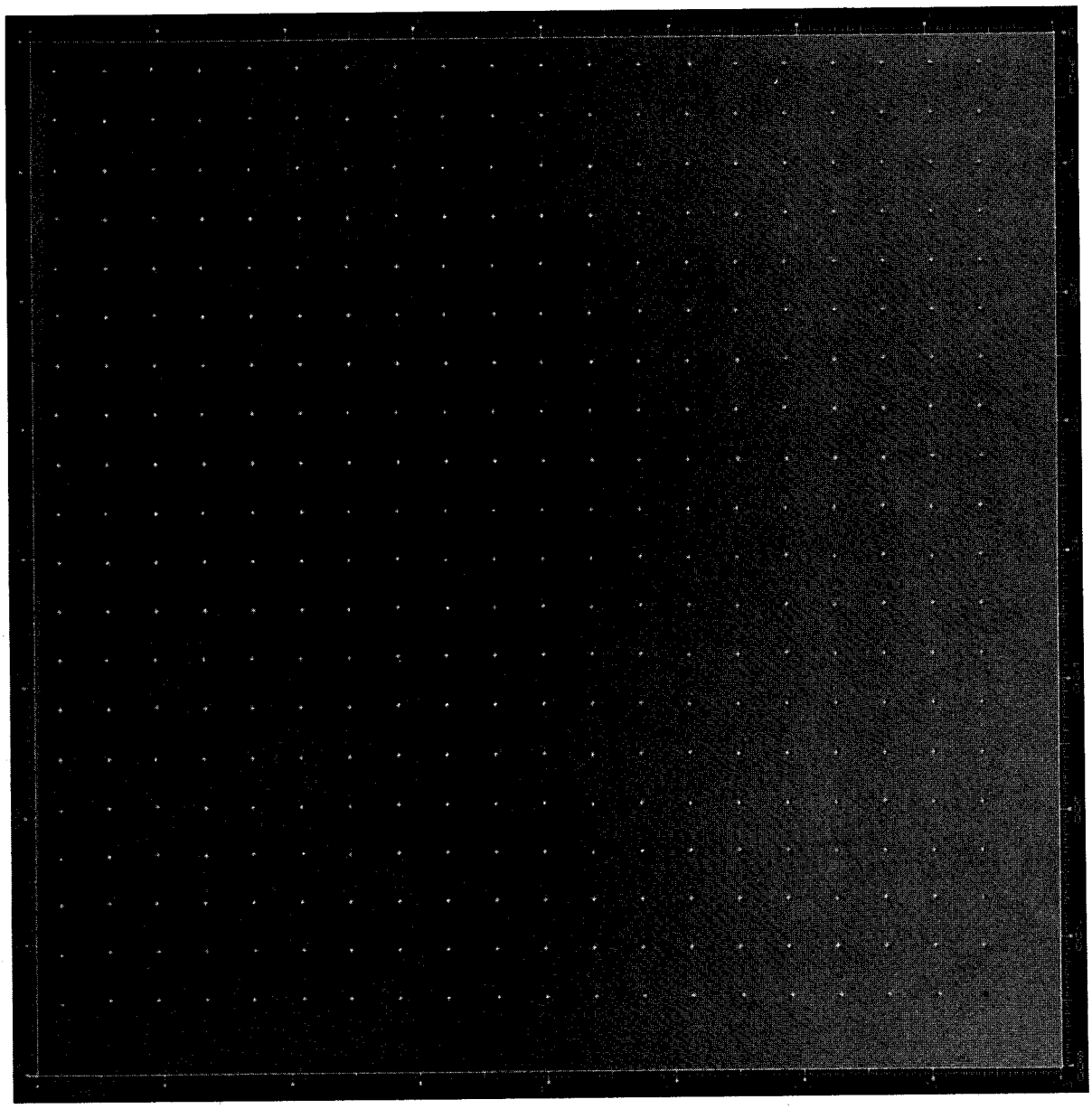

Figure 5-2. Geometric distortion residuals exaggerated 10x showing cancellation of the SSI pincushion distortion when using the MVM collimator.

Section VI - Image Entropy

Differential entropy is a measure of the level of pixel-to-pixel DN variations within an image and is an important indicator of how much the image data can be compressed before information is lost. Entropy is generally expressed in units of bits/pixel. The SSI data compressor is allocated an average of 3.24 bits/pixel across each image line (i.e., 2592 bits/line). As image entropy within a line approaches this limit, information will begin to be lost in the process of data compression. The SSI compressor can be operated in either of two modes, the selection of which determines how information is lost when the entropy in an image exceeds the allocated number of bits/pixel. In the "information preserving" mode, the number of pixels that are returned in each line is reduced if necessary, but the DN of every returned pixel can be reconstructed perfectly. In the "rate controlled" mode, the compressor truncates least significant bits (LSBs) from the pixel DN values as needed to meet the overall bit allocation for each line. LSBs are truncated over 64-pixel blocks within a line. Blocks are selected for LSB truncation in order of their entropy with the highest entropy block being selected first. As many blocks have LSBs dropped as is necessary to meet the bit allocation for a line. If necessary, a given block may have more than one LSB dropped up to a miximum of three. If dropping 3 LSBs is not sufficient to meet the bit allocation, pixels will be truncated from the end of the line as in the "information preserving" mode.

The differential entropy in an image is produced by several sources: instrument read noise, pixel-to-pixel sensitivity variations, ADC quantization noise, signal shot noise, radiation-induced noise spikes, and scene contrast. The first four of these entropy sources will be present in every image, and the entropy they produce will represent a lower limit for the entropy value in any image. These lower-limit entropy values have been determined using flat-field images at various signal levels in each gain state. Figure 6-1 plots the differential entropy vs. mean signal level measured in these flat-field images. Note that the data compressor limit of 3.24 bits/pixel is exceeded even for flat fields for average signal levels above about 70 DN in the highest gain state (gain 4) and is approached at near-full-scale signal levels in the lower gain states. The shape of the curves is determined by the dominant source of entropy at any given signal level. For low gain states, entropy is primarily due to ADC quantization noise at low signal levels and to CCD pixel-to-pixel sensitivity variations at high signal levels. For gain state 4, entropy is dominated by signal shot noise at high signal levels and by read noise at low signal levels.

Figure 6-2 shows the average amount of information loss that will occur in SSI images as a function of the image entropy level. The loss can either be in LSB truncation (in the rate-controlled mode) as shown on the scale on the left of the plot or in pixel truncation from the end of each line (in the information-preserving mode) as shown on the scale on the right.

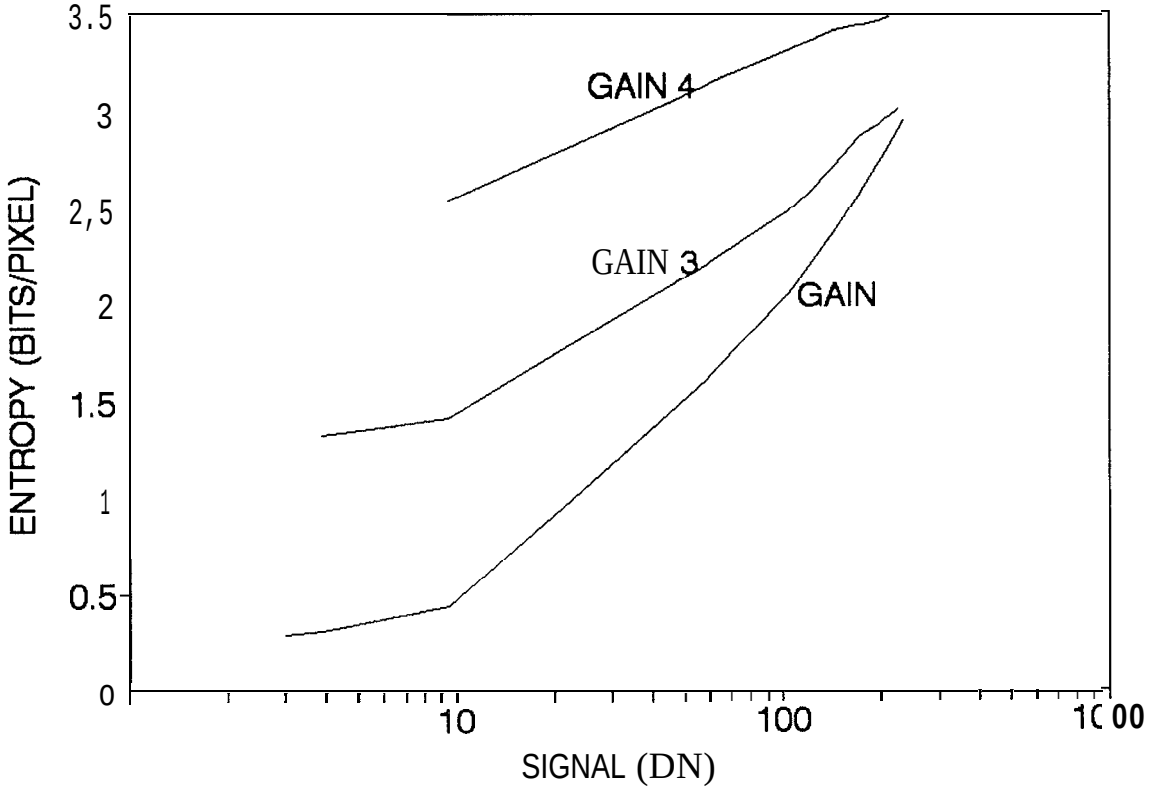

Figure 6-1. Differential entropy in SSI **flat-field** images

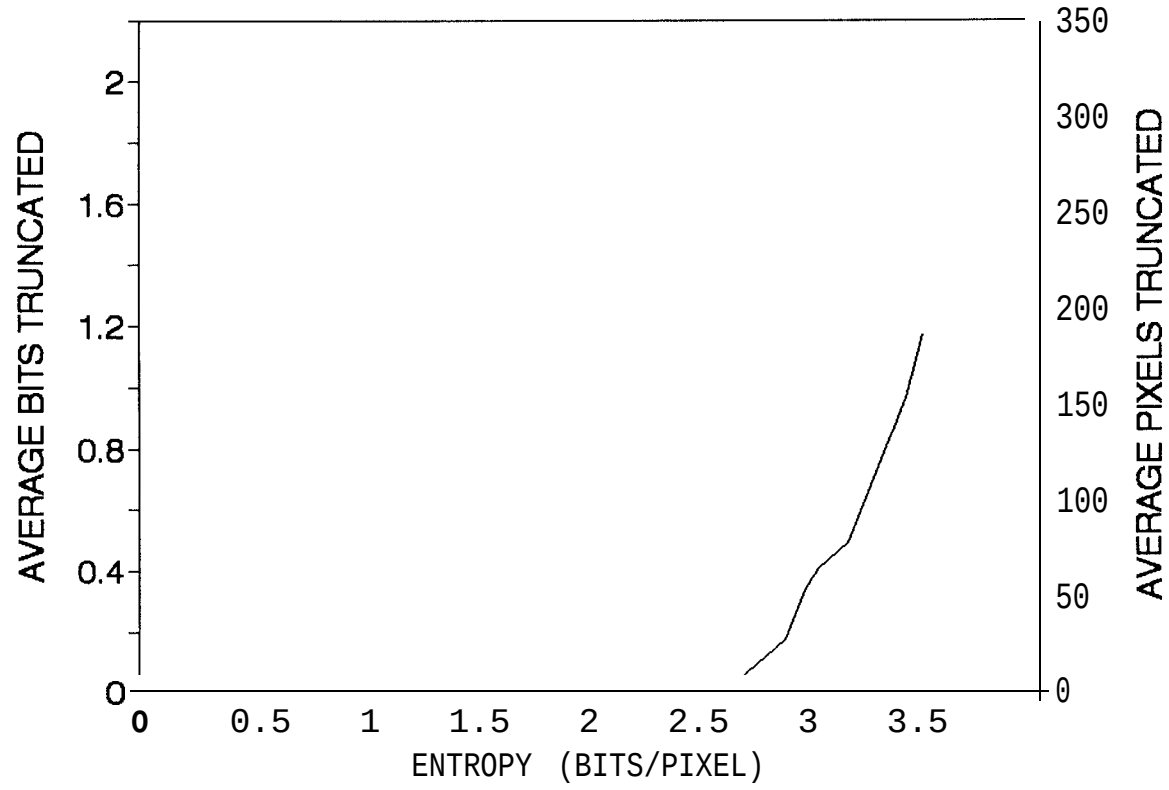

Figure 6-2. Information loss as a function of differential **entropy** level in compressed SSI images

Note that information loss begins at average entropies of about 2.6 bits/pixel or greater because at this level some lines begin to have entropies exceeding the 3.24 bits/pixel limit. By comparing Figure 6-1 and 6-2, one sees that information can be expected to be lost during SSI data compression in virtually all images of extended sources in gain state 4 and for images with average signal levels exceeding about 125 DN in gain 3 and 170 DN in gain 2. Contrast in real images and the effects of radiation noise will further reduce these threshold DN levels for information-preserving operation.

Section VII - References

1. Solid-State Imaging Subsystem Calibration Report: Part 1, H. Breneman and K. Klaasen, JPL Document D-5880, November 1, 1988

2. "Uneven Bit Weighting Analysis of 1989 SSI Calibration Data," H. Breneman to Distribution, JPL Interoffice Memorandum, 11 May 1989